Lonely Cores: Molecular Line Observations Of Isolated Star Formation

by
Ciara Quinn

A thesis submitted to

Cardiff University

for the degree of

Doctor of Philosophy

August 2013

DECLARATION

This work has not previously been accepted in substance for any degree and is not being concurrently submitted in candidature for any degree.

Signed .....

Date .....

STATEMENT 1

This thesis is being submitted in partial fulfillment of the requirements for the degree of PhD.

Signed .....

Date .....

STATEMENT 2

The work presented in this thesis is all my own work carried out under the supervision of Prof. D. Ward-Thompson and Prof A. Whitworth with the exception of the following: I did not take the SIMBA observations of the isolated core, or calibrate or reduce the data, although I carried out all of the analysis; Spitzer data was observed as part of the *c2d* and *Lonely Cores* program and were reduced and calibrated by the c2d consortia. I did not perform the colour-excess method to identify YSOs from Spitzer data; I did not produce the presented 2MASS extinction maps. I did take the CO observations of the isolated cores, using the Mopra telescope, between 2010 & 2011, and I carried out the data reduction and analysis for all of the data. This work is carried out in collaboration with Dr T. Bourke (Havard-Smithsonian - CfA). A bibilography is appended.

Signed .....

Date .....

STATEMENT 3

I hereby give consent for my thesis, if accepted, to be available for photocopying and for inter-library loan, and for the title and summary to be made available to outside organisations.

Signed .....

Date .....

ACKNOWLEDGMENTS

Firstly, I would like to thank Professor Derek Ward-Thompson for giving me the opportunity to undertake this research, and for his help and support during the PhD. I promise that I have learned that data is the plural of datum, and the presence of any 'data is' found in this thesis is just to keep him on his toes. I thank Professor Ant Whitworth for his guidance and help for the past year when he filled the role of supervisor.

I would also like to thank Dr Tyler Bourke (Harvard CfA) for allowing me to take over his research project and for helpful discussion and comments, and Dr Peter Barnes (University of Florida) for teaching me how to operate Mopra, and his invaluable help with data reduction.

The star formation group at Cardiff University have proved to be a great bunch, so I thank them all (past and present) for their help, support and friendship over the years. A special thanks goes to Dave Nutter and Jason Kirk for putting up with an endless stream of questions and cheek, and for handling my ignorance with humour and minimal teasing.

Thanks to all the postgrads/friday night pub crew at Cardiff. You have made this experience enjoyable, and it's good to know we are never alone, no matter how badly things seem to be going! Cassie and Victoria, thank you for all your moral support, weekend adventures and afternoon teas!

Annabel and Antonio, thank you for a lively and suitably intimidating viva exam, and for the comments and sugggestions that have improved this work.

Finally thanks to my family: it is finished! I give you permission to ask how things are going now! Thanks for letting me complain endlessly and never once pointing out that I was the one who got myself into this in the first place. I couldn't have done it without you, your faith in me has meant a great deal.

ABSTRACT

In this thesis, I present molecular line & continuum data of a sample of small, southern, isolated cores. I present a multi-wavelength view of the cores, by utilising optical images, 2MASS extinction maps, CO integrated intensity maps and 1.2mm continuum images of each of the cores. Spitzer data are used to identify young stellar objects local to each core, which may influence the evolution of the core.

Column densities and masses are calculated for each core. The column densities calculated from the CO and 1.2mm continuum tracers are shown to be in excellent agreement with each other, and with the peak extinction, as seen on the 2MASS extinction maps. A comparison of column density derived from 1.2mm continuum and $C^{18}O$ observations suggest that a fraction of the gas has frozen out onto the dust grains in the densest parts of the core.

The masses derived from ^{13}CO, $C^{18}O$ and 1.2mm continuum observations are compared with the virial mass calculated from the observed linewidths. The cores are found to be within 3σ of virial equilibrium in all cases, which suggests that all cores may be gravitationally bound.

I find that the observed linewidths of the isolated cores are consistent with models of star formation by turbulent dissipation. The $C^{18}O$ linewidth is observed to be narrower than the ^{13}CO linewidth, which is narrower than the ^{12}CO linewidth in all cases. This suggests that as the density of the tracer increases, the linewidth decreases. Therefore, turbulent support against collapse is removed from the inside out, resulting in stars forming in the densest parts of the cores.

I also present a proposed evolutionary diagram, based on the observed ^{12}CO and ratio of $^{12}CO/C^{18}O$ linewidths. I hypothesise that a young core will have large ^{12}CO and $C^{18}O$ linewidths. In an older core, the turbulence will have had time to dissipate in the core centre, and so the $C^{18}O$ linewidth will be narrower. For the oldest cores, the dissipation of turbulence will have occurred in the outer parts of the core and so the $^{12}CO/C^{18}O$ ratio will be small, indicating a more evolved core.

Contents

List of Figures

List of Tables

Chapter 1

An Introduction to Star Formation

1.1 Introduction

Star formation is one of the most important processes in the Universe. Stars are the building blocks of the structure we see in the Universe. The star formation process generates the mass distribution of stars and also determines the rate at which stars form in the Galaxy. To understand many aspects of galaxy evolution, planet formation and cosmology, an understanding of star formation is required.

Low mass stars, which are defined as stars with masses from $0.5M_{\odot}$ up to a few times that of the Sun, may exist for millions of years, fusing hydrogen to helium in their cores.

High mass stars, with masses greater than 8 times that of the Sun, live brief lives, quickly depleting the hydrogen in the core. Although less abundant than their low mass counterparts, high mass stars have a very dramatic effect on their envi-

ronment. They burn very brightly, and have high surface temperatures, producing stellar winds and ionising radiation, which shape the surrounding environment. At the end of their lifetimes, high-mass star turn into supernovae, ejecting elements into the surrounding interstellar space. This debris enriches the local region, so primordial gas is mixed with heavier elements, creating a system in which complex molecules can form, and which may eventually form stars and planetary systems which are observed to be rich in metals, such as the solar system.

1.2 The Interstellar Medium

The interstellar medium (ISM) is the material that fills the space between stars. The gas in the ISM is found in three phases (Field, Goldsmith, & Habing, 1969): atomic; molecular; and ionised, as described below.

1.2.1 Atomic gas

This component of the ISM is traced by observing the 21 cm line emitted by atomic hydrogen. Since its discovery in 1951 (Ewen & Purcell, 1951), the 21cm line has been of huge importance for revealing the nature of the interstellar medium in our own and external galaxies.

The atomic ISM is divided into two regimes, the cold atomic hydrogen medium and the warm atomic hydrogen medium. Throughout the Galaxy, most of the cold atomic hydrogen gas is found in discrete clumps known as HI clouds (e.g Djorgovski, 1990). Although cloud properties vary broadly, typical number densities lie in the range from 10 to 100cm^{-3}, and diameters range from 1 to 100pc (e.g.

Lo & Sargent, 1979). The warm atomic gas is observed to have number densities of $\sim 0.5 \mathrm{cm}^{-3}$ and temperatures of $\sim 8 \times 10^3 \mathrm{K}$ (e.g. Wolfire et al., 1995). The term neutral is not strictly correct for either the cold or warm gas, since some metals in both are ionised by stellar photons.

The atomic hydrogen gas in the interstellar medium is found in the Galactic disk, with a scale height of about 100pc between 4 and 8.5kpc from the Galactic center. In the outer Galaxy, the scale height appears to increase linearly with radius. Within the central bulge of the Milky Way, the HI density is very low, but it rises to a fairly uniform level between radii of 4 and 14 kpc. At larger radii the surface density declines, but in a manner that is rather uncertain because of the poorly known Galactic rotation at these distances (e.g. Gazol, Vázquez-Semadeni, & Kim, 2005).

1.2.2 Molecular Gas

Atoms can bond together to form molecules. As the most abundant atom in the Universe is H, the most abundant molecule is H_2, followed by molecules combining C, N, O and He. However the bonds between molecules are very weak, and gaseous molecules only exist in the densest regions of the ISM, where they are shielded from sources of ionisation. Molecular hydrogen is formed on the surface of dust grains in molecular clouds (Cohen, 1976). A hydrogen atom is adsorbed onto the grain surface. When subsequent hydrogen atoms strikes the grain surface, they also stick to the grain surface. Hydrogen atoms travel across the surface and eventually two will meet. The two hydrogen atoms bind to form a hydrogen molecule (H_2). The binding energy released by the formation of the molecule allows the H_2 molecule

to subsequently be released back into the gas-phase.

The global distribution of H_2 is quite different from HI. There is little molecular gas outside 10kpc, but the surface density inside climbs quickly, reaching a maximum centered at 4 - 6kpc (Savage et al., 1977). The origin of this massive molecular ring is uncertain, but is thought to be related to Galactic spiral structure. Inside 4 -6kpc of Galactic center, the density of molecular gas is seen to decrease, which is consistent with the decline in the measured star formation rate in this region (e.g. Schuller et al., 2005). Molecular gas is more closely confined to the Galactic plane than the atomic component with a scale height of 60pc at 8.5kpc from Galactic center.

1.2.3 Ionised Gas

In addition to its atomic and molecular forms, interstellar hydrogen also exists in the ionised state. Some of this gas is confined to HII regions surrounding individual O and B stars. HII regions vary greatly in their physical properties. They range in size from ultra-compact (UCHII) regions, with diameters $\leq$ 0.1pc (e.g. Hoare et al., 2007), to giant HII regions with diameters $>$ 100 pc (e.g. Melnick, 1977). Their size depends on the intensity of the source of ionising photons and the density of the region. The densities of HII regions range from over a million particles per cm^3 in the ultra-compact regions, to only a few particles per cm^3 in the largest and most extended regions. This implies total masses between 100 to $10^5 M_\odot$ (e.g. Anderson et al., 2009). Typically HII region reach temperatures of 10,000K (e.g. Anderson et al., 2009).

1.3 Sites of Star Formation

1.3.1 Molecular Clouds

Typically, the star formation process has been studied in very large, massive structures, known as Giant Molecular Clouds (GMCs). GMCs are giant structure of interstellar gas and dust. GMCs are most likely formed by compression of gas in the spiral arms of the Galaxy (Williams, Blitz, & McKee, 2000; Pringle, Allen, & Lubow, 2001). GMCs have masses of 10^5 - 10^6 $M_\odot$, diameters of the order of 10-50pc and mean hydrogen number densities of around $10^2 cm^{-3}$ (Williams et al., 2000).

High column densities shield molecular cloud interiors and prevent molecules being photodissociated by interstellar UV radiation. Cooling occurs by emission from molecules and dust grains and this, combined with the shielding, gives a typical interior temperature of 10-20K (e.g., Johnstone et al., 2001; Stamatellos, Whitworth, & Ward-Thompson, 2007). Such low temperatures mean that the cloud's thermal support is reduced and gravitational instabilities form. In turn these may become stars.

1.3.2 Isolated Dense Cores

This work considers the process of low mass star formation, in smaller, isolated clouds, known as dense cores, or Bok Globules (Bok & Reilly, 1947). Bok & Reilly (1947) observed a number of small, isolated extinction features against the background starlight on survey photographic plates. They were found to be small molecular clouds, much smaller than the GMCs described previously. They tend

to be isolated, and not associated with any GMC structures. They have masses in the range 1 - 100$M_\odot$ and diameters on the order of ∼0.1 - 0.5 pc. The majority of this thesis will study such isolated dense cores.

1.4 Constituents of the ISM

1.4.1 Interstellar Dust

The existence of interstellar dust was first inferred from obscuration or extinction of starlight (Trumpler, 1935). Much of our knowledge of interstellar dust is based on studies of the wavelength-dependence of attenuation (e.g. Draine, 2003). The wavelength-dependence strongly constrains the grain size distribution, and spectral features reveal the chemical composition. The typical dust grain size is $\sim 1\mu$m, comparable to the wavelength of visible light. The grains are mostly composed of carbon and silicon compounds (Mathis, 1990).

Although dust forms only $\sim 1\%$ of the mass of the ISM, dust grains play a central role in the astrophysics of the interstellar medium, from the thermodynamics, and chemistry of the gas, to the dynamics of star formation. In addition, dust shapes the spectra of galaxies: radiation at short wavelengths is attenuated, and energy is radiated in the infrared. It is estimated that 30% or more of the energy emitted as starlight in the Universe is re-radiated by dust in the infrared (Bernstein, Freedman, & Madore, 2002). By observing at different wavelengths, we are able to probe different dust temperatures, which allows us to investigate a range of core environments, from dust in cores that have been heated by an embedded source, to cold, dark cores that have yet to form stars.

Dust grains provide a surface where active chemical reactions can take place. They are essential for the formation of molecules in the ISM. If two atoms collide in the ISM, the most likely outcome is they simply bounce off each other. A third body is normally required to carry away the excess energy and allow the two atoms to form one molecule. The surface of a dust grain can act as an energy sink in this case. An atom can impact on the surface of the dust grain and will be held by Van der Waals forces. This binding allows the atom to move across the surface of the dust grain and interact with another atom also bound to the dust grain surface. UV radiation subsequently releases the newly formed molecule from the dust grain back into the gas phase (e.g. Shaw, 2006).

1.4.2 Interstellar Gas

The major constituent of the ISM is gas. Molecular line studies of the gas can be used to complement dust studies and increase our understanding of the sites of star formation. The gas is molecular for two reasons: firstly, the high density in molecular clouds provides a short mean free path for collisions between atomic gas and dust grains (molecule formation occurs on the surface of dust grains) and hence a higher formation rate of molecules; and secondly the molecules are not dissociated by the ultraviolet component of the interstellar radiation field (ISRF), because the embedded dust extinguishes the UV radiation and shields the molecules. Self-shielding by H_2 gas creates the same effect, and stops the radiation from destroying molecules.

Hydrogen: H_2

Hydrogen is the most abundant atom in the Universe. The most abundant molecule is H_2. H_2 is homonuclear and does not have a permanent dipole moment. Therefore its electric dipole transitions are forbidden. There are two forms of H_2: para-H_2, which occupies rotational states with even quantum numbers J=0,2,4,6 etc.: and ortho-H_2, which occupies rotational states with odd quantum numbers J=1,3,5 etc (Sternberg & Neufeld, 1999). Conversion of para- to ortho-H_2, or ortho- to para-H_2, occurs very slowly at low temperatures.

Following the allowed transitions for H_2 (selection rule J $=0 \pm 2$), the first rotationally excited state of para-H_2 is at

$$\Delta E = E(J=2) - E(J=0) = \frac{3h^2}{4\pi \mathcal{I}_{H_2}}$$

where $\mathcal{I}$ is the moment of inertia of the molecule.

$$\Delta E \simeq 7.5 \times 10^{-21} J = kT$$

$$\Rightarrow \mathrm{T} = 540K$$

At the typical temperatures observed in molecular clouds (T $\simeq$ 10 - 40K), H_2 is not significantly excited, and therefore is not a suitable tracer for molecular clouds.

Carbon Monoxide

Since H_2 is hard to observe in molecular clouds, CO is used as a tracer of molecular gas. CO is non-symmetric and so it has a permanent dipole moment. CO is abundant and relatively stable. Because it is a massive molecule, it has a large

moment of inertia and so its rotational energy levels are closely spaced and easily excited at the low temperatures encountered in molecular clouds (Combes, 1991). The first rotationally excited level of CO has energy

$$\Delta E = E(J=1) - E(J=0) = \frac{h^2}{4\pi \mathcal{I}_{CO}}$$

$$\simeq 7.6 \times 10^{-23} J = kT$$

$$\Rightarrow \mathrm{T} = 5.5K$$

which means that CO is easily excited in molecular clouds.

The most abundant isotope of CO is $^{12}C^{16}O$ (hereafter ^{12}CO). This high abundance, coupled with its low critical density, which means the ^{12}CO molecule is excited in low density regions of molecular clouds, ^{12}CO is the easiest molecule to detect. Due to the high optical depth of the ^{12}CO molecule, it is observed to trace the least dense, outer shell of the core where it remains optically thin, and information about the inner parts of the core is lost. However other, rarer isotopologues of CO, namely $^{13}C^{16}O$ (hereafter ^{13}CO) and $^{12}C^{18}O$ (hereafter $C^{18}O$) can be used to study the regions not observable with ^{12}CO.

The next most abundant isotopologue of CO is ^{13}CO. The critical density of ^{13}CO is higher than the critical density of ^{12}CO and so traces a denser region of the core. ^{13}CO is observed to be optically thick at moderate distances into the core, and so it only traces a shell of material denser than the ^{12}CO shell, before it turns optically thick. $C^{18}O$ has the highest critical density of the three isotopologues, and so is found in the densest regions of the core where star formation is expected to occur. It is also the rarest of the three isotopologues, and therefore, the hardest to detect. $C^{18}O$ remains optically thin even to the densest part of the core. Therefore, by observing the 3 isotopologues ^{12}CO, ^{13}CO and $C^{18}O$, we are

able to probe the environment of molecular cloud cores.

Other molecules

Vast numbers of molecules have been identified and detected in the ISM. CO is the most common tracer of molecular clouds, as it abundant and so is expected to have bright emission lines. However CO eventually becomes optically thick at moderate depths into the cloud, and so information about the very center of the cores is lost using only CO. Therefore it is necessary to observe other molecules. In the star formation process, the most studied molecules are carbon- or nitrogen-bearing species. NH_3, remains optically thin to larger depths than CO and so is needed for the study of very dense molecular cloud cores. NH_3 has a much more complex set of transitions than CO so is a more sensitive diagnostic of cloud conditions. Models of the inversion lines of NH_3 can be used to reproduce the internal conditions of the cloud, allowing accurate temperatures and optical depths of the densest parts of the core to be recorded.

N_2H^+ is a "late-type" tracer of star formation. It is only found in older, more evolved cores, compared to CO and NH_3 which are regarded as young core tracers. N_2H^+ does not freeze-out onto dust grains in the conditions found in dense starless cores (Tafalla et al., 2002) and so can be used to trace very dense gas. The excitation temperature and optical depth can be found by fitting the hyperfine structure which yields a direct estimate of the column density of the core and the velocity dispersion of the gas.

1.5 Spectral Emission Lines

The emission lines of CO can give information about the kinematics of gas in molecular clouds. Specifically, by studying the linewidths we can deduce information about the motion of the gas in the cloud (e.g. Emerson, 1996).

1.5.1 Line Broadening

Emission lines are not infinitesimally narrow, but are broadened by a number of processes. These processes can be grouped under two broad headings:

- Microscopic processes. These processes are mechanisms that occur on length scales smaller than the photon mean free path.
- Macroscopic processes, which operate on length scales greater than the photon mean free path, e.g. the rotational broadening.

The primary microscopic processes responsible for the finite breadth of the emission line are:

- Natural Linewidth

  From the Uncertainty Principle, any given atomic energy level i does not have a perfectly defined energy E_i, but is rather a superposition of possible states spread around E_i. As a result, transitions of electrons between any two energy levels do not correspond to an exact energy difference but a range of energies.

- Thermal Line Broadening

  In a gas at kinetic temperature T_k, individual atoms have random motions, some component of which can be away from or towards the observer, leading to red or blue frequency shifts:

$$\sigma_t = \sqrt{8 \ln 2} \sqrt{\frac{2kT}{m}} \tag{1.1}$$

  where T is the gas temperature and m is the mass of the molecular species. ^{12}CO has a molecular mass of $(12 + 16) = 28\ u$ (where u is the unified atomic mass unit = 1.66×10^{-27} kg). Therefore, the thermal linewidth of ^{12}CO is σ_t = 0.128 km/s, at 10K. ^{13}CO has a molecular mass of (13 + 16) =29u. Its thermal linewidth is σ_t = 0.126 km/s at 10K. C^{18}O has a molecular mass of (12 + 18) = 30u, and a thermal linewidth of σ_t = 0.123 km/s at 10K.

- Pressure Broadening

  Pressure broadening is caused by the presence of nearby particles affecting the radiation emitted by an individual particle. The collision of other particles with the emitting particle interrupts the emission process and by shortening the characteristic time for the process, increasing the uncertainty in the energy emitted. The duration of the collision is much shorter than the lifetime of the emission process. This effect depends on both the density and the temperature of the gas.

The primary macroscopic processes are:

- Turbulent Broadening

  This broadening process is not well defined physically. This is the linewidth that is due to non-thermal motions in the core. Non-thermal motions may

be caused by turbulence in the core, or material infalling onto the core. The broadening due to such motions can not easily be predicted.

The thermal plus nonthermal linewidth is obtained by adding the thermal and nonthermal widths in quadrature,

$$\sigma^2 = \sigma_{turb}^2 + \sigma_t^2. \tag{1.2}$$

- Self-absorption

  Electromagnetic radiation emitted at a particular point in space can be absorbed as it travels through space. This absorption depends on wavelength. The line is broadened because photons at the linewings have a smaller reabsorption probability than photons at the line center. The absorption near the line center may be so great as to cause a self-reversal in which the intensity at the center of the line is less than in the wings. This process is also called self-absorption.

- Macroscopic Doppler broadening

  Radiation emitted from a distant rotating body, such as a star or cloud, is broadened due to line-of-sight variations in velocity on opposite sides of the star. The greater the rate of rotation, the broader the line.

1.6 Cloud Collapse

1.6.1 Gravitational instability

If a star is to form in a molecular cloud, then the cloud must become gravitationally unstable, and subsequently collapse (Foster & Chevalier, 1993). We assume the cloud has an initial uniform density ρ_0 and uniform isothermal sound speed a_0. Due to a random statistical fluctuation a small part of the medium becomes slightly more dense. The density perturbation is a molecular core.

Whether a core becomes denser due to its self-gravity, or the internal pressure causes it to expand back to the same density as the surrounding medium depends upon the size of the core. There is a characteristic length for a core where thermal energy of the core which causes it to expand is counteracted by gravity, which causes collapse. The critical radius where both are equal is known as the Jeans length (R_J) (Jeans, 1902).

The Jeans length is derived by balancing the outward push of the core due to the internal pressure, and the inward pull due to self-gravity. The outward pressure due to the internal pressure is $\nabla P/\rho_0$. Since $\nabla P \sim P/r$ and $P = a_0^2\rho_0$, we have

$$\frac{\nabla P}{\rho_0} \sim \frac{a_0^2}{r}.$$

The inward pull due to self-gravity is $-GM/r^2$, where M is the mass of the core. Since $M = r^3\rho$ we have

$$\frac{-GM}{r^2} \sim -G\rho_0 r.$$

Therefore, the equation of motion is

$$\ddot{r} \sim \frac{a_0^2}{r},$$

For increasing density, $\ddot{r} < 0$, therefore

$$G\rho_0 \geq \frac{a_0^2}{r^2}$$

leading to the critical length for collapse:

$$r > r_J \sim \frac{a_0}{(G\rho_0)^{1/2}}. \tag{1.3}$$

r_J is called the Jeans length. Cores with initial radius $r > r_J$ have sufficient self-gravity to overcome the internal pressure, meaning that collapse can occur. Cores with initial radius $r < r_J$ have insufficient self-gravity to overcome the internal pressure, and so the core disperses.

1.6.2 The Jeans mass

There is an equivalent minimum initial mass,M, associated with the Jeans length. Cores more massive than a critical mass will collapse, those less massive will expand. There is an equilibrium mass where neither contraction due to gravity nor expansion due to internal pressure will occur. This is known as the Jeans Mass (Jeans, 1902)

$$M = \frac{3}{4}\pi\rho_0 r_J^3$$

$$M_J = \frac{3\pi a_0^3}{4(G^3\rho_0)^{1/2}}. \tag{1.4}$$

M_J is called the Jeans mass.

1.6.3 Theoretical collapse solutions

If we model the cloud as spherical, isothermal, with uniform density and if we impose the condition that the cloud is initially pressureless, then it will collapse in a free-fall time, t_{ff}, given by

$$t_{ff} = \left(\frac{3\pi}{32G\rho_0}\right)^{1/2} \tag{1.5}$$

where ρ_0 is the initial density.

1.6.4 The virial theorem

A molecular cloud can be treated as a collection of particles, of mass m_i, position r_i, and velocity v_i, moving in their mutual gravitational field. The moment of inertia of the cloud $\mathcal{I}$ is given by

$$\mathcal{I} = \sum_i (m_i \mathbf{r_i} \cdot \mathbf{r_i}) \Rightarrow \mathcal{I} = \sum_{\mathbf{i}} (\mathbf{m_i r_i^2}).$$

We define a scalar G as the time derivative of $\mathcal{I}$:

$$2G = \frac{d\mathcal{I}}{dt} = 2\sum_i (\frac{d\mathbf{r_i}}{dt} \cdot \mathbf{r_i}),$$

$$= 2\sum_i (m_i \mathbf{v_i} \cdot \mathbf{r_i}),$$

$$= 2\sum_i (\mathbf{p_i} \cdot \mathbf{r_i}).$$

The time derivative of the scalar is:

$$\frac{dG}{dt} = \sum_i \mathbf{p}_i \cdot \frac{d\mathbf{r}_i}{dt} + \sum_i \frac{d\mathbf{p}_i}{dt} \cdot \mathbf{r_i}.$$

So

$$\frac{dG}{dt} = \sum_i (m_i \frac{d\mathbf{r_i}}{dt} \cdot \frac{d\mathbf{r_i}}{dt}) + \sum_i \mathbf{F_i} \cdot \mathbf{r_i}$$

as $dp_i/dt = \mathbf{F_i}$ is the net force on the particle

$$\sum_i (m_i \mathbf{v_i} \cdot \mathbf{v_i}) + \sum_{\mathbf{i}} \mathbf{F_i} \cdot \mathbf{r_i}$$

$$= 2\mathcal{T} + \sum_i \mathbf{F_i} \cdot \mathbf{r_i}.$$

Where $\mathcal{T}$ is the total kinetic energy of the particles in the cloud, due to thermal and nonthermal motions. The second term of this equation can be called $\ddot{\mathcal{I}}$.

For an isolated cloud, $\mathbf{F}_i$ represents the forces acting on i due to all the other particles j, i.e.

$$\mathbf{F_i} = \sum_{\mathbf{j \neq i}} \mathbf{F_{ij}}$$

where $\mathbf{F}_{ij}$ is the force on particle i due to particle j. Thus

$$\ddot{\mathcal{I}} = \sum_i \sum_{j \neq i} (\mathbf{F_{ij}} \cdot \mathbf{r_i}) = \sum_{\mathbf{i}} \sum_{\mathbf{j \neq i}} (\mathbf{F_{ij}} \cdot \mathbf{r_i} + \mathbf{F_{ji}} \cdot \mathbf{r_j}).$$

According to Newton's third law, $\mathbf{F}_{ij}$ = -$\mathbf{F}_{ji}$, this becomes

$$\ddot{\mathcal{I}} = \sum_i \sum_{j \neq i} (\mathbf{F_{ij}} \cdot [\mathbf{r_i} - \mathbf{r_j}]).$$

We can therefore neglect short-range forces with $\mathbf{r}_i$ - $\mathbf{r}_j \ll 1$.

As equilibrium is reached when the kinetic and gravitational forces are equal,

the right-hand side of this equation must represent the force due to gravity, and so

$$F_{ij} = \frac{Gm_i m_j}{|\mathbf{r_i} - \mathbf{r_j}|^3}(\mathbf{r_i} - \mathbf{r_j}).$$

therefore

$$\ddot{\mathcal{I}} = \sum_i \sum_{j \neq i} \left(\frac{Gm_i m_j}{|\mathbf{r_i} - \mathbf{r_j}|^{\mathbf{3}}}(\mathbf{r_i} - \mathbf{r_j}) \right) = \Omega_G$$

where Ω_G is the self-gravitational potential energy of the cloud.

Combining these results we have

$$\frac{dG}{dt} = \Omega_G + 2\mathcal{T}$$

The time derivative of G must equal zero, so:

$$0 = \Omega_G + 2\mathcal{T} \tag{1.6}$$

This relation is called the virial theorem. It is a necessary condition for equilibrium. An external pressure force aids the gravitational collapse, and so the extra terms must be added to the right hand side of Equation 1.6, e.g.

$$3P_{ext}V = \Omega_G + 2\mathcal{T}. \tag{1.7}$$

1.6.5 Virial Mass

For a spherical cloud of mass M, radius R, and velocity dispersion σ, we have

$$\mathcal{T} = \frac{1}{2}M\sigma^2 \tag{1.8}$$

and

$$\Omega_G \sim -\frac{GM}{R}. \tag{1.9}$$

Substituting these into the virial theorem,

$$\sigma^2 \sim \frac{GM}{R}.$$

Therefore, there is a mass, the virial mass, at which the energies are in equilibrium, given by:

$$M_{vir} = \frac{\sigma^2 R}{G} \tag{1.10}$$

If the mass of a cloud is roughly equal to its virial mass, then it is close to virial equilibrium. If a cloud has a mass greater than its virial mass, then it will collapse unless supported by some other mechanism.

If a cloud has a mass less than its virial mass, then it is not gravitationally bound, and will probably disperse under the action of its own internal actions, unless it is confined by an external pressure.

1.7 Support Against Collapse

Molecular clouds appear to have lifetimes greater than the time it takes the cloud to collapse under gravity. This suggests that there must be support mechanisms in the cloud acting to halt collapse the due to gravity. Two possible support mechanisms are discussed below.

1.7.1 Magnetic Fields in molecular clouds

Mestel & Spitzer (1956) proposed that magnetic fields permeating the ISM could play a part in GMC evolution, and provide support against gravitational collapse. The magnetic field lines can be though of as tubes of flux frozen into the gas. Magnetic pressure provides resistance to collapse parallel to the field lines, and so acts as a support mechanism against gravitational collapse. There exists a critical mass, akin to the Jeans mass, for which the magnetic support of the cloud balances the pull of gravity and the cloud is in equilibrium,

$$M_C \approx \frac{\phi}{G^{1/2}} \tag{1.11}$$

where ϕ is the magnetic flux threading the cloud which is equal to $\pi R^2 B$ where B is the magnetic field strength, and G is the gravitational constant. If the cloud mass M is greater than the critical mass M_C it is said to be supercritical. The gravitational force exceeds the magnetic support, and so, the cloud is unstable to collapse. If the cloud mass M is less than the critical mass M_C, the cloud is subcritical. The magnetic force exceeds the gravitational force and so the cloud is stable to collapse. However, the magnetic support can be dissipated over time in a process called ambipolar diffusion Fiedler & Mouschovias (1992).

A molecular cloud is made up both neutral particles and ionised (charged) particles, created when the molecular cloud is stuck by cosmic rays or incident ultraviolet radiation. The charged particles are frozen to the magentic field lines, and move around them in roughly helical motions. The neutrals are not influenced by the magnetic field directly and drift across field lines according to the direction of gravitational attraction.

In most environments, the charged particles and neutral particles are closely

coupled, so that any motion of the charged component is transferred to the neutral component through collisions and vice-versa, and so the gas is tied to field lines. However, when the ionisation fraction (that is the fraction of charged particles) is low, such as the conditions found in molecular clouds where the high column density of the cloud shields it from ionisation, the assumption that the gas is frozen to the field lines breaks down. The charged particles remain tied to the field lines, but collisions between charged and neutrals are few, due to the low number of charged particles. As a result, the neutral gas, which dominates the mass, remains unaffected by the magnetic field and so can flow past the field lines under the influence of gravity. As the neutrals collapse towards the centre of the cloud, the total magnetic flux threading the cloud decreases, and so, according to Equation 1.11 the critical mass decreases. Eventually the core mass exceeds the critical mass and the core becomes unstable to collapse.

There is a characteristic timescale associated with the drift of neutrals past the charged particles and field lines, known as the ambipolar diffusion timescale. The velocity reached by a neutral before it collides with an ion is given by

$$v \sim gt \tag{1.12}$$

where v is the velocity of the neutrals, g is the gravitational acceleration, and t is the time between collisions. Under the assumption that the thermal velocities greatly exceed the drift velocity, the collisions can then be be estimated by averaging the cross section and the thermal velocity dispersion. Then

$$t = \frac{1}{n_i \langle \sigma u \rangle} \tag{1.13}$$

where n_i is the number density of ions, and $\langle \sigma u \rangle$ is the average over a Maxwellian velocity distribution of the product of the collision cross-section and the thermal

velocity. Then the time for the neutrals to drift past the ions is given by the ambipolar diffusion timescale

$$\tau_{AD} \sim \frac{R}{\nu} = \frac{Rn_i\langle\sigma u\rangle}{(GM/R^3)} = \frac{3\langle\sigma u\rangle}{4\pi G m_H}x \tag{1.14}$$

where R is the radius of the cloud, n_H is the gas density, $x = n_i/n_H$ is the fractional ionisation and m_H is the mass of the hydrogen atom. The typical ambipolar diffusion timescale for a cloud at temperature 10K is

$$\tau_{AD} = 7.3 \times 10^{13} yr\dot{x} \tag{1.15}$$

Thus ambipolar diffusion is a very slow process in regions of very low ionisation.

The presence of the magnetic field has an effect on the shape of the collapsing cloud. Tension between field lines provides resistance to collapse perpendicular to the field lines. Therefore the neutrals, which dominate the mass, collapse along the field lines, producing a flattened oblate spheroid, with long axes perpendicular to the magnetic field lines. Eventually, when the central density of the collapsing core is high enough, the core begins to contract perpendicular to the field direction, dragging the field lines with it, leading to a narrowing of the field lines at the centre of the core. Further out along the magnetic field, no narrowing is seen, leading to an hourglass appearance of the field lines.

Rotating clouds, in the absence of a magnetic field, will also produce flattened oblate spheroids as they collapse. In a rotating cloud, the rotation provides an outward force which counteracts the inward pull of gravity. As the cloud collapses, the radius decreases, and due to the conservation of angular momentum, the rotational speed increases. The centripetal force at the poles is small, as the distance from the axis of rotation is small, therefore the gravitational force exceeds the force opposing it, and so the material collapses along the axis of rotation. Along

the equator, the centripetal force provides adequate resistance to graviational collapse, and so the result is a flattened oblate spheroid, similar to that formed in the presence of a magnetic field.

1.8 Turbulence in Molecular clouds

Myers (1983) observed non-thermal motions in molecular line profiles of molecular clouds. Broad molecular line profiles were deduced to be the result of hydrodynamic turbulence as the observed line profiles cannot be explained by thermal broadening alone. There is additional broadening which must be attributed to bulk turbulent motions (Stone, Ostriker, & Gammie, 1998) within the clouds.

The physical processes by which kinetic energy gets converted into turbulence are not well understood. The main sources for large-scale motions are: (a) stars, whose energy input is in the form of protostellar winds, expanding HII regions, O star winds and supernovae (van Buren, 1985); (b) galactic rotation in the shocks of spiral arms (Fleck & Clark, 1981); and (c) Kelvin-Helmholtz and other forms of instabilities.

Turbulent behaviour occurs across a range of size-scales and is predicted to lead a scale-free geometry. One particular form of turbulence involves a scale-free turbulent cascade of eddies in which energy is input on the largest scales and cascades down to small scales, where it is dissipated by heating the molecular cloud (Kolmogorov, 1941). The motion of a turbulent cascade in an incompressible fluid produces a characteristic relationship between the size-scale of a turbulent eddy L and the velocity dispersion σ of that eddy, of the form

$$\sigma \propto L^{1/3} \tag{1.16}$$

This is known as the Kolomogorov-Obukhov law (Kolmogorov, 1941; Obukhov, 1962). Other sources for small-scale turbulence include sonic reflections of shock waves hitting clouds (Ikeuchi & Spitzer, 1984), cosmic ray streaming (Wentzel, 1969) and motions of field stars (Deiss, Just, & Kegel, 1990).

The cascading nature of turbulence means that eventually, the turbulence will dissipate in the molecular clouds, and so the turbulent support will decrease. Simulations of turbulent molecular clouds suggest that the turbulence decays in less than a crossing time (Mac Low, 1999). This implies that if the turbulence is to support the cloud against collapse for its lifetime, the source of turbulence must be replenished, or the cloud will collapse under gravity.

1.9 Prestellar and Starless Cores

A starless core is defined as a dense core that lacks a central condensation, which may or may not be gravitationally bound (e.g. di Francesco et al., 2007; Ward-Thompson et al., 2007). A subset of starless cores which are gravitationally bound are named pre-protostellar, or prestellar cores (Ward-Thompson et al., 1994).

Starless cores were first detected by Myers, Linke, & Benson (1983). They selected a sample of 90 regions of high optical extinction from the Palomar Observatory Sky Survey. In their survey, each of the 90 extinction peaks were observed in ^{13}CO and C^{18}O. The study showed that within regions of high optical extinction, a typical C^{18}O core was found to be 0.3pc in size with a mass of $\sim$30M$_\odot$, and gas temperature 10K. The observed sizes and temperatures of the cores were not consistent with equilibrium models, but appeared more consistent with models of core collapse.

A follow-up survey in ammonia by Myers & Benson (1983) found cores of

mass 0.5 to 10$M_\odot$ and size of $\sim$0.3pc. A small number of cores had very strong emission lines, which allowed the shape of the line to be examined. The lines were observed to be Gaussian, which is consistent with small-scale turbulence or collapse. However, there was no indication that star formation had started in the cores. When the observed properties of the cores were compared to models of spherical, isothermal clouds, it was deduced that if the clouds were only supported by thermal pressure, then they are either collapsing, or unstable to collapse, and most of the cores would be expected to form low mass stars within a few free-fall times.

Beichman et al. (1986) cross-checked the IRAS sky survey with the positions of the CO and NH_3 cores and found that half contained infrared point sources. Those without infrared sources were named 'starless' cores.

Ward-Thompson et al. (1994) surveyed 21 of the closest starless cores in ^{13}CO using the JCMT. Peak column densities were found for 17 of them. Each core was found to have a mass at least comparable to its virial mass, indicating that some may be gravitationally bound.

1.9.1 Density Profiles

Ward-Thompson et al. (1994) found that the density profiles of prestellar cores were more centrally condensed than constant density spheres but less so than those of an inverse square density profile. They suggested a flatter profile $\rho(r) \propto r^{-1.25}$ at the center which steepens to $\rho(p) \propto r^{-2}$ (the density profile of a hydrostatic core) beyond a radius of around 4000AU, a so called two-tier density structure.

Subsequent maps at improved resolutions confirmed that the profile was flatter at the center (Andre, Ward-Thompson, & Motte, 1996),(Ward-Thompson, Motte,

& Andre, 1999). Mid-infrared absorption studies also agreed and showed that for some cores the profile was seen to steepen again at 10,000AU or beyond to r^{-3} or r^{-4} (Bacmann et al., 2000).

When mapped at high enough resolution, prestellar cores show an inner, flattened dense region (e.g. Ward-Thompson et al., 1994, 1999). Protostellar envelopes are generally centrally condensed (Motte, Andre, & Neri, 1998). Ward-Thompson et al. (1999) reasoned that this change in the density profile occurs at the end of the life of the prestellar core.

1.9.2 Core Temperatures

The dust in the molecular cloud in which a prestellar core forms shields it from much of the interstellar radiation field (ISRF). As a result, the core is warmer at the edges, and the interior of the core is cooler as it is shielded by the outer layers of the core. Prestellar cores have no internal heating source and are very cold, and so emit nearly all their radiation at far-infrared and longer wavelengths. Observing the long-wavelength continuum emission allows us to study the dust and use it as a tracer of the total cloud mass.

Dust temperatures can be obtained by fitting a grey-body curve to the observed emission of the form

$$F_\nu = B_\nu(T_{dust})[1 - exp(-\tau_\nu)]\Omega, \tag{1.17}$$

a Spectral Energy Distribution (SED), where $B_\nu(T_{dust})$ is the Planck function at frequency ν for a dust temperature T_{dust}, τ_ν is the dust optical depth and Ω is the source solid angle.

A scaling law for the optical depth is used, of the form $\tau \propto \nu^{-\beta}$ with $\beta \simeq 1.5$ - 2. This is found to be the range of values appropriate for the long-wavelength regime (wavelength > 1mm). A good fit is obtained with T_{dust} = 13K and β =2. This confirms the lack of any warm dust in such cores, and consequently the lack of any embedded star or protostar.

Ward-Thompson, André, & Kirk (2002) used ISOPHOT data (90,170 and 200μm) to analyse the far-infrared properties of 18 prestellar cores. All but one showed little or no emission at 90μm. ISOCAM absorption data (Bacmann et al., 2000) allowed the calculation of energy balance for these cores. It was shown that they are externally heated by the radiation field. Using additional data from SCUBA and IRAM they were also able to create SEDs for the sample. The SED fits resulted in dust temperatures of T=10-15K for the cores.

1.10 Protostars

Once a prestellar core has evolved and become a centrally condensed, hydrostatic object, it has formed a protostar, which goes through a well studied evolution to reach the main sequence (e.g. Stahler, Shu, & Taam, 1980; Kenyon & Hartmann, 1995).

1.10.1 Early stages of Protostars

Once a protostar has formed, what remains of the core will accrete onto a circumstellar disk, and eventually onto the star itself, or it will be pushed outward from the star by emerging radiation pressure. Ultimately the star accretes most of the

mass in the system from the envelope surrounding it (Andre, Ward-Thompson, & Barsony, 2000). The four classes of a protostar's life, denoted 0, I, II and III (Andre, Ward-Thompson, & Barsony, 1993); (Lada, 1987), make up the evolutionary sequence of the protostar. Class III protostars subsequently move onto the main sequence and become stars.

Class 0 Protostars

Class 0 objects are the youngest cores which have evidence for a central hydrostatic object, as indicated by the detection of a compact centimeter-wave radio continuum source. The radio continuum indicates the presence of an internal heating source, as the emission is caused by an accretion shock formed at the surface of the protostar as material from the circumstellar disk accretes onto the protostar. Andre et al. (1993) discovered the first Class 0 object in the ρ Ophiuchus molecular cloud complex. Class 0 protostars are defined as having accreted less than half of their final main sequence mass, i.e. $M_* < M_{env}$ (where M_{env} is the mass of the circumstellar envelope). They also have no detectable infrared counterpart. Class 0 protostars are distinguished from other protostellar classifications by their large submm luminosity (L_{smm}) compared to their bolometric luminosity (L_{bol}) (Andre et al., 1993), which suggests the envelope mass M_{env} exceeds the protostellar mass M_*. L_{smm} is defined as the luminosity longward of 350μm, and is proportional to the mass of the circumstellar envelope, i.e.,

$$L_{smm} \propto M_{env}. \tag{1.18}$$

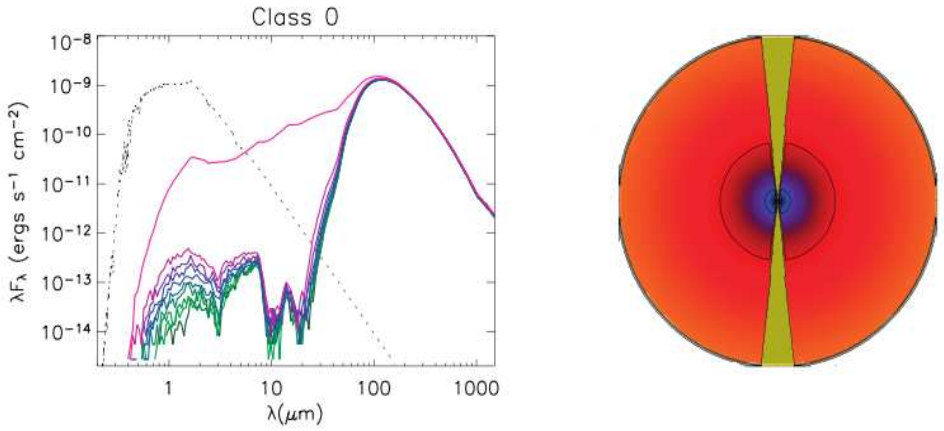

Figure 1.1: Example spectral energy distribution (SED) and illustration of a Class 0 protostar. The SED shows a flat inner profile, at short wavelengths, as the protostar is deeply embedded in the cloud and is not seen. There is a large peak at longer wavelengths, caused by dust emission in the circumstellar envelope surrounding the protostar. The SED resembles a single temperature blackbody at T= 15 - 30K. Image from Whitney et al. (2003).

Andre et al. (1993) used the equation,

$$L_{bol} = \frac{GM_*\dot{M}_{acc}}{R_*}, \tag{1.19}$$

to estimate M_* based on L_{bol}. M_* and R_* are the mass and radius of the central object respectively, $\dot{M}_{acc}$ is the accretion rate and G is the gravitational constant. Using the ratio L_{smm}/L_{bol}, it is possible to infer M_{env}/M_*.

The circumstellar envelope around a protostar is centrally peaked and has a density profile of the form,

$$\rho(r) \propto r^{-p} \tag{1.20}$$

where $p \sim$1.5 - 2 (Motte et al., 1998),(Motte & André, 2001).

Figure 1.1 shows an example SED for a Class 0 protostar. The SED resembles a single temperature blackbody at dust temperature $T \sim$ 10-30K.

Classes I, II and III were defined from the Lada & Wilking (1984) ρ Oph survey.

Class	T_{bol}	Spectral Index
	K	α
Class 0	Tbol < 70 K	$\alpha < 2$
Class I	70K <Tbol < 650 K	$0 < \alpha < 2$
Class II	650 < T_{bol} < 2880 K	-1.5 < α < 0
Class III	2800K < T_{bol}	$\alpha < -1.5$

Table 1.1: Bolometric temperature and spectral indices for Class 0 - Class III protostars

The classification is defined by the spectral slope α of the continuum spectra of a source between 2 and 25μm, defined as

$$\alpha = \frac{d\log(\lambda F_\lambda)}{d\log(\lambda)} \tag{1.21}$$

An alternative evolutionary indicator is the bolometric temperature, T_{bol} (Myers & Ladd, 1993). Using this concept, the range of values for T_{bol} for each of the classes is defined in Table 1.1 as originally defined by Myers and Ladd (1993).

Class I protostars

Class I sources are those which have now accreted more than half of their final mass, i.e. $M_* > M_{env}$. The SED rises between 2 -25μm and has two parts, one from the protostar and one from the surrounding envelope.

Class II protostars

Class II protostars are those where the envelope mass has either been accreted or dispersed. These objects are no longer shielded by their protostellar envelopes and have become visible in optical light. The SEDs of Class II sources resemble

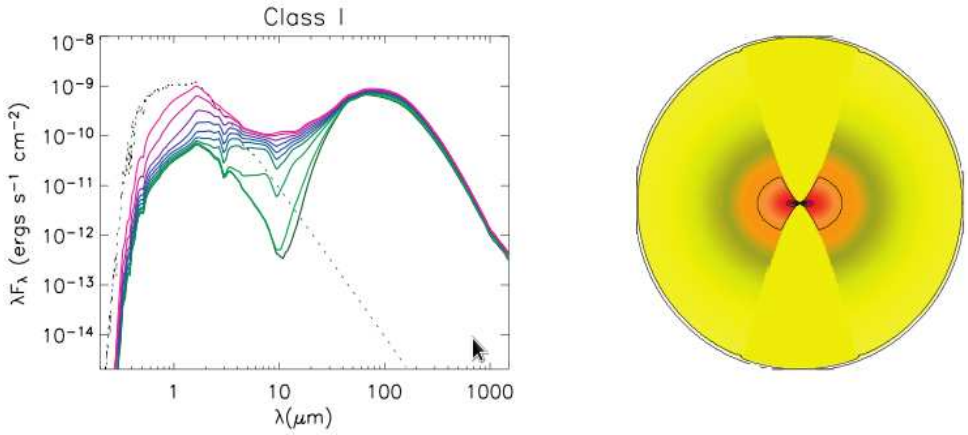

Figure 1.2: Example spectral energy distribution (SED) and illustration of a Class I protostar. As can be seen in this illustration, the circumstellar envelope is much less dense, which means that the protostar can be viewed directly. This corresponds to a sharp rise in the SED between 2 - 25μm, followed by a second peak, caused by dust emission in the circumstellar envelope. Image from Whitney et al. (2003).

a blackbody, with an additional large infrared excess, generated by the optically thick dust around the protostar. An example is shown in Figure 1.3 The slope of the SED has flattened from the Class I stage, and has a slope between 2 and 25μm, of $-1.5 < \alpha < 0$.

Class II protostars are Classical T-Tauri stars (CTTs) (Andre & Montmerle, 1994), which are young, low mass stars approaching the main sequence (Appenzeller & Mundt, 1989). They have masses in the range 0.2 - 20$M_\odot$ and luminosities in the range 0.1 - 20$L_\odot$. CTTs were first identified because they have strong emission lines in their spectra, in particular Hα. These emission lines are believed to arise in the hot gas accreting onto the central star.

Class III protostars

Class III objects have optically thin circumstellar disks, and their SEDs are reddened blackbody functions. The circumstellar disk has either been swept up by

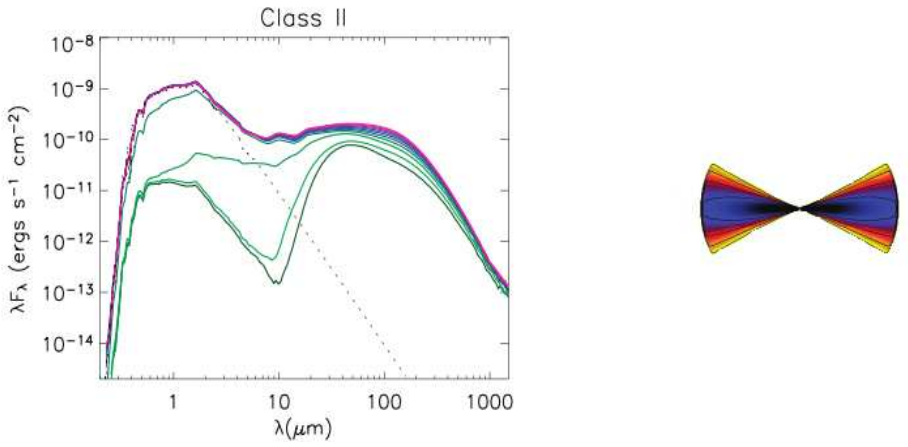

Figure 1.3: Example spectral energy distribution (SED) and illustration of a Class II protostar. As the illustration shows, the circumstellar envelope has diminished, and is now optically thin. The protostar can be viewed. This corresponds to an SED which is a reddened blackbody, but with a large infrared excess, caused by the optically thin disk. Image from Whitney et al. (2003).

forming planets or diminished due to dust coagulation into plantessimals, dispersed by the stellar wind, or accreted onto the central star. The SED has a steep, negative slope between 2-25μm, with $\alpha > -1.5$, an example is shown in Figure 1.4. These objects are weak-line T-Tauri stars (WTTs), and will subsequently join the main sequence. WTTs have weaker emission lines than CTTs (Appenzeller & Mundt, 1989). This implies there is less material accreting onto the star, and so WTTs must be at a later stage of evolution than CTTs.

1.10.2 Protostellar Lifetimes

The earliest estimates for the lifetime of Class 0 objects (0.01Myr) were based on the very small number of objects in Ophicuhus (Andre et al., 1993). The first Class 0 discoveries had powerful collimated outflows which suggested a rapid accretion rate (Andre et al., 2000). The Class 0 phase appears to be a relatively short, energetic phase following the formation of the central hydrostatic object.

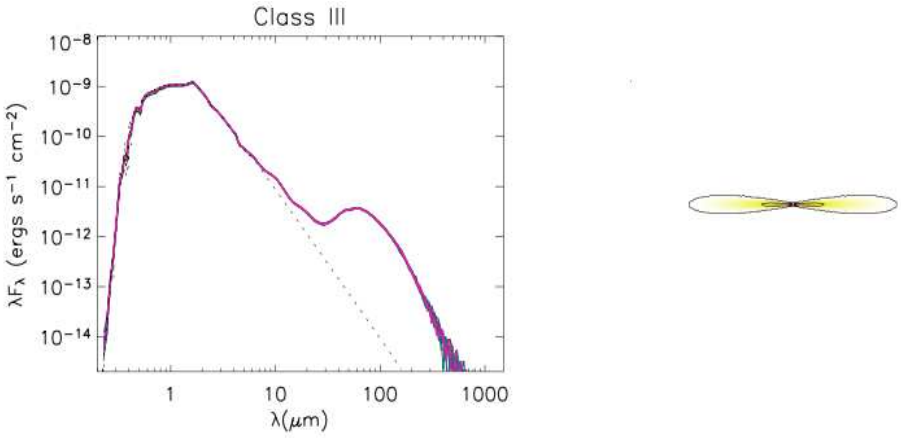

Figure 1.4: Example spectral energy distribution (SED) and illustration of a Class III protostar. The circumstellar disk has been swept up by forming planets, or dispersed by the stellar wind. This corresponds to a steep negative slope between 2 and 25μm , followed by a very small peak at longer wavelengths due to the presence of a small circumstellar disk. Image from Whitney et al. (2003).

Protostellar lifetimes were determined by Wilking, Lada, & Young (1989) using relative number counts of objects in Ophiuchus. Class II sources were estimated to be roughly 0.4 Myr old by calculating the Kelvin-Helmholtz contraction time since the end of the accretion phase (Thomson, 1892). The survey revealed equal numbers of Class I and Class II objects, which suggested equal lifetimes. However, a further study of Ophiuchus by Greene et al. (1994) found a quarter to three-quarters fewer Class I objects to Class II objects, suggesting that the Class II phase is longer than the Class I phase.

Kenyon & Hartmann (1995) showed that the situation in the Taurus region was completely different. They found roughly 10 times as many Class II and Class III sources as Class I. They suggested Class II plus Class III lifetimes to be of the order of 2 Myr. This is consistent with recent studies by Cieza et al. (2007) and Spezzi et al. (2008).

Most of these estimates were based on samples of 50-100 objects and are cloud specific. The c2d Spitzer Legacy project (Evans et al., 2009) used images and pho-

Prestellar	Class 0	Class I	Class II	Class III
0.61	0.16	0.38	1.4	0.29

Table 1.2: Table showing the length of pre- and proto-stellar ages (in Myr), for each classification of YSO, (Evans et al., 2009)

tometry from the IRAC and MIPS instruments to measure the properties of over 1000 YSO sources in five large, nearby molecular clouds (Serpens, Perseus, Ophiuchus, Lupus and Chameleon). The protostellar lifetimes calculated by Evans et al. (2009) are shown in Table 1.2. The lifetime estimates were updated by averaging across all clouds, although cloud-to-cloud differences exist.

Relative population counting is not an ideal approach to calculating protostellar lifetimes. It assumes that star formation in the region has been continuous and steady since the oldest members of the population formed. It is most problematic when there are low numbers of objects available. Nevertheless, it remains the best tool for estimating the relative lifetimes of protostellar phases.

1.11 Isolated Cores Sample

This thesis explores the physical conditions of 36 isolated small dense cores, akin to Bok Globules. Due to their simple nature, isolated dense cores are the best places to study the process of low mass star formation. They are free from the confusing effects witnessed in large molecular clouds and clusters. In the latter regions, it is hard to separate environmental influences from the intrinsic properties of star forming cores.

Despite the importance of understanding the role of environment on star formation, due to observational restrictions, previous studies of isolated objects have been restricted to a few well studied subjects, such as B68 (e.g Alves, Lada, &

Lada, 2001) and L1544 (e.g. Tafalla et al., 1998). Only recently, due to advances in detector sensitivity and mapping speed, have larger surveys started to address concerns about whether these isolated examples are typical (e.g. Ward-Thompson et al., 1999; Evans et al., 2001; Kirk, Ward-Thompson, & André, 2005; Kauffmann et al., 2008).

The sample of cores studied in this work were initially identified as extinction features on optical maps of Hartley et al. (1986) in the southern sky and Clemens & Barvainis (1988) (hereafter CB) in the northern sky, supplemented with the optical catalogue of Lee & Myers (1999). A number of cores were subsequently observed as part of a IRAS survey (Bourke et al., 1995). These observation suggested that most of the cores ($\sim$75%) are starless, in the sense that they have no associated IRAS source above a sensitivity of a few $\times 0.1$ L$\odot$ (Myers et al., 1987), and have low peak extinction values, which make them ideal for the study of initial conditions of star formation.

The cores were observed with Spitzer as as part of the Legacy program '*From Molecular Cores to Planet-forming Disks* here after (*c2d*) (Evans et al., 2003) and the follow up *Lonely Cores* program (Bourke et al., 2008). The combination of the *c2d* and *Lonely Cores* samples allows us to study star formation in isolated cores in a range of environments. The *c2d* sample includes a number of cores that are located around the edges of larger cloud complexes, and so may be directly influenced by this proximity. This, combined with the observations of more isolated cores, offers an excellent opportunity to study the effect of environment on the star formation process. The *c2d* sample contains a larger number of evolved centrally concentrated cores with mean densities $> 10^5 \mathrm{cm}^{-3}$ over younger lower density cores, or chemically younger cores. It is difficult to identify young, lower density cores (low peak A_V) in larger star-forming molecular clouds as they have a low contrast against the intercore medium, and so are not easily detected using

low-resolution large-scale dust emission, extinction or molecular line maps. The relative importance of internal and external influences on core evolution cannot be evaluated with only a sample of cores embedded within large cores. The *Lonely Cores* sample, consisting primarily of very well isolated cores and cores of low peak A_V, was introduced to address the biases of the *c2d* sample. Only with this combined sample can the full range of core evolution be studied, from recently formed cores, to chemically young starless cores, to evolved starless cores close to forming protostars, and finally protostellar cores, covering a range of environments.

The combination of *c2d* and *Lonely Cores* produces a sample of cores which are:

- Small (a few $\times$ 0.1 pc)
- Nearby; they show a lack of foreground stars, indicating they are likely to be nearby, and probably $<$ 600 pc.
- At least 3 - 4 core diameters from any neighbouring cores, so that the cores are isolated, i.e. not part of any large cloud complex.
- Not embedded within lower extinction material ($>1A_V$).
- Low extinction clouds: A_V peak > 3 in the 2MASS maps.

The positions of the cores and their distances are presented in Table 1.3. The listed Right Ascension and Declination positions are taken from the peak of the 2MASS extinction. The distances are taken from literature values. The superscripts in distance column describe the following: *(a)* Cores that are associated with the Vela Gum Nebula, and so lie at a distance of 400pc; *(b)* Cores associated with The Coalsack and lie at a distance of 175pc; *(c)* Cores associated with Chamaeleon III which are thought to lie at a distance of 200pc; *(d)* reddening estimates from Bourke et al. (1995). Clemens & Barvainis (1988) (CB) cores without a superscript

Core	Right Ascension (hh:mm:ss)	Declination (^{o} ' ")	Distance (pc)
CB29	05:22:17.4	-03:40:16	600^e
BHR17	07:19:21.3	-44:34:54	400^a
BHR31	08:18:43.7	-49:43:28	300^d
BHR42	08:26:14.9	-51:39:04	500^f
BHR34	08:26:33.2	-50:40:17	400^a
BHR41	08:27:29.7	-51:09:34	400^a
BHR40	08:32:01.1	-50:33:41	500^f
BHR38	08:34:11.1	-50:18:58	300^d
BHR39	08:34:15.9	-50:23:53	300^d
BHR56	08:44:04.1	-59:54:12	500^f
BHR48	09:36:04.0	-48:53:24	300^d
BHR49	09:36:44.0	-48:51:54	300^d
BHR50	09:41:23.0	-48:41:07	300^d
DC2983-131a	11:40:06.4	-75:16:22	500^f
DC2983-131b	11:37:52.8	-75:19:15	500^f
BHR68	11:50:00.0	-58:33:31	350^d
BHR74	12:22:46.8	-66:27:52	175^b
BHR73	12:26:46.8	-57:06:57	175^b
BHR76	12:28:24.9	-65:53:58	175^b
DC3023-177	12:35:27.5	-80:29:57	200^d
BHR79	12:37:16.4	-69:29:14	200^c
BHR80	12:37:32.7	-70:01:14	200^c
BHR81	12:39:31.1	-65:25:24	200^c
DC3162+51	14:26:07.8	-55:20:51	300^d
BHR95	14:53:23.3	-61:36:02	300^d
BHR99	15:25:45.6	-61:01:58	350^d
BHR100	15:25:45.6	-61:06:58	350^d
BHR97	15:27:14.7	-62:22:26	500^f
BHR119	16:03:05.6	-43:16:42	300^d
BHR159	17:19:13.1	-33:27:17	200^d
CB101	17:53:08.6	-08:27:00	600^e
CB112	18:08:35.8	-01:50:18	600^e
L422	18:12:05.3	-08:05:48	300^d
CB175	19:02:07.5	-05:18:45	600^e
CB176	19:02:14.4	-04:22:52	600^e

Table 1.3: The Right Ascension and Declination positions are taken from the peak of the 2MASS extinction. The quoted distances are literature values. The superscripts represent the following: *a* Associated with Gum Nebula, so expected to lie at a distance of 400pc; *b* Cores associated with The Coalsack and lie at a distance of 175pc; *c* Cores associated with Chamaeleon III which are thought to lie at a distance of 200pc; *d* reddening estimates from Bourke et al. (1995);*e* CB cores have no distance estimates and so are assigned a distance of 600pc, which was the far distance estimated by CB, (Clemens & Barvainis, 1988); *f* BHR cores without a distance measurement are assigned a far distance of 500pc, as assumed in Bourke et al. (1995).

have no distance estimates and so were assigned a distance of 600pc by the authors of CB, which is estimated to be the furthest distance a dense core could be resolved (Clemens & Barvainis, 1988) The same distance is adopted in this work. BHR cores with no superscript have no distance estimates and so are assigned a far distance of 500pc, as described by the authors.

All the 36 cores considered in this work, have been observed in J=1→0 transitions of ^{12}CO, ^{13}CO and C^{18}O. Each core has been observed at 3.6, 4.5, 5.8, 8μm and a number at 24μm with Spitzer. 2MASS extinction maps have been created for all cores. A subsample of cores have been observed at 1.2mm using the SIMBA detector on SEST. Combining gas and multi-wavelength dust observations provides us with an ideal laboratory to study the initial conditions of star formation in isolated cores.

1.12 Thesis Outline

In Chapter 2, I describe the telescopes and detectors used to observe the cores as part of the multi-wavelength survey presented here. I describe the data reduction techniques employed to remove observing artifacts from the data, and describe recipes used to make maps of the surveyed regions.

In Chapter 3, I present the data collected by the instruments described in Chapter 2, optical images taken by the DSS survey, 2MASS extinction maps, ^{12}CO, ^{13}CO and C^{18}O integrated intensity maps and 1.2mm continuum intensity maps. I record observed parameters such as peak temperatures, core sizes and observed linewidths of every core at each wavelength. I used Spitzer data to study the protostellar content of each core.

In Chapter 4, I describe the data analysis techniques employed to calculate physical properties of the cores, such as optical depths, column densities and masses. The observed linewidth of the CO data is also used to calculate the virial mass of the cores.

In Chapter 5, I discuss the results of the data analysis. I present a comparison of column density estimates derived from ^{13}CO, C^{18}O and 1.2mm continuum observations. The gravitational stability of the cores is assessed by comparing the observed mass with the virial mass of the cores. The linewidths observed at each isotopologue is compared for every core.

Finally, the results of the thesis are summarised in Chapter 6, and final conclusions are presented. Future work is also discussed.

1.13 Summary

In this chapter, I have discussed our current understanding of the low mass star formation process. I have discussed the nature of the interstellar medium and the sites of star formation. I introduce the key concepts of studying spectral emission lines, and discussed mechanisms for broadening of spectral lines. I have discussed the processes of cloud collapse and the mechanisms supporting the clouds against collapse. I have given an overview of the protostellar evolution from a starless core to a Main Sequence object. I have explained the need to study the isolated star formation process and introduced the sample studied in this work.

Chapter 2

Telescopes & Data Reduction Methods

2.1 Introduction

In this Chapter, I discuss the telescopes and detectors used to observe the data presented in the following Chapters. I describe the data reduction techniques employed to produce datasets in a format suitable for further analysis, and the steps used to remove any degrading artifacts from the data.

2.2 Mopra Telescope

The Mopra Telescope is a 22-m single-dish radio telescope located at the edge of the Warrumbungle Mountains near Coonabarabran, approximately 450km north-west of Sydney. The Telescope is operated by the Commonwealth Scientific and

Frequency Band	16-27 GHz	30-50 GHz	76-117 GHz	
	(12mm)	(7mm)	(3mm)	
Central Observing Frequency	@ 24GHz	@ 42 GHz	@ 90 GHz	@ 115 GHz
Beamwidth (FWHM)	119"	82"	38"	30"
Average T_{sys}	70K	80K	200K	600K
Antenna Efficiency	0.6	0.6	0.5	0.4

Table 2.1: Receiver parameters for the Mopra detectors. The telescope is equipped with three receivers for single dish observations at 3mm, 7mm and 12mm.

Industrial Research Organisation (CSIRO) Astronomy and Space Science division. Along with the Parkes Telescope and the Australia Telescope Compact Array near Narrabri in north-west New South Wales, Mopra forms part of the Australia Telescope National Facility (ATNF).

Mopra is situated at a latitude and longitude of -31^{o}16'04" S, 149^{o}05'59" E and an elevation of 866m. The telescope is primarily used for 3-mm spectroscopy and VLBI experiments.

For single dish observations, which are of concern for this thesis, Mopra is equipped with three receivers for single-dish observations. These have wavelength and frequency coverage of:

- 2.5 - 3.99 mm band, or 76 to 117 GHz
- 6 - 10 mm band, or 30 to 50 GHz
- 11 -18 mm band, or 16 to 27 GHz

The receivers use Indium Phosphide (InP) High Electron Mobility Transistor (HEMT) Monolithic Microwave Integrated Circuits (MMICs) as the amplifying elements. The receiver systems require no tuning and include noise diodes for system temperature determination.

Table 2.1 summarises the parameters for the three receiver systems. The only system used for this work is the 2.5 - 3.99 mm band, the others are shown for completeness.

2.2.1 MOPS: The MOPra Spectrometer

The MOPra Spectrometer (Wilson & Ferris, 2006) MOPS is a digital filterband. This separates input signal into multiple components, each one carrying a sub-band of the original signal, and allows for simultaneous observations at multiple frequencies. The mm receivers on the telescope record an 8-GHz broadband signal which is transmitted to MOPS, installed in the Mopra equipment room, via fibre optic links. MOPS offers two configurations as shown in Figure 2.1:

1. Wideband Mode

In wideband mode, continuous coverage over 8 GHz is achieved using 4 overlapping sub-bands. Each sub-band is 2.2 GHz wide with 2 x 8096 channels (1 x 8096 channels for each polarisation). Each dataset contains a total of 64768 channels (4 x 8096 x 2).

2. Zoom Mode

In Zoom Mode, the 2.2GHz wide sub-bands described above are further divided in to 138MHz wide "zoom windows". Each zoom window has 4096 velocity channels for each polarisation.

Up to four zoom windows from each sub-band are selected to produce observations in up to 16 zoom windows. This means that up to 16 molecular species can be observed in identical weather conditions simultaneously.

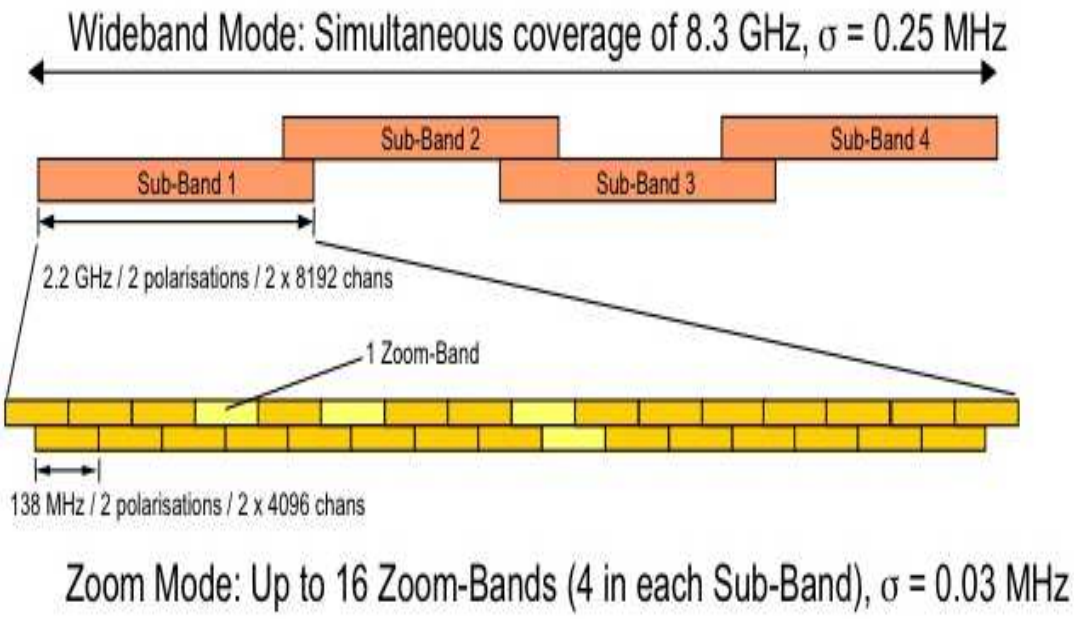

Figure 2.1: The Mopra Spectrometer, MOPS, offers two configurations, wideband and zoom mode. In wideband mode, the 8.3GHz receiver is split into four 2.2GHz overlapping sub-bands. Data are received continuously across the sub-bands. In zoom-mode, the sub-bands are further split into 138MHz wide "zoom windows". Up to 4 independent zoom windows can be selected from each sub-band, allowing observation of up to 16 different, independent frequencies simultaneously.

Receiver	Wideband Mode		Zoom Mode	
	Bandwidth	Resolution	Bandwidth	Resolution
12-mm (22GHz)	112 050 km/s	3.38 km/s	1863 km/s	0.41 km/s
7-mm (44GHz)	56 025 km/s	1.69 km/s	932 km/s	0.21 km/s
3-mm (90GHz)	30 378 km/s	0.915 km/s	505km/s	0.11km/s

Table 2.2: This Table presents the bandwidth and resolution of two observing modes offered by MOPS, Wideband and Zoom mode. As can be seen, greater bandwidth is achieved in Wideband mode, but higher spectral resolution is achieved with Zoom mode.

Table 2.2 details the bandwidth and spectral resolution achieved with both wideband and zoom mode. Each configuration has advantages and disadvantages. As can be seen from Table 2.2, higher resolutions are reached with zoom mode, but this means the frequency band is narrowed, and the number of lines detected is limited. Wideband mode allows for a vast study, over a large frequency range, but has lower spectral resolution.

My work concerns mapping isolated cores in the J=(1→0) transition of ^{12}CO, ^{13}CO and C^{18}O. As this was a CO focused study, I observed the cores in zoom mode, to take advantage of the higher spectral resolution.

2.2.2 Observing Modes

MOPS observes in an ON-OFF configuration. In this mode, an integration is acquired while the telescope tracks the target(ON) position, yielding a spectrum. An example of an ON spectrum is shown in Figure 2.2. The ON spectrum contains not only signal from the source, but also background emission, telescope system noise and attenuation and emission from the atmosphere. The ON signal needs to be corrected to retrieve the source spectrum. This is done by means of a second integration, which is acquired while the telescope is pointed toward a nearby position free of line emission (OFF). The reference spectrum is recorded. An example

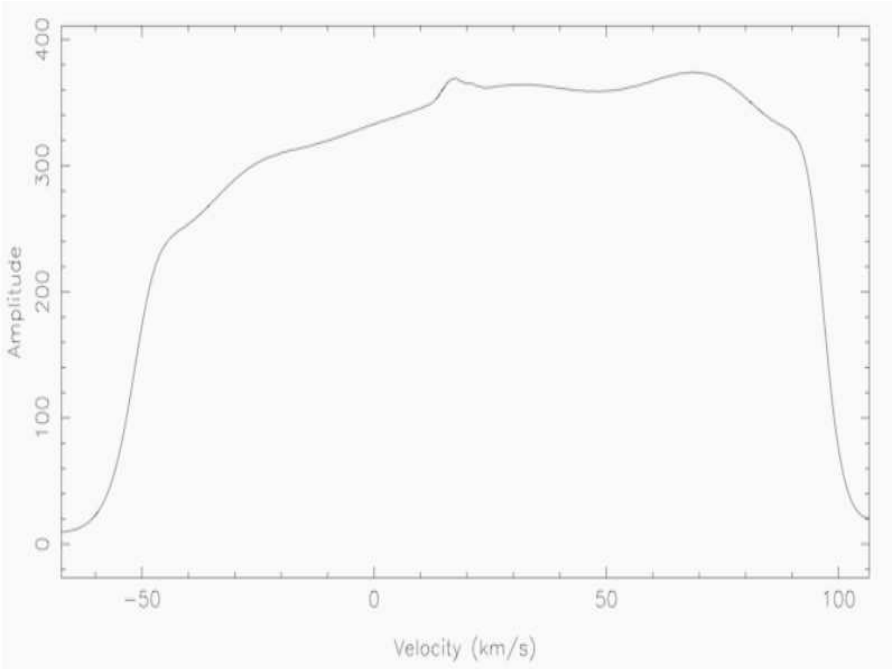

Figure 2.2: An example ON spectrum. The spectrum contains a contribution from the target source, but also noise from the sky background, and the telescope system itself. The signal also suffers from some attenuation from the atmosphere. To retrieve the source signal, the ON spectrum must be corrected using a reference OFF spectrum.

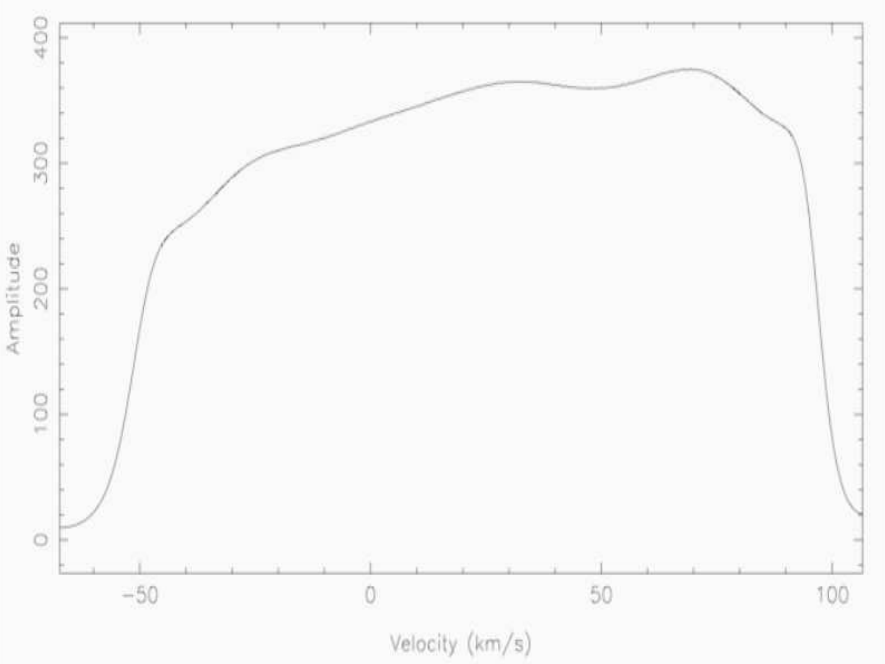

Figure 2.3: Example spectrum from a reference or OFF position. The OFF position is chosen to be within 1^o of the source, and is free of line emission. The OFF spectrum contains the same contribution from the sky background and telescope system as the ON spectrum. It also suffers from identical attenuation due to the atmosphere. The OFF spectrum is subtracted from the ON spectrum to produce a spectrum which contains only signal from the soure.

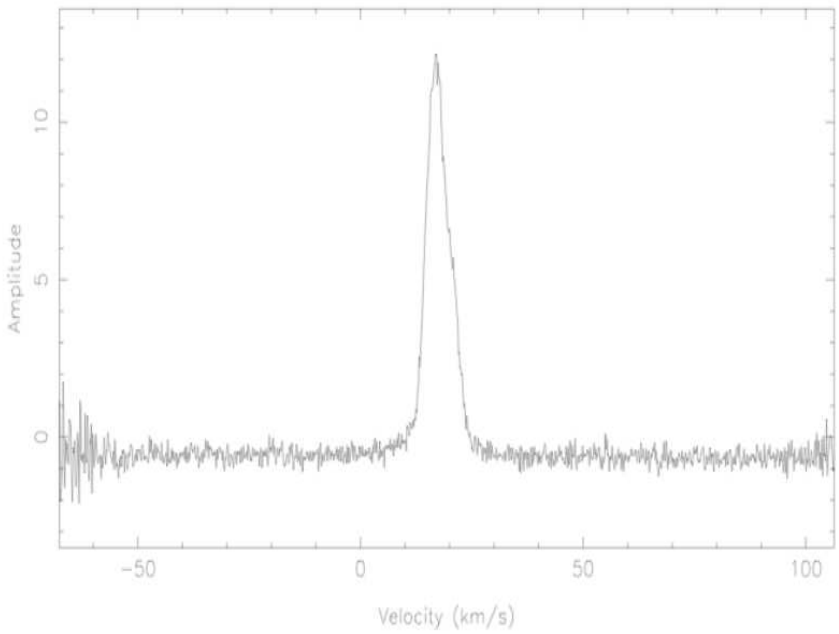

Figure 2.4: The OFF spectrum is subtracted from the ON spectrum. Eventually, when other noise sources are removed, as described in the text, the signal from the source is recovered.

is shown in Figure 2.3. The OFF position was identified in the CO maps of (Dame et al., 1987), as regions free of ^{12}CO emission. The OFF position is required to be within 1^o of the ON position, so that the OFF spectrum contains nearly identical background emission, telescope system noise and attenuation and emission from the atmosphere. The OFF spectrum is subtracted from the ON spectrum to reveal the quotient (source) spectrum. An example is shown in Figure 2.4. For longer on-source integration times, such as those used in this Mopra observing campaign, this process is repeated many times, and the reference spectrum averaged. MOPS offers two observing modes under the ON-OFF configuration:

1.Position Switching Mode

This mode moves the telescope back and forth between the target position (ON) and a reference position offset from the target (OFF), recording a spectrum at

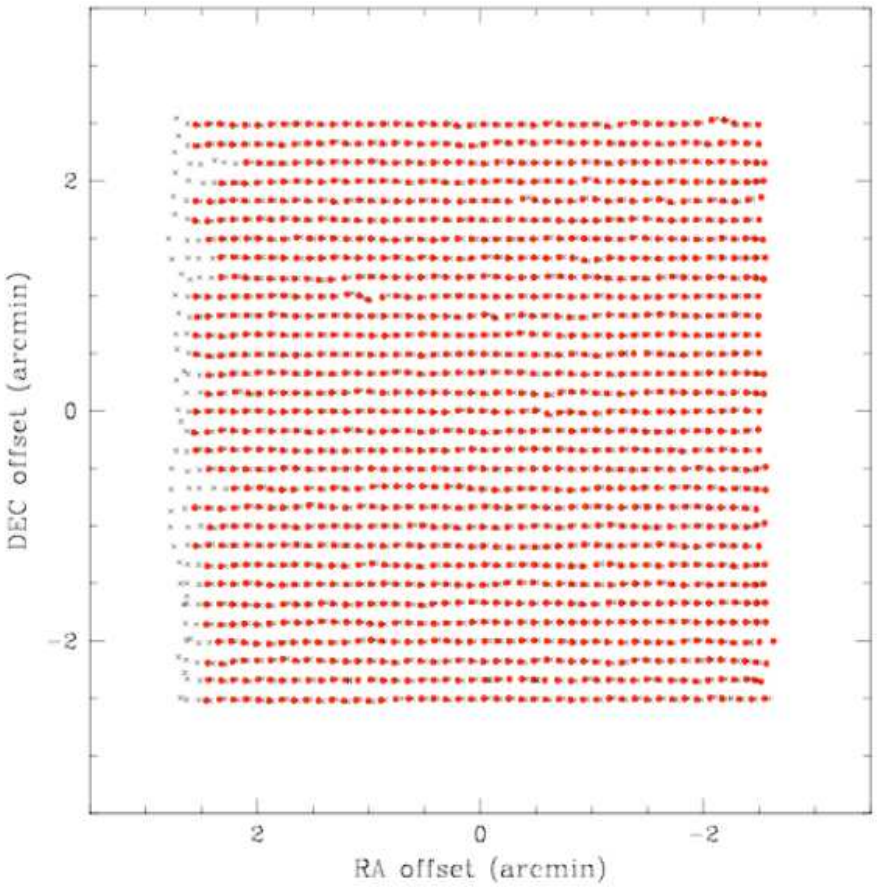

Figure 2.5: Example on-the-fly (OTF) or raster map. The telescope scans along the row, sending 2s long OTF samples of data to the correlator, indicated by each dot on the map. Each row is offset from the previous by 12" (1/3 telescope beam width). At the end of every second row, the telescope records a reference (OFF) spectrum. When the map is complete, the area is mapped again, in the orthogonal raster direction. This reduces rastering artifacts and improves the signal-to-noise of the map.

each position. The primary advantage of this position switching mode is that it produces spectra with flat baselines. However, for the purposes of this study, this advantage is far out-weighed by the large amount of time lost slewing the antenna back and forth between the ON and OFF positions.

2.On-the-fly Mapping (OTF)

On-the-fly (OTF) mapping, or raster mapping is the optimal method for spectral line mapping. As shown in Figure 2.5, in this mode, data are continuously taken while scanning along a row between pre-defined points A and B. Data are sent to the correlator in 2s intervals. The telescope is driven in a raster pattern across the sky. Each raster row is then offset by 12 arcsec from the previous row, until a square map with a size chosen by the user is built up. At the end of every two rows, a single pointed observation at a reference (OFF) position is recorded. OTF mapping is a very efficient mode of observing as it reduces the number of OFF positions necessary per observation and uses telescope drive times for data acquisition. A second map is made of the same field, in an orthogonal rastering direction to reduce any scanning artifacts and to further improve signal-to-noise.

The isolated cores were observed using on-the-fly mode to increase observing efficiency. As shown in Figure 2.6, the three isotopologues of CO, ^{12}CO, ^{13}CO and C^{18}O can be observed simultaneously in zoom mode, with high spectral resolution.

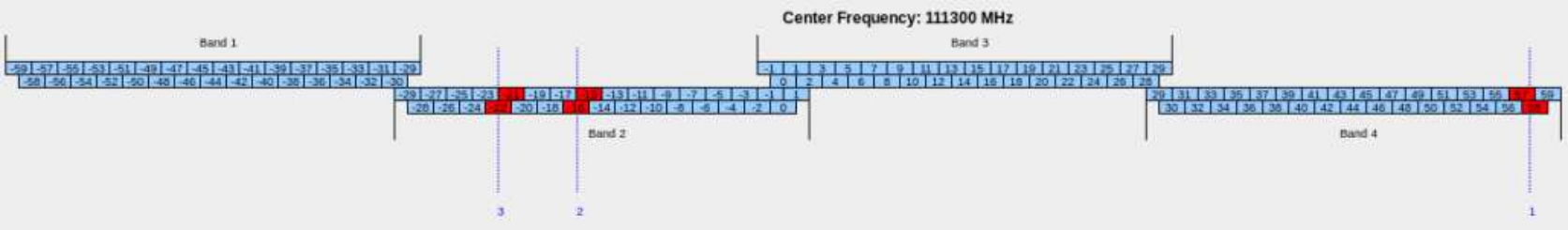

Figure 2.6: The figure shows how all isotopologues of CO can be observed simultaneously in zoom mode. The 8.3 GHz broadband coverage is divided into four overlapping sub-bands, which are then further divided into 138 MHz wide zoom windows. The highlighted zoom windows are the ones used for the CO observations. The zoom window labeled 1 is ^{12}CO (115.271 GHz), 2 is ^{13}CO (110.210 GHz) and 3 is C^{18}O (109.782 GHz)

2.2.3 Pointing

The pointing accuracy of the telescope was assessed approximately every 90 minutes by conducting a short pointing observation on a strong SiO maser.

In a pointing observation, the telescope points at 5 locations around the maser, at the center, and at both positive and negative azimuth and elevation positions relative to the center. The line profile observed at each of these locations is compared to the pointing model and suggestions for corrections to the current version are provided.

For the observations of the isolated cores, a pointing observation was made between each OTF map. The pointing accuracy was better than 10" for each observation.

2.2.4 Calibration

For MOPS spectra there are two flux temperature scales, the corrected antenna temperature T_a, and the main-beam brightness temperature T_R.

T_a is the power detected by a telescope expressed in terms of an equivalent blackbody temperature. T_a contains systematic effects from the Mopra system (receiver noise, back scattered radiation, side lobe contributions, ohmic losses etc, all of which are incorporated into a system temperature (T_{sys}) measurement) as well as the effects of atmospheric attenuation. This is essentially the Mopra temperature scale.

T_R is the calibrated antenna temperature after correction for the mainbeam efficiency of the telescope. T_R is the true brightness temperature of a source that just fills the main beam. It is a telescope-independent temperature scale which allows comparison between data taken with Mopra and data taken with a different

telescope.

T_a can easily be converted to T_R using the antenna efficiency, η, (Rohlfs & Wilson, 2004) at the observation frequency by following the relation:

$$T_R = \frac{T_a}{\eta} \tag{2.1}$$

The antenna efficientcy at 3-mm is $\sim$0.5 Ladd et al. (2005) The temperature recorded during each scan needs to calibrated, to remove telescope systematics and the effect of the atmosphere, as follows:

System Temperature

The uncorrected T_a temperature scale has contributions due to the telescope systematics and the atmosphere. The telescope systematics are constantly measured by a noise diode in the telescope's receivers. The values of the system temperature are used to correct the output spectra from MOPS (T_a).

Atmospheric Attenuation

The system temperature measurement does not take into account the attenuation of the spectral emission line caused by the atmosphere, and an electron gain caused by instrumental electronics. This can be removed from the observed signal by using the paddle/vane (or chopper wheel) method (Ulich & Haas, 1976). This procedure consists of the measurement of the receiver output when an ambient microwave absorber is placed in front of the feedhorn (a hot load), and the measurement of the receiver output when the telescope is directed towards an OFF position, which is deemed to be an area of blank sky (cold load).

The Planck blackbody equation is:

$$S(\nu) = \frac{2h\nu^3}{c^2}\frac{1}{1 - e^{h\nu/kT}} \tag{2.2}$$

where S(ν) is the power per unit frequency, ν is the frequency of radiation detected, and T is the temperature. Under the assumption of the Rayleigh-Jeans approximation $e^{h\nu/kT} = 1 + h\nu/kT$, so the equation becomes:

$$S(\nu) = \frac{2h\nu^3 kT}{h\nu c^2} = \frac{2kT}{\lambda^2} \tag{2.3}$$

For a hot load, i.e. the microwave absorber at ambient temperature placed in front of the feedhorn, the power received by the detector is

$$S_{amb} = \frac{2kT_{amb}G}{\lambda^2} \tag{2.4}$$

where G is the electronic gain. For a cold load, the telescope is pointed at a blank area of sky (i.e. an OFF position) and the power received by the detector is:

$$S_{cold} = \frac{2kT_{cold}G}{\lambda^2}. \tag{2.5}$$

The electronic gain can be removed by comparing the power received from the hot load, with the power received from the cold load, i.e.:

$$S_{amb} - S_{cold} = \frac{2kG}{\lambda^2}(T_{amb} - T_{cold}) = S_{cal}$$

$$\frac{S_{amb} - S_{cold}}{T_{amb} - T_{cold}} = \frac{2kG}{\lambda^2}$$

$$G = \frac{\lambda^2}{2k}\frac{S_{amb} - S_{cold}}{T_{amb} - T_{cold}}$$

Therefore, the signal received through the atmosphere is

$$\Delta S_{sig} = GT'_A e^{-\tau_\nu}$$

where τ_ν is the atmospheric absorption and T'_A is the antenna temperature of the source outside the earth's atmosphere. The corrected antenna temperature, T_A, can be defined as

$$T_A = \frac{\Delta S_{sig}}{S_{cal}} T_{amb} \tag{2.6}$$

In good weather conditions the system-temperature measurements (updated continuously via a noise diode) are revised with a new τ correction (using a paddle measurement) every 20 mins. The advantage of the paddle method is that it is fast and suited to changeable weather conditions.

An alternative method for measuring τ is to use a skydip procedure whereby the power is measured at several different elevation settings. The change in power with elevation yields a measurement for τ. The skydip method is time consuming ($\sim$10 mins to complete) and is only suitable for very stable weather patterns (cloud free skies), and so was not employed during my observing campaign.

2.2.5 Isolated Core Observations

I observed the isolated core sample with Mopra during June/July 2010 and May 2011. 3-mm observing only occurs with Mopra during the (southern hemisphere) Winter semester, as the atmosphere is expected to be more stable, with clearer skies and little rain.

MOPS was used in zoom-mode using the OTF mapping mode, meaning that the three isotopologues of CO that are of interest to this study were observed si-

multaneously. 5×5 arcmin maps were taken of each core. Each core was observed twice, once scanning in the Right Ascension direction, and then a second time in the Declination direction. This helped reach target sensitivity by improving signal-to-noise, and removed any rastering artifacts in the maps. As far as possible, both maps were taken in quick succession, to ensure that both maps were observed in similar observing conditions.

2.2.6 Mopra Data Reduction

The Mopra OTF data were reduced and regridded using ATNF dedicated packages "LIVEDATA" and "GRIDZILLA" (Barnes et al., 2001), as follows.

LIVEDATA

Robust Bandpass Estimation

The dominant component in a raw spectrum is the system bandpass spectrum, which varies with time because of slow fluctuations in the physical temperature of the receivers, and external influences, such as atmospheric conditions which change with pointing direction. Traditionally, bandpass removal is accomplished by observing in ON-OFF mode (Barnes et al., 2001) - as described above.

The basic method for removing the bandpass from a target spectrum, is to estimate the shape of the bandpass spectrum at the time the spectrum was acquired, and then divide the target spectrum by the bandpass estimate. Estimation of the bandpass is achieved by taking a channel-by-channel mean of the reference

spectrum, so that the bandpass estimate is the mean reference spectrum (Barnes et al., 2001).

Post-Bandpass Calibration

The primary advantage of position switching mode is that it produces very flat baselines, as mentioned above. OTF mapping mode does not produce flat baselines. However, this can be overcome during the post-bandpass calibration phase of the data reduction. For all the isolated cores observed with Mopra, a second order polynomial is fitted to emission-free regions of the line profile. This polynomial fit is then subtracted from the spectrum, resulting in flat baselines, as shown in Figure 2.7. The upper panel shows the spectrum before a polynomial was removed. The boxes illustrate the line-free regions where the baseline was estimated. The lower panel shows the spectrum after the polynomial has been removed. The baseline is now observed to be flat.

The observed frequency of a spectral line can be related to the radial velocity between the observer and the source. The relativistic expression relating frequency to radial velocity is

$$v = c\left(1 - \frac{\nu}{\nu_0}\right)$$

where v is the radial velocity, ν the observed frequency, ν_0 the rest frequency, and c is the speed of light.

In defining a velocity, a rest frame must also be given. Because of the Earth's spin on its axis and its rotation around the sun, the Earth's surface is not a good rest frame. The data is rescaled to the Kinematic Local Standard of Rest (LSKR)

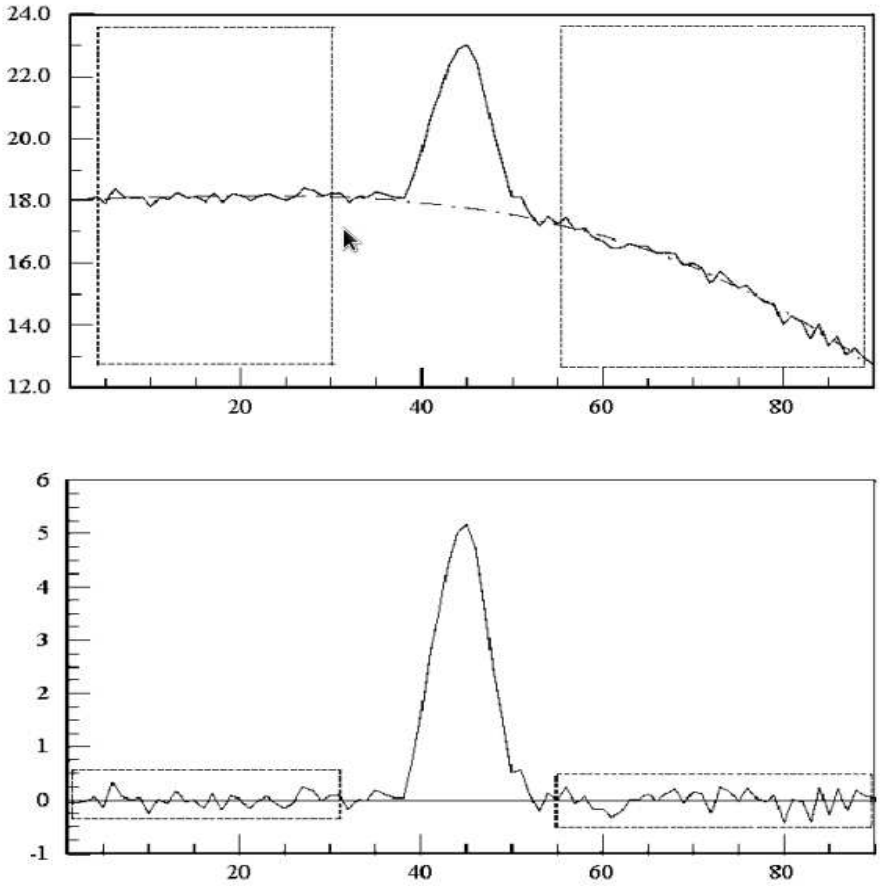

Figure 2.7: The upper panel shows an example of a source spectrum, before baseline correction, using the line free channels, shown here as the region of the spectrum in the rectangles. The baseline is estimated as a 2nd order polynomial. The polynomial fit is shown as the dashed line in the upper panel. The polynomial fit is removed from the spectrum. The result is a spectrum with flat baselines, as shown in the lower panel.

Doppler frame which accounts for motion of the solar system relative to a collection of local stars, and so makes it an appropriate rest frame for Galactic Astronomy.

The spectra were also scaled and shifted by a fraction of a channel so the reference frequency is an integer multiple of the original channel spacing, to be compatible with the gridder routine described in the next section.

GRIDZILLA

The above section described how the 2s long OTF samples were "cleaned-up" and calibrated. However, the 2s long samples need to be combined to produce a map of the entire core. The 2s-long OTF samples are converted into position-position-velocity cubes. This requires placing the individual spectra on a regular grid of 12" pixels, i.e., gridding. The objective of gridding is to reconstruct the flux at a certain position (pixel) on the sky.

For each pixel in the map, the gridding process:

1. determines which OTF spectra will contribute to the pixel, using the positional information included in the header of each spectrum;
2. rejects those spectra which appear to contain corrupt data, when the T_{sys} measurement was above the threshold value;
3. assigns a weight of T_{sys}^{-2} of each remaining spectrum, and
4. calculates the value of the pixel based on the input data and weights.

The effective telescope half-power beam-width (HPBW) is smoothed to 40" from the intrinsic 36". This improves the signal-to-noise ratio (S/N) without compromising on resolution.

The spectral line data-cubes produced by following this data reduction technique have low, somewhat variable rms noise levels, due to variations in weather and coverage, as discussed in the next Chapter.

2.3 The Swedish ESO Southern Telescope: SEST

The Swedish-ESO Submillimeter Telescope (SEST - Booth et al. (1989)), was a 15m diameter radio telescope, that operated in the frequency range 70-365 GHz. It was built in 1987 on the ESO site of La Silla, in the Chilean Andes, at an altitude of 2400 meters and latitude and longitude of 29^{o}15'34" (S), 70^{o}44'04" (W). The telescope was built on behalf of the Swedish Research Council and the European Southern Observatory (ESO). At the time, it was the only large millimeter /sub-millimeter telescope in the southern hemisphere. SEST was operated by the Swedish National Facility of Radio Astronomy, Onsala Space Observatory at Chalmers University of Technology, which was responsible for the receivers and the computer software. ESO were responsible for the Mechanical and computer hardware maintenance as well as maintenance of the control building. The telescope was decommissioned in 2003.

2.3.1 The SEST IMaging Bolometer Array: SIMBA

SIMBA was a 37-channel hexagonal bolometer array, operating on SEST at 1.2mm. The HPBW of a single element was 24 arcsec, the separation between elements on the sky was 44 arcsec. Observations were taken using a fixed secondary mirror in

a fast scanning observing mode, with a typical scan speed of 80 arcsec s^{-1}. The resultant pixel size of the maps, after processing, was 8 arcsec/s.

Due to the absence of a chopping secondary mirror, the detector was used in ON-OFF mode, where four pairs of elements were used to form output channels. Each channel gave the differential signal between each pair. One channel was used to monitor and to reduce the sky fluctuations.

2.3.2 Isolated Core Observations

The isolated cores were observed between June 2001 and August 2003. The typical map size was 600 arcsec $\times$ 1000 arcsec. On average, each core was covered by nine maps taken at different hour angles, in order to reduce fast-scanning artefacts and the noise level. The median of the residual noise in the center of the final co-added maps is 10mJy/beam (RMS). The edges of the maps are noisier due to lower coverage caused by the observing technique. Sky dips were performed at least once every three hours to determine the atmospheric opacity. The zenith opacity values during the observations ranged from 0.10 to 0.45. The positional accuracy was determined to be 2-3 arcsec by performing frequent pointing measurements on Centaurus A, η Carina and Uranus. Maps of Uranus and Neptune were taken for calibration purposes.

2.3.3 Data Reduction

The cores were observed by SEST in fast-scanning observing mode, with regular skydips in order to monitor the sky conditions and to correct for the opacity in the data reduction procedure. Regular pointings were also taken in order to maintain

source pointing accuracy.

Data reduction was performed using the MOPSI (Mapping On-Off Pointing Skydip Imaging) software package, which was developed by Robert Zylka (Zylka, 1996) [1]. At the time of SIMBA's inception, the fast-scanning method of observation was still a relatively new technique and accordingly, an entire set of reduction procedures had to be established. The reduction procedure is structured into several steps as described here, each of which is necessary in order to attain reliable results.

1. Gain Elevation Correction

   Over time, the telescope dish suffered from deformation and slight variation of its optimal shape, which was as a consequence of its own weight. The distortion of the shape of the main dish was elevation dependent. The distortion was responsible for changing the effective intensity on the sky as the elevation varied and thus ultimately must be corrected for.

2. Opacity Correction

   Radiation from a source did not arrive at the telescope unaltered from the form in which it was emitted. Instead, as radiation passed through the atmosphere, it was modified by atmospheric extinction. The data must therefore be corrected for the air-mass it traversed on its way through the atmosphere. The elevation-dependent factors for opacity correction were derived from the zenith opacity measures as $\tau_0 \sec\theta$, where τ_0 was determined from the skydip measurements.

3. Baseline Fitting

   Fluctuations in the sky background and/or electronic instabilities in the in-

[1] The data have been reduced with the mapping software package developed by Robert Zylka. This software uses the "restoring" algorithm for Emerson, Klein and Haslam (1979), the "converting" algorithm of Chris Salter (1983), and partly the NOD2 and GILDAS libraries.

strument caused baseline drifts. In addition, each of the detectors had different zero-point offsets. In order to minimise or remove these influences, baselines were subtracted. Baselines were fitted to the whole time-series of the data with a polynomial of order x, where x is user-specified. The area (base range) in the channel maps, where the pending baseline fit was carried out, is defined in the on-line reduction program.

4. Despiking

   Spikes arise in the data from electronic discharges or cosmic rays. It is essential to remove spikes, which can cause artificially high noise levels, mimic real emission, or even modify the measured flux of a source. However, despiking can damage strong sources by clipping the peak intensity distribution, and this step should be skipped for these sources.

5. Deconvolution

   The fast-scanning mode of operation requires AC coupling of the single bolometers in order to reduce the noise at low frequencies. This is achieved with a high-pass filter within the bolometer electronics. The amplifier adds a low-pass filter, which produces a bandpass modifying the real signal in an unusual way. As a consequence of the electronics, the fast-scanning mode creates signal distributions with a negative dip. Therefore the signal was restored with a deconvolution procedure, which divided it by the bandpass filter function. Essentially, deconvolution restores the original shape of the source signal.

6. Sky-noise Reduction

   Atmospheric fluctuations contributed greatly to noise in the image and needed to be removed from the data, as they can drastically increase the signal-to-noise ratio. Improper settings in the skynoise reduction can also reduce the

intensity of the source.

7. Map Creation

   All channel maps were co-added and the coordinate system was transformed from horizontal to equatorial.

Data reduction was performed using a modified on-line data reduction script which encompasses the aforementioned procedures. For a thorough and advanced data reduction, it was necessary to perform these procedures in three consecutive and iterative steps, with slight changes between the steps. The initial stage enabled baseline fitting to the data, whilst the second reduction iteration created a source model which was applied in the final reduction step to create the map.

The data were also calibrated using observations of the planets. Mars is a common submillimeter calibration source. It has a well established elliptical orbit, meaning that the Sun-Mars distance can be calculated accurately. The reflective properties of the surface of the planet have been modeled e.g. Wright (1976), by combining information on the albedo, specific heat, density and conductivity of the planetary surface. Combining the information on the Sun-Mars distance and the reflective nature of Mars allows us to calculate the amount of radiation incident on and reflected by the surface of the planet. The counts received at the telescope are converted into the expected flux for Mars, and all other observations are calibrated relative to this. The models for the expected brightness temperature of Mars are expected to be accurate to within $\pm$ 5%. If Mars is not observable, calibration is achieved by observing other planets, such as Jupiter and Uranus (Griffin et al., 1986) (Griffin & Orton, 1993). However, models for the brightness temperature for the secondary calibrator sources are based around the Mars model and so have larger uncertainties.

Secondary calibration sources can be used when planets are unavailable. The

secondary calibrators include protostars and proto-planetary nebulae. Some of the sources are variable, but are well understood due to a large number of observations. The secondary calibrator sources are calibrated using the primary sources.

The data will be discussed in Chapter 3.

2.4 Spitzer Space Telescope

The Spitzer Space Telescope (SST) was built as the final mission in NASA's Great Observatories Program - a family of four space-based observatories, each observing the universe at a different wavelength. It was launched in August 2003 and observed at 3-180μm with an 0.85m mirror. The focal plane was cooled to 5.5K and consisted of three instruments: the Infrared Array Camera, IRAC (Fazio et al., 2004), the Infrared Spectrograph, IRS (Houck et al., 2004) and the Multiband Imaging Photometer, MIPS (Rieke et al., 2004).

2.4.1 Spitzer Detectors

Infrared Array Camera (IRAC)

The Infrared Array Camera (IRAC - Fazio et al. (2004)) is one of the three science instruments on Spitzer. It is an imaging camera, designed to detect light at near- and mid-infrared wavelengths between 3.6 and 8.0 microns. It is a general purpose camera that was used by observers for a wide range of astronomical research programs.

IRAC is a four-channel camera, each channel measuring light at one particular

wavelength. It takes simultaneous images at wavelengths of 3.6, 4.5, 5.8 and 8.0 microns, and each of the four detector arrays in the camera is 256 × 256 pixels in size. IRAC uses two types of material in the detector arrays: the two shorter wavelength channels have detectors made of indium and antimony, and the two longer-wavelength channels have detectors that have been treated with arsenic.

Multiband Imaging Photometer (MIPS)

MIPS (Rieke et al., 2004) is an imaging camera, which observes at the far-infrared wavelengths of 24, 70 and 160 microns. MIPS is also capable of simple spectroscopy. The detector array for the 24 micron mode is 128 × 128 pixels, and is made of silicon that has been treated with arsenic. The 70 micron and 160 micron arrays are much smaller, being 32 × 32 and 2 × 20 pixels respectively. Both are made of germanium treated with gallium. The 70 micron detector array is also used to take simple spectra from 50 - 100 microns. MIPS can observe a 5'× 5'section of the sky at any one time at 24 microns. At 160 microns it observes a smaller patch of sky measuring 0.5'× 5'.

Isolated Core Observations

The isolated cores in this sample were observed with IRAC and MIPS as part of the c2d (Evans et al., 2003) and 'Lonely Cores' (Bourke et al., 2008) surveys, between 2004 and 2008. The Spitzer surveys covered both northern and southern hemispheres, but only the cores that were sufficiently far south to be observed by Mopra are included in this work.

2.4.2 Spitzer Data Reduction

All Spitzer data reduction was performed using Cluster Grinder, an IDL software package Gutermuth et al. (2008) as summarised below. The modules within the package rely heavily on the IDL Astronomy Users Library (Landsman, 1993).

The raw IRAC and MIPS images were reduced by the Spitzer Science Centre (SSC) using the standard IRAC pipeline to produce Basic Calibrated Data (BCD) images (Makovoz et al., 2006). These BCD images were created by subtracting the dark and bias levels from the raw data, followed by flat-fielding and sky subtraction.

Dark and bias levels were removed by observing a region of sky near the north ecliptic pole. The data were combined in such a way as to reject stars and other astronomical objects. The resulting image of the minimal uniform sky background contains both bias and dark current, and, when subtracted from the science data, removes both of these instrumental signatures. This procedure also subtracts a component of true celestial background. A COBE-based model estimate of this component is added back on to mitigate this effect (Arendt et al., 1998).

The images were also flat-fielded. A flat-field image was derived from many observations of high zodical background regions of the sky in the ecliptic plane, which ensured a relatively uniform illumination with sufficient flux on all pixels such that observations were relatively quick to perform. The data were combined with object identification and outlier rejection, creating an object-free image of the uniform celestial background. An identical observation made at the north ecliptic pole was subtracted and the result normalised to create the flat-field. The science images were divided by the flat-field image to remove the pixel-to-pixel gain variation across the array.

In addition, the SSC pipeline improves BCD images with custom treatments

for bright source artifacts “pulldown”, “muxbleed” and “banding”; (Hora et al. (2004) - Pipher et al. (2004)). Muxbleed occurs across rows around moderately bright sources. It is believed to be a result of operating the arrays at unusually cold temperatures. When a bright source is read out, the cold electronics do not return to their quiescent state immediately. The result is a ghosting effect along the pixel readout channels. The flux is not real and it needs to be removed from the image. The effect is removed by applying a modified polynomial correction to each pixel. The correction applied at each pixel depends on its proximity to the bleeding pixel and the severity of the muxbleed.

Pull-down occurs when a bright star or cosmic ray on the array reaches such a detection level that there is a change in the intensity of the column in which the signal is found. When pull-down occurs, the intensities of the pixels above and below the source within the same column are lowered. The effect is limited to the brightest sources. The amplitude of the column pull-down does not scale linearly with the flux of the source or the brightest pixel. Corrections involve taking the mean of each column, identifying columns that deviate from the local average by more than some threshold, and then adding back on a constant to the apparently affected columns.

All images were calibrated using primary and secondary calibrator stars. Primary stars are used to monitor the long-term variations in the absolute calibration. The secondary calibrators were used to monitor short-term variations in the absolute calibration. All frames are combined into mosaics with WCSmosaic (Gutermuth et al., 2008) such that rotation and spatial scale distortion are performed in one transformation, to minimize smoothing. IRAC mosaics were constructed at their native pixel scale of 1.2” per pixel. Redundancy-based outlier detection and removal is also performed during mosaic construction, eliminating transient signals such as cosmic ray hits.

2.5 2MASS

The Two Micron All-Sky Survey (2MASS - Kleinmann (1992)) is a ground-based near-infrared survey. The University of Massachusetts (UMass) was responsible for the overall management of the project, and for developing the infrared cameras and on-site computing systems at its two facilities. The Infrared Processing and Analysis Centre (IPAC) is responsible for all data processing through the production pipeline, and the construction and distribution of the data products. As 2MASS is a ground based survey, atmospheric transmission and ambient thermal background significantly constrain the choice of wavelength bands. The longest wavelength atmospheric band that is not severely compromised by thermal background emission is the K band (Johnson, 1962). The project's name, 2MASS, derived from the desire to produce a complete and reliable survey at the longest wavelength accessible, with good sensitivity from the ground: 2μm.

Distinguishing the effects of interstellar extinction and identifying stellar and extra-galactic populations requires at least three bandpasses. The two infrared atmospheric bandpasses immediately shortward of the K band, namely the J band (1.2μm) and H band (1.6μm), were obvious choices for 2MASS.

2.5.1 Telescopes and Detectors

The necessary sensitivity level required by the main science drivers of the survey, constrained by the practical limitations of resources available to survey the sky in the mid-1990s, established the pixel size, array format, telescope size and integra-

tion time for the 2MASS.

Integration time per sky pixel in an all-sky survey scales with the number of detector pixels available in each band. An ideal survey instrument contains a large number of large-format arrays for each wavelength band. When 2MASS was first proposed in the early 1990s the only near-infrared array format reliably available in quantity was 256 × 256 pixels.

2MASS selected a 2.0" × 2.0" pixel scale with 7.8s of integration devoted to each sky location. Since background Poisson noise would dominate the system read noise in exposures of more than 1s, even in the low-background J band, the total integration time was divided into six 1.3s exposures. In addition to improving reliability, this redundant imaging enabled recovery of sky area that fell on non-functioning pixels, and pixels affected by transient events such as cosmic rays and meteors.

2MASS required telescope facilities in both the northern and southern hemispheres in order to observe the entire celestial sphere. Achieving milliJansky sensitivity in the allotted integration time necessitated telescope apertures larger than 1m. Existing telescopes could have been modified to serve the needs of 2MASS. However the cost of modifications was a significant fraction of the cost of new facilities. Furthermore, identical facilities would simplify operations and aid in the generation of a more uniform final product. Two identical 1.3m aperture telescopes were constructed at Mount Hopkins Arizona, and Cerro Tololo, Chile, for the sole purpose of carrying out 2MASS observations. The northern 2MASS facility began routine operations in 1997, and the southern facility in 1998. Survey operations were complete for both hemispheres in February 2001.

During observations, the telescope scanned in the declination direction. The secondary mirror tilted smoothly throughout the observation to continuously observe the same 8.5'×8.5' field of view, despite the telescope motion in the declina-

tion direction. At the end of the exposure, the secondary mirror moved back to its start position, while the camera electronics read-out and reset the arrays.

The survey was conducted as a series of "tiles", which overlapped in the Right Ascension direction by ∼50arcsec and by 8.5 arcmin in the Declination direction. The overlaps ensured that there were no gaps between adjacent tiles. Any gaps that did appear during the survey were due to telescope pointing errors, and occurred very rarely.

Data Reduction

The data were processed using 2MAPPS (2MASS Production Pipeline System - Skrutskie et al. (2006)). This was an automated software pipeline, which processed a night's raw science and calibration data and produced calibrated images and tables of extracted source characteristics. Reduction of the data involved instrumental calibration of raw images, to correct for instrumental signatures present in the data, and photometric calibration, to calibrate the observed fluxes.

Photometric calibration was achieved by regular observation of calibration tiles. Calibration tiles were centered on primary calibrator stars drawn from Near-Infrared Camera and Multi-Object Spectrometer (NICMOS) calibrations from the Hubble Space Telescope (HST) (Persson et al., 1998). Observation of calibrator stars allowed for the determination of frame zero points. Several calibration tiles were observed per night, at a range of zenith angles. Equatorial calibration tiles were shared by both telescopes.

The instrumental calibration involved subtracting a dark frame, dividing by a flat-field and subtracting a sky-illumination correction image. A dark frame was obtained by imaging a cold shutter covering the detectors. This image contained no astronomical signal and so could be subtracted from the science images.

The background removal for each band was considered separately, as the dominant component is wavelength dependent. In all cases, bright sources were masked, and a 3rd-order polynomial function was removed from the data. This method relied on the assumption that, for the most part, the background variation was smooth enough that it can be fitted by a polynomial.

Flat-fielding was achieved by imaging the rapidly brightening or dimming of the twilight sky by charting the relative change in intensity seen in every pixel in response to changing illumination levels.

The entire 2MASS data set was processed twice. The first, preliminary processing was conducted while observations were ongoing and used a version of 2MAPPS that evolved continuously in response to instrumental changes and improving understanding of hardware and software performance and calibration. Preliminary processing supported planning and telescope operations, as well as the generation of early data sets for public release. Following the completion of telescope operations the entire data set was reprocessed with the ultimate version of the 2MAPPS pipeline. The final version of 2MAPPS incorporated the best knowledge of calibration, sky conditions, and system performance accumulated over the life of the survey.

2.6 Summary

In this Chapter, I have described the telescopes and detectors used to observe the data used in this thesis. I have also outlined the data reduction processes used for each dataset. The reduced data are presented in the next Chapter.

Chapter 3

The Data

3.1 Introduction

In this chapter, I will present the data gathered from the instruments described in the previous chapter. I will begin by showing optical images of the cores, as observed by the DSS (Digitised Sky Survey) (Weir, 1994). Secondly, I will show extinction maps created from 2MASS data (Kleinmann, 1992), and briefly discuss the method used to make the maps. This will be followed by integrated intensity maps and line profiles of each of the observed CO isotopologues. Finally, I will show SIMBA 1.2mm continuum maps for the subset of cores in this work that were observed as part of the SIMBA survey (Nyman et al., 2001).

3.2 Optical Images

Figures 3.1 - 3.6 show DSS (Digitized Sky Survey) (Weir, 1994) Red band (630μm) images of all the cores in the sample. In these figures, and in subsequent tables and figures, the cores are arranged in order of increasing Right Ascension.

The map size varies from core to core. The map size was chosen in each case to enclose all of the emission from the core. The maps are small, which suggests the cores are isolated. The cores do not appear to be part of, or to be associated with, a larger molecular cloud structure.

The figures also suggest that the cores span a range of extinction values. In these images, some cores appear in very stark contrast to the surrounding bright stars (e.g. BHR74 in Figure 3.3), suggesting that they are very dark, and have a high extinction. Others appear in low contrast with the surrounding bright stars (e.g. BHR73 in Figure 3.3), which could suggest a lower extinction.

The morphology of the cores varies greatly. Some cores appear to be quite circular, (e.g. CB112 & CB176 in Figure 3.6), while others are better fit as an ellipse (e.g. BHR80 and BHR81 in Figure 3.4). Several cores show evidence of having tails (e.g. BHR17 in Figure 3.1) and others are very irregularly shaped (e.g. BHR34 in Figure 3.1).

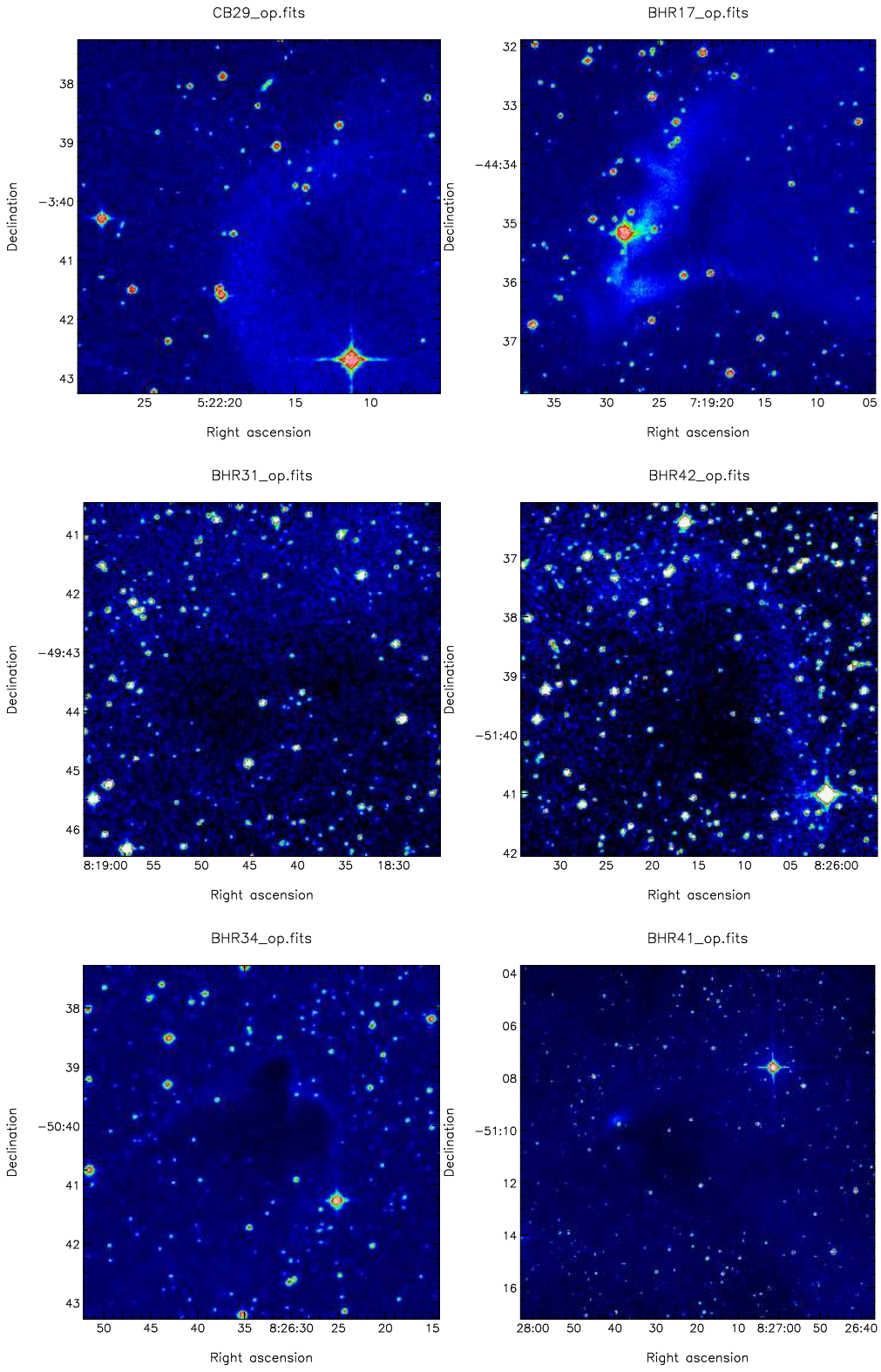

Figure 3.1: DSS red band (optical) images of isolated cores (a)CB29, (b)BHR17, (c)BHR31, (d)BHR42, (e)BHR34, (f)BHR41. The cores appear to span a range extinction values, and have shapes which deviate from spherical geometry. In this and in subsequent tables and figures, the cores are presented in order of increasing Right Ascension.

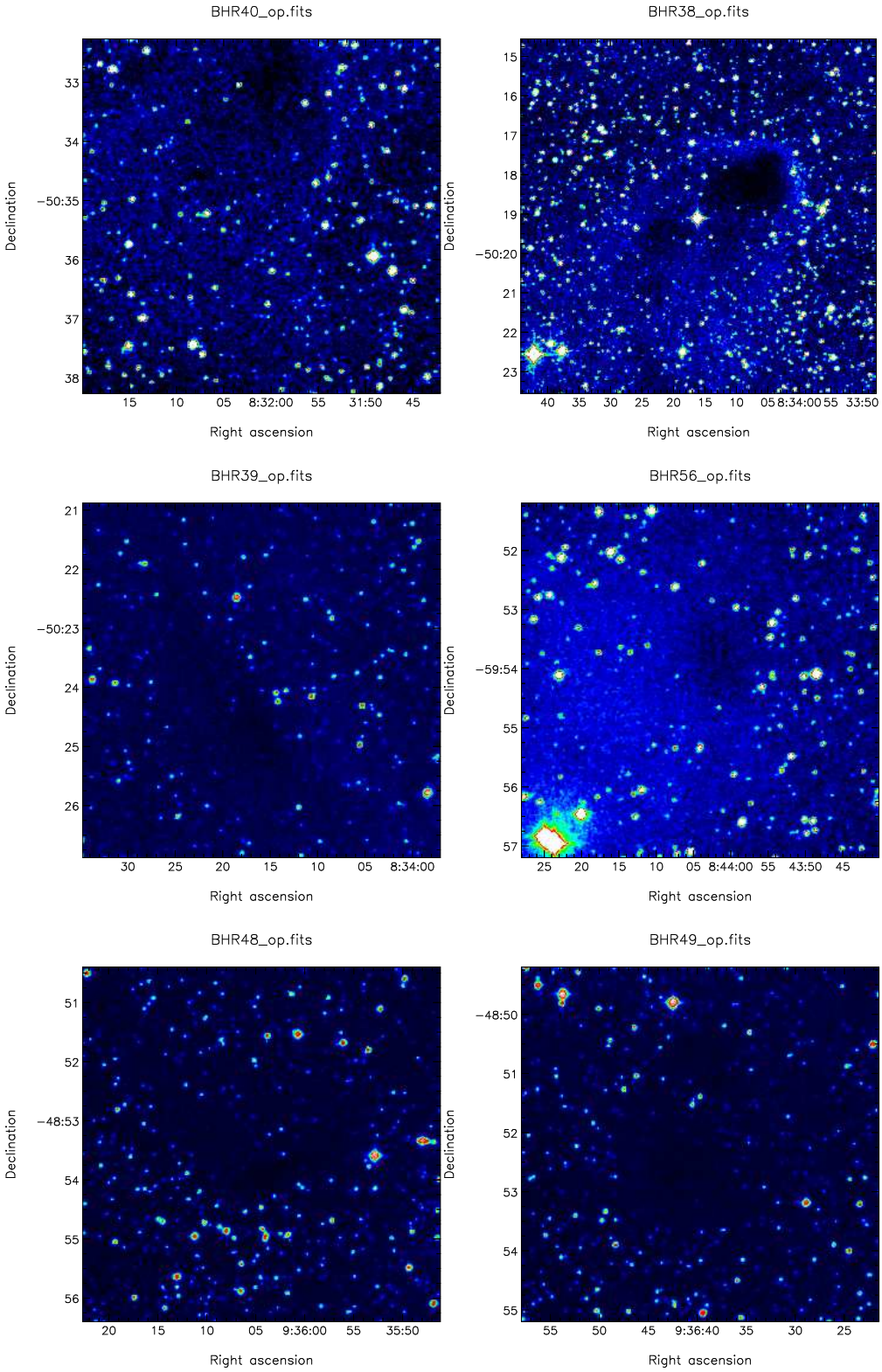

Figure 3.2: DSS red band (optical) images for cores (a)BHR40, (b)BHR38, (c)BHR39, (d)BHR56, (e)BHR48, (f)BHR49.

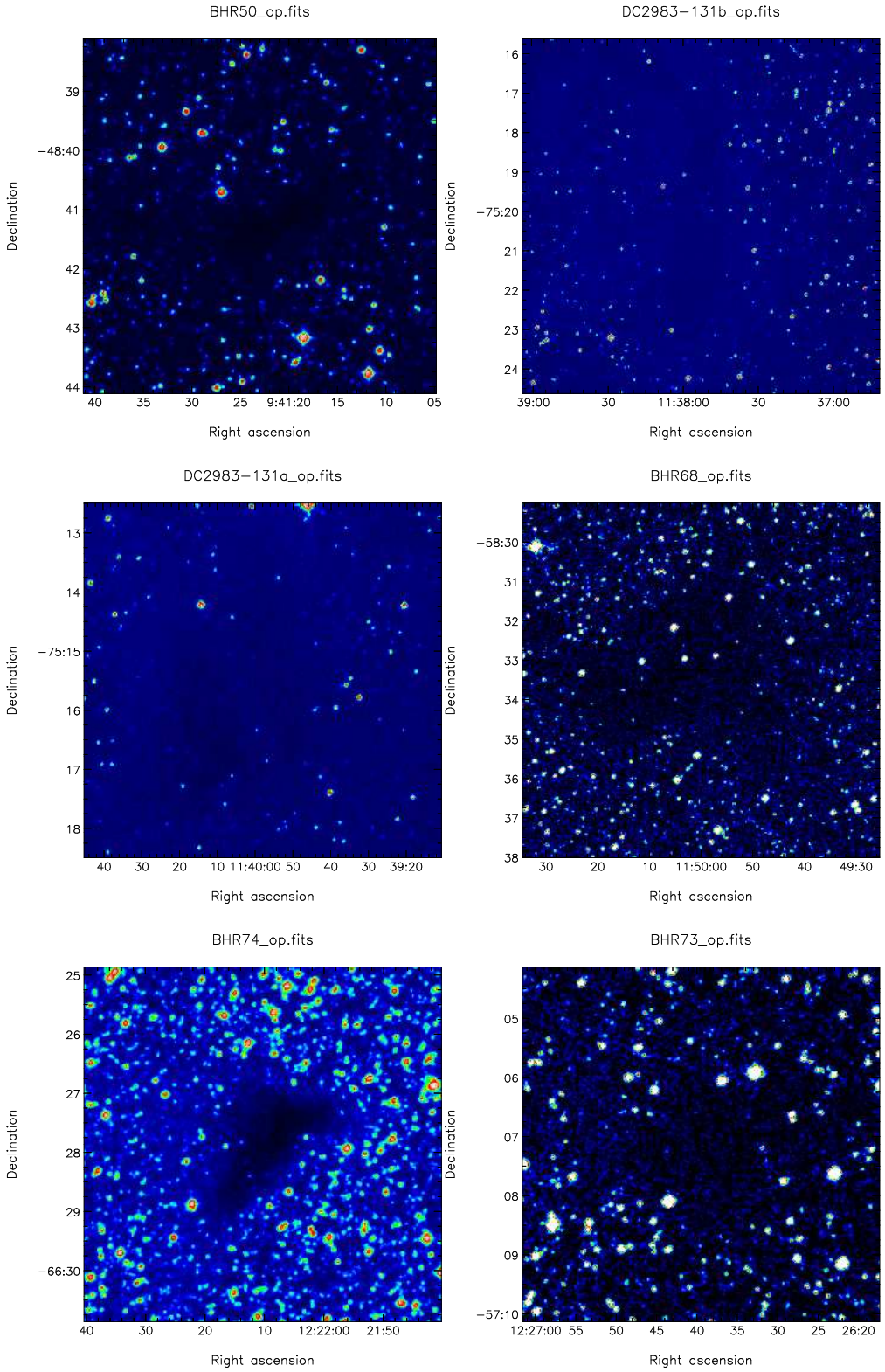

Figure 3.3: DSS red band (optical) images for cores (a)BHR50, (b)DC2983-131b, (c)DC2983-131a, (d)BHR68, (e)BHR74, (f)BHR73.

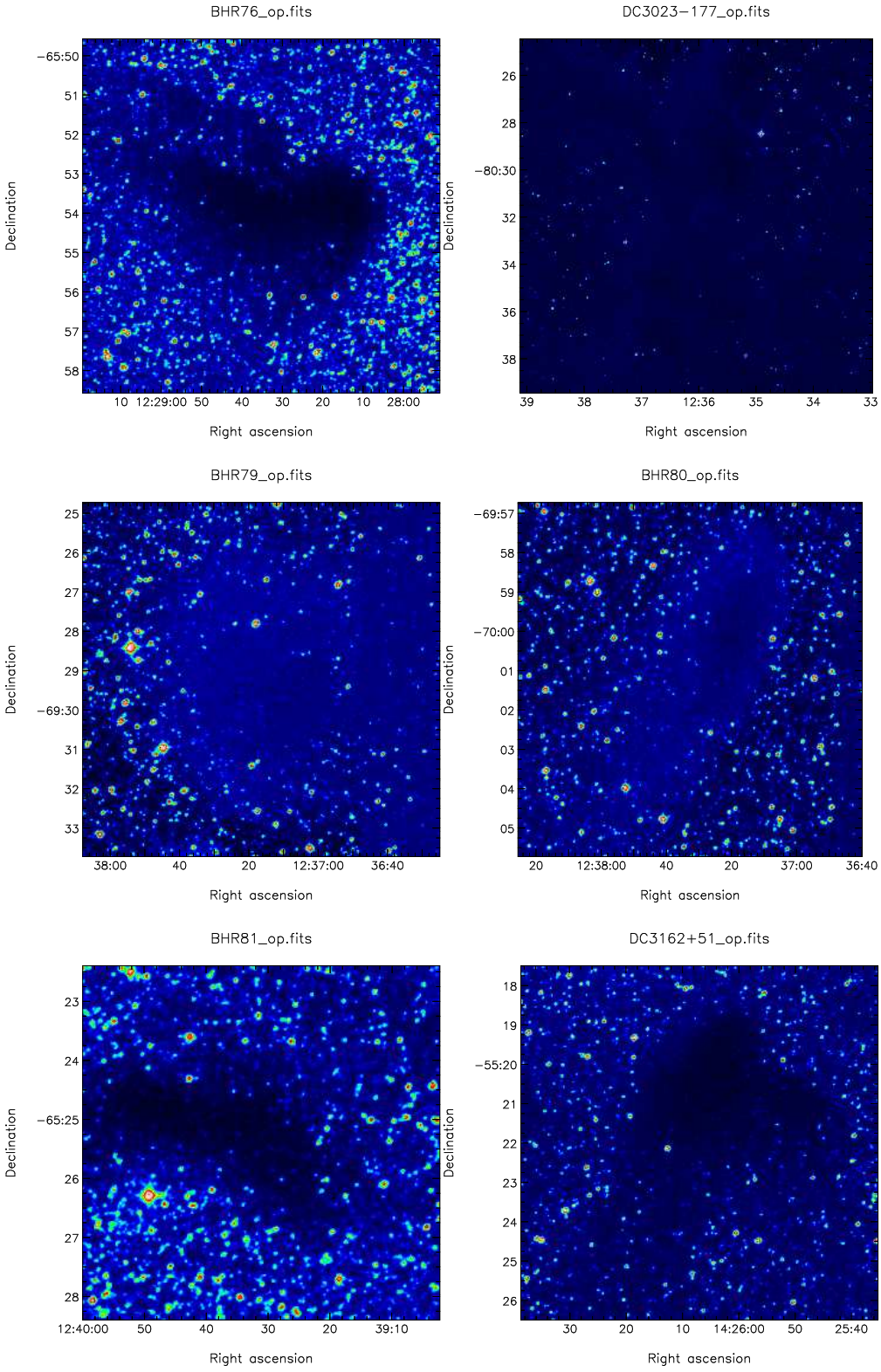

Figure 3.4: DSS red band (optical) images for cores (a)BHR76, (b)DC3023-177, (c)BHR79, (d)BHR80, (e)BHR81, (f)DC3162+51.

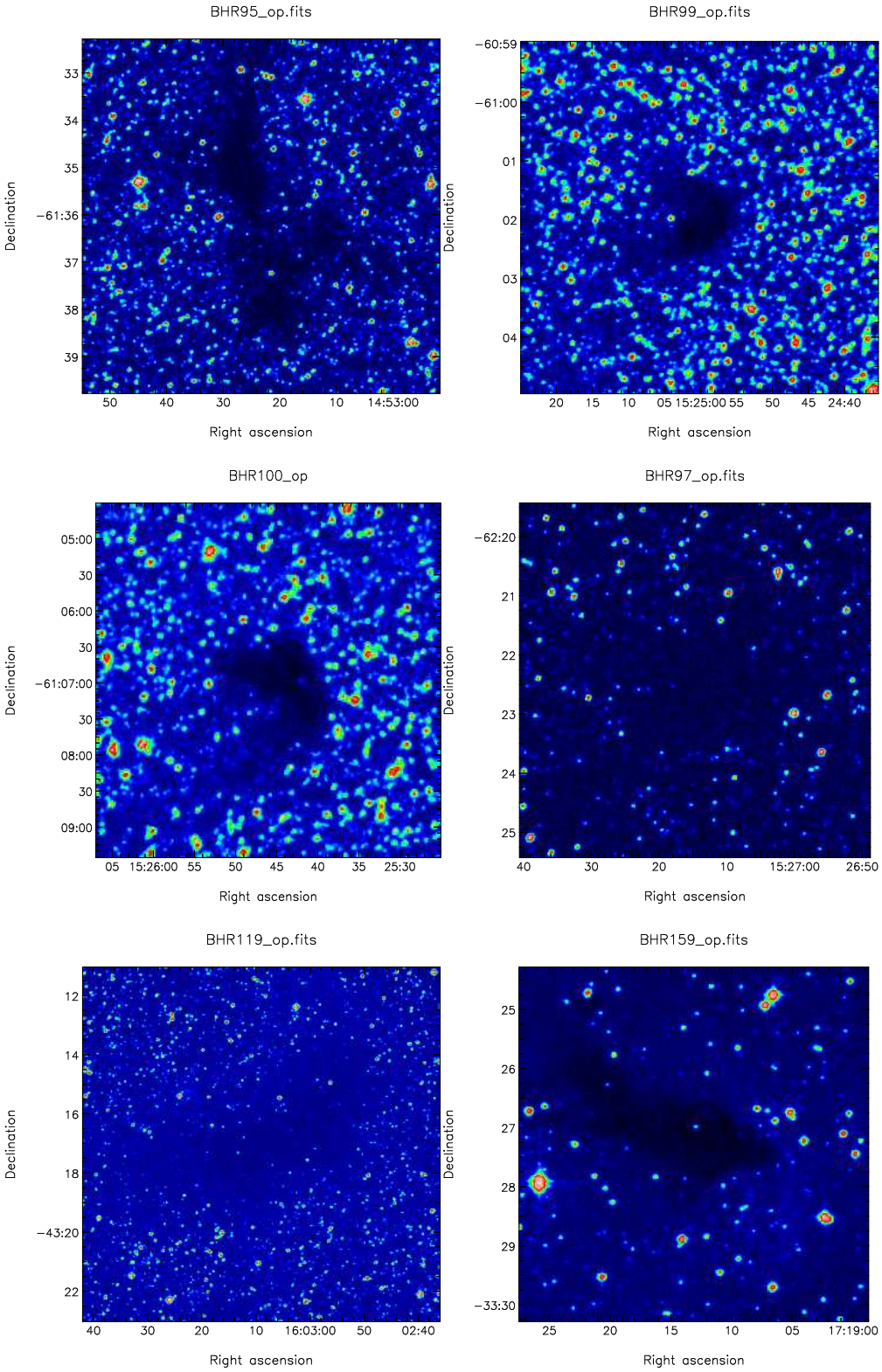

Figure 3.5: DSS red band (optical) images for cores (a)BHR95 (b)BHR99, (c)BHR100, (d)BHR97, (e)BHR119, (f)BHR159.

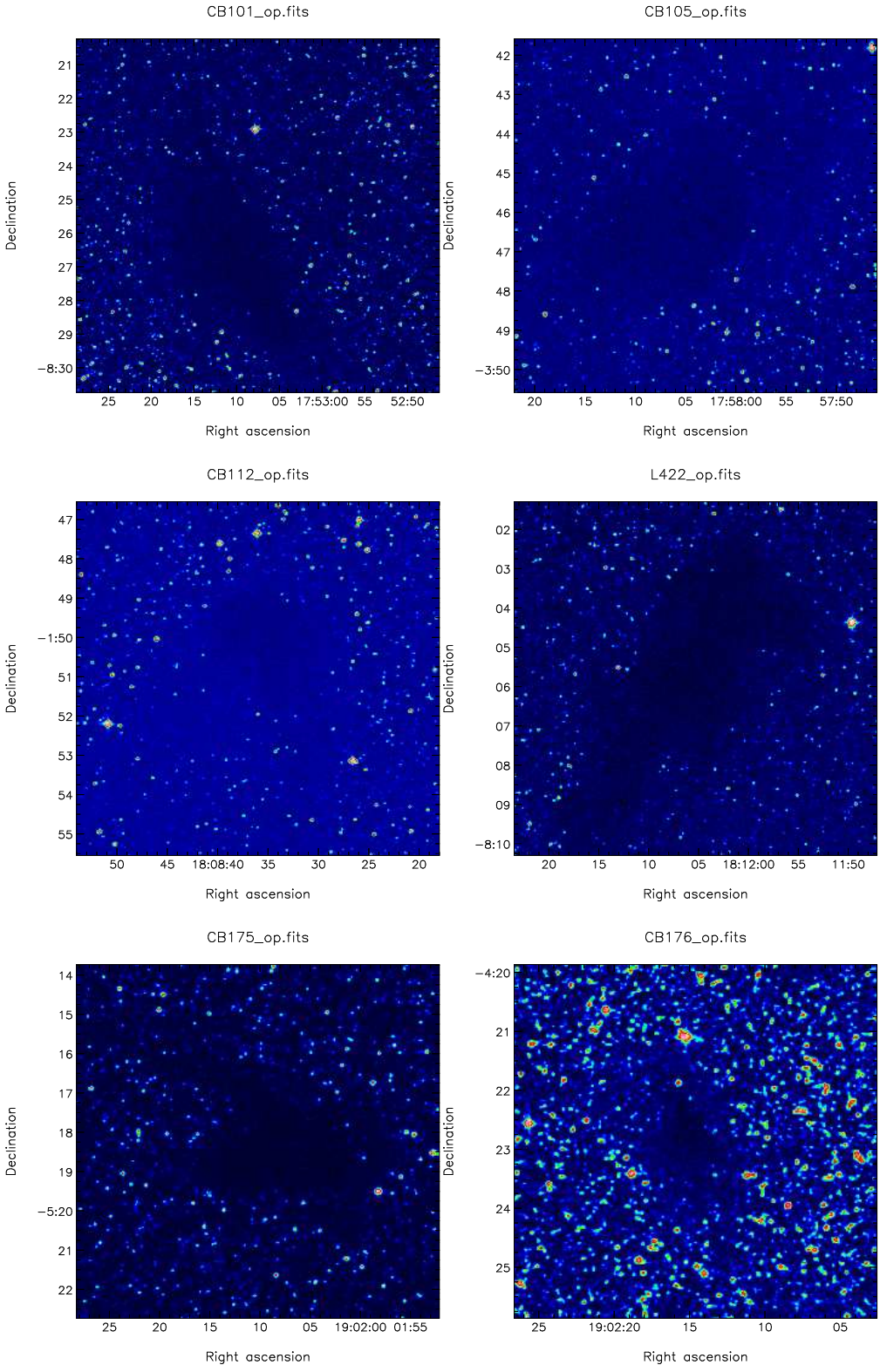

Figure 3.6: DSS red band (optical) images for cores (a)CB101, (b)CB105, (c)CB112, (d)L422, (e)CB175, (f)CB176.

3.3 2MASS extinction maps

Visual extinction is often used as a measure of dust column density. As described later, the column density is used to estimate the mass of the core (Lilley, 1955), (Jenkins & Savage, 1974) which is of interest to this study.

2MASS near infrared colour excesses were used to produce extinction maps of each core. The maps were produced using a modified version of the Near-Infrared Colour Excess Revisited, NICER (Lombardi & Alves, 2001) technique, using the method outlined in Gutermuth et al. (2005) and summarised briefly below.

NICER is an optimised, multi-band method for extinction estimation based on the near infrared excess of background starlight. The line-of-sight extinction of an individual star can be directly determined from knowledge of its colour excess and the extinction law. The colour excess, $E(H-K)$ can be directly derived from observations provided the intrinsic colour of the star is known.

$$E(H-K) = (H-K)_{obs} - (H-K)_{int} \tag{3.1}$$

where H and K represent the 2MASS H and K_S band, centred on 1.65μm and 2.2μm respectively, $(H-K)_{obs}$ in the observed $(H-K)$ colour and $(H-K)_{int}$ is the intrinsic colour of the star.

The observed $(H-K)$ value is measured for 20 of the nearest field stars to the molecular cloud. The mean and standard deviation of the $(H-K)$ values are calculated, and any star with a $(H-K)$ value more than 3σ from the mean is discarded. This step is taken to reject any foreground stars which suffer no extinction due to the cloud.

The intrinsic colour of the stars is difficult to determine accurately. Observations of field stars in a nearby unobscured control region off the target cloud can be

used to over come this difficulty, provided that the control field stars themselves do not suffer significant additional extinction in comparison to the stars in the target field. Field stars are observed to be typically K and M stars, spanning a narrow range of brightnesses (0.1 - 0.3 mag). With the assumption that all the background field stars observed through the molecular cloud are identical in nature to those in the unobscured control field, we can use the mean $(H-K)$ value of the unobscured stars to represent the mean $(H-K)$ value of the obscured stars, i.e.:

$$(H-K)_{int} = \langle (H-K) \rangle control = 0.2 \tag{3.2}$$

The infrared colour excess is related to the extinction by the interstellar reddening law of Cohen et al. (1981):

$$A_K = 1.385(H-K)_{obs} - (H-K)_{tr}) \tag{3.3}$$

The resultant K-band extinction can be converted to visual extinction (A_V) using the relation (Cardelli, Clayton, & Mathis, 1989):

$$\frac{A_{K_S}}{A_V} = 0.112 \tag{3.4}$$

The extinction maps are shown in Figures 3.7 - 3.12. The maps are presented on an inverted grey-scale, so the regions of high extinction at the centres of the cores appear as the darkest regions on the maps. The grey scale bar to the right of each map shows the full A_V range of each core. The units of the maps are magnitudes. The peak A_V value can be used to estimate the peak column density of a core, as described later. The peak value is measured by locating the brightest pixel in the map and recording the value listed. The peak A_V value of each core is recorded in Table 3.1.

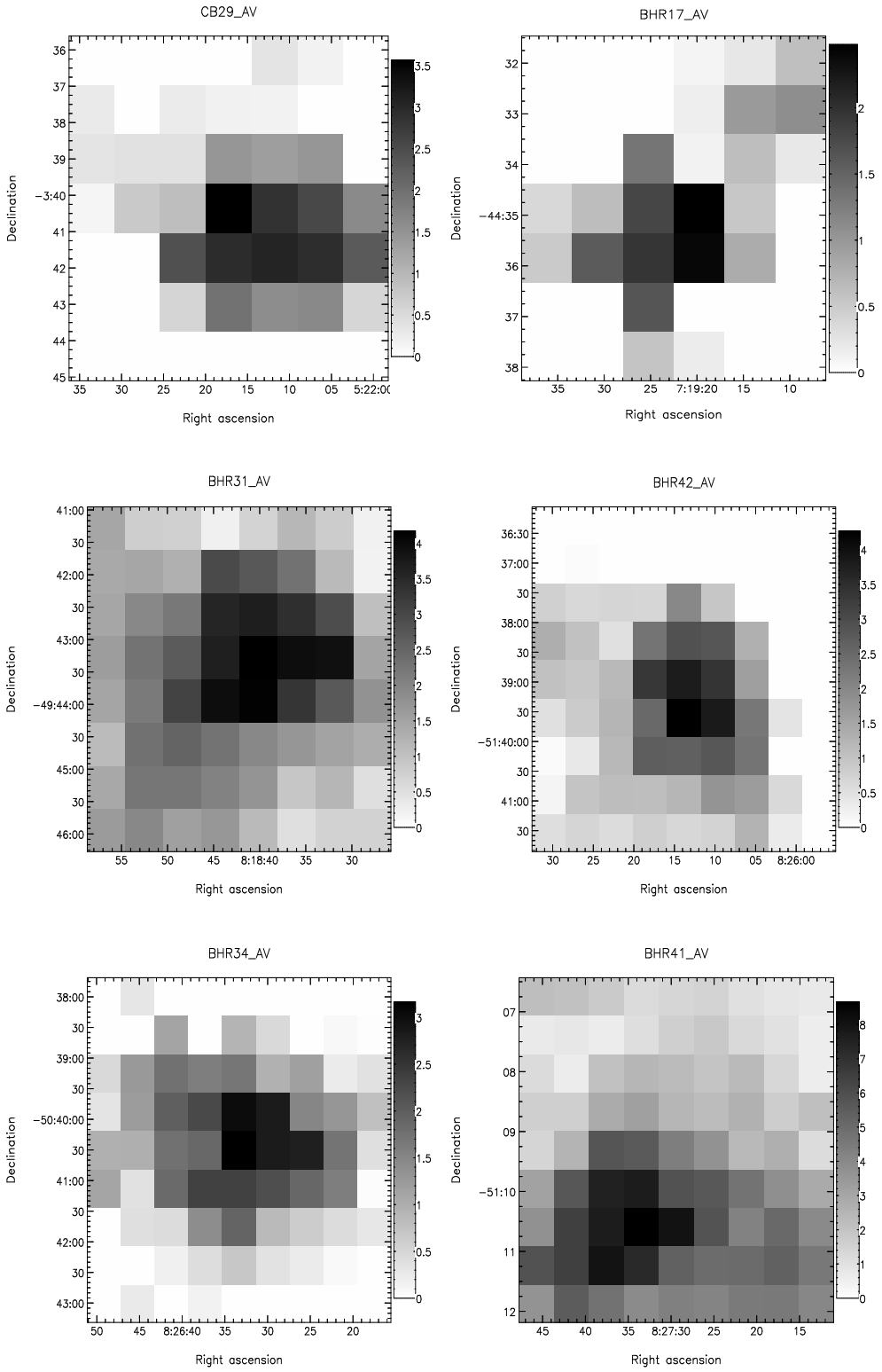

Figure 3.7: Visual extinction maps for cores (a)CB29, (b)BHR17, (c)BHR31, (d)BHR42, (e)BHR34, (f)BHR41. The images are presented in an inverted grey scale. The cores span a range of extinction values. The full range of extinction for each core is shown in the grey scale bar to the right of each image.

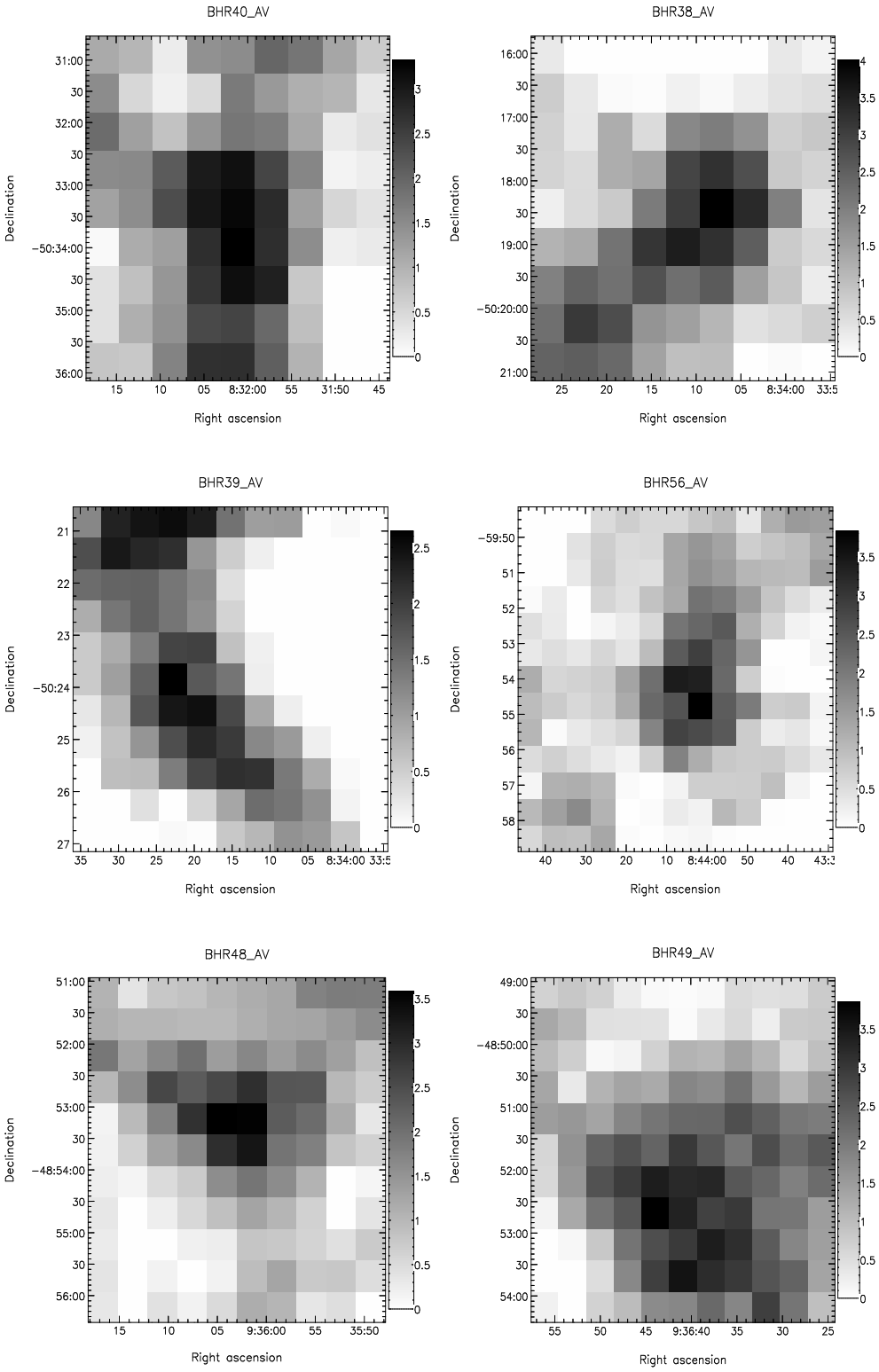

Figure 3.8: Visual extinction images for cores (a)BHR40, (b)BHR38, (c)BHR39, (d)BHR56, (e)BHR48, (f)BHR49. The images are presented in an inverted grey scale. The cores span a range of extinction values. The full range of extinction for each core is shown in the grey scale bar to the right of each image.

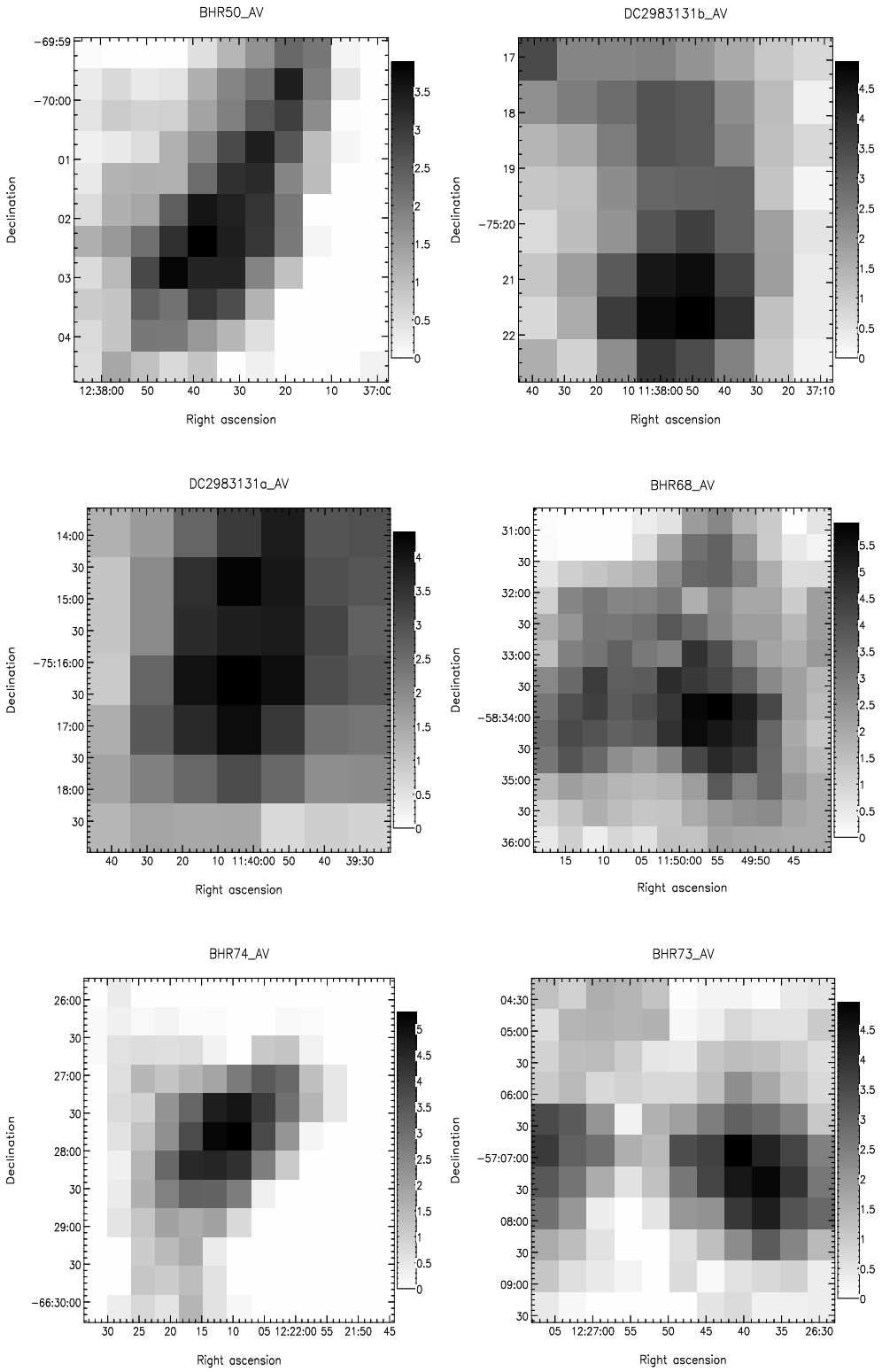

Figure 3.9: Visual extinction images for cores (a)BHR50, (b)DC2983-131b, (c)DC2983-131b, (d)BHR68, (e)BHR74, (f)BHR73. The images are presented in an inverted grey scale. The cores span a range of extinction values. The full range of extinction for each core is shown in the grey scale bar to the right of each image.

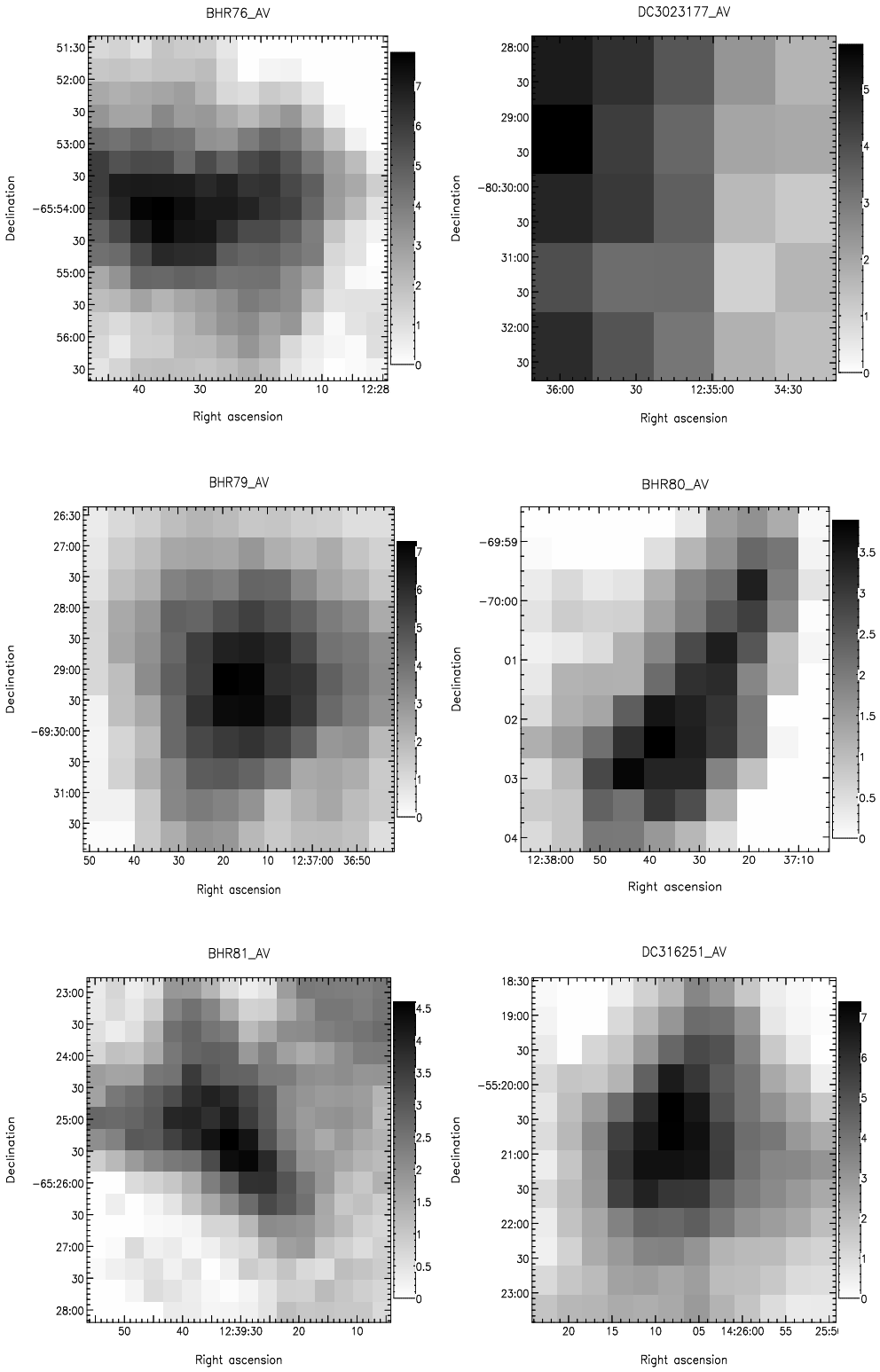

Figure 3.10: Visual extinction images for cores (a)BHR76, (b)DC3023-177, (c)BHR79, (d)BHR80, (e)BHR81, (f)DC3162+51. The images are presented in an inverted grey scale. The cores span a range of extinction values. The full range of extinction for each core is shown in the grey scale bar to the right of each image.

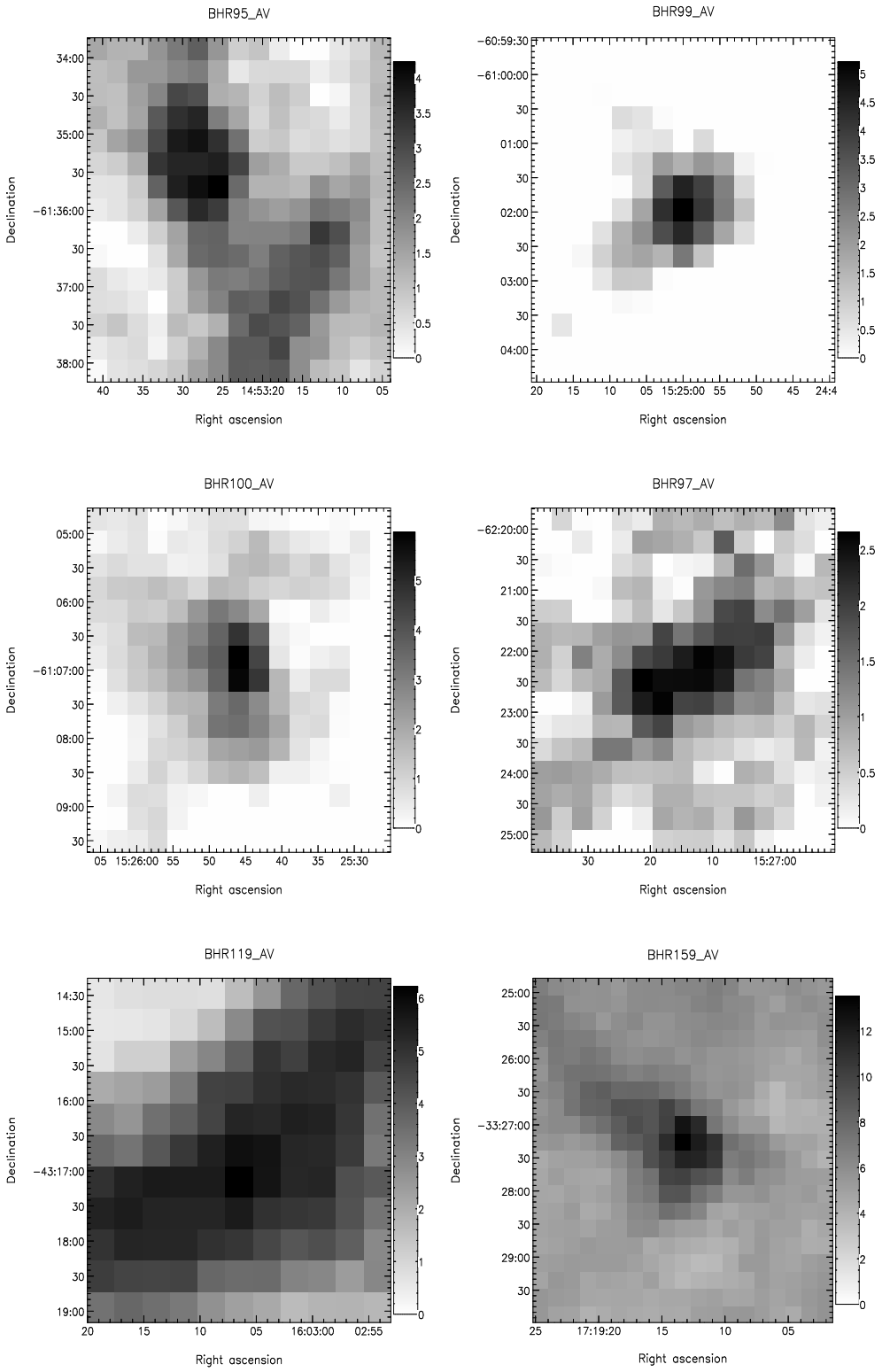

Figure 3.11: Visual extinction images for cores (a) BHR95, (b) BHR99, (c) BHR100, (d) BHR97, (e) BHR119, (f) BHR159. The images are presented in an inverted grey scale. The cores span a range of extinction values. The full range of extinction for each core is shown in the grey scale bar to the right of each image.

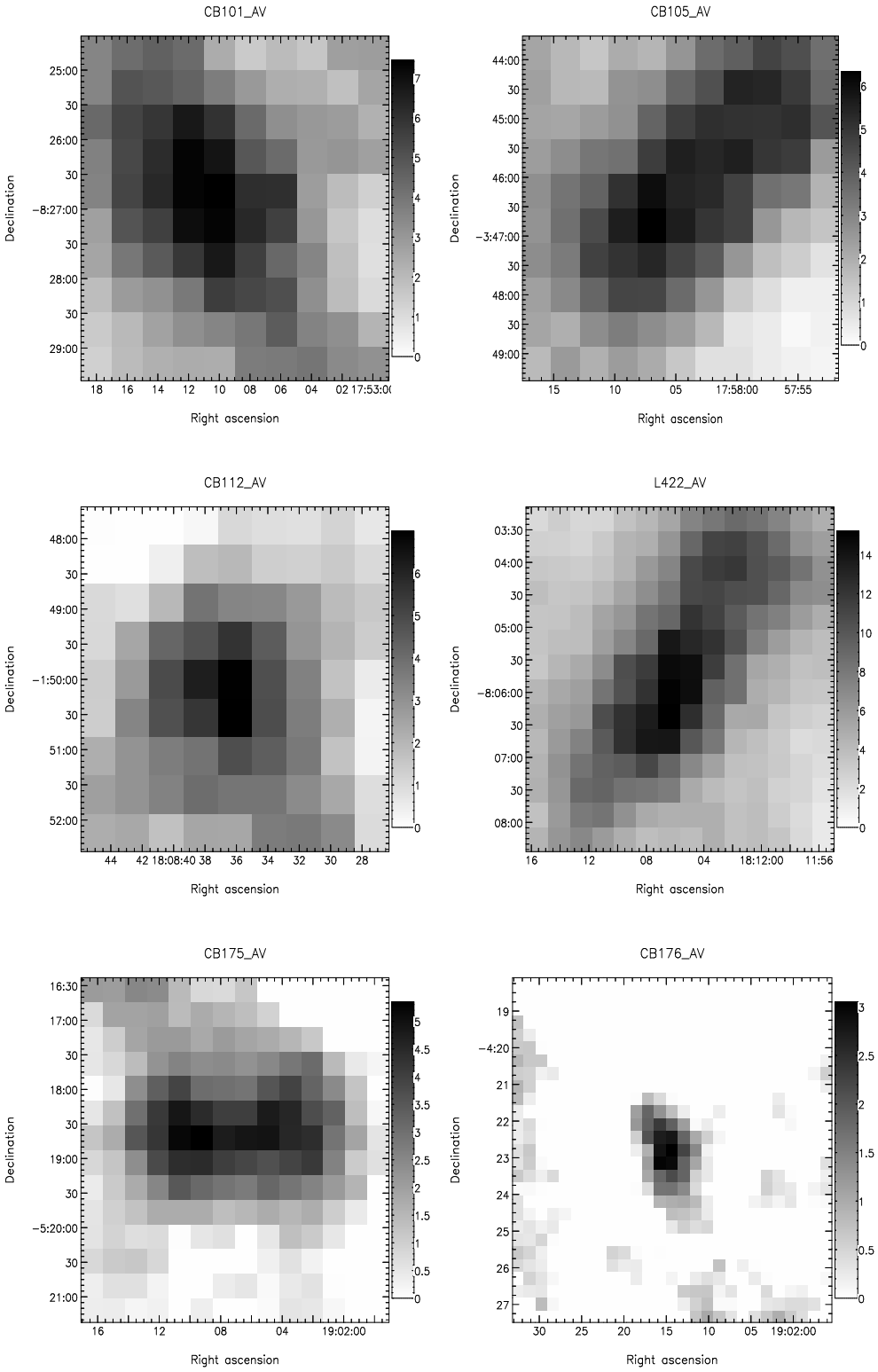

Figure 3.12: Visual extinction images for cores (a)CB101, (b)CB105, (c)CB112, (d)L422, (e)CB175, (f)CB176. The images are presented in an inverted grey scale. The cores span a range of extinction values. The full range of extinction for each core is shown in the grey scale bar to the right of each image.

Core	Peak 2MASS A_V
	mag
CB29	3.60
BHR17	2.56
BHR31	4.21
BHR42	4.34
BHR34	3.23
BHR41	3.66
BHR40	3.31
BHR38	4.07
BHR39	2.69
BHR56	3.88
BHR48	3.65
BHR49	3.82
BHR50	3.63
DC2983-131a	4.41
DC2983-131b	4.95
BHR68	5.96
BHR74	5.38
BHR73	4.92
BHR76	7.83
DC3026-177	5.78
BHR79	7.25
BHR80	3.88
BHR81	3.59
DC3162+51	7.37
BHR95	4.22
BHR99	5.20
BHR100	6.00
BHR97	2.70
BHR119	6.20
BHR159	13.50
CB101	7.44
CB105	6.32
CB112	6.99
L422	15.2
CB175	5.34
CB176	3.05

Table 3.1: Peak A_V value for each core. In this table, and in all subsequent Tables and Figures, the sources are listed in increasing order of Right Ascension. The Peak 2MASS A_V is the A_V value reported in the brightest pixel in the extinction maps shown in Figures 3.7 - 3.12. The extinction values are quoted in magnitudes.

3.4 CO Data

Figures 3.13 - 3.48 show integrated intensity maps of the sample of isolated cores for each of the three observed CO isotopologues, ^{12}CO, ^{13}CO and C^{18}O. An integrated intensity map is created by summing the emission in each pixel across a specified velocity range. In each of the Figures, the top left hand image is the ^{12}CO integrated intensity map, the middle left hand image is ^{13}CO, and the lower left hand image is C^{18}O. The range of each map is different and was chosen to match the full range of emission in each case. The linear scale bar to the right of each integrated intensity map shows the full range of the emission in the core in units of K km s^{-1}. The red contours show the 1-10σ levels, where σ is the RMS noise level measured over line-free channels in the map.

The peak integrated intensity ($\int T_b dv$) is measured as the value of the brightest pixel on the integrated intensity map for each core. Using the integrated intensity maps, the angular scale of the cores can be measured by approximating the geometry of the emission above the 3σ level of each core as an ellipse with semi-major and semi-minor axes Θ_{maj} and Θ_{min}.

Beside each integrated intensity map is the line profile at the peak emission of each isotopologue. The line profile was used to determine the velocity range over which the integrated intensity maps were computed. The velocity is shown on the x-axis. The y-axis is presented on the brightness temperature (T_b) scale. T_b can be calculated from the antenna temperature using the beam efficiency η_c from Ladd et al. (2005). The beam efficiency at the frequency of each observed isotopologue is shown in Table 3.2. From each map and line profile pair, a number of cloud parameters can be calculated. These parameters are recorded in Tables 3.3, 3.4 & 3.5.

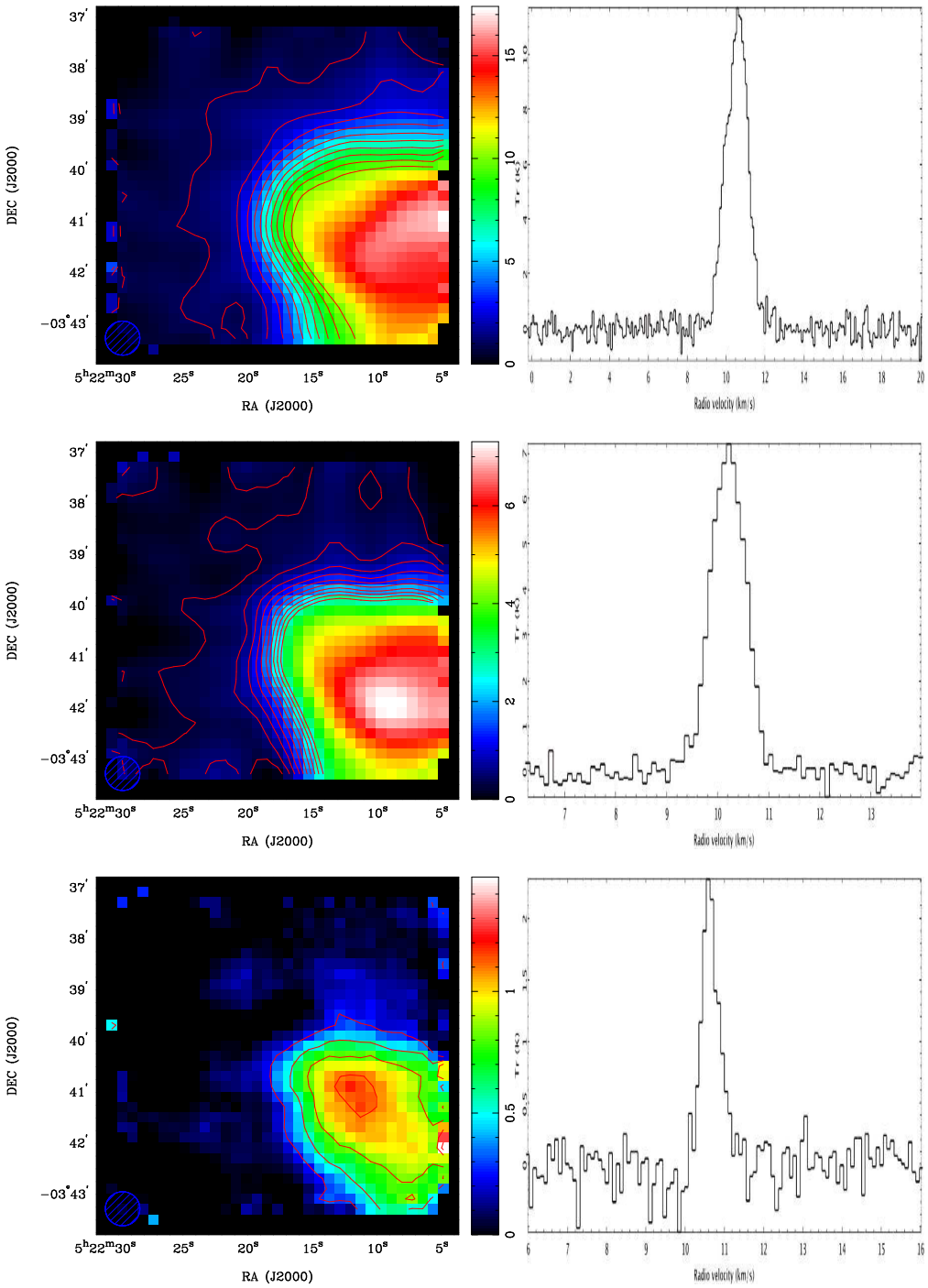

Figure 3.13: Integrated intensity plots for CB29 in each of the observed CO isotopologues. The ^{12}CO map is shown in the top left image. The top right image is the line profile of the core. This image was used to determine over which velocities the integrated intensity plot was produced. The line profile shows a peak from 8 - 13km/s and so this is the velocity range used to compute the integrated intensity plots for each of the 3 isotopologues. The ^{13}CO integrated intensity map and line profile is shown in the middle left and right images respectively. The C^{18}O integrated intensity plot and line profile is shown in the lower left and right images.

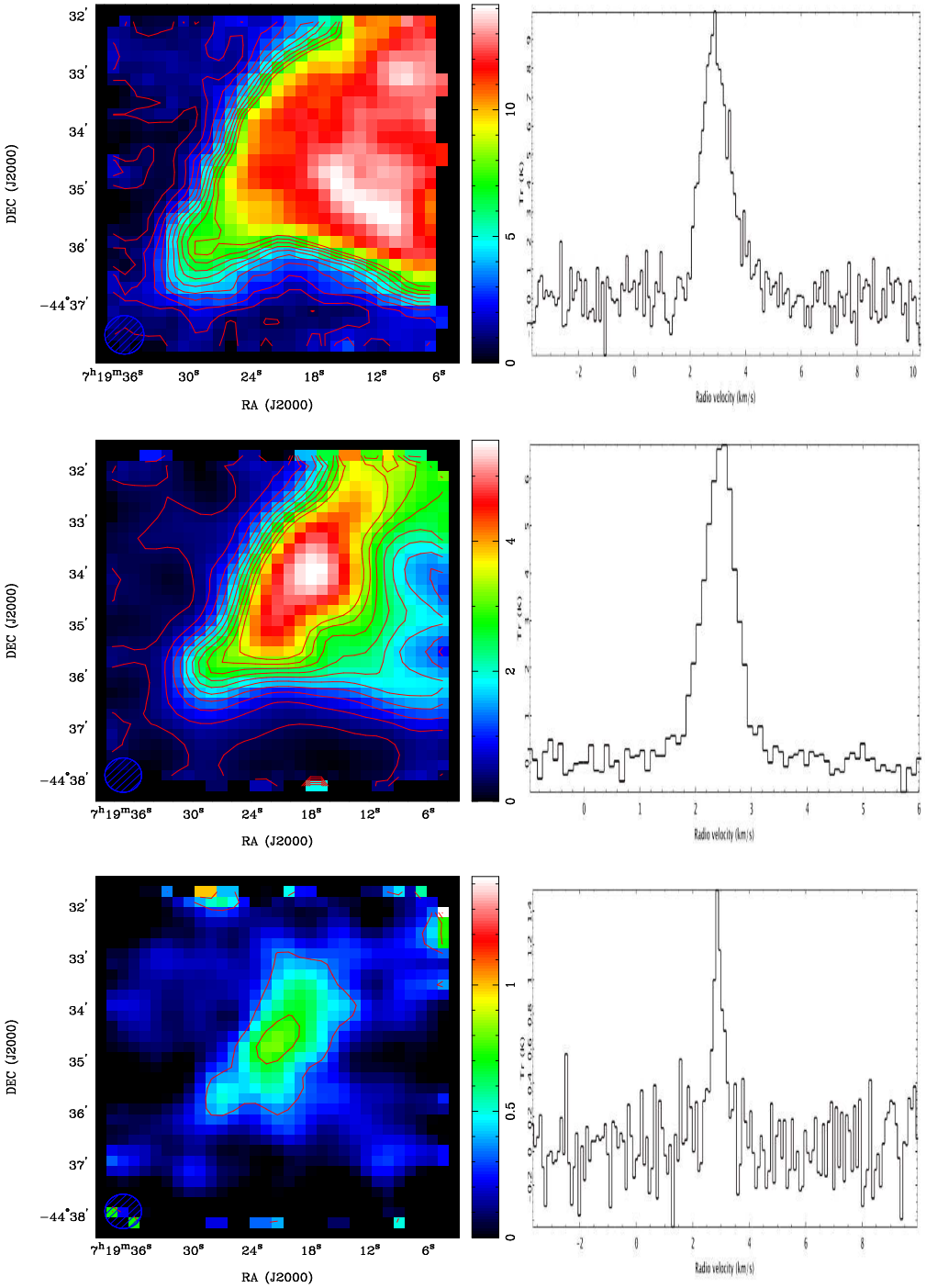

Figure 3.14: Integrated intensity plots for BHR17 in each of the observed CO isotopologues. The ^{12}CO map is shown in the top left image. The top right image is the line profile of the core. This image was used to determine over which velocities the integrated intensity plot was produced. The line profile shows a peak from 0 - 6km/s and so this is the velocity range used to compute the integrated intensity plots for each of the 3 isotopologues. The ^{13}CO integrated intensity map and line profile is shown in the middle left and right images respectively. The C^{18}O integrated intensity plot and line profile is shown in the lower left and right images.

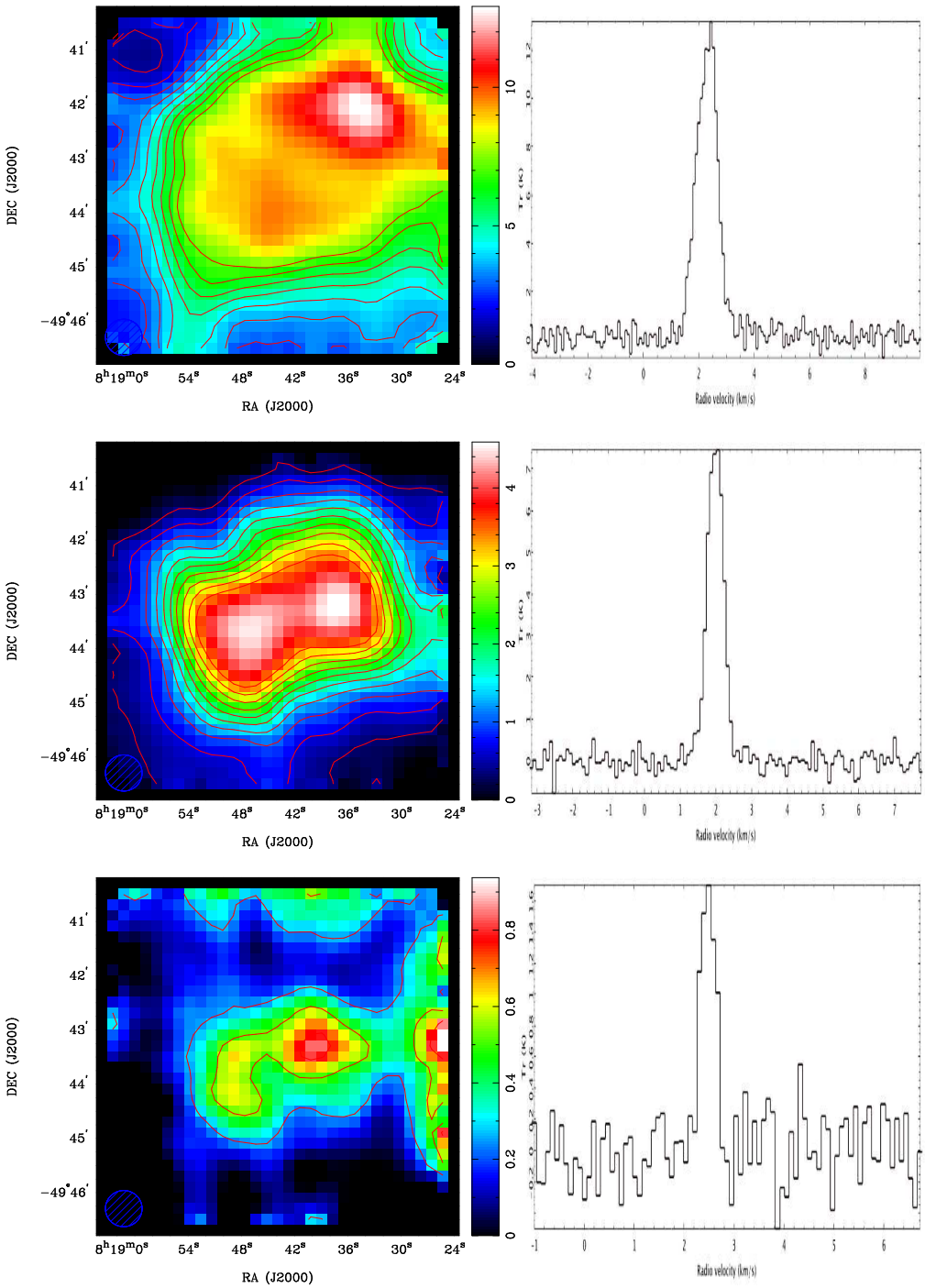

Figure 3.15: Integrated intensity plots for BHR31 in each of the observed CO isotopologues. The ^{12}CO map is shown in the top left image. The top right image is the line profile of the core. This image was used to determine over which velocities the integrated intensity plot was produced. The line profile shows a peak from 1 - 4km/s and so this is the velocity range used to compute the integrated intensity plots for each of the 3 isotopologues. The ^{13}CO integrated intensity map and line profile is shown in the middle left and right images respectively. The C^{18}O integrated intensity plot and line profile is shown in the lower left and right images.

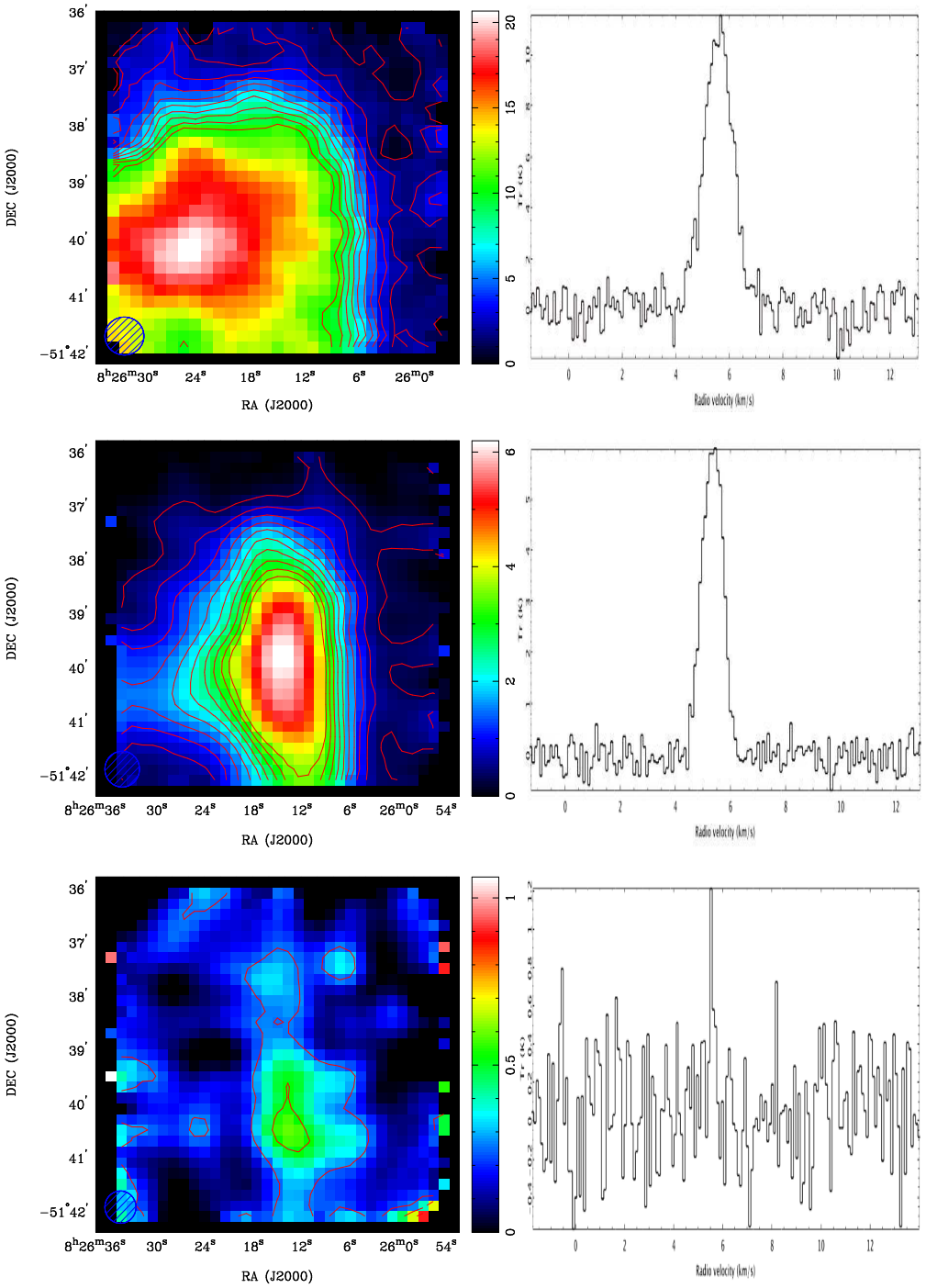

Figure 3.16: Integrated intensity plots for BHR42 in each of the observed CO isotopologues. The ^{12}CO map is shown in the top left image. The top right image is the line profile of the core. This image was used to determine over which velocities the integrated intensity plot was produced. The line profile shows a peak from 2 - 6km/s and so this is the velocity range used to compute the integrated intensity plots for each of the 3 isotopologues. The ^{13}CO integrated intensity map and line profile is shown in the middle left and right images respectively. The C^{18}O integrated intensity plot and line profile is shown in the lower left and right images.

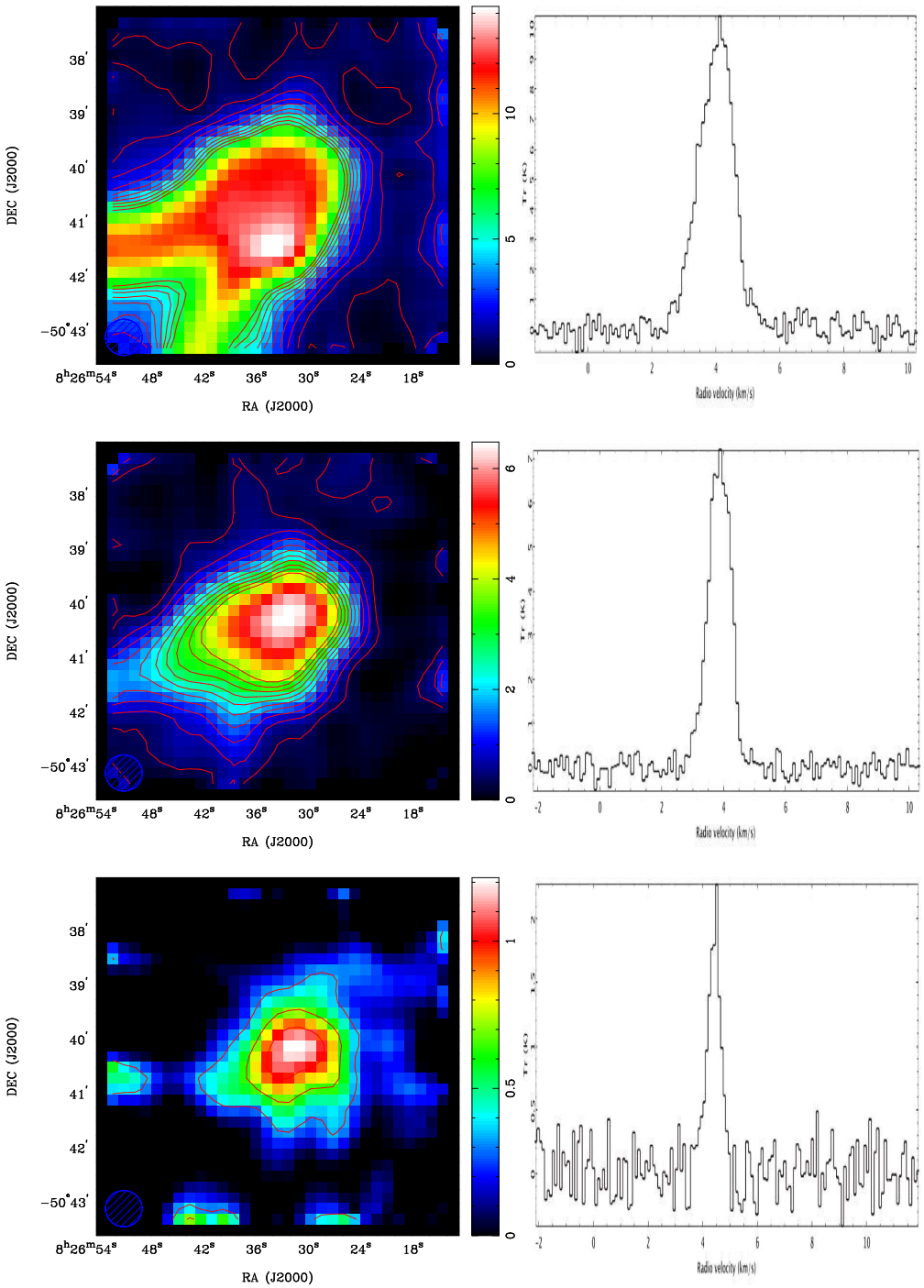

Figure 3.17: Integrated intensity plots for BHR34 in each of the observed CO isotopologues. The ^{12}CO map is shown in the top left image. The top right image is the line profile of the core. This image was used to determine over which velocities the integrated intensity plot was produced. The line profile shows a peak from 2 - 6km/s and so this is the velocity range used to compute the integrated intensity plots for each of the 3 isotopologues. The ^{13}CO integrated intensity map and line profile is shown in the middle left and right images respectively. The C^{18}O integrated intensity plot and line profile is shown in the lower left and right images.

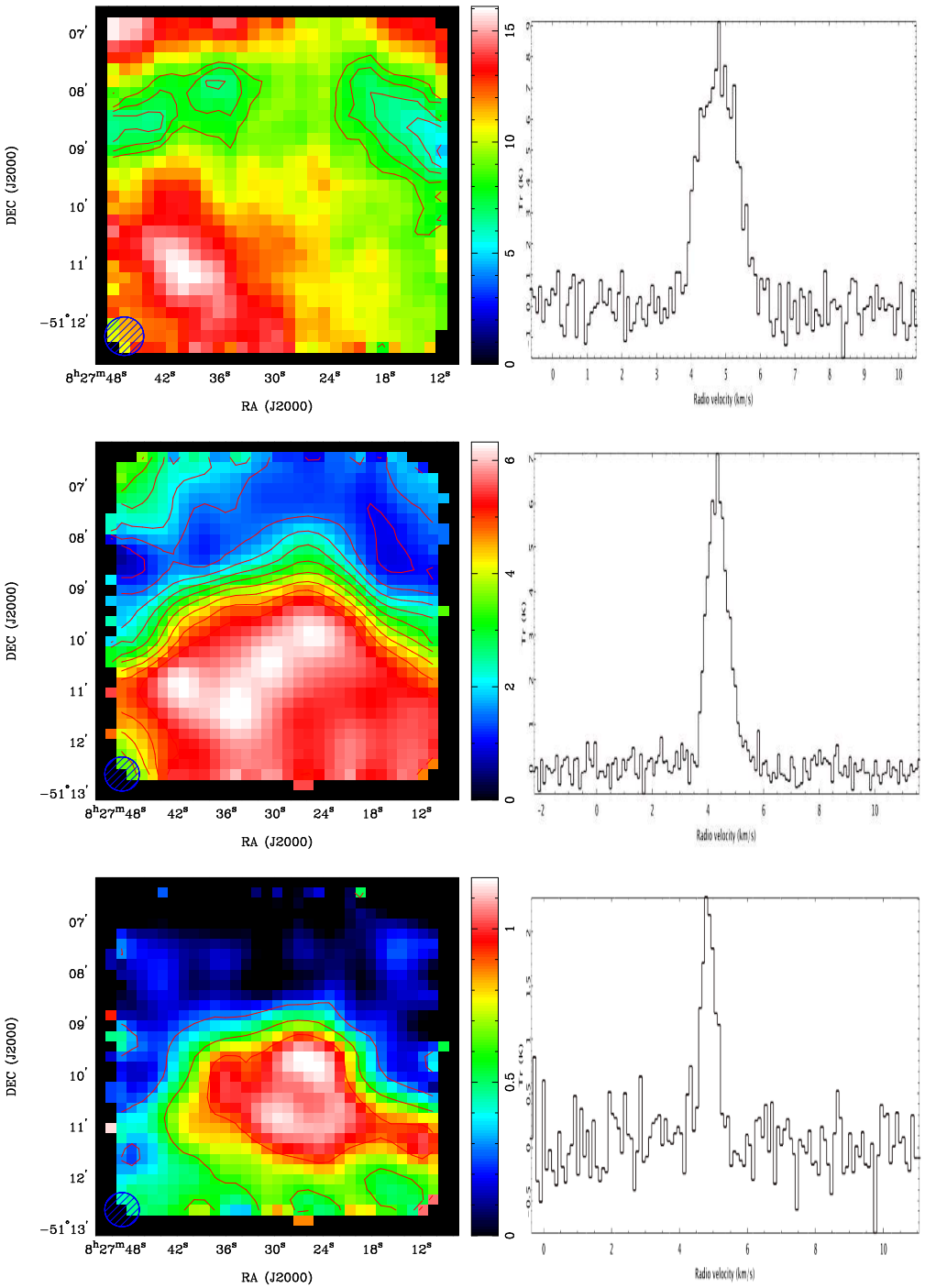

Figure 3.18: Integrated intensity plots for BHR41 in each of the observed CO isotopologues. The ^{12}CO map is shown in the top left image. The top right image is the line profile of the core. This image was used to determine over which velocities the integrated intensity plot was produced. The line profile shows a peak from 3 - 7km/s and so this is the velocity range used to compute the integrated intensity plots for each of the 3 isotopologues. The ^{13}CO integrated intensity map and line profile is shown in the middle left and right images respectively. The C^{18}O integrated intensity plot and line profile is shown in the lower left and right images.

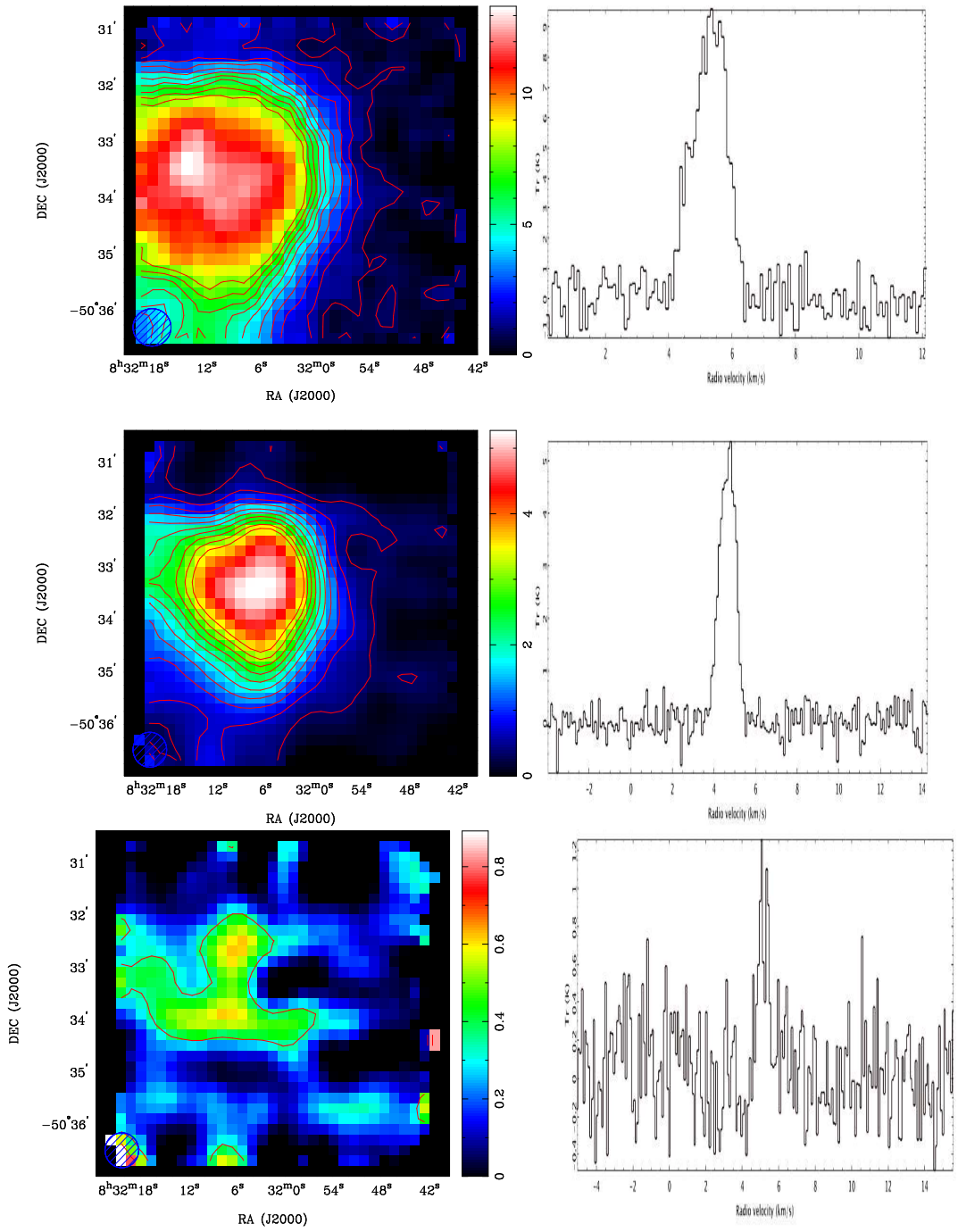

Figure 3.19: Integrated intensity plots for BHR40 in each of the observed CO isotopologues. The ^{12}CO map is shown in the top left image. The top right image is the line profile of the core. This image was used to determine over which velocities the integrated intensity plot was produced. The line profile shows a peak from 3 - 7km/s and so this is the velocity range used to compute the integrated intensity plots for each of the 3 isotopologues. The ^{13}CO integrated intensity map and line profile is shown in the middle left and right images respectively. The C^{18}O integrated intensity plot and line profile is shown in the lower left and right images.

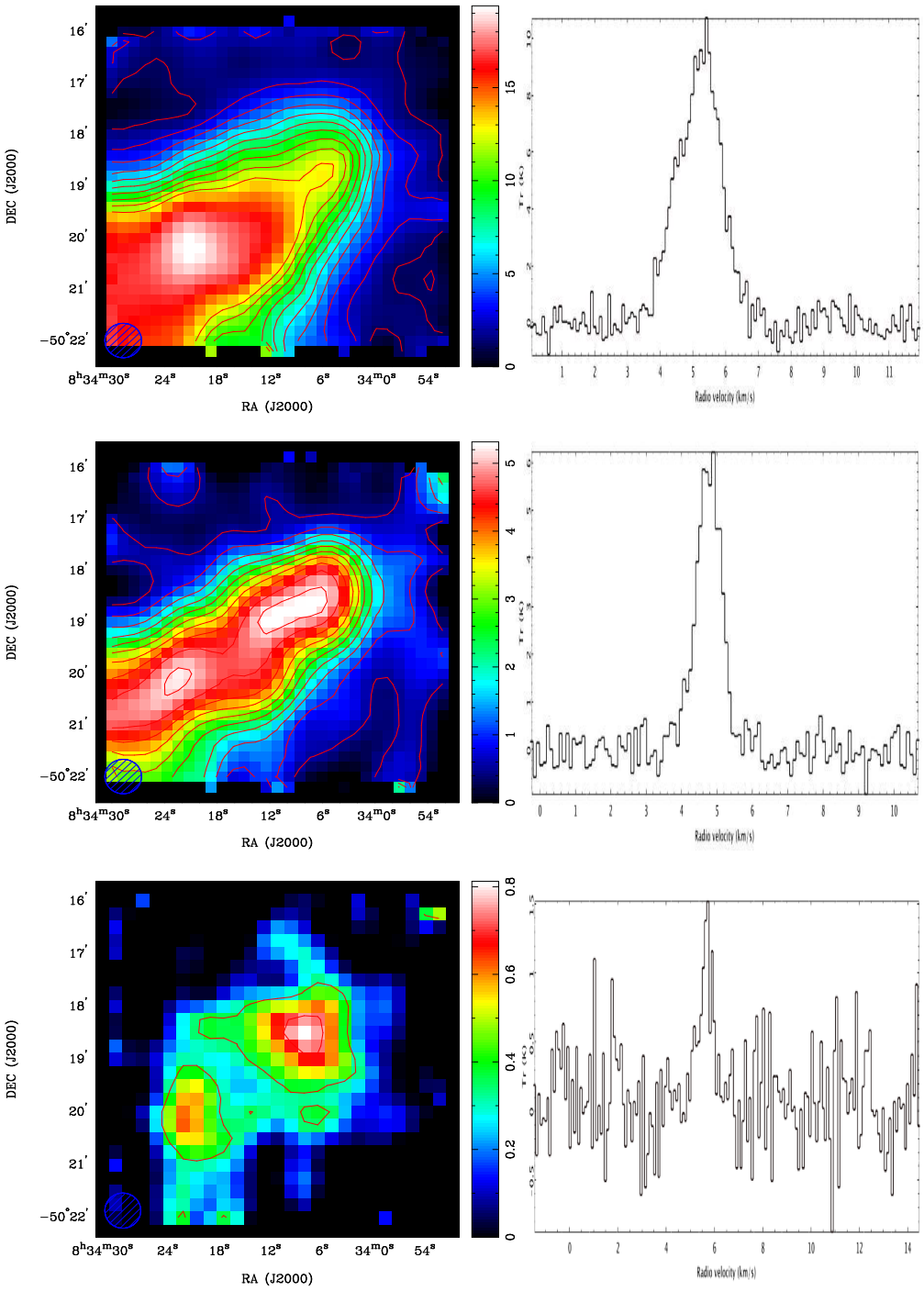

Figure 3.20: Integrated intensity plots for BHR38 in each of the observed CO isotopologues. The ^{12}CO map is shown in the top left image. The top right image is the line profile of the core. This image was used to determine over which velocities the integrated intensity plot was produced. The line profile shows a peak from 3 - 7km/s and so this is the velocity range used to compute the integrated intensity plots for each of the 3 isotopologues. The ^{13}CO integrated intensity map and line profile is shown in the middle left and right images respectively. The C^{18}O integrated intensity plot and line profile is shown in the lower left and right images.

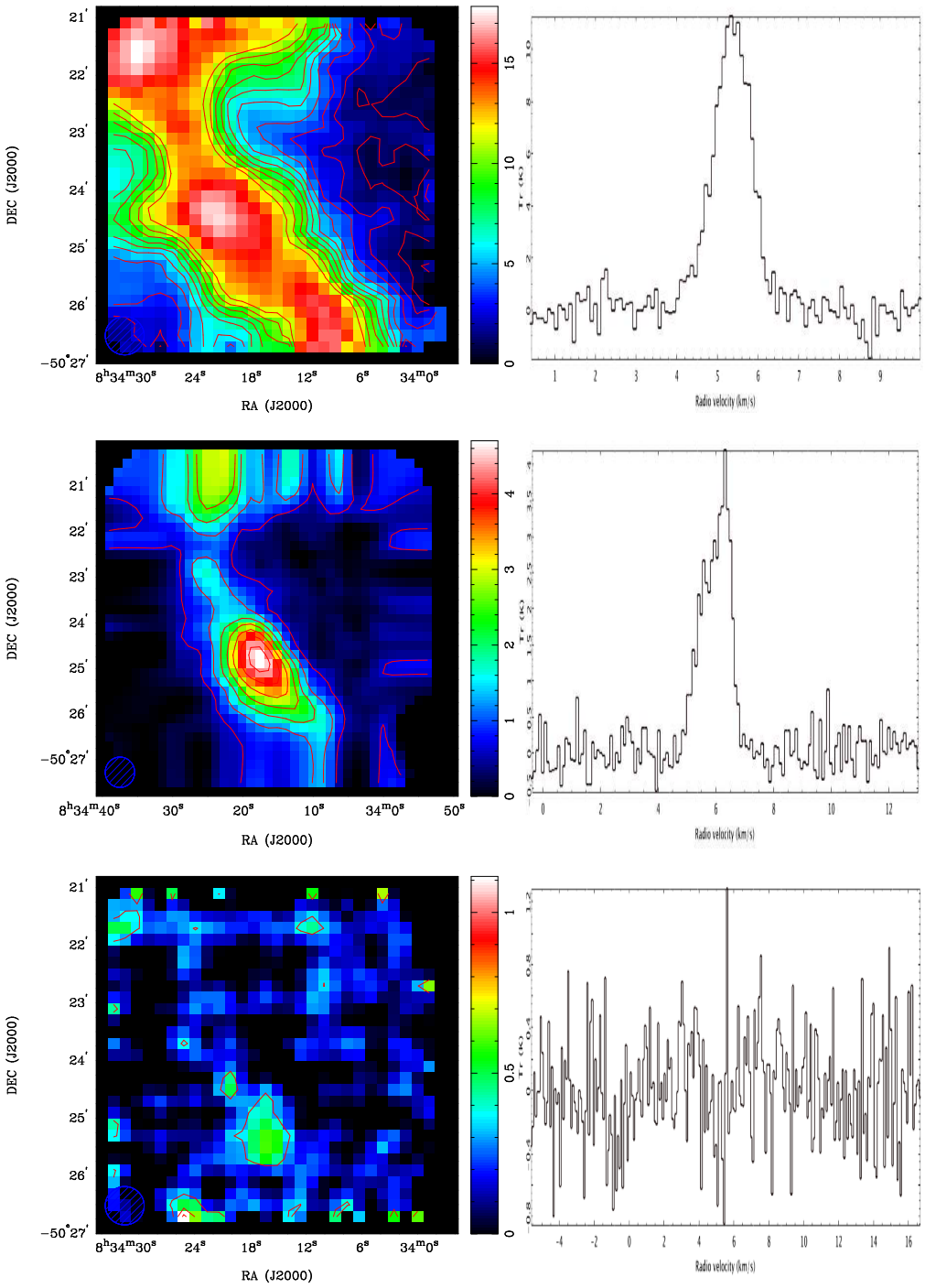

Figure 3.21: Integrated intensity plots for BHR39 in each of the observed CO isotopologues. The ^{12}CO map is shown in the top left image. The top right image is the line profile of the core. This image was used to determine over which velocities the integrated intensity plot was produced. The line profile shows a peak from 3 - 7km/s and so this is the velocity range used to compute the integrated intensity plots for each of the 3 isotopologues. The ^{13}CO integrated intensity map and line profile is shown in the middle left and right images respectively. The C^{18}O integrated intensity plot and line profile is shown in the lower left and right images.

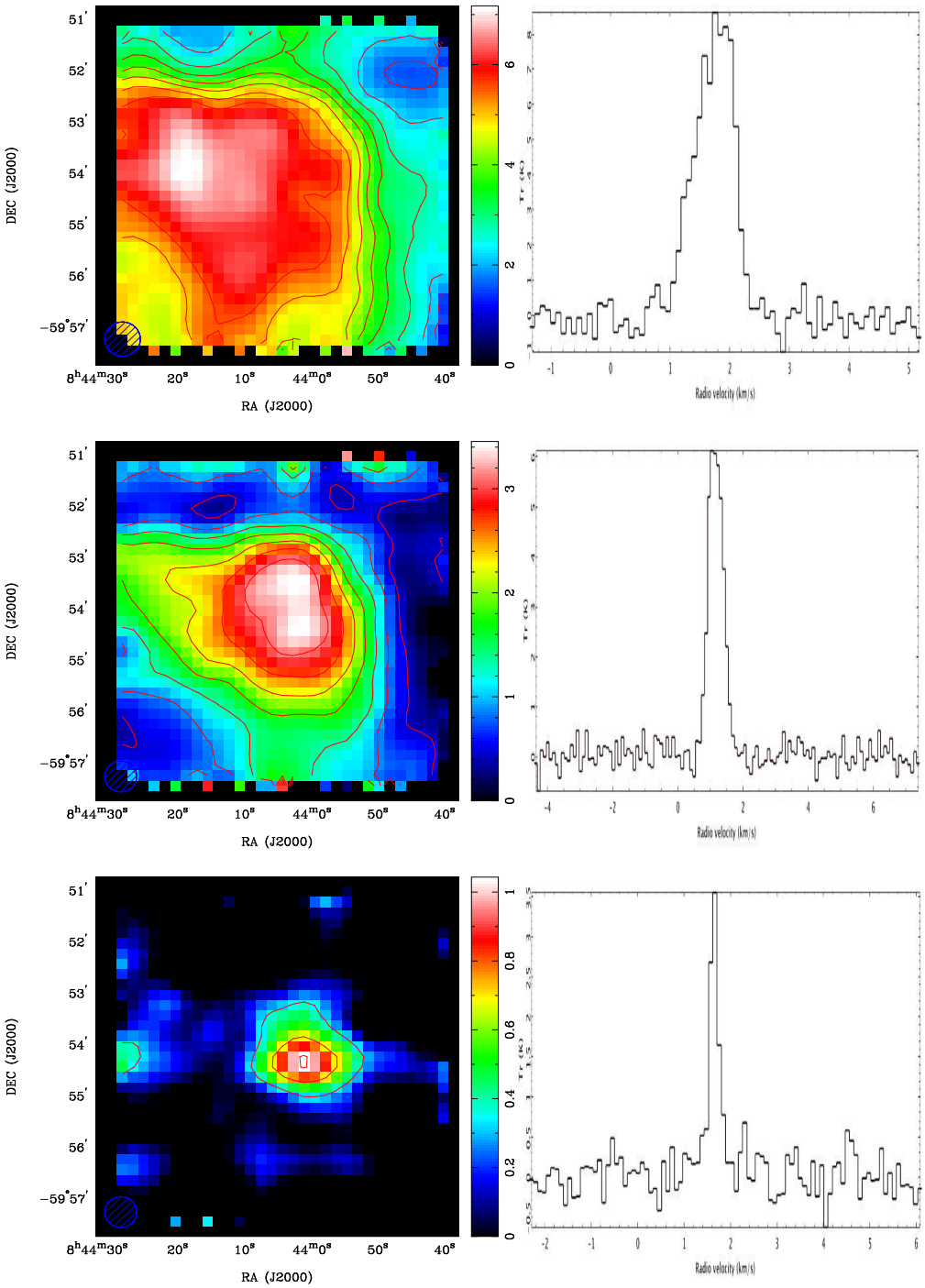

Figure 3.22: Integrated intensity plots for BHR56 in each of the observed CO isotopologues. The ^{12}CO map is shown in the top left image. The top right image is the line profile of the core. This image was used to determine over which velocities the integrated intensity plot was produced. The line profile shows a peak from 0 - 3km/s and so this is the velocity range used to compute the integrated intensity plots for each of the 3 isotopologues. The ^{13}CO integrated intensity map and line profile is shown in the middle left and right images respectively. The C^{18}O integrated intensity plot and line profile is shown in the lower left and right images.

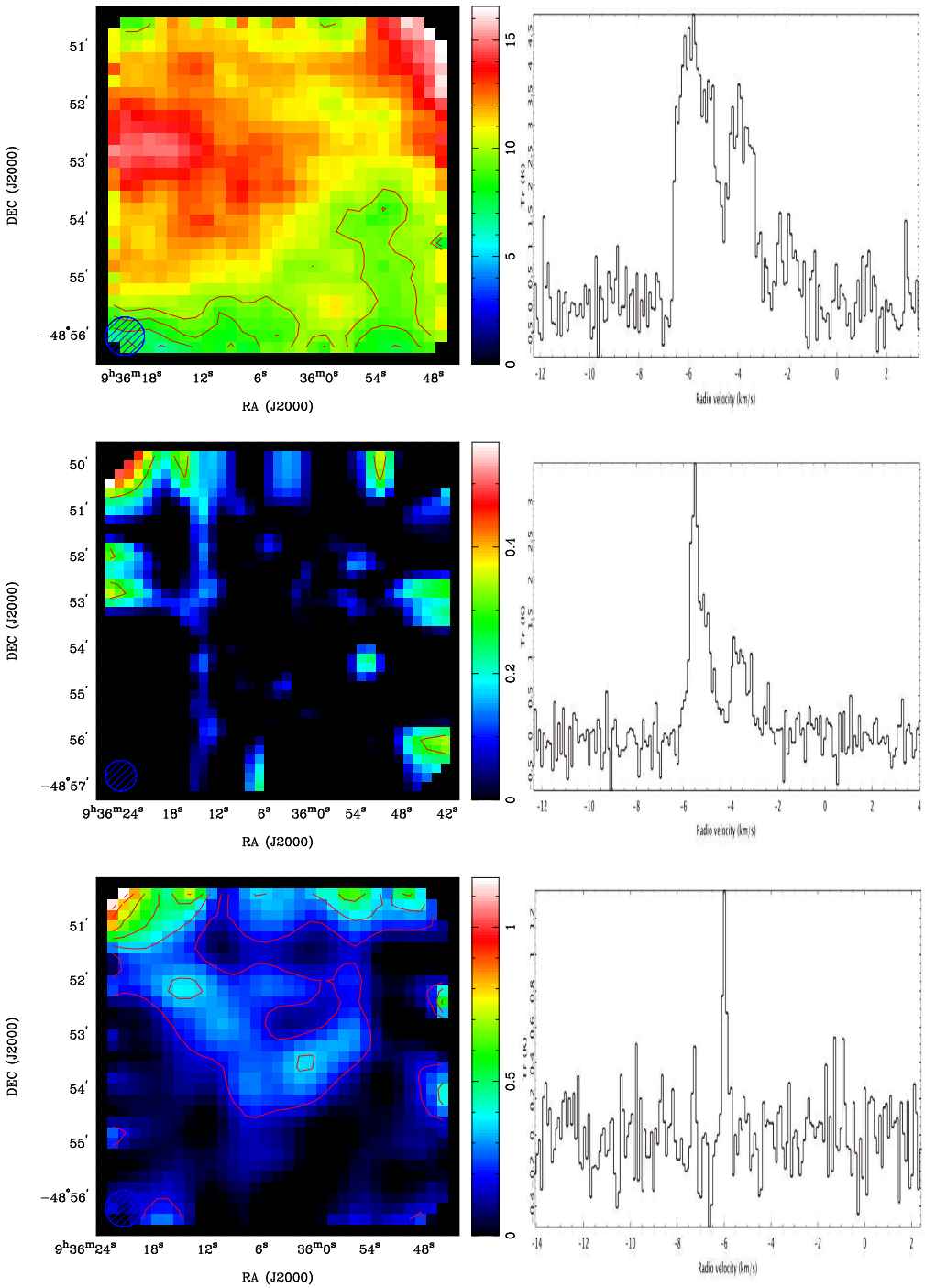

Figure 3.23: Integrated intensity plots for BHR48 in each of the observed CO isotopologues. The ^{12}CO map is shown in the top left image. The top right image is the line profile of the core. This image was used to determine over which velocities the integrated intensity plot was produced. The line profile shows a peak from -8 - -1km/s and so this is the velocity range used to compute the integrated intensity plots for each of the 3 isotopologues. The ^{13}CO integrated intensity map and line profile is shown in the middle left and right images respectively. The C^{18}O integrated intensity plot and line profile is shown in the lower left and right images.

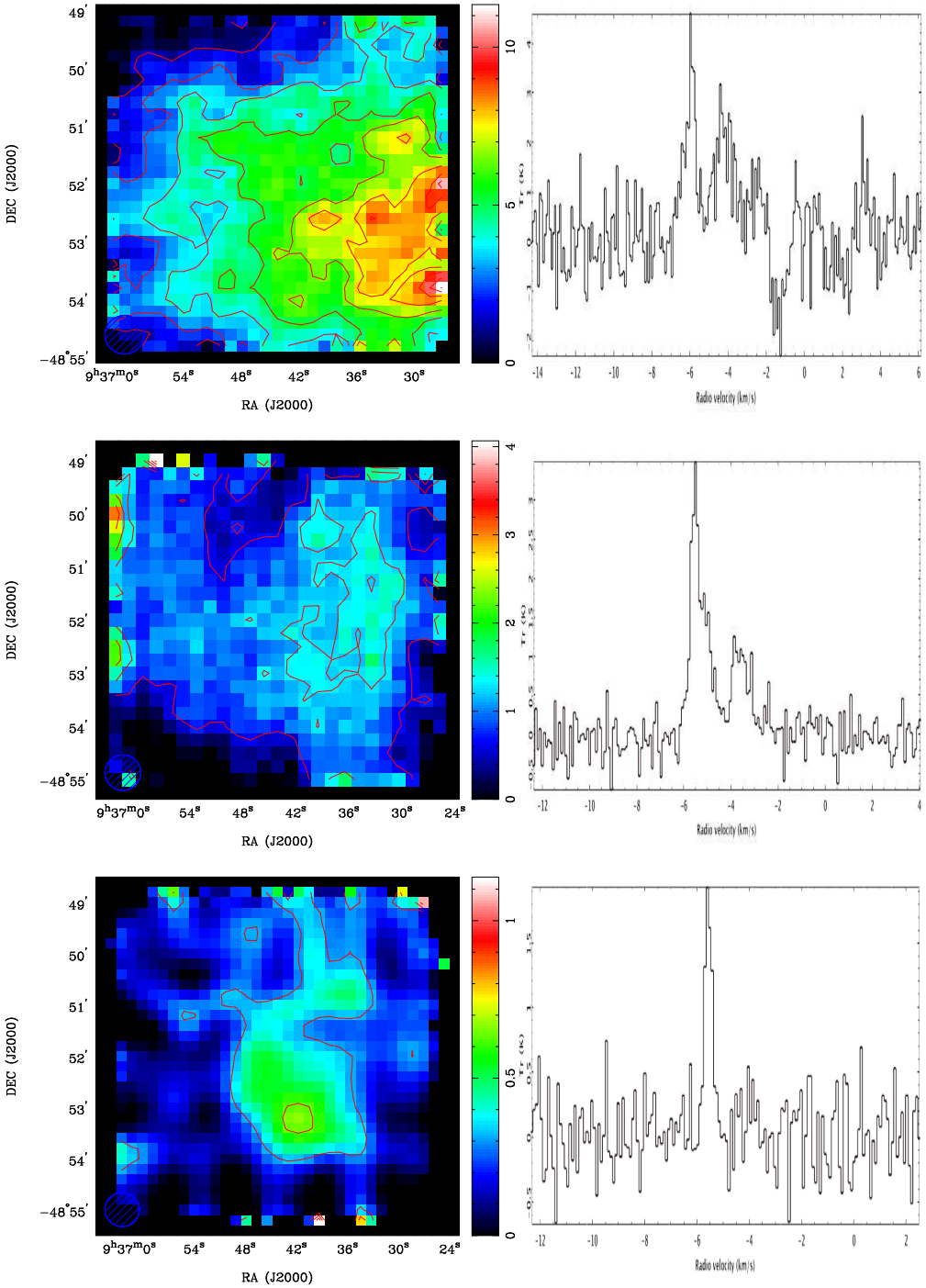

Figure 3.24: Integrated intensity plots for BHR49 in each of the observed CO isotopologues. The ^{12}CO map is shown in the top left image. The top right image is the line profile of the core. This image was used to determine over which velocities the integrated intensity plot was produced. The line profile shows a peak from -8 - -1km/s and so this is the velocity range used to compute the integrated intensity plots for each of the 3 isotopologues. The ^{13}CO integrated intensity map and line profile is shown in the middle left and right images respectively. The C^{18}O integrated intensity plot and line profile is shown in the lower left and right images.

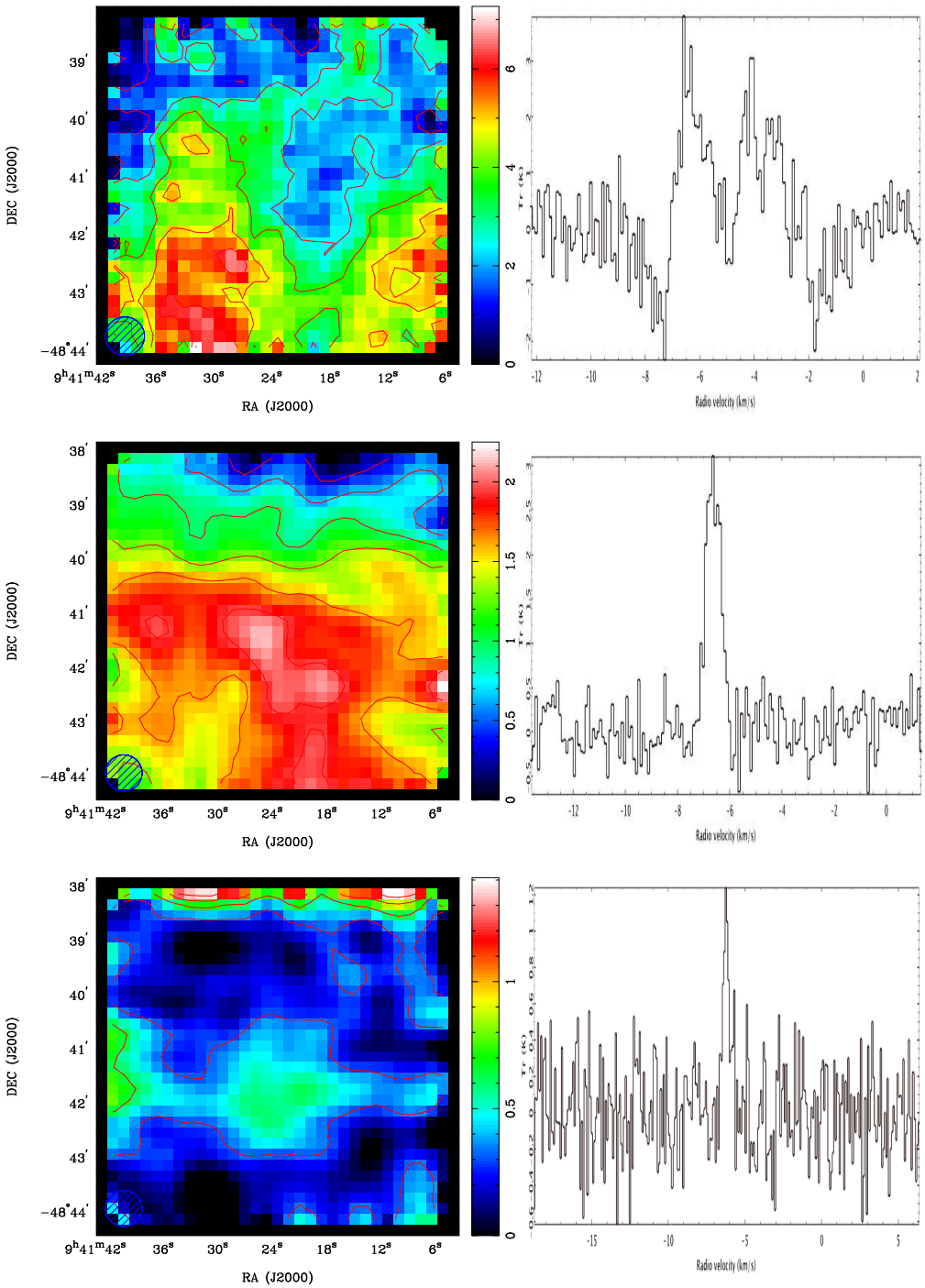

Figure 3.25: Integrated intensity plots for BHR50 in each of the observed CO isotopologues. The ^{12}CO map is shown in the top left image. The top right image is the line profile of the core. This image was used to determine over which velocities the integrated intensity plot was produced. The line profile shows a peak from -8 - -2km/s and so this is the velocity range used to compute the integrated intensity plots for each of the 3 isotopologues. The ^{13}CO integrated intensity map and line profile is shown in the middle left and right images respectively. The C^{18}O integrated intensity plot and line profile is shown in the lower left and right images.

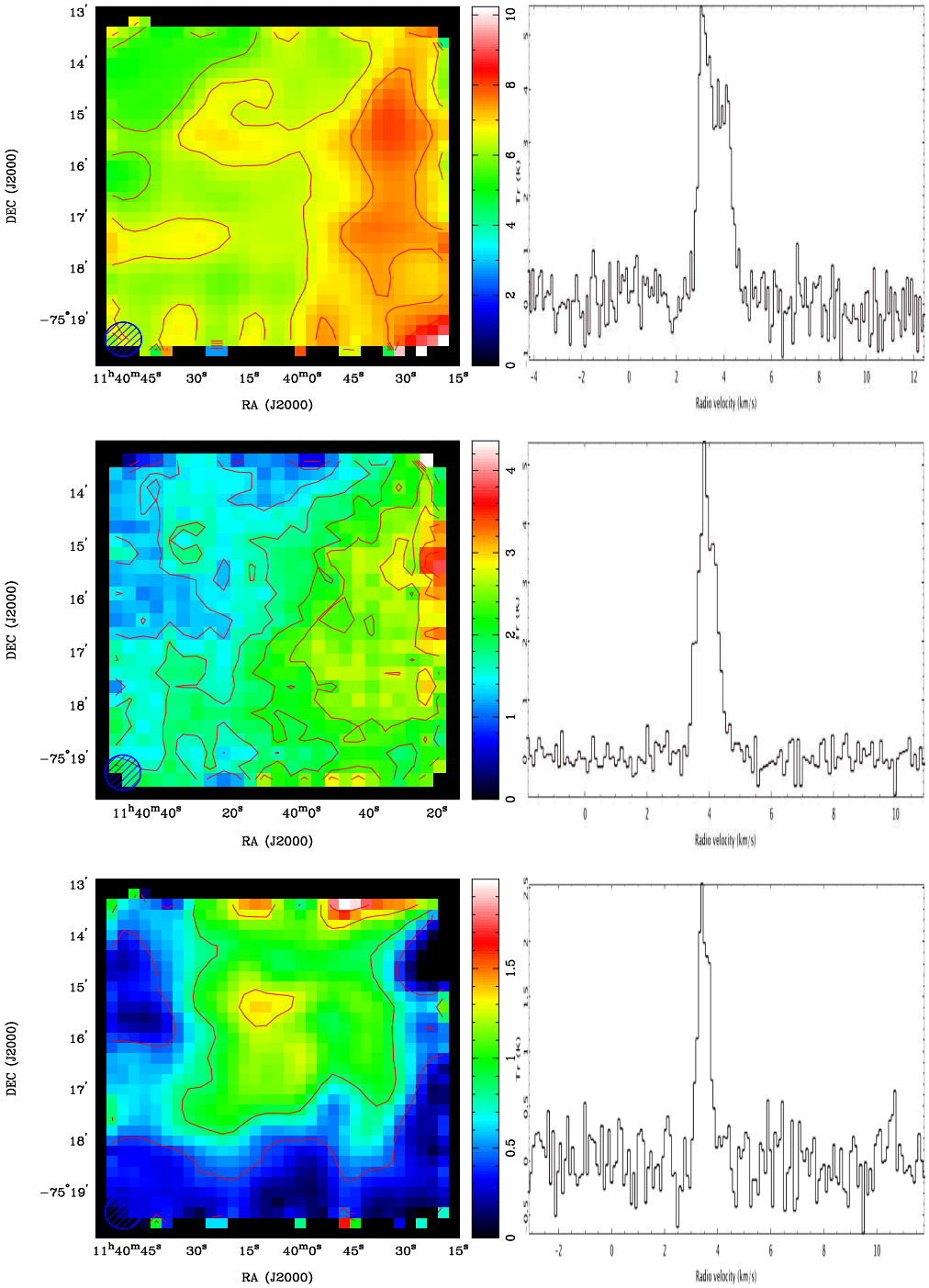

Figure 3.26: Integrated intensity plots for DC2983-131a in each of the observed CO isotopologues. The ^{12}CO map is shown in the top left image. The top right image is the line profile of the core. This image was used to determine over which velocities the integrated intensity plot was produced. The line profile shows a peak from 1 - 6km/s and so this is the velocity range used to compute the integrated intensity plots for each of the 3 isotopologues. The ^{13}CO integrated intensity map and line profile is shown in the middle left and right images respectively. The C^{18}O integrated intensity plot and line profile is shown in the lower left and right images.

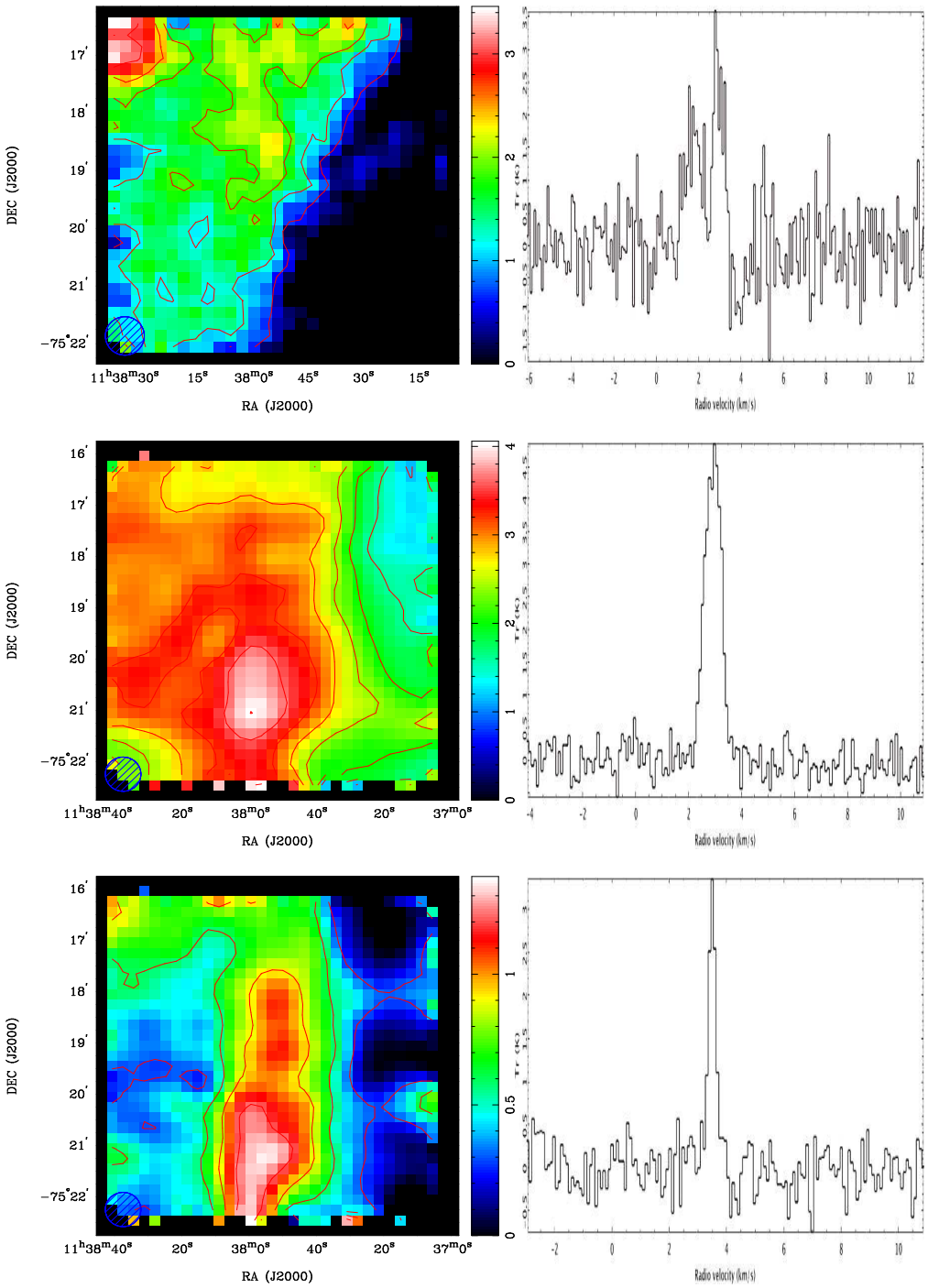

Figure 3.27: Integrated intensity plots for DC2983-131b in each of the observed CO isotopologues. The ^{12}CO map is shown in the top left image. The top right image is the line profile of the core. This image was used to determine over which velocities the integrated intensity plot was produced. The line profile shows a peak from 0 - 4km/s and so this is the velocity range used to compute the integrated intensity plots for each of the 3 isotopologues. The ^{13}CO integrated intensity map and line profile is shown in the middle left and right images respectively. The C^{18}O integrated intensity plot and line profile is shown in the lower left and right images.

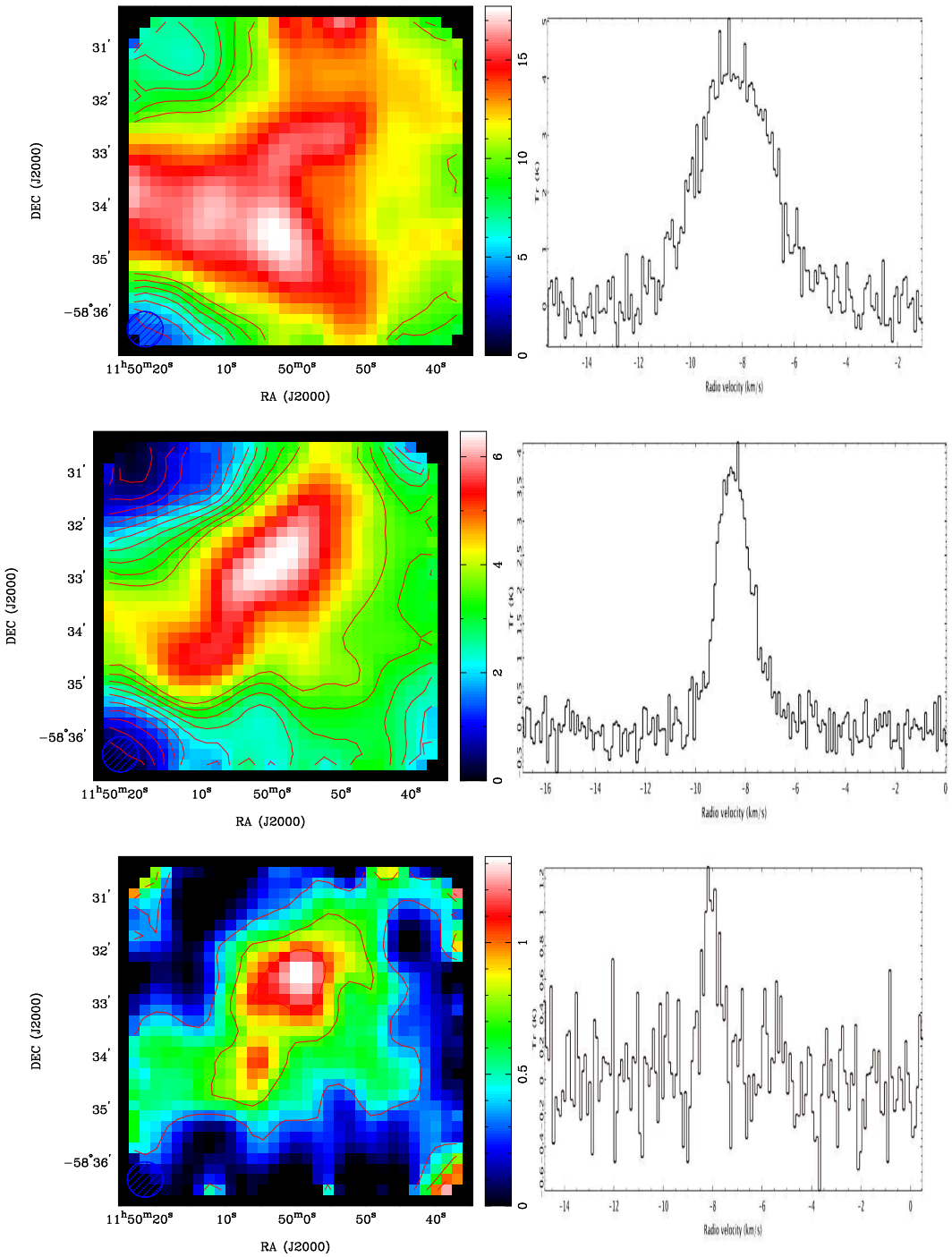

Figure 3.28: Integrated intensity plots for BHR68 in each of the observed CO isotopologues. The ^{12}CO map is shown in the top left image. The top right image is the line profile of the core. This image was used to determine over which velocities the integrated intensity plot was produced. The line profile shows a peak from -12 - -6km/s and so this is the velocity range used to compute the integrated intensity plots for each of the 3 isotopologues. The ^{13}CO integrated intensity map and line profile is shown in the middle left and right images respectively. The C^{18}O integrated intensity plot and line profile is shown in the lower left and right images.

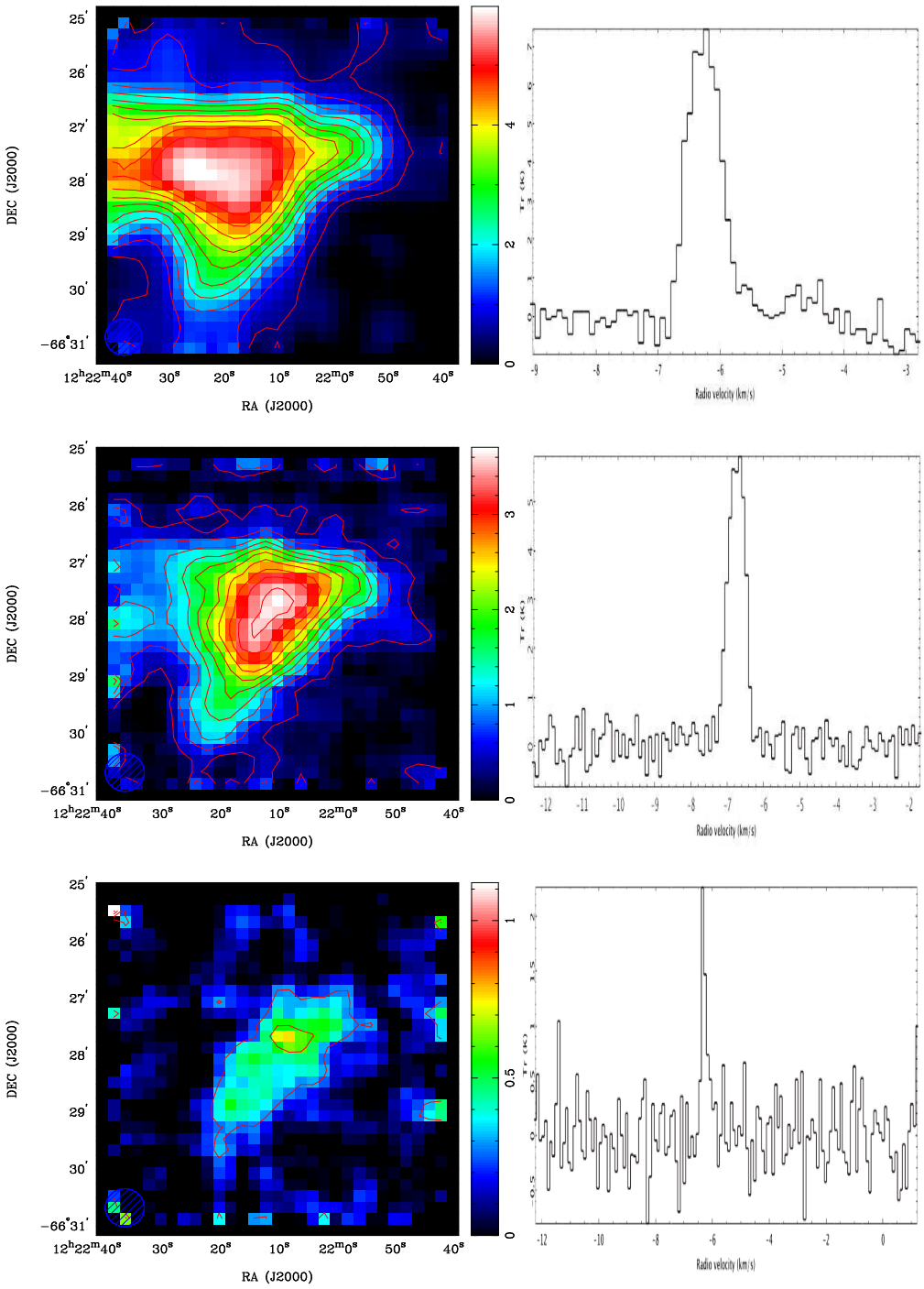

Figure 3.29: Integrated intensity plots for BHR74 in each of the observed CO isotopologues. The ^{12}CO map is shown in the top left image. The top right image is the line profile of the core. This image was used to determine over which velocities the integrated intensity plot was produced. The line profile shows a peak from -7 - -5km/s and so this is the velocity range used to compute the integrated intensity plots for each of the 3 isotopologues. The ^{13}CO integrated intensity map and line profile is shown in the middle left and right images respectively. The C^{18}O integrated intensity plot and line profile is shown in the lower left and right images.

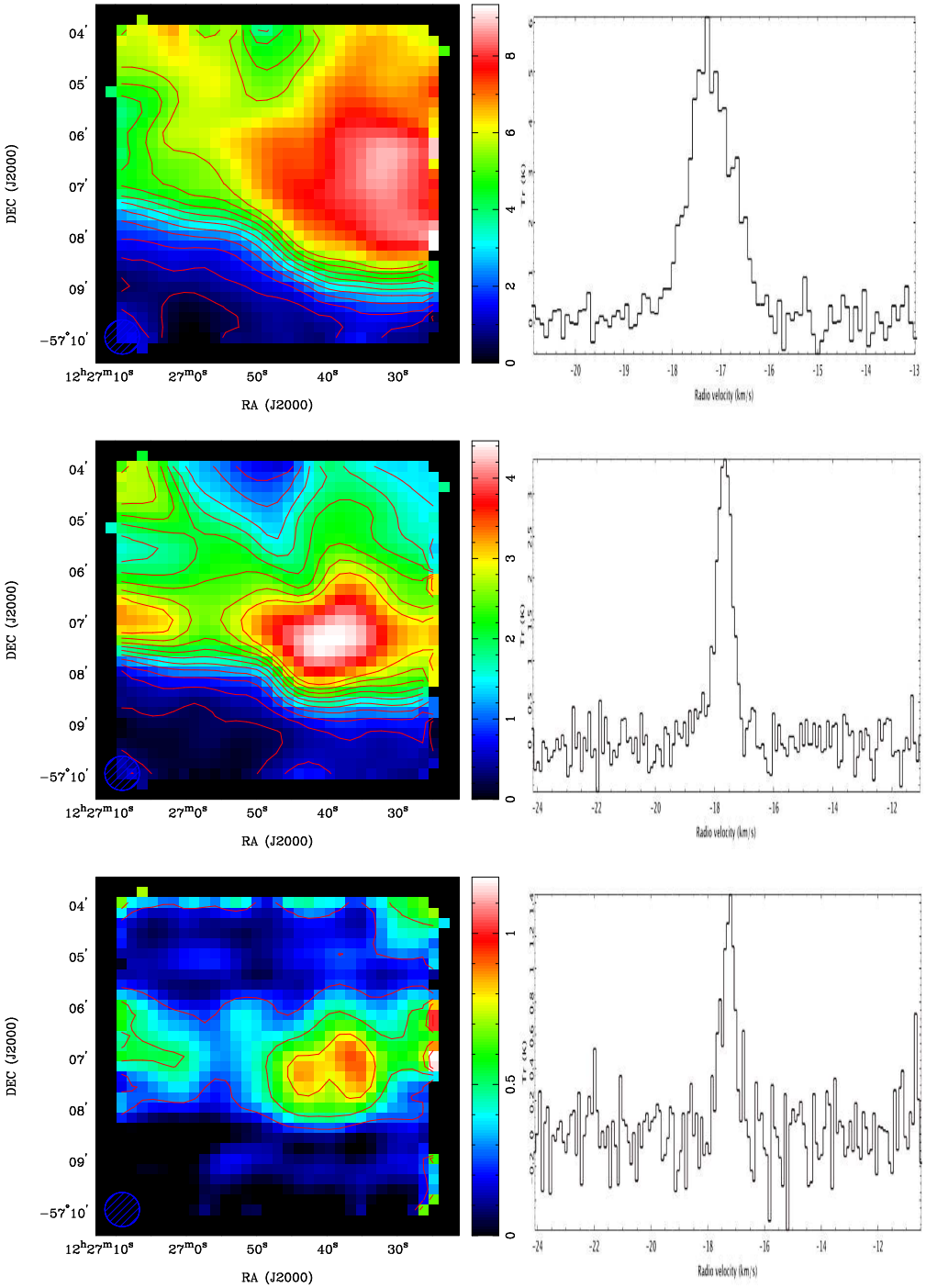

Figure 3.30: Integrated intensity plots for BHR73 in each of the observed CO isotopologues. The ^{12}CO map is shown in the top left image. The top right image is the line profile of the core. This image was used to determine over which velocities the integrated intensity plot was produced. The line profile shows a peak from -19 - -16km/s and so this is the velocity range used to compute the integrated intensity plots for each of the 3 isotopologues. The ^{13}CO integrated intensity map and line profile is shown in the middle left and right images respectively. The C^{18}O integrated intensity plot and line profile is shown in the lower left and right images.

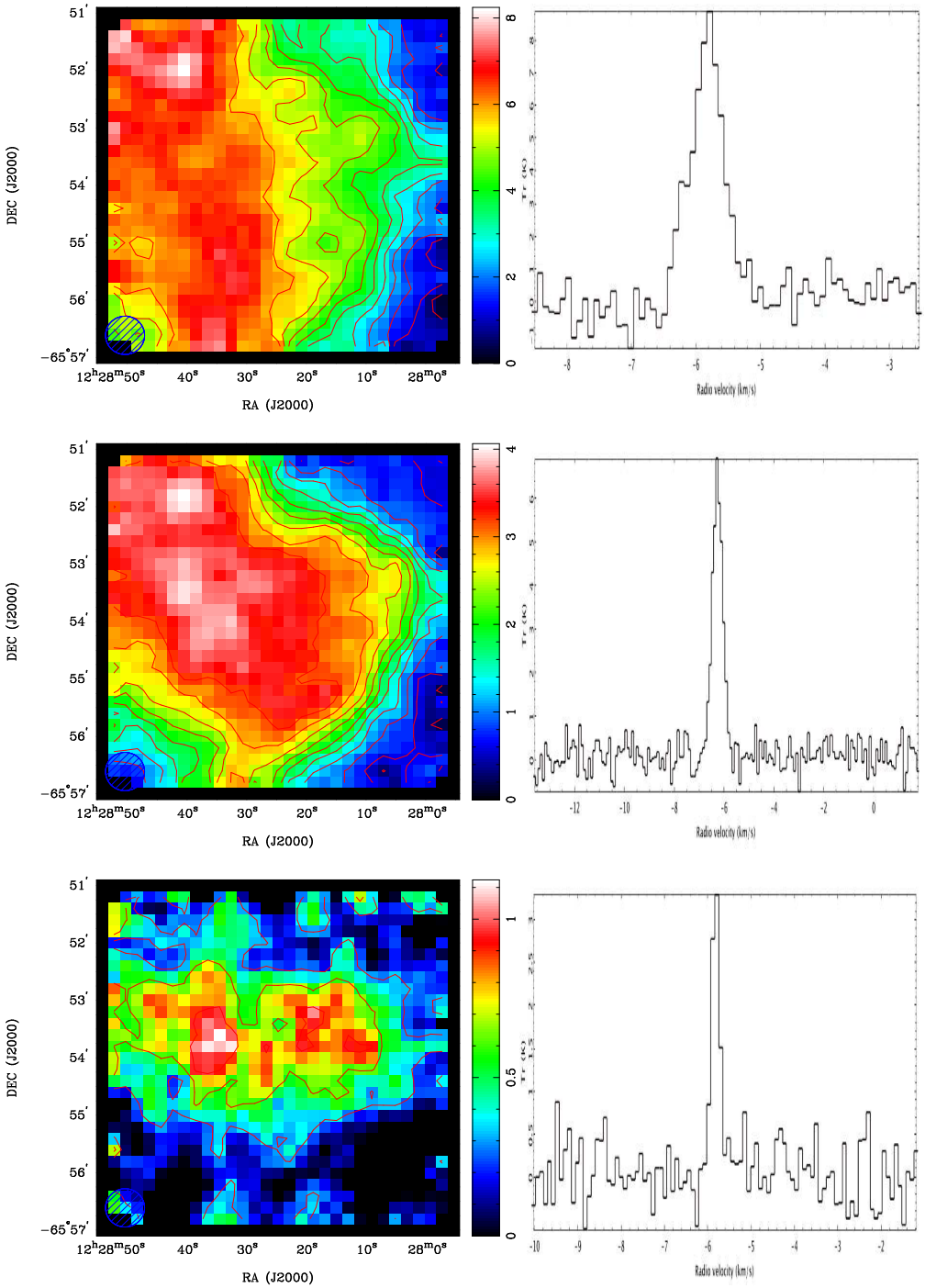

Figure 3.31: Integrated intensity plots for BHR76 in each of the observed CO isotopologues. The ^{12}CO map is shown in the top left image. The top right image is the line profile of the core. This image was used to determine over which velocities the integrated intensity plot was produced. The line profile shows a peak from -7 - -5km/s and so this is the velocity range used to compute the integrated intensity plots for each of the 3 isotopologues. The ^{13}CO integrated intensity map and line profile is shown in the middle left and right images respectively. The C^{18}O integrated intensity plot and line profile is shown in the lower left and right images.

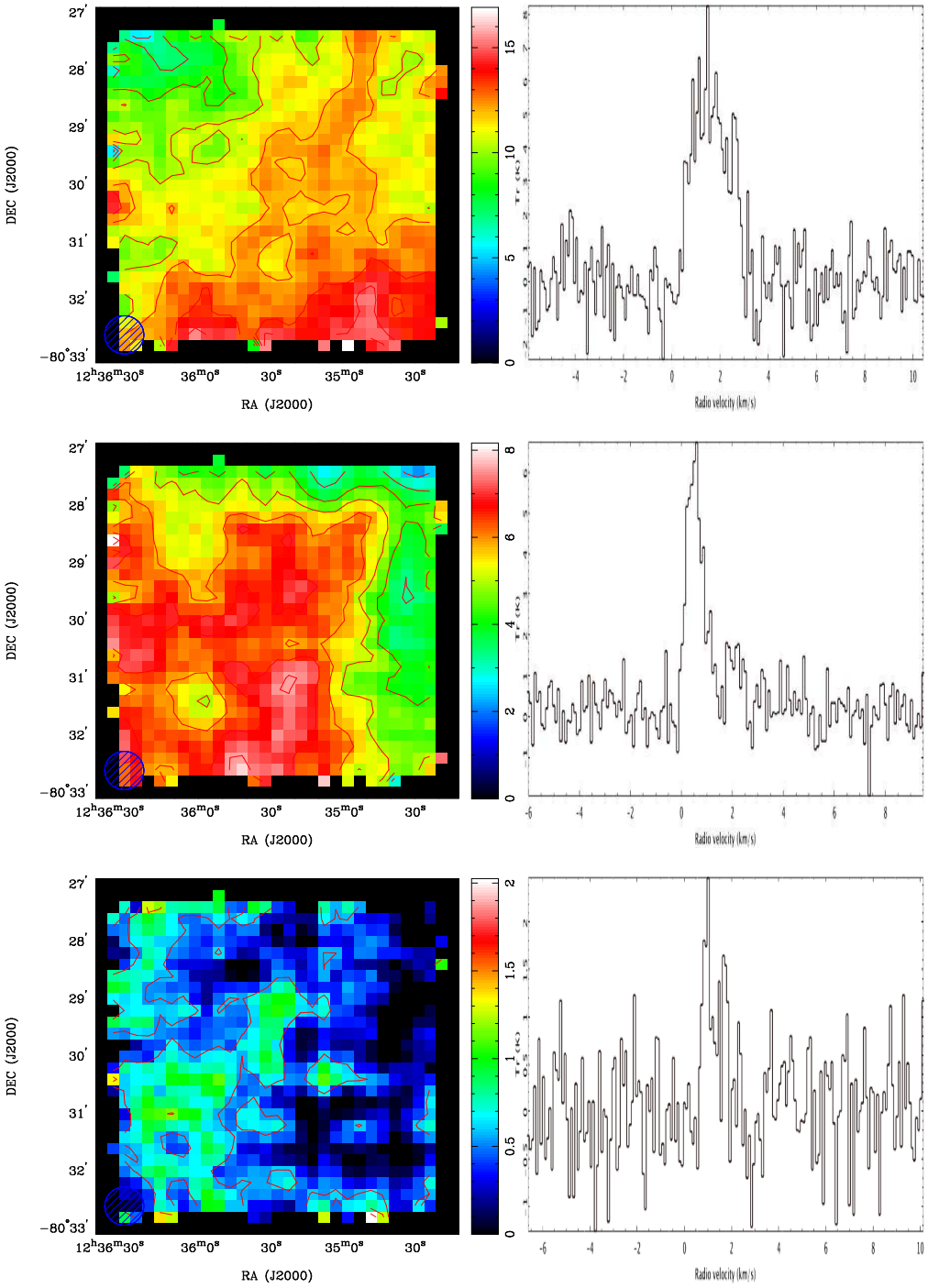

Figure 3.32: Integrated intensity plots for DC3023-177 in each of the observed CO isotopologues. The ^{12}CO map is shown in the top left image. The top right image is the line profile of the core. This image was used to determine over which velocities the integrated intensity plot was produced. The line profile shows a peak from -1 - 4km/s and so this is the velocity range used to compute the integrated intensity plots for each of the 3 isotopologues. The ^{13}CO integrated intensity map and line profile is shown in the middle left and right images respectively. The C^{18}O integrated intensity plot and line profile is shown in the lower left and right images.

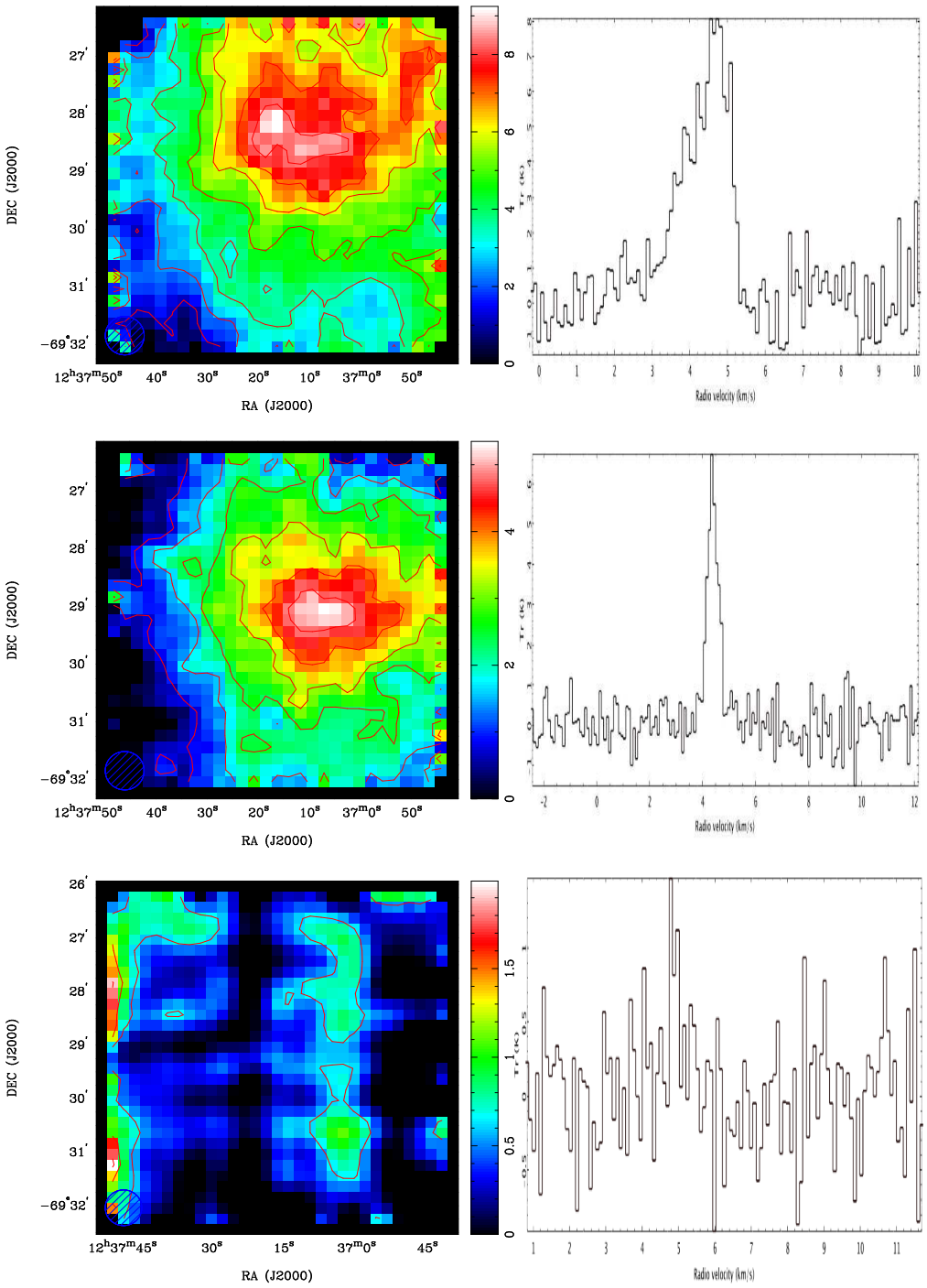

Figure 3.33: Integrated intensity plots for BHR79 in each of the observed CO isotopologues. The ^{12}CO map is shown in the top left image. The top right image is the line profile of the core. This image was used to determine over which velocities the integrated intensity plot was produced. The line profile shows a peak from 2 - 6km/s and so this is the velocity range used to compute the integrated intensity plots for each of the 3 isotopologues. The ^{13}CO integrated intensity map and line profile is shown in the middle left and right images respectively. The C^{18}O integrated intensity plot and line profile is shown in the lower left and right images.

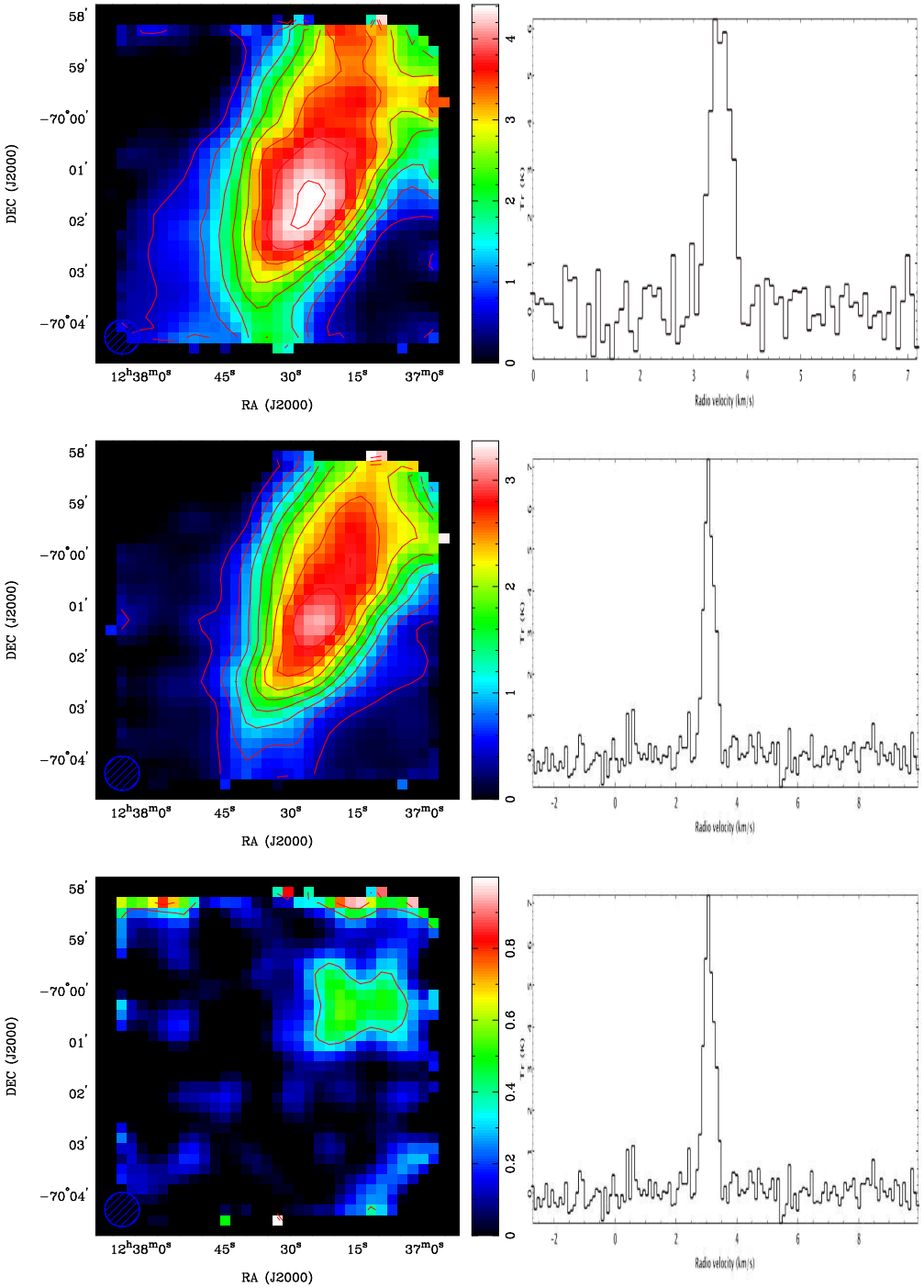

Figure 3.34: Integrated intensity plots for BHR80 in each of the observed CO isotopologues. The ^{12}CO map is shown in the top left image. The top right image is the line profile of the core. This image was used to determine over which velocities the integrated intensity plot was produced. The line profile shows a peak from 2 - 5km/s and so this is the velocity range used to compute the integrated intensity plots for each of the 3 isotopologues. The ^{13}CO integrated intensity map and line profile is shown in the middle left and right images respectively. The C^{18}O integrated intensity plot and line profile is shown in the lower left and right images.

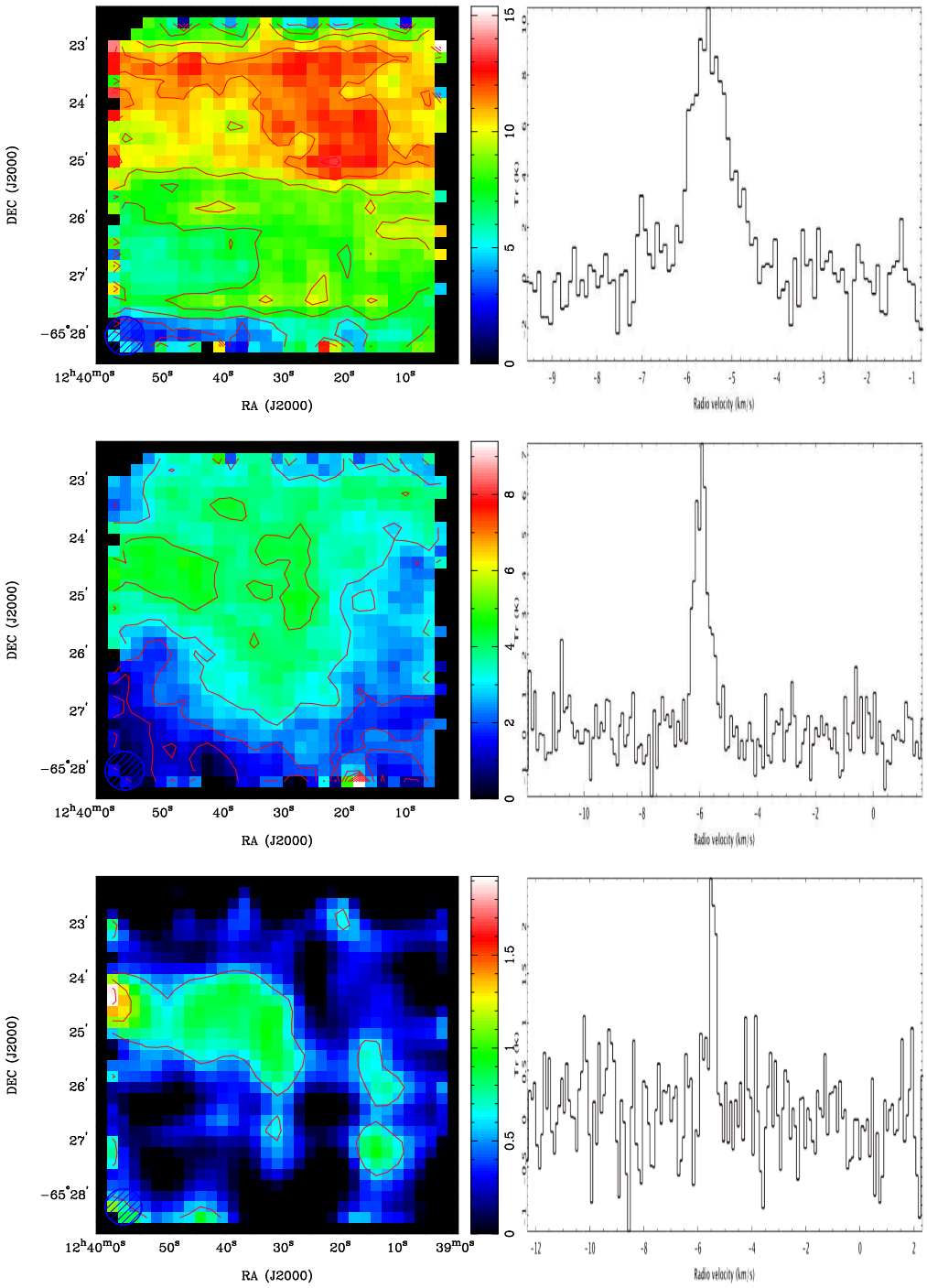

Figure 3.35: Integrated intensity plots for BHR81 in each of the observed CO isotopologues. The ^{12}CO map is shown in the top left image. The top right image is the line profile of the core. This image was used to determine over which velocities the integrated intensity plot was produced. The line profile shows a peak from -7 - -4km/s and so this is the velocity range used to compute the integrated intensity plots for each of the 3 isotopologues. The ^{13}CO integrated intensity map and line profile is shown in the middle left and right images respectively. The C^{18}O integrated intensity plot and line profile is shown in the lower left and right images.

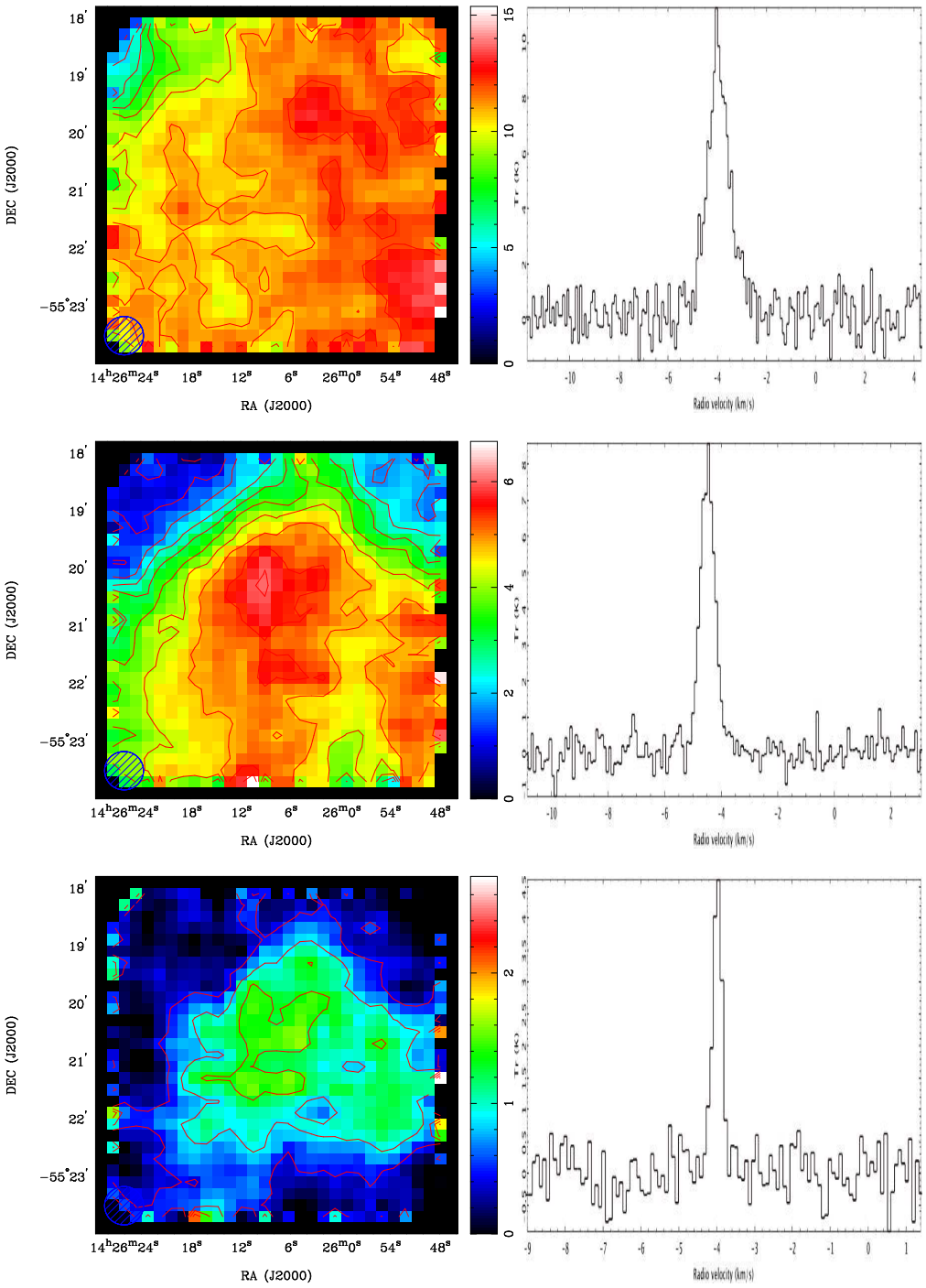

Figure 3.36: Integrated intensity plots for DC3162+51 in each of the observed CO isotopologues. The ^{12}CO map is shown in the top left image. The top right image is the line profile of the core. This image was used to determine over which velocities the integrated intensity plot was produced. The line profile shows a peak from -6 - -2km/s and so this is the velocity range used to compute the integrated intensity plots for each of the 3 isotopologues. The ^{13}CO integrated intensity map and line profile is shown in the middle left and right images respectively. The C^{18}O integrated intensity plot and line profile is shown in the lower left and right images.

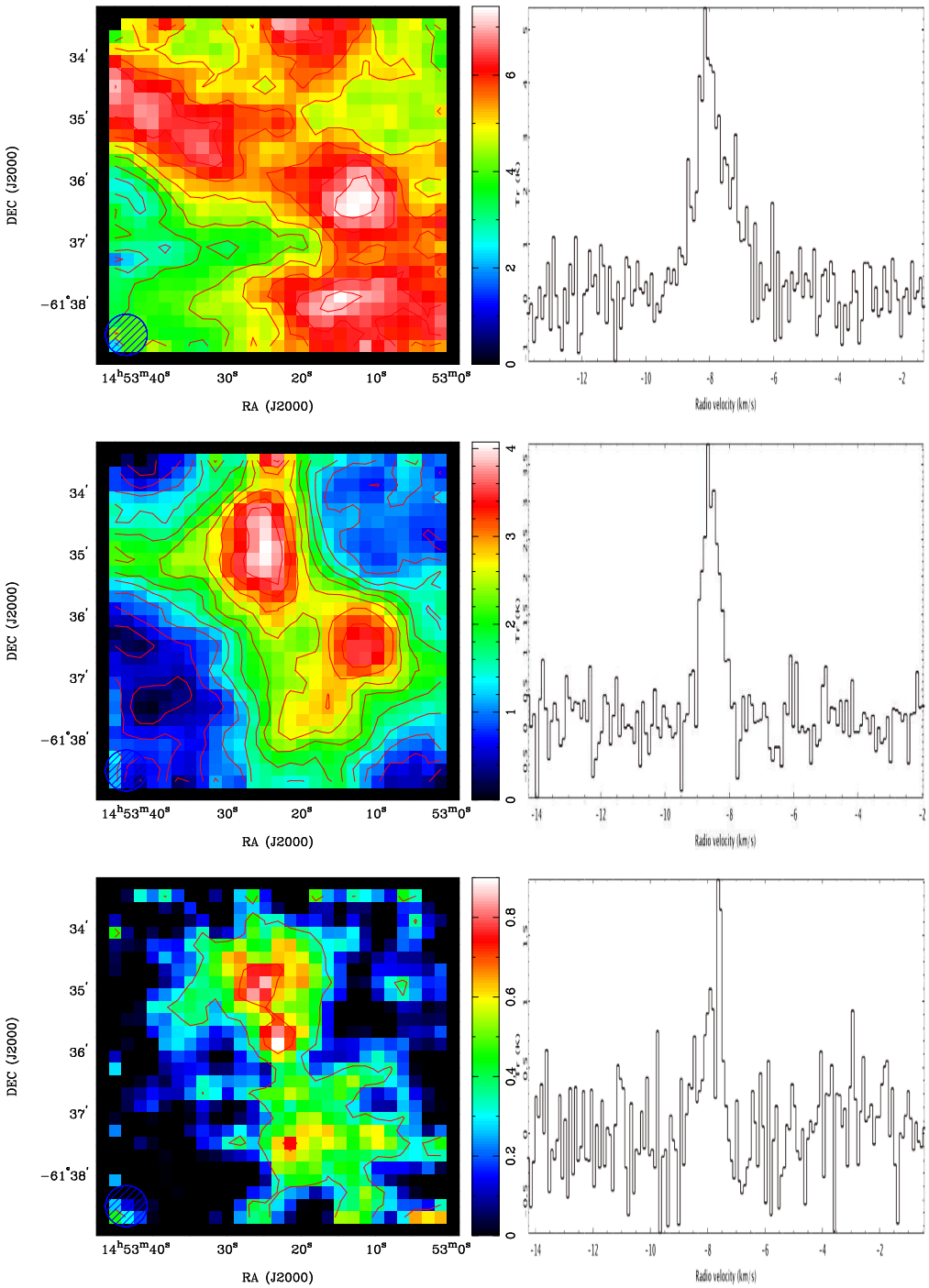

Figure 3.37: Integrated intensity plots for BHR95 in each of the observed CO isotopologues. The ^{12}CO map is shown in the top left image. The top right image is the line profile of the core. This image was used to determine over which velocities the integrated intensity plot was produced. The line profile shows a peak from -10 - 6km/s and so this is the velocity range used to compute the integrated intensity plots for each of the 3 isotopologues. The ^{13}CO integrated intensity map and line profile is shown in the middle left and right images respectively. The C^{18}O integrated intensity plot and line profile is shown in the lower left and right images.

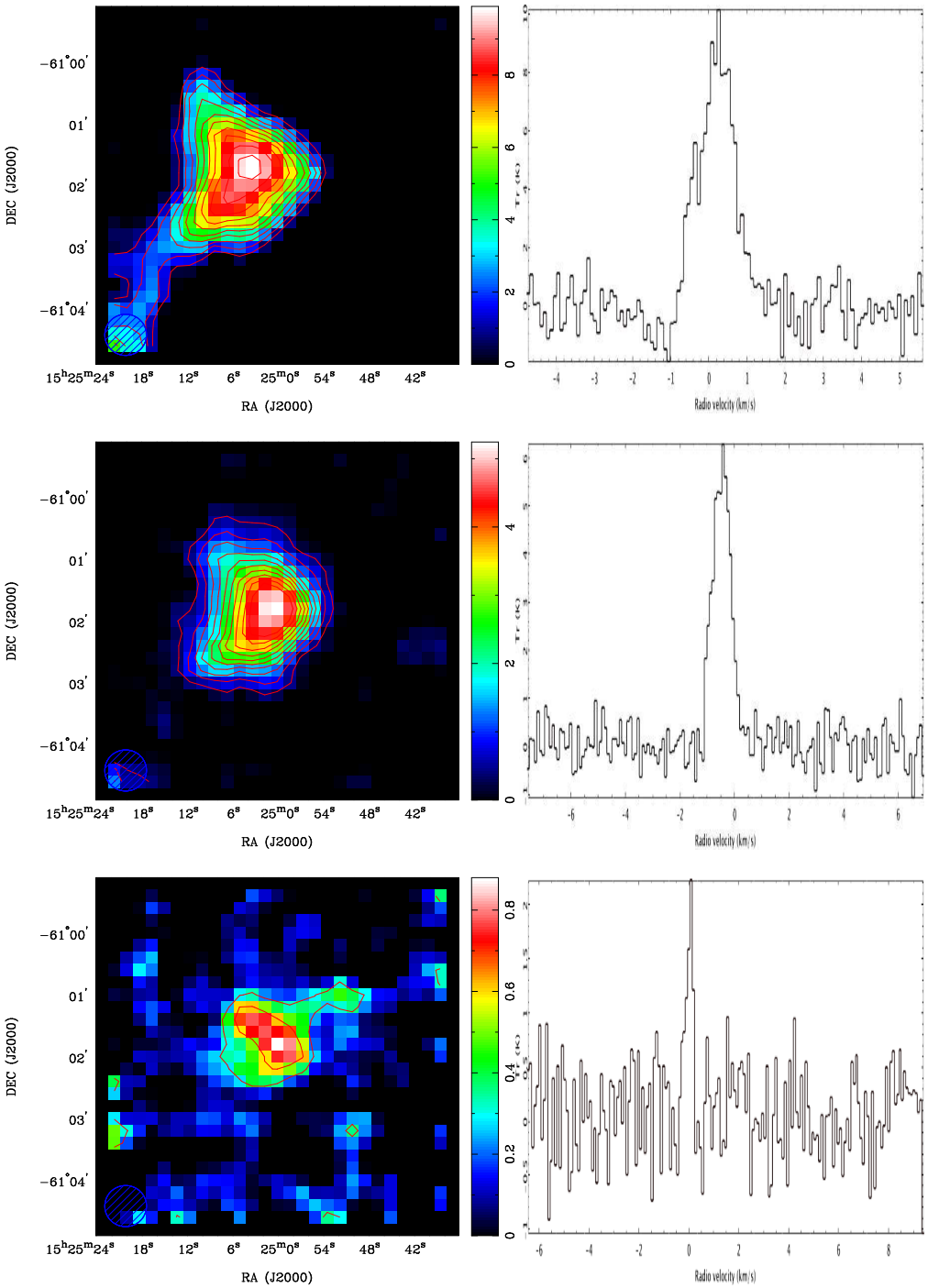

Figure 3.38: Integrated intensity plots for BHR99 in each of the observed CO isotopologues. The ^{12}CO map is shown in the top left image. The top right image is the line profile of the core. This image was used to determine over which velocities the integrated intensity plot was produced. The line profile shows a peak from -1 - 2km/s and so this is the velocity range used to compute the integrated intensity plots for each of the 3 isotopologues. The ^{13}CO integrated intensity map and line profile is shown in the middle left and right images respectively. The C^{18}O integrated intensity plot and line profile is shown in the lower left and right images.

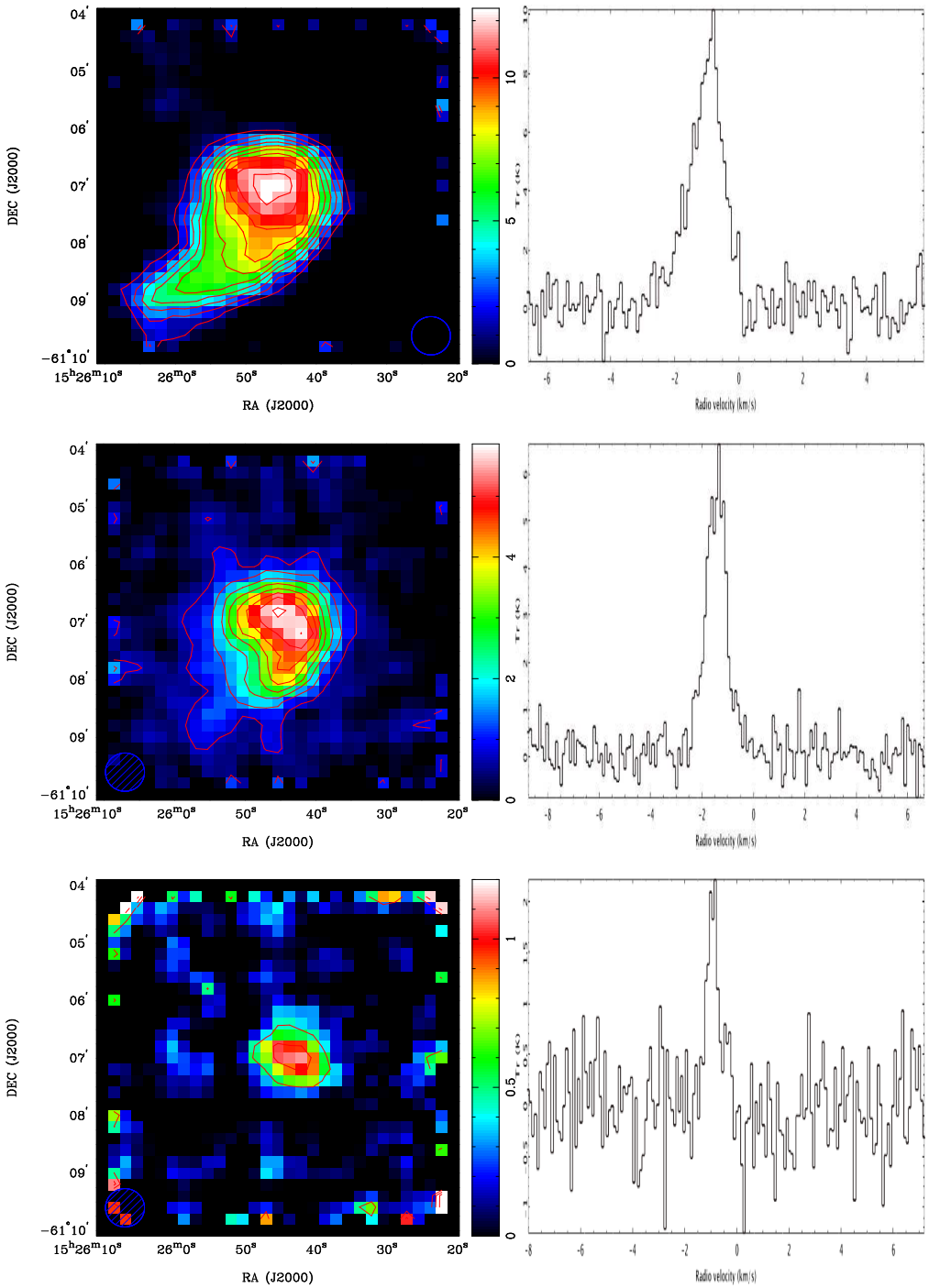

Figure 3.39: Integrated intensity plots for BHR100 in each of the observed CO isotopologues. The ^{12}CO map is shown in the top left image. The top right image is the line profile of the core. This image was used to determine over which velocities the integrated intensity plot was produced. The line profile shows a peak from -3 - 1km/s and so this is the velocity range used to compute the integrated intensity plots for each of the 3 isotopologues. The ^{13}CO integrated intensity map and line profile is shown in the middle left and right images respectively. The C^{18}O integrated intensity plot and line profile is shown in the lower left and right images.

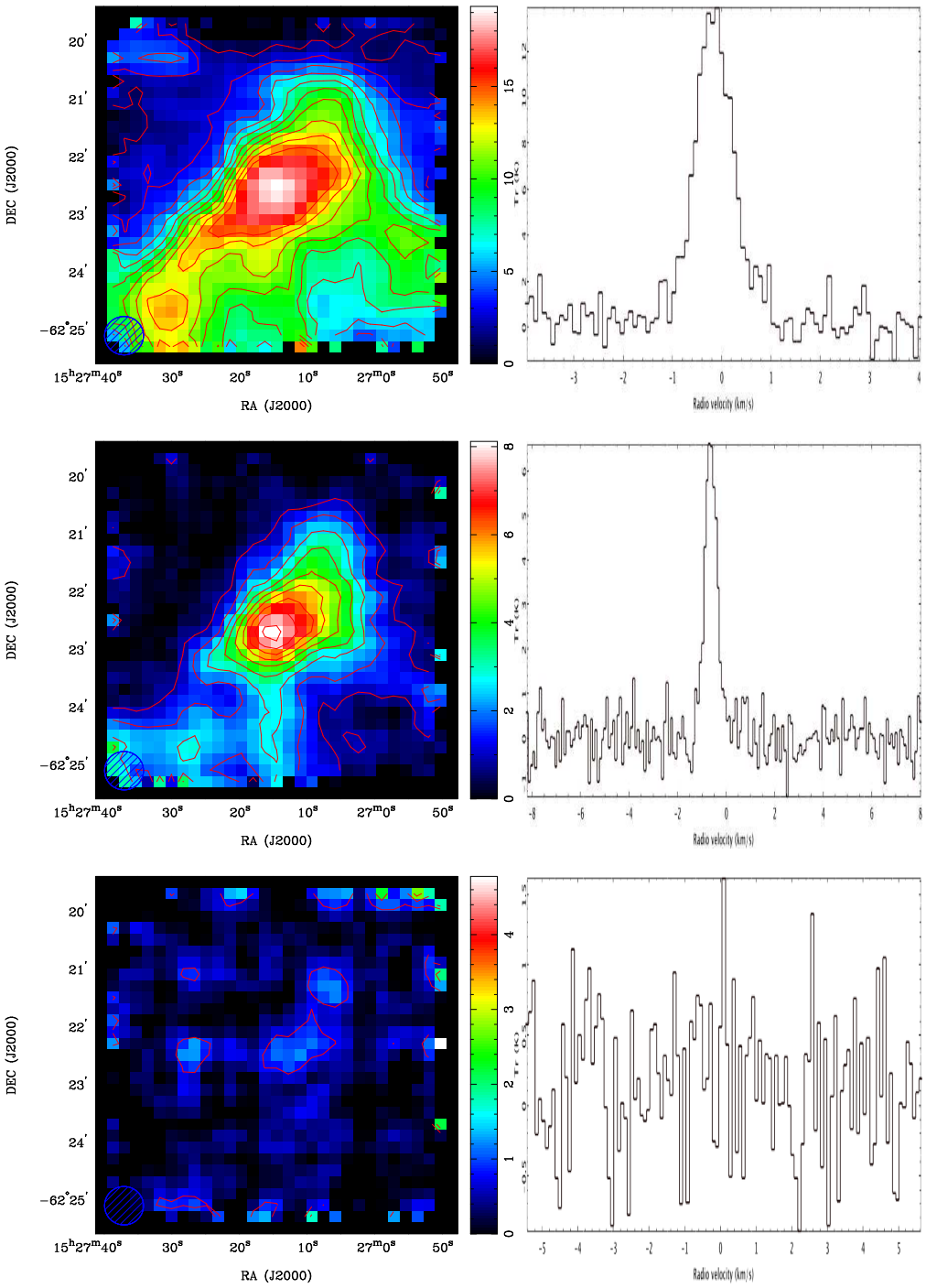

Figure 3.40: Integrated intensity plots for BHR97 in each of the observed CO isotopologues. The ^{12}CO map is shown in the top left image. The top right image is the line profile of the core. This image was used to determine over which velocities the integrated intensity plot was produced. The line profile shows a peak from -2 - 1km/s and so this is the velocity range used to compute the integrated intensity plots for each of the 3 isotopologues. The ^{13}CO integrated intensity map and line profile is shown in the middle left and right images respectively. The C^{18}O integrated intensity plot and line profile is shown in the lower left and right images.

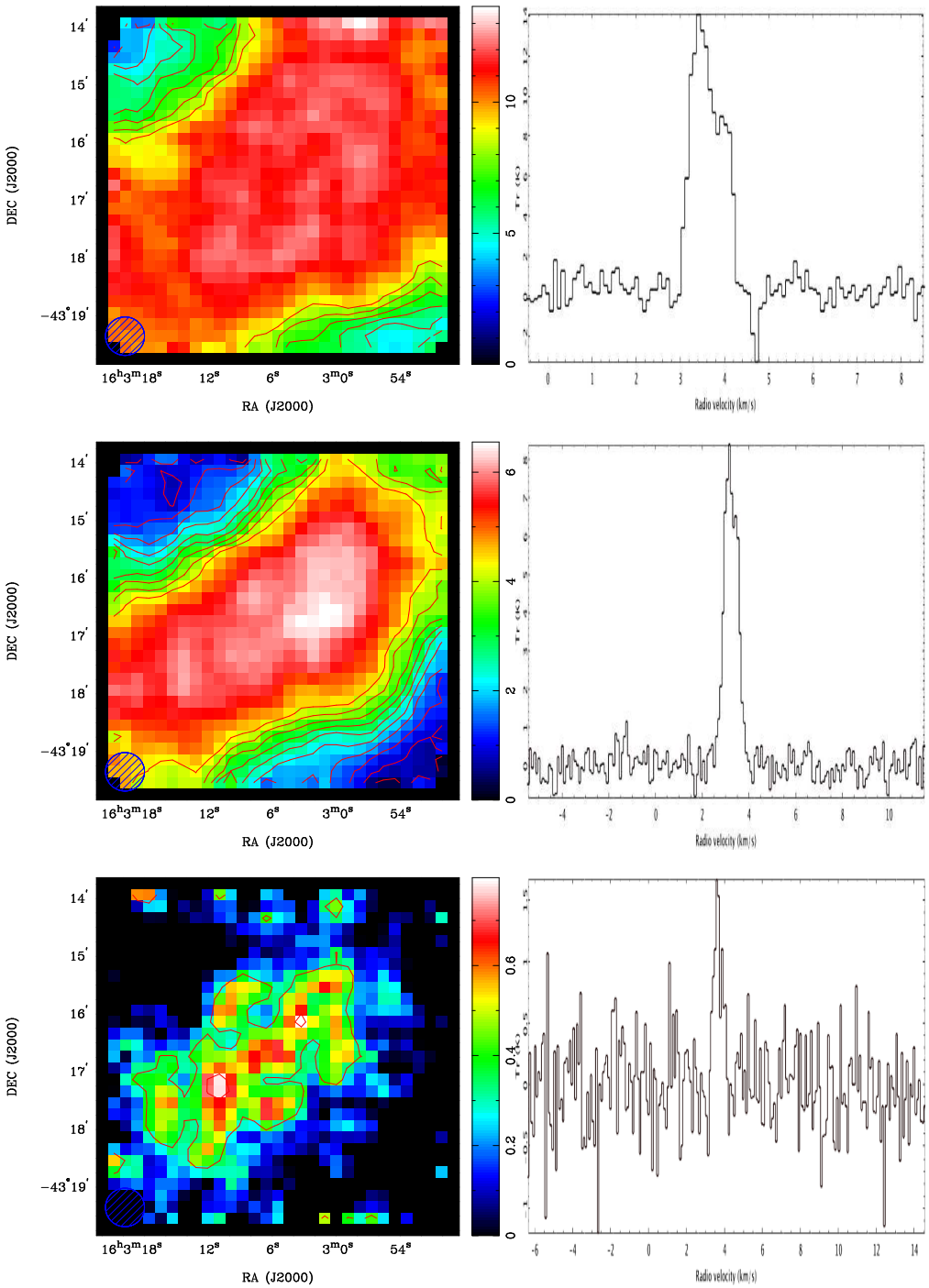

Figure 3.41: Integrated intensity plots for BHR119 in each of the observed CO isotopologues. The ^{12}CO map is shown in the top left image. The top right image is the line profile of the core. This image was used to determine over which velocities the integrated intensity plot was produced. The line profile shows a peak from 2 - 5km/s and so this is the velocity range used to compute the integrated intensity plots for each of the 3 isotopologues. The ^{13}CO integrated intensity map and line profile is shown in the middle left and right images respectively. The C^{18}O integrated intensity plot and line profile is shown in the lower left and right images.

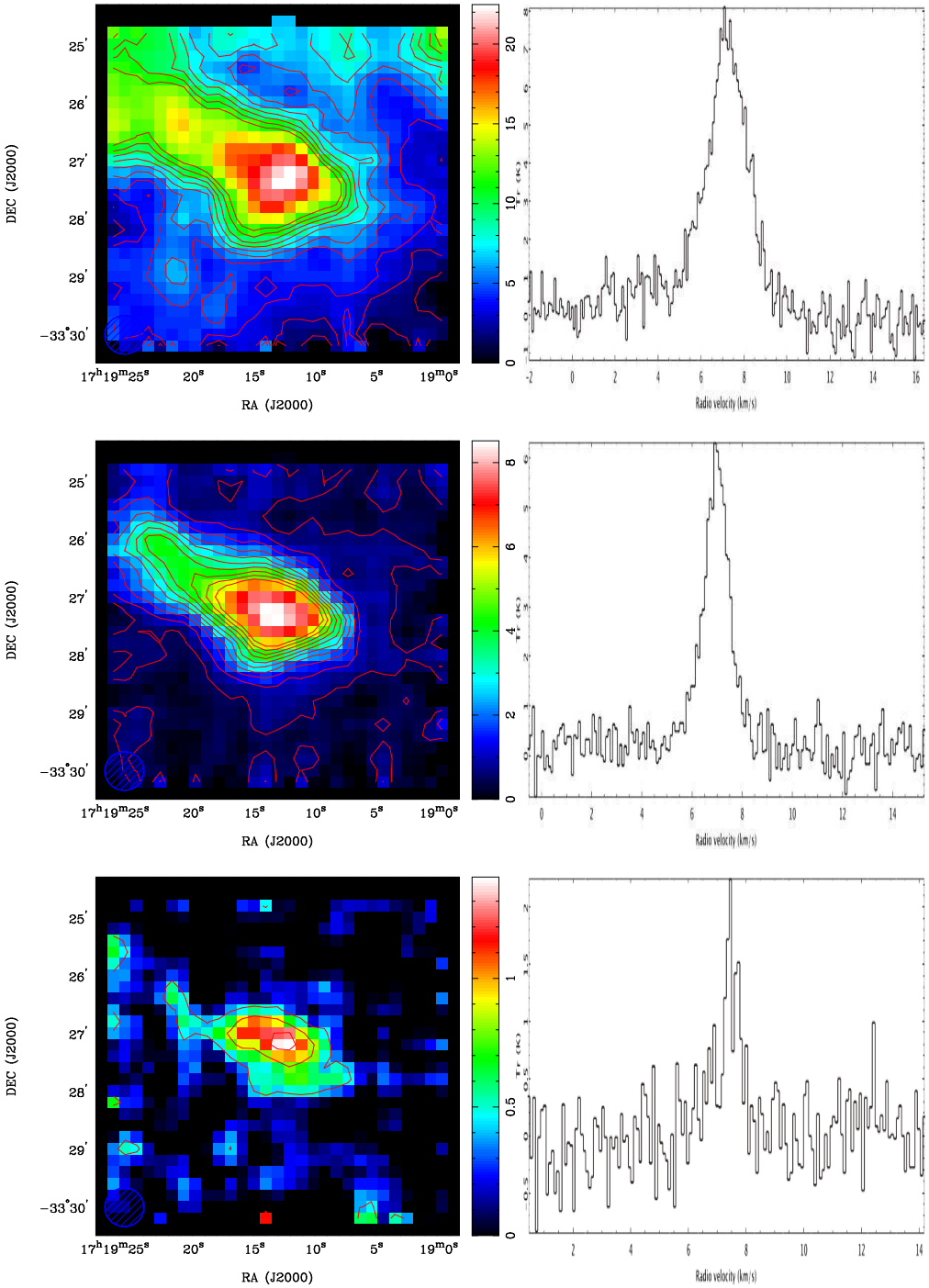

Figure 3.42: Integrated intensity plots for BHR159 in each of the observed CO isotopologues. The ^{12}CO map is shown in the top left image. The top right image is the line profile of the core. This image was used to determine over which velocities the integrated intensity plot was produced. The line profile shows a peak from 4 - 10km/s and so this is the velocity range used to compute the integrated intensity plots for each of the 3 isotopologues. The ^{13}CO integrated intensity map and line profile is shown in the middle left and right images respectively. The C^{18}O integrated intensity plot and line profile is shown in the lower left and right images.

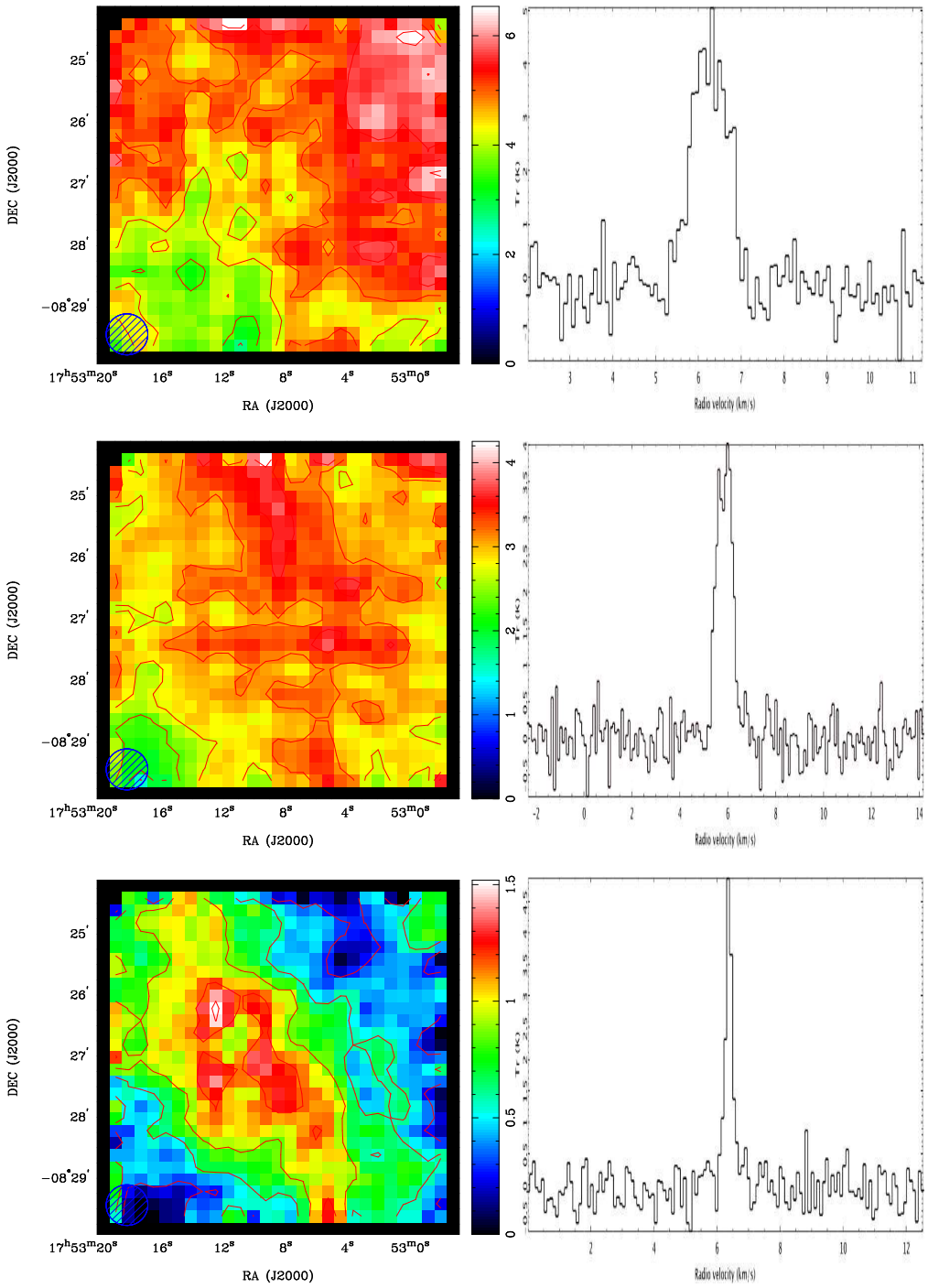

Figure 3.43: Integrated intensity plots for CB101 in each of the observed CO isotopologues. The ^{12}CO map is shown in the top left image. The top right image is the line profile of the core. This image was used to determine over which velocities the integrated intensity plot was produced. The line profile shows a peak from 5 - 8km/s and so this is the velocity range used to compute the integrated intensity plots for each of the 3 isotopologues. The ^{13}CO integrated intensity map and line profile is shown in the middle left and right images respectively. The C^{18}O integrated intensity plot and line profile is shown in the lower left and right images.

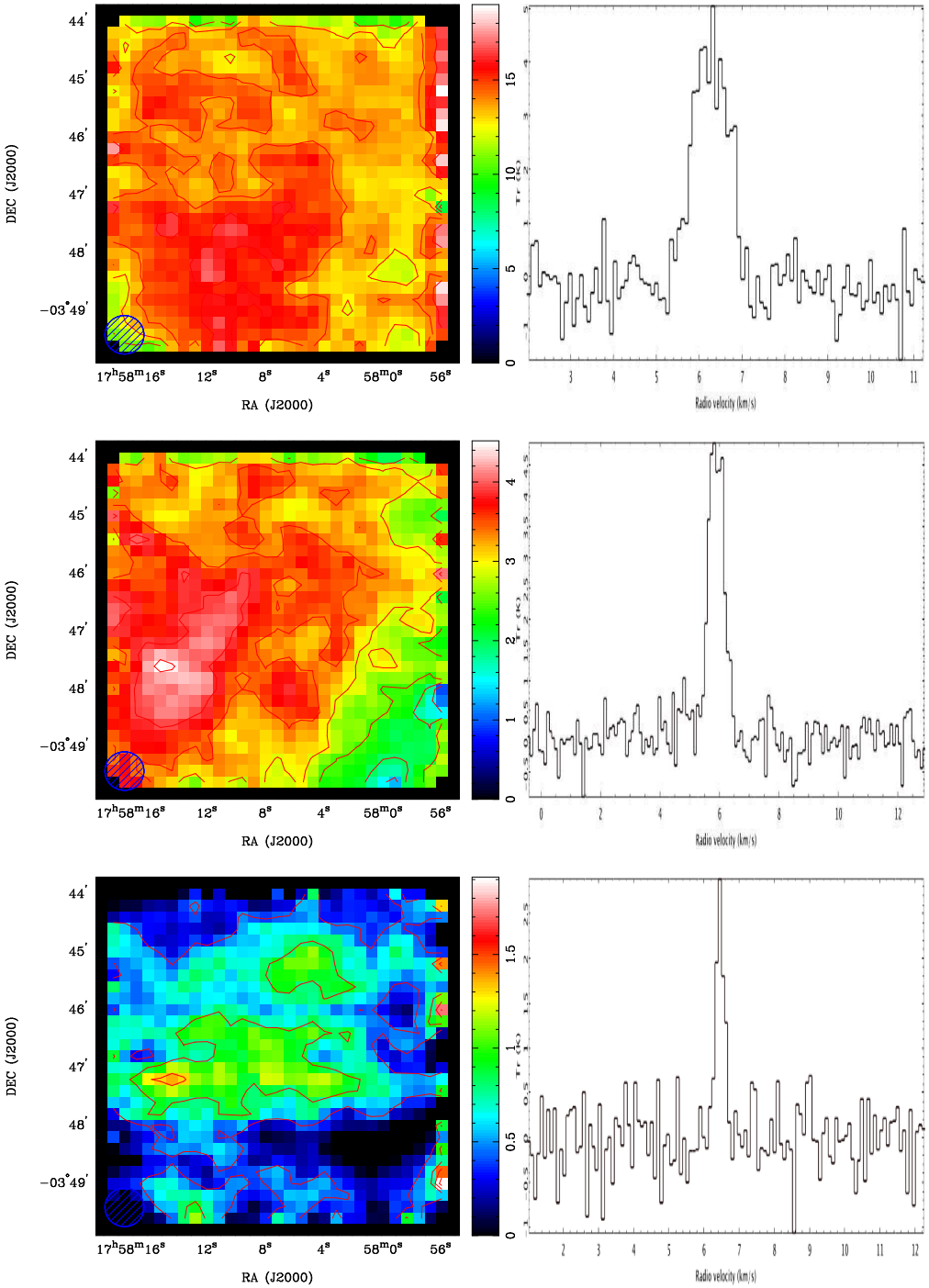

Figure 3.44: Integrated intensity plots for CB105 in each of the observed CO isotopologues. The ^{12}CO map is shown in the top left image. The top right image is the line profile of the core. This image was used to determine over which velocities the integrated intensity plot was produced. The line profile shows a peak from 5 - 8km/s and so this is the velocity range used to compute the integrated intensity plots for each of the 3 isotopologues. The ^{13}CO integrated intensity map and line profile is shown in the middle left and right images respectively. The C^{18}O integrated intensity plot and line profile is shown in the lower left and right images.

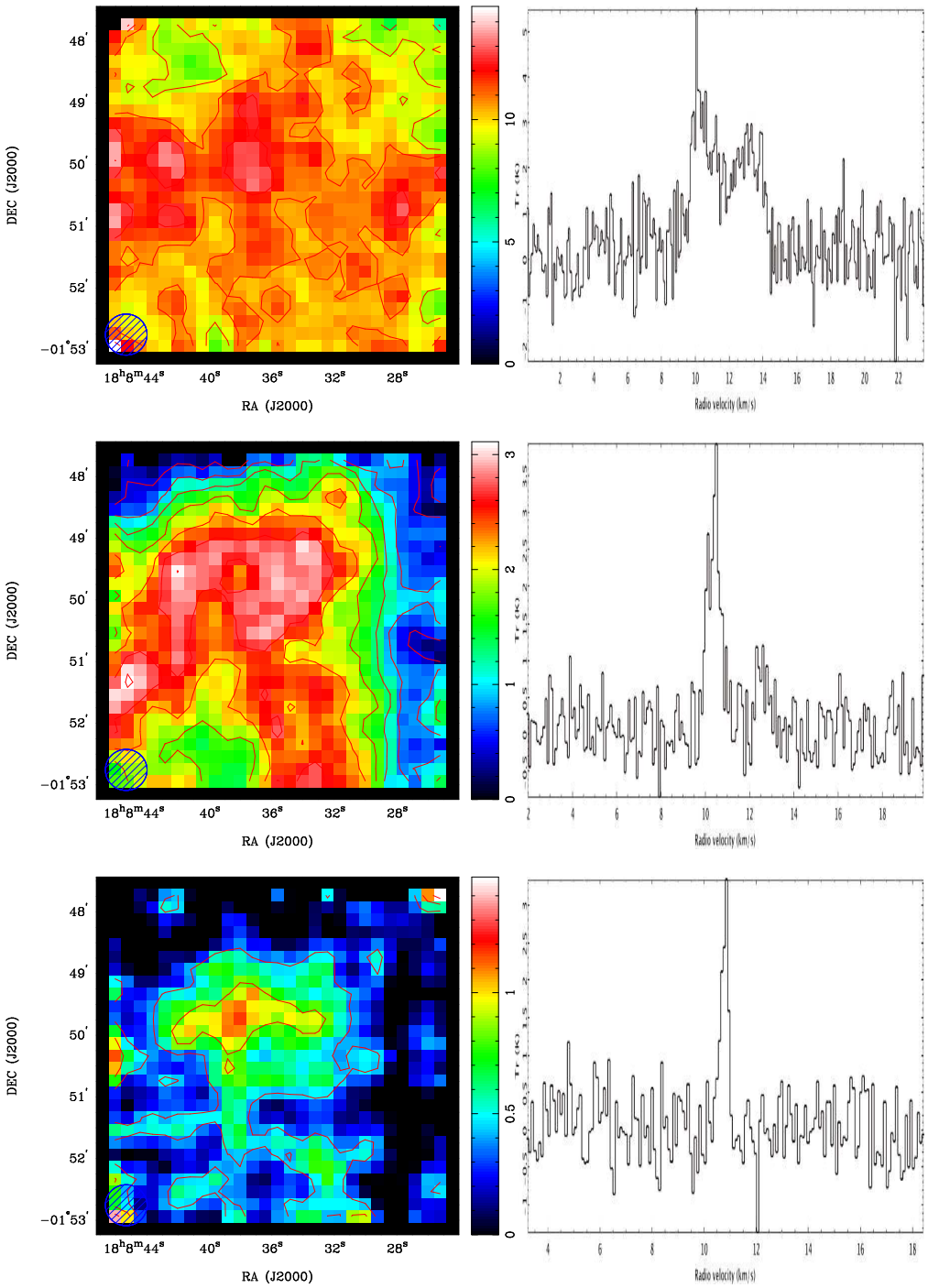

Figure 3.45: Integrated intensity plots for CB112 in each of the observed CO isotopologues. The ^{12}CO map is shown in the top left image. The top right image is the line profile of the core. This image was used to determine over which velocities the integrated intensity plot was produced. The line profile shows a peak from 8 - 14km/s and so this is the velocity range used to compute the integrated intensity plots for each of the 3 isotopologues. The ^{13}CO integrated intensity map and line profile is shown in the middle left and right images respectively. The C^{18}O integrated intensity plot and line profile is shown in the lower left and right images.

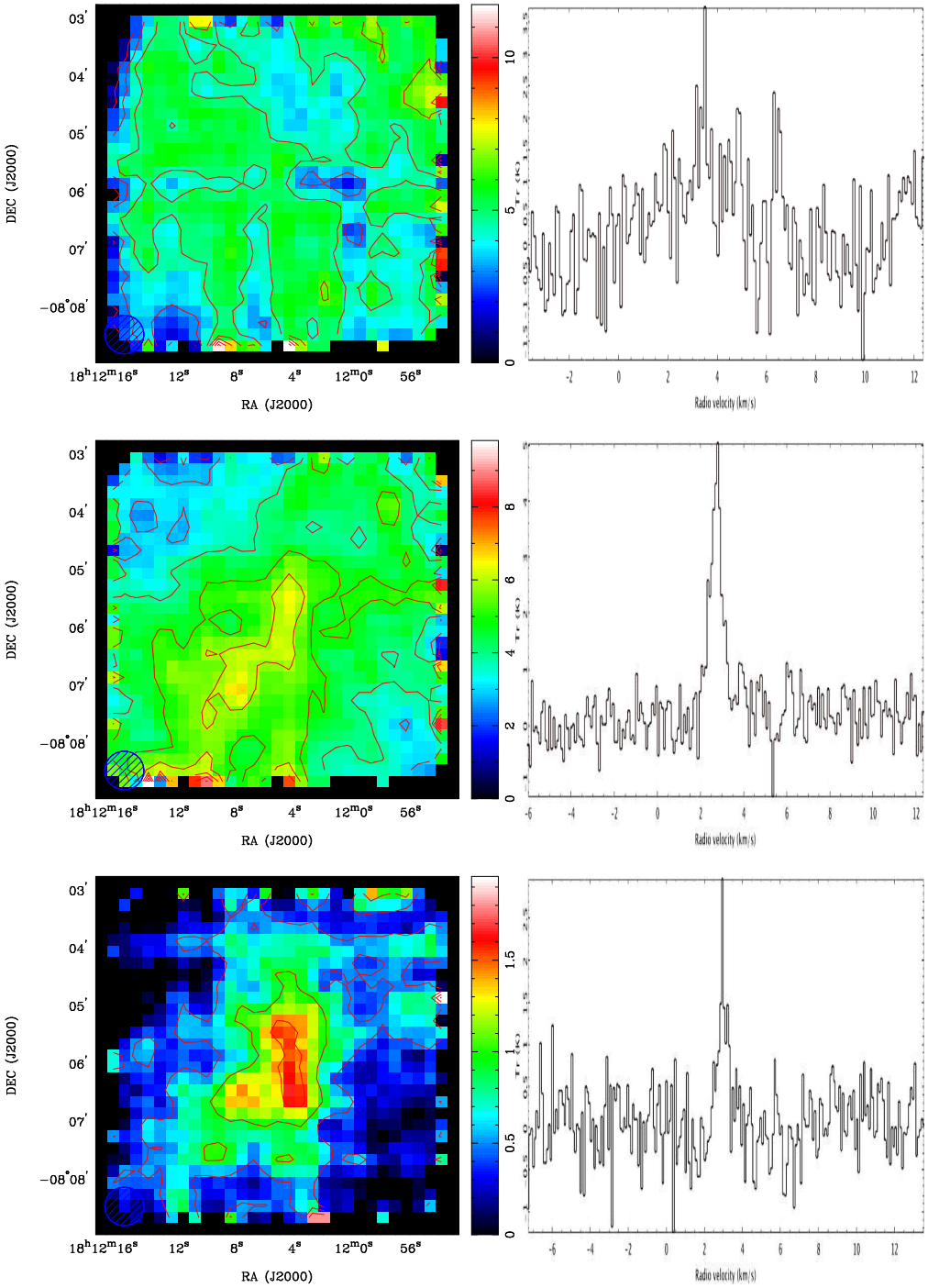

Figure 3.46: Integrated intensity plots for L422 in each of the observed CO isotopologues. The ^{12}CO map is shown in the top left image. The top right image is the line profile of the core. This image was used to determine over which velocities the integrated intensity plot was produced. The line profile shows a peak from 2 - 6km/s and so this is the velocity range used to compute the integrated intensity plots for each of the 3 isotopologues. The ^{13}CO integrated intensity map and line profile is shown in the middle left and right images respectively. The C^{18}O integrated intensity plot and line profile is shown in the lower left and right images.

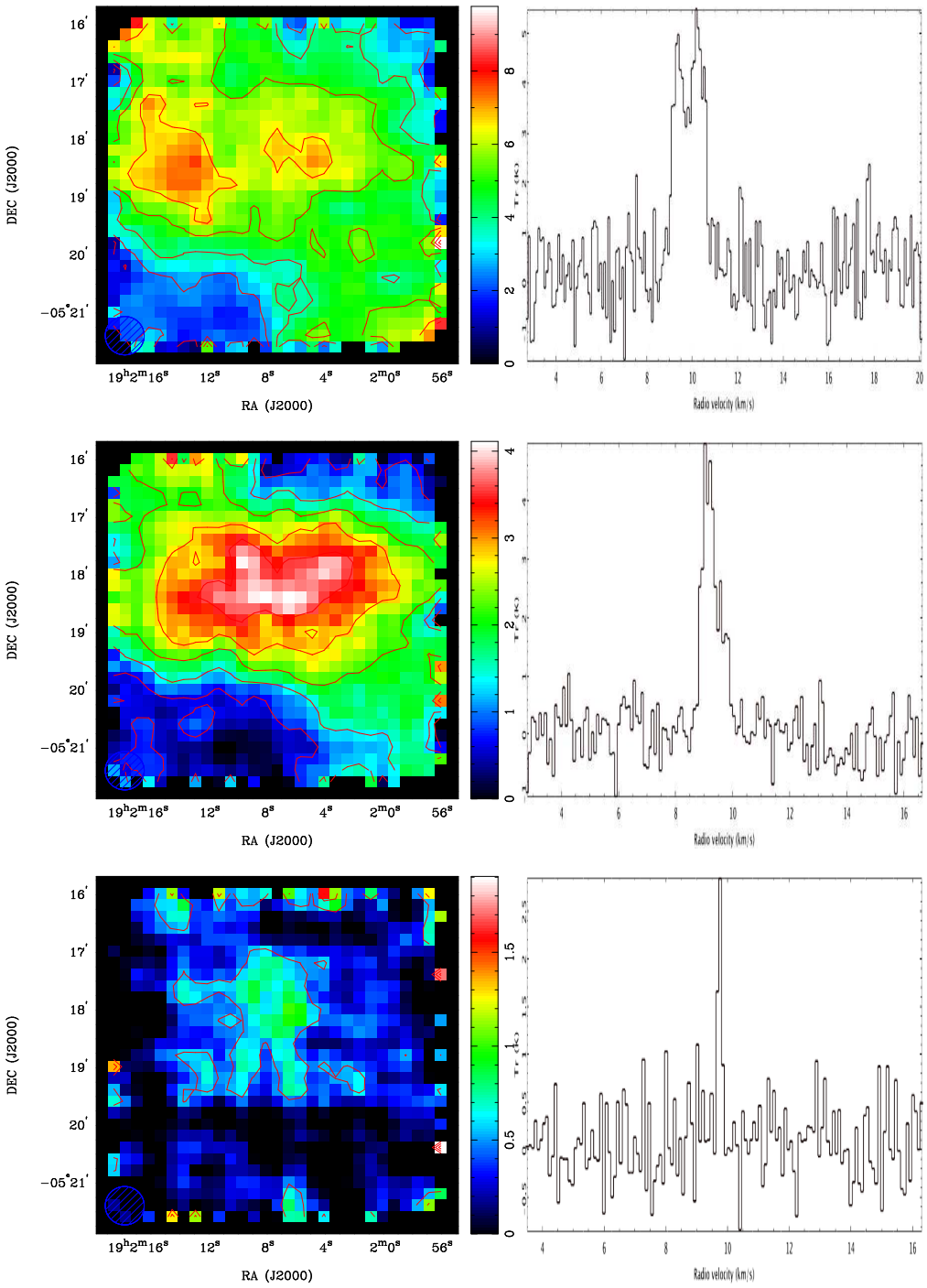

Figure 3.47: Integrated intensity plots for CB175 in each of the observed CO isotopologues. The ^{12}CO map is shown in the top left image. The top right image is the line profile of the core. This image was used to determine over which velocities the integrated intensity plot was produced. The line profile shows a peak from 5 - 11km/s and so this is the velocity range used to compute the integrated intensity plots for each of the 3 isotopologues. The ^{13}CO integrated intensity map and line profile is shown in the middle left and right images respectively. The C^{18}O integrated intensity plot and line profile is shown in the lower left and right images.

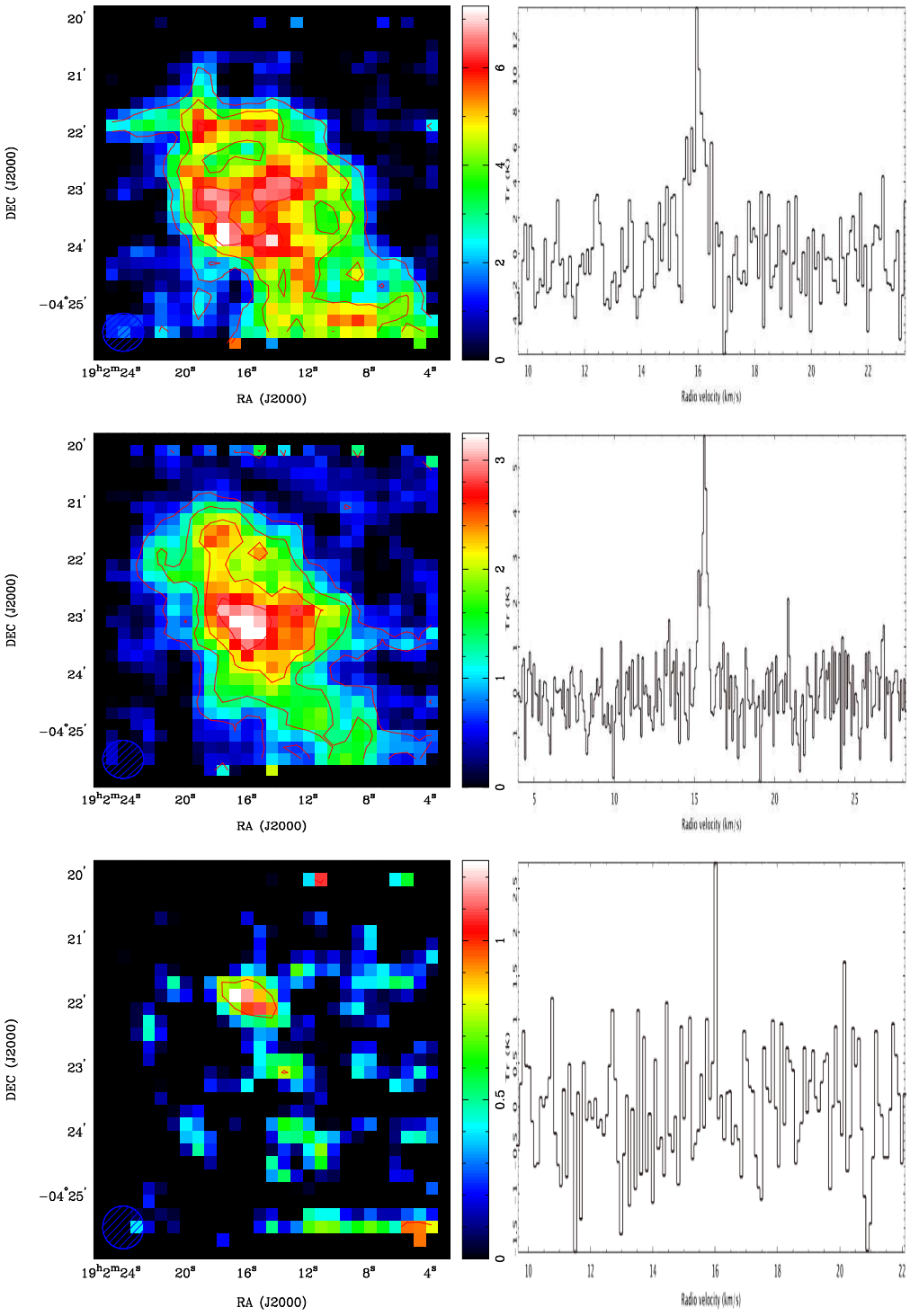

Figure 3.48: Integrated intensity plots for CB176 in each of the observed CO isotopologues. The ^{12}CO map is shown in the top left image. The top right image is the line profile of the core. This image was used to determine over which velocities the integrated intensity plot was produced. The line profile shows a peak from 15 - 17km/s and so this is the velocity range used to compute the integrated intensity plots for each of the 3 isotopologues. The ^{13}CO integrated intensity map and line profile is shown in the middle left and right images respectively. The C^{18}O integrated intensity plot and line profile is shown in the lower left and right images.

Observed Transition	Central Frequency	η_c
	GHz	
^{12}CO (J=1→0)	115.271	0.55
^{13}CO (J=1→0)	110.201	0.56
C^{18}CO (J=1→0)	109.782	0.57

Table 3.2: Central frequencies (Lovas, 1992) and beam efficiencies (Ladd et al. 2005) for each of the observed CO isotopologue transitions.

Table 3.3 records the ^{12}CO observed properties. The columns show: (1) The core name, taken from the BHR(1995)or CB(1988) catalogue; (2) the Local Standard of Rest (LSR) velocity. The error in this value is the average variation in the velocity in the 8 pixels surrounding the peak; (3) The peak line profile is fitted with a Gaussian, and the Full Width Half Maximum (FWHM) of this fit is recorded as the linewidth. The reported error is the error measured from the FWHM of the Gaussian fit; (4) the measured peak antenna temperature (T_a); (5) is the calculated peak brightness temperature (T_b). The reported errors are the rms noise in line free channels; (6) The peak integrated intensity value if the map. The error is calculated by summing the error in temperature across the specified velocity range; (7) and (8) The angular extent of the cloud. These quantities are measured by drawing a contour around the 3σ level of emission and approximating the shape with an ellipse. θ_{maj} is the semi major axis, and θ_{min} is the semi-minor axis. The estimated uncertainty on these two values is $\pm$6 arcsec for each core, the angular size of half a pixel, which is the estimated accuracy to which the ellipse can be measured.

Core	V_{LSR}	FWHM	T_A	T_b	$\int T_b dV$	θ_{maj}	θ_{min}
	kms^{-1}	kms^{-1}	K	K	$Kkms^{-1}$	arcsec	arcsec
CB29	+10.77±0.03	1.57±0.03	6.60±0.18	12.00±0.32	17.39±0.51	137	119
BHR17	+2.91±0.01	1.20±0.05	6.30±0.39	11.45±0.70	14.15±0.38	179	123
BHR31	+2.33±0.01	0.70±0.02	6.70±0.25	12.18±0.44	12.92±0.35	183	130
BHR42	+5.63±0.01	1.41±0.04	5.90±0.35	10.73±0.63	20.67±0.52	152	116
BHR34	+4.29±0.05	1.14±0.02	5.71±0.28	10.38±0.51	14.27±0.32	157	98
BHR41	+4.47±0.01	1.29±0.04	5.14±0.32	9.35±0.59	16.10±0.43	153	145
BHR40	+5.39±0.01	1.38±0.04	5.80±0.36	10.55±0.66	13.36±0.39	149	107
BHR38	+5.60±0.01	1.36±0.04	5.41±0.31	9.84±0.56	19.38±0.63	182	87
BHR39	+5.45±0.03	1.39±0.04	6.46±0.32	11.75±0.59	17.84±0.57	160	72
BHR56	+1.67±0.01	0.75±0.03	5.00±0.21	9.09±0.38	7.17±0.28	184	156
BHR48	−5.92±0.01	3.10±0.22	3.14±0.27	5.71±0.49	16.56±0.47	142	105
BHR49	−5.54±0.01	3.09±0.35	3.00±0.34	5.45±0.62	11.35±0.63	160	125
BHR50	−6.32±0.02	0.89±0.14	2.54±0.30	4.62±0.55	7.27±0.60	143	88
DC2983-131a	+3.54±0.01	1.37±0.06	3.41±0.29	6.20±0.53	10.23±0.41	185	91
DC2983-131b	+3.48±0.01	1.75±0.12	2.38±0.42	4.33±0.77	3.45±0.30	191	123

Core	V_{LSR}	FWHM	T_A	T_b	$\int T_b dV$	θ_{maj}	θ_{min}
	kms^{-1}	kms^{-1}	K	K	$Kkms^{-1}$	arcsec	arcsec
BHR68	−8.05±0.02	4.01±0.10	3.00±0.21	5.45±0.39	17.72±0.50	181	156
BHR74	−6.32±0.07	0.50±0.02	5.10±0.24	9.27±0.43	5.98±0.25	141	107
BHR73	−17.47±0.02	1.31±0.04	3.30±0.21	6.00±0.38	9.34±0.28	155	107
BHR76	−5.76±0.01	0.62±0.03	5.51±0.30	10.02±0.54	8.25±0.29	172	153
DC3023-177	+0.94±0.01	1.82±0.13	4.80±0.50	8.73±0.91	16.92±0.74	140	116
BHR79	+4.48±0.01	1.76±0.14	5.50±0.52	10.00±0.94	9.24±0.59	165	102
BHR80	+3.56±0.02	0.48±0.02	5.00±0.29	9.09±0.52	4.42±0.27	198	84
BHR81	−5.58±0.01	0.97±0.09	6.30±0.74	11.45±1.35	15.39±0.92	170	83
DC3162+51	−4.06±0.01	1.06±0.05	6.10±0.35	11.09±0.64	9.24±0.58	190	152
BHR95	−8.44±0.02	1.42±0.09	3.20±0.26	5.82±0.48	16.91±0.74	168	98
BHR99	−0.05±0.01	1.06±0.05	5.60±0.42	10.18±0.76	9.91±0.47	107	79
BHR100	−1.15±0.01	1.27±0.05	5.90±0.34	10.73±0.62	12.43±0.59	133	78
BHR97	+0.01±0.01	0.92±0.03	6.70±0.46	12.18±0.84	19.33± 0.72	205	114
BHR119	+3.71±0.01	0.87±0.04	7.90±0.38	14.36±0.69	13.65±0.43	215	127
BHR159	+7.31±0.03	2.44±0.06	4.40±0.26	8.00±0.48	22.47±0.59	150	80

Core	V_{LSR}	FWHM	T_A	T_b	$\int T_b dV$	θ_{maj}	θ_{min}
	kms^{-1}	kms^{-1}	K	K	$Kkms^{-1}$	arcsec	arcsec
CB101	+6.31±0.01	1.07±0.06	3.00±0.26	5.45±0.48	6.54±0.35	165	92
CB105	+6.47±0.03	2.35±0.12	5.30±0.48	9.64±0.88	18.99±0.78	162	95
CB112	+10.75±0.02	3.75±0.33	3.70±0.43	6.73±0.79	14.63±0.76	176	121
L422	+3.07±0.01	3.89±0.44	2.40±0.39	4.36±0.71	11.74±0.78	191	132
CB175	+9.43±0.02	1.24±0.09	3.40±0.36	6.18±0.65	9.77±0.65	188	114
CB176	+15.98±0.03	0.68±0.07	5.10±1.14	9.27±2.07	7.27±0.99	187	99

Table 3.3: ^{12}CO observed properties. The columns show: (1) The core name, taken from BHR(1995) or CB(1988) catalogue; (2) the observed LSR Velocity; (3) the measured line width of the line profile at the peak of emission; (4) observed antenna temperature; (5) calculated brightness temperature; (6) the peak integrated intensity value of the ^{12}CO emission; (7)&(8) semi-major and minor axes of the core when the shape is approximated to an ellipse.

The ^{13}CO results are shown in Table 3.4. The columns show:(1) The core name, taken from the BHR(1995) or CB(1988) catalogue; (2) The linewidth i.e. the FWHM of a Gaussian fit to the observed peak line profile. The reported error is the error on the measured FWHM of the Gaussian fit; (3) The observed antenna temperature (T_A); (4) The peak brightness temperature T_b of the source, calculated by dividing the observed peak antenna temperature by the beam efficiency at the frequency of the ^{13}CO J=1→0 transition as quoted in Table 3.2; (5) the peak integrated intensity value of the ^{13}CO emission. The error is calculated by summing the error in temperature across the specified velocity range; (6) & (7) the semi-major and minor extent of the core when the 3σ contour is approximated as an ellipse.

The C^{18}O results are shown in Table 3.5. The columns show:(1) The core name from BHR(1995) and CB(1988); (2) The linewidth i.e. the FWHM of a Gaussian fit to the observed peak line profile; (3) The observed antenna temperature (T_A); (4) The peak brightness temperature T_b of the source, calculated by dividing the observed peak antenna temperature by the beam efficiency at the frequency of the C^{18}O J=1→0 transition as quoted in Table 3.2; (5) The peak integrated intensity of the C^{18}O emission; (6) & (7) the semi-major and minor extent of the cloud when the 3σ contour is approximated as an ellipse.

It is clear from all integrated intensity maps that the different isotopologues trace different density material. The core size as judged by the ^{12}CO emission is seen to be much larger than the size of the core measured in ^{13}CO, which in turn is larger than the C^{18}O core. This suggests that the ^{12}CO emission is tracing the outer envelope of the core, where the density is relatively low and the optical depth

Core	FWHM	T_A	T_b	$\int T_b dV$	θ_{maj}	θ_{min}
	kms^{-1}	K	K	$Kkms^{-1}$	arcsec	arcsec
CB29	1.25±0.01	3.64±0.10	6.50±0.18	8.09±0.16	120	90
BHR17	0.70±0.02	3.79±0.11	6.77±0.20	5.55±0.17	168	47
BHR31	0.52±0.01	4.20±0.13	7.50±0.23	4.59±0.17	127	84
BHR42	0.92±0.02	3.39±0.15	6.05±0.26	6.20±0.18	133	55
BHR34	0.68±0.02	3.88±0.11	6.93±0.20	6.48±0.19	124	88
BHR41	0.86±0.03	3.90±0.17	6.96±0.31	6.32±0.26	127	97
BHR40	0.91±0.04	2.97±0.12	5.30±0.22	5.27±0.17	86	61
BHR38	0.80±0.03	3.40±0.20	6.07±0.35	5.31±0.23	151	68
BHR39	1.23±0.06	3.40±0.18	6.07±0.32	4.70±0.31	134	33
BHR56	0.55±0.02	3.46±0.12	6.18±0.22	3.82±0.24	108	99
BHR48	0.60±0.05	1.56±0.16	2.79±0.29	5.66±0.14	109	95
BHR49	0.61±0.07	1.55±0.24	2.77±0.42	4.07±0.32	118	29
BHR50	0.56±0.04	1.67±0.17	2.98±0.31	2.25±0.16	152	129
DC2983-131a	0.81±0.03	2.90±0.13	5.18±0.23	4.36±0.17	119	63
DC2983-131b	0.75±0.03	1.80±0.16	3.21±0.28	4.06±0.20	175	114
BHR68	1.62±0.04	2.30±0.13	4.11±0.24	6.47±0.18	174	125
BHR74	0.55±0.02	3.36±0.18	6.00±0.32	3.70±0.18	98	50
BHR73	0.86±0.03	2.40±0.13	4.29±0.24	4.47±0.15	145	35
BHR76	0.51±0.02	3.80±0.21	6.79±0.38	4.06±0.16	149	89
DC3023-177	0.79±0.06	3.70±0.31	6.61±0.55	8.16±0.42	145	85
BHR79	0.53±0.05	3.40±0.27	6.07±0.49	5.35±0.40	154	56
BHR80	0.44±0.02	3.90±0.20	6.96±0.36	3.37±0.18	124	54
BHR81	0.62±0.04	4.10±0.36	7.32±0.64	9.40±0.52	137	106
DC3162+51	0.63±0.02	4.80±0.22	8.57±0.40	6.76±0.29	140	78
BHR95	0.85±0.04	2.00±0.18	3.57±0.33	4.07±0.18	164	83
BHR99	0.83±0.03	3.52 ±0.66	6.28±0.37	5.25±0.21	85	52
BHR100	0.98±0.03	3.37±0.66	6.01±0.37	5.86±0.36	59	45
BHR97	1.34±0.04	3.24±0.25	5.78±0.44	8.12±0.44	134	49
BHR119	0.72±0.02	4.7±0.22	8.39±0.40	6.55±0.21	192	88
BHR159	1.28±0.04	3.50±0.19	6.25±0.34	8.52±0.27	146	85
CB101	0.75±0.04	2.10±0.17	3.75±0.30	4.25±0.19	167	75
CB105	0.62±0.04	3.10±0.22	5.54±0.35	4.52±0.24	168	77
CB112	0.67±0.04	2.30±0.22	4.11±0.40	3.11±0.22	136	98
L422	1.04±0.06	2.40±0.24	4.29±0.42	9.82±0.49	191	83
CB175	0.71±0.05	2.50±0.24	4.46±0.43	4.11±0.35	138	81
CB176	0.52±0.06	2.40±0.38	4.29±0.68	3.25±0.34	121	55

Table 3.4: ^{13}CO observed core properties. The columns show: (1) The core name, taken from BHR(1995) or CB(1988); (2) the observed linewidth of the line profile at the peak of the emission; (3) the observed antenna temperature; (4) the measured peak brightness temperature; (5) peak integrated intensity of the ^{13}CO emission; (6) & (7) semi-major and semi-minor core axis.

Core	FWHM	T_A	T_b	$\int T_b dV$	θ_{maj}	θ_{min}
		K	K	Kkms^{-1}	arcsec	arcsec
CB29	0.68±0.05	1.20±0.10	2.11±0.18	1.18±0.14	119	87
BHR17	0.52±0.02	0.80±0.12	1.40±0.21	0.81±0.12	129	75
BHR31	0.32±0.04	1.30±0.13	2.28±0.24	0.84±0.13	54	42
BHR42	0.90±0.19	0.74±0.14	1.30±0.25	0.60 ±0.13	119	71
BHR34	0.63±0.04	1.10±0.11	1.93±0.19	1.22±0.16	116	89
BHR41	0.51±0.06	1.30±0.16	2.28±0.28	1.17±0.15	116	63
BHR40	0.71±0.11	0.66±0.14	1.16±0.24	0.62±0.17	80	46
BHR38	0.41±0.09	0.78±0.19	1.37±0.34	0.81±0.18	50	31
BHR39	0.69±0.08	0.70±0.19	1.23±0.34	0.60±0.17	61	11
BHR56	0.24±0.02	2.00±0.13	3.51±0.22	1.04±0.17	76	60
BHR48	0.23±0.03	0.65±0.11	1.14±0.20	0.38±0.09	38	22
BHR49	0.35±0.03	0.94±0.15	1.65±0.27	0.67±0.26	94	55
BHR50	0.50±0.16	0.78±0.13	1.37±0.24	0.62±0.16	118	63
DC2983-131a	0.51±0.04	1.34±0.15	2.35±0.27	1.37±0.21	89	43
DC2983-131b	0.30±0.02	1.60±0.16	2.81±0.28	1.37±0.15	149	54
BHR68	1.11±0.10	0.80±0.13	1.40±0.22	1.33±0.18	131	98
BHR74	0.32±0.05	1.25±0.17	2.19±0.30	0.80±0.14	96	56
BHR73	0.87±0.07	0.74±0.12	1.30±0.21	0.92±0.13	69	53
BHR76	0.25±0.02	2.20±0.18	3.86±0.32	1.12±0.15	92	44
DC3023-177	0.49±0.12	1.40±0.30	2.46±0.53	1.12±0.28	46	24
BHR79	0.13±0.06	0.70±0.21	1.23±0.37	1.10±0.31	79	34
BHR80	0.18±0.02	1.60±0.18	2.81±0.33	0.55±0.17	75	48
BHR81	0.25±0.04	1.56±0.23	2.74±0.41	0.94±0.29	97	52
DC3162+51	0.32±0.02	2.40±0.21	4.21±0.37	1.62±0.22	121	98
BHR95	0.60±0.05	1.00±0.16	1.75±0.28	0.90±0.17	144	48
BHR99	0.37±0.22	1.22±0.23	2.14±0.40	0.88±0.15	74	44
BHR100	0.51±0.10	1.03±0.22	1.81±0.38	1.10 ±0.20	46	38
BHR97	0.71±0.10	0.80±0.15	1.40±0.27	1.21±0.19	79	35
BHR119	0.16±0.08	0.97±0.20	1.70±0.35	0.80±0.17	140	59
BHR159	0.83±0.11	1.20±0.17	2.11±0.30	1.39±0.20	51	24
CB101	0.26±0.02	2.00±0.16	3.51±0.28	1.52±0.15	162	64.8
CB105	0.34±0.04	1.80±0.19	3.16±0.34	1.36±0.21	131	54
CB112	0.21±0.04	1.80±0.20	3.16±0.36	1.16±0.21	89	57
L422	0.45±0.05	1.40±0.23	2.46±0.41	1.66±0.24	98	40
CB175	0.31±0.08	1.5±0.22	2.63±0.40	1.01±0.31	84	34
CB176	0.33±0.10	1.50±0.28	2.63±0.49	1.25±0.20	37	20

Table 3.5: $C^{18}O$ observed properties. The columns show: (1) the core name from BHR(1995) or CB(1988); (2) linewidth of the line profile of the peak emission; (3) observed antenna temperature; (4) measured brightness temperature; (5) peak integrated intensity value of the emission; (6)&(7) the semi-major and minor axis of the cloud.

is high. The ^{13}CO emission traces denser material of the core inner envelope. In this region, the emission is expected to be optically thin, and the observed core size is smaller than that seen in the ^{12}CO line. The smallest core size is seen in the C^{18}O emission. C^{18}O traces the inner, densest part of the core, and may be the region where stars are forming.

3.5 SIMBA data

Only a small sub-sample of cores were observed and found to be above the detection limit of SIMBA. The 13 cores in the sample that were detected are presented below. As above, the maps are presented on an inverted grey scale to clearly show the full range of the emission. The cores observed at 1.2mm therefore appear as the darkest regions on the maps. The scale bar to the right of each map shows the range of the emission. The units of the scale bar are MJy/Sr, which can be converted to mJy/beam by using the equation

$$\left(\frac{I_V}{Jy/Sr}\right) = 3.754479\times10^{10}\times\left(\frac{HPBW_{maj}}{arcsec}\right)^{-1}\times\left(\frac{HPBW_{min}}{arcsec}\right)^{-1}\times\left(\frac{S}{Jy/beam}\right) \tag{3.5}$$

The noise in each map was estimated by measuring the standard deviation of the background emission in off-source regions of the map. The results are shown in columns (2) and (3) of Table 3.6, in units of mJy/beam and MJy/Sr respectively. The peak 1.2mm emission for each core was measured by identifying the brightest pixel in the map and recording its value in columns (4)&(5) of Table 3.6 in units of mJy/beam and MJy/Sr. Also recorded in column (6) of Table 3.6 is the total flux density of the core, measured in Jy. This value is calculated by summing the emission enclosed by a contour tracing the 3σ rms noise level. This value is the

signal from the source, measured in mJy/beam. The average background count per pixel is removed from every pixel in the signal to produce a background subtracted source count. To convert this to Jy, a correction for the beam size needs to be applied.

Inspection of the data shows that the 1.2mm emission traces roughly the same region of the core as the $C^{18}O$ emission as shown in the integrated intensity maps presented in the section above. This indicates that both tracers are observing approximately equal regions of gas and dust, and this must be the densest inner region of the core.

3.6 Summary

In this chapter, I have presented the data collected by the instruments described in Chapter 2. I showed optical images of each of the cores from the Digitized Sky Survey (DSS). I have also described the process taken to compute extinction maps from 2MASS H and K colour excesses of field stars.

Also shown in this chapter are integrated intensity maps and peak line profiles of all of the cores as seen in 3 isotopologues of CO. The core size is seen to decrease as the density of the tracer increases, so that the ^{12}CO core is larger than the ^{13}CO core, which in turn is larger than the $C^{18}O$ core. From the integrated intensity maps, the Antenna temperature, peak integrated intensity and the semi-major and semi-minor axis of the cores is recorded. The peak line profiles are used to find the FWHM line width and the velocity range over which the integrated intensity plots are computed.

The final dataset shown in this chapter is the sub-sample of cores which were observed with the SIMBA bolometer array. The 1.2mm emission is seen to trace

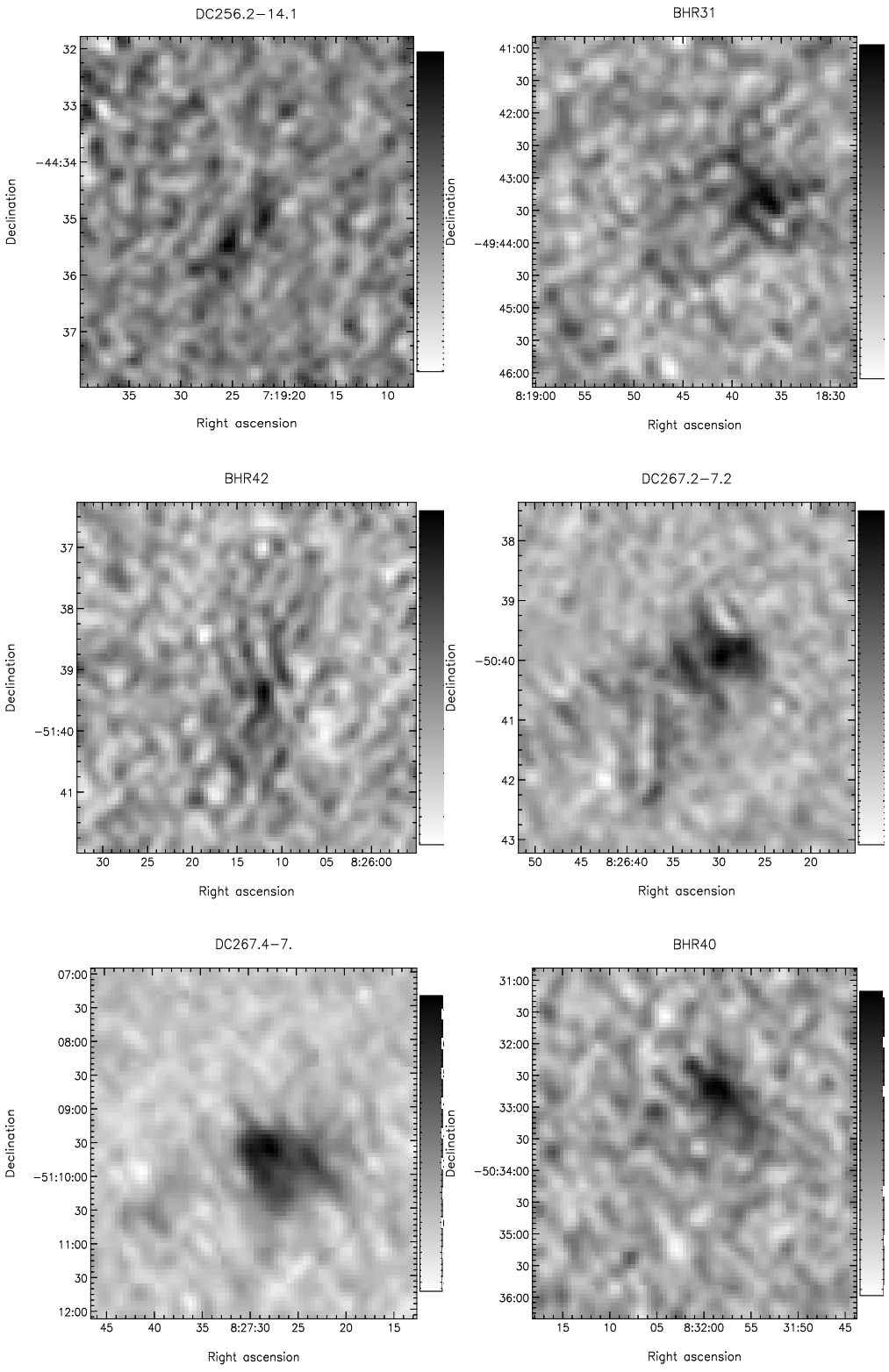

Figure 3.49: SIMBA data of cores (a)BHR17, (b)BHR31, (c)BHR42, (d)BHR34, (e)BHR41, (f)BHR40

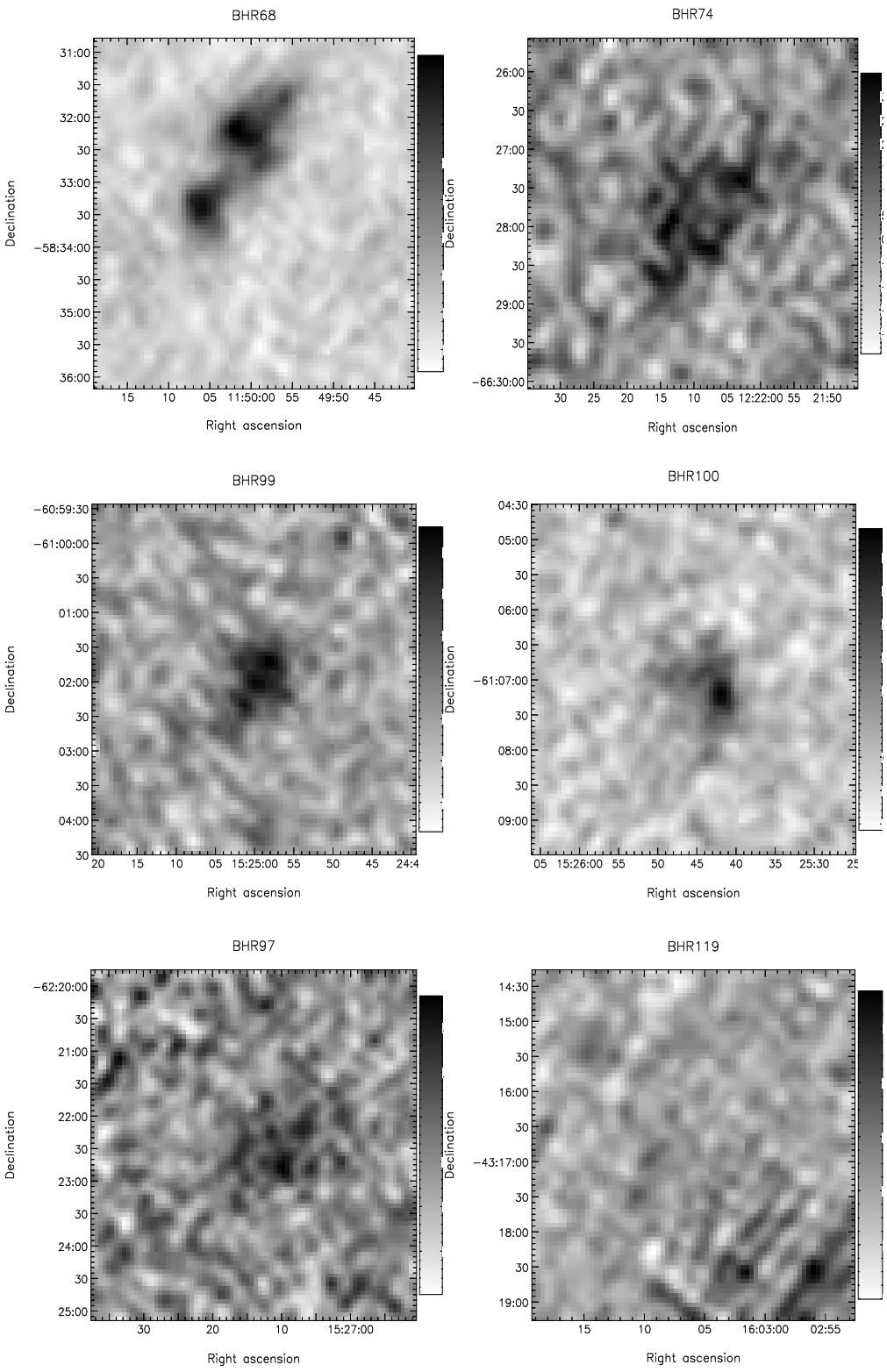

Figure 3.50: SIMBA data of cores (a)BHR68, (b)BHR74, (c)BHR99, (d)BHR100, (e)BHR97, (f)BHR119

Core	RMS noise		Peak Intensity		Signal	Flux Density
	mJy/beam	MJy/Sr	mJy/beam	MJy/Sr	mJy/beam	Jy
BHR17	10.25	0.67	58.96	3.84	1500	0.04
BHR31	23.19	0.50	48.53	3.16	3100	0.08
BHR42	5.69	0.37	49.92	3.25	3100	0.08
BHR34	7.30	0.48	78.38	5.10	13100	0.32
BHR41	5.58	0.36	75.78	4.94	14700	0.36
BHR40	5.69	0.37	40.05	2.61	4800	0.12
BHR68	9.34	0.61	136.90	8.90	37300	0.91
BHR74	6.90	0.45	34.89	2.30	1900	0.05
BHR99	7.22	0.47	45.81	3.00	5200	0.13
BHR100	6.28	0.41	68.42	4.50	7800	0.19
BHR97	9.03	0.59	37.11	2.40	1000	0.02
BHR119	11.39	0.50	120.71	4.81	4200	0.1
L422	7.65	0.74	73.86	7.87	35100	0.86

Table 3.6: Observed core parameters from SIMBA observations. The columns show: (1) the core name from BHR(1995); (2)&(3) the observed noise σ in the maps in mJy/beam and MJy/Sr; (4) & (5) the peak 1.2mm intensity in mJy/beam and MJy/Sr;(6) the background subtracted signal from the source; (7) the total flux density from the source.

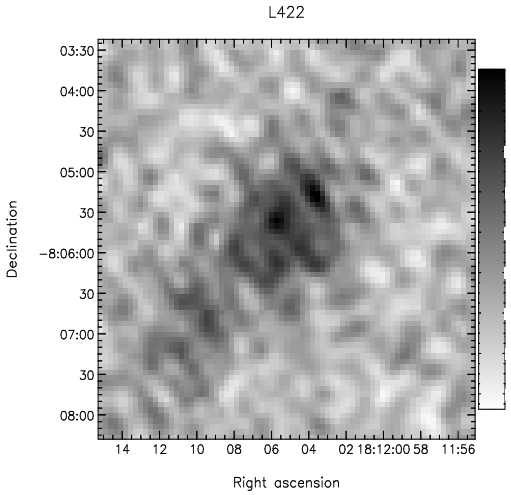

Figure 3.51: SIMBA data of cores (a)L422. The image is presented on an inverted grey-scale.

a similar area to the $C^{18}O$ emission.

Chapter 4

Data Analysis

4.1 Introduction

In this Chapter, the CO and SIMBA observed core parameters, presented in the previous chapter, are used to calculate the main physical parameters of the cores. The gravitational stability of the cores is assessed to determine their star formation potential. Existing young stellar objects in or near the cores are identified using Spitzer data.

I begin by considering the CO isotopologue data. Secondly, I perform the same analysis on the cores detected at 1.2mm by SIMBA. I end the chapter by investigating the star formation history of the cores by performing a multi-wavelength colour-excess examination of the cores, using Spitzer data. The interpretation of this analysis appears in Chapter 5.

4.2 CO Data

In this section, I make use of the observed parameters derived in Tables 3.3, 3.4 & 3.5 from the previous chapter, to derive physical parameters for the cores. I begin by assessing the excitation temperature of the cores, using the observed ^{12}CO peak brightness temperature of each core.

4.2.1 Excitation Temperature

To undertake the assessment of the column density and mass of the cores, it is necessary to first calculate their excitation temperature, using the following equation (e.g. Rohlfs & Wilson, 2004).

$$T_R = T_0 \left(\frac{1}{e^{T_0/T_{ex}} - 1} - \frac{1}{e^{T_0/T_{bg}} - 1} \right) (1 - e^{-\tau_\nu}) \tag{4.1}$$

where T_R is the peak brightness temperature of the source, T_0 is the transition temperature, T_{ex} is the excitation temperature, T_{bg} is the temperature of the cosmic background (2.7K) and τ_ν is the optical depth, at frequency ν (assuming the source is a blackbody).

The transition temperatures are calculated using the equation (Lovas & Krupenie, 1974)

$$T_0 = \frac{h\nu}{k}$$

where h is the Planck constant (=6.63×10^{-34}J s), ν is the line rest frequency (listed in Table 4.1) and k is the Boltzmann constant (=1.38×10^{-23}J/K). The transition temperatures for each of the isotopologues are listed in Table 4.1.

There are two unknowns in this relation, τ_ν and T_{ex}. We remove one by

Isotopologue	Line Rest Frequency (GHz)	Transition Temperature (K)
^{12}CO	115.271	5.53
^{13}CO	110.201	5.29
C^{18}O	109.782	5.27

Table 4.1: Line rest frequency and transition temperatures for the J=1→0 transition of ^{12}CO, ^{13}CO and C^{18}O isotopologues.

utilising the observed property that low velocity ^{12}CO emission is optically thick. An optical depth $\tau_\nu >> 1$ is assumed for the ^{12}CO line. Therefore the (1-e$^{-\tau_\nu}$) term on the right-hand side of the Equation 4.1 is assumed to be equal to 1 and so:

$$T_R = T_0 \left(\frac{1}{e^{T_0/T_{ex}} - 1} - \frac{1}{e^{T_0/T_{bg}} - 1} \right).$$

The unknown term is the excitation temperature, so rearranging to solve for T_{ex}:

$$T_{ex} = T_0 \left[\ln \left[\frac{1}{\frac{T_R}{T_0} + \frac{1}{e^{T_0/T_{ex}} - 1}} + 1 \right] \right]^{-1} \tag{4.2}$$

Using the ^{12}CO brightness temperature of each core, reported in column 5 of Table 3.3, the excitation temperature for each core is calculated. The results are shown in Table 4.2.

4.2.2 Optical Depth

Returning to Equation 4.1, we see that we must also calculate the optical depth of the CO isotopologues to continue the investigation of the column density and mass. The ^{12}CO emission is assumed to be optically thick, and so the investigation is limited to the ^{13}CO and C^{18}O isotopologues. From Equation 4.1, the unknown

Core	T_{ex} (K)	τ^{13CO}	$\tau^{C^{18}O}$
CB29	13.74±0.37	0.98±0.04	0.23±0.02
BHR17	13.19±0.81	1.16±0.08	0.15±0.02
BHR31	13.93±0.5	1.23±0.06	0.24±0.03
BHR42	12.45±0.73	1.09±0.08	0.15±0.03
BHR34	12.1±0.59	1.30±0.07	0.23±0.02
BHR41	11.04±0.69	2.30±0.18	0.35±0.05
BHR40	12.27±0.76	0.90±0.07	0.14±0.03
BHR38	12.47±0.65	1.09±0.08	0.16±0.04
BHR39	13.48±0.68	0.91±0.07	0.13±0.06
BHR56	10.97±0.45	1.75±0.10	0.63±0.05
BHR48	7.29±0.63	1.14±0.15	0.33±0.06
BHR49	7.02±0.79	1.28±0.24	0.56±0.11
BHR50	6.14±0.73	5.19±0.81	0.61±0.13
DC2983-131a	7.80±0.64	1.96±0.16	0.49±0.07
DC2983-131b	5.83±1.01	2.59±0.46	0.65±0.30
BHR68	7.02±0.50	2.66±0.25	0.46±0.08
BHR74	10.97±0.51	1.53±0.11	0.34±0.05
BHR73	7.60±0.48	3.78±0.32	0.35±0.06
BHR76	11.73±0.63	1.64±0.13	0.61±0.06
DC3023-177	10.41±1.08	2.63±0.35	0.42±0.10
BHR79	11.71±1.1	1.28±0.16	0.16±0.05
BHR80	10.78±0.62	2.67±0.21	0.47±0.06
BHR81	13.19±1.55	1.36±0.20	0.33±0.06
DC3162+51	12.82±0.74	2.34±0.17	0.46±0.06
BHR95	7.41±0.61	1.89±0.23	0.54±0.10
BHR99	11.90±0.88	1.32±0.13	0.29±0.06
BHR100	12.45±0.72	1.08±0.09	0.22±0.05
BHR97	13.93±0.96	0.79±0.08	0.14±0.03
BHR119	16.13±0.78	1.07±0.07	0.14±0.03
BHR159	9.67±0.58	3.82±0.31	0.40±0.06
CB101	7.02±0.62	3.77±0.45	0.95±0.29
CB105	11.34±1.03	1.17±0.13	0.50±0.07
CB112	8.34±0.98	1.62±0.25	0.96±0.16
L422	5.87±0.96	0.58±0.11	0.96±0.53
CB175	7.79±0.82	3.78±0.54	0.86±0.16
CB176	10.97±2.45	0.82±0.22	0.42±0.12

Table 4.2: Column (1) shows the core name; Column (2) shows the excitation temperature calculated from optically thick 12CO observations; Column (3) shows the peak ^{13}CO optical depth; and column (4) shows the peak C^{18}O optical depth calculated using the LTE analysis described in the text.

value is τ_ν, on the right-hand-side. Rearranging to solve for τ_ν:

$$-\tau_\nu = ln\left[1 - \frac{T_R}{T_0\left(\frac{1}{e^{T_0/T_{ex}}-1} - \frac{1}{e^{T_0/T_{bg}}-1}\right)}\right] \tag{4.3}$$

Assuming that ^{13}CO and C^{18}O excitation temperature is equal to the ^{12}CO excitation temperature, using the excitation temperatures from Table 4.2 and the peak brightness temperatures listed in Table 3.4 for ^{13}CO emission, and Table 3.5 for the C^{18}O emission, the peak optical depth for each core was calculated. The results are shown in Table 4.2.

The results show that the ^{13}CO emission is often optically thick. The C^{18}O emission appears to be optically thin in most cases.

4.2.3 Column Density

Under the condition of Local Thermodynamic Equilibrium (LTE), the column density of a linear molecule can be expressed as (e.g. Lang, 1980):

$$N_X = 93.5\frac{g_l\nu^3}{g_u A_{ul}}\frac{Z}{1-\exp\left(\frac{-h\nu/k}{T_{ex}}\right)}\int \tau_\nu dV \text{ cm}^{-2} \tag{4.4}$$

where N_X is the column density of species X, g_l (=2J$_l$+1) and g_u (=2J$_u$ +1) are the statistical weights of the lower and upper rotational levels respectively, A_{ul} is the Einstein coefficient for spontaneous transition from the upper level to the lower level, ν is the frequency of the transition (the line rest frequency) and Z is the partition function.

The transitions of all isotopologues under consideration here are from the

Isotopologue	Einstein Coefficient [s^{-1}]
^{13}CO	6.40×10^{-8}
C^{18}O	6.23×10^{-8}

Table 4.3: Einstein coefficients for the J=1→0 transition of ^{13}CO and C^{18}O.

J=1→0 level, so g_l=1 and g_u=3. The Einstein coefficient A_{ul} needs to be calculated before discussion of column density can continue. The expression for A_{ul} is:

$$A_{ul} = \frac{64\pi^4}{3hc^3}\nu^3|\mu_{ul}|^2 \tag{4.5}$$

where ν is the line rest frequency, μ_{ul} is the dipole moment (measured in Debye). Working out the numerical constants in Equation 4.5, in CGS units gives:

$$A_{ul} = 1.161 \times 10^{-11}\nu^3\mu^2\frac{2J_u+1}{2J_l+1} \tag{4.6}$$

Using a value of μ=0.1101 Deybe (Burrus, 1958) for the dipole moment of CO, and the line rest frequencies quoted in Table 4.1, the Einstein co-efficient for the CO isotopologues are calculated. The results are recorded in Table 4.2.3.

Substituting these values into Equation 4.4 and reducing all numerical constants gives the following equations for the ^{13}CO and C^{18}O column density:

$$N_{tot}^{^{13}CO} = 3.70 \times 10^{14}\frac{T_R}{1-exp[\frac{-5.53}{T_{ex}}]}\int \tau_\nu dv \mathrm{cm}^{-2}, \tag{4.7}$$

$$N_{tot}^{C^{18}O} = 3.77 \times 10^{14}\frac{T_R}{1-exp[\frac{-5.27}{T_{ex}}]}\int \tau_\nu dv \mathrm{cm}^{-2}, \tag{4.8}$$

where v is velocity. The $\int \tau_\nu dv$ term can be assumed to be equal to the FWHM of

a Gaussian fit to the line profile of the source, multiplied by the optical depth τ_ν.

The results of this analysis are shown in Table 4.4. Also shown in the Table are the corresponding values for the peak H_2 column density. To convert between the molecular species, multiply by X, the abundance of CO and its isotopologues relative to H_2 using the currently accepted abundance ratios between the different isotopes of CO, X[^{12}CO]=8.5×10^{-5} (Wilson & Rood, 1994), X[^{13}CO]=1.10×10^{-6} (Frerking, Langer, & Wilson, 1982) and X[C^{18}O]=2.01×10^{-7} (Frerking et al., 1982).

Several problems are inherent in the determination of column density from ^{13}CO measurements. The ^{13}CO emission is observed to be optically thick in many cases, so the column density will be underestimated as it is only probed to a moderate depth into the cloud. The relative abundance of ^{13}CO and ^{12}CO may be enhanced by chemical fractionation (Langer et al., 1980) and photo-destruction of certain isotopes (Bally & Langer, 1982). By comparison, the C^{18}O emission is less susceptible to such effects and therefore may provide a more reliable probe of the total column density.

As will be discussed further in Section 5.2.1, the core column density derived from ^{13}CO emission is often larger than the column density derived from C^{18}O emission. However, this suggests that the observations are not sensitive to C^{18}O in the outer regions of the core, and so the size of the core traced by C^{18}O is smaller than the size of the core traced by ^{13}CO. This agrees with what is seen in Figures 5.1 - 5.6.

Core	$N_{tot}^{^{13}CO}$ ($\times 10^{15} cm^{-2}$)	$N_{tot}^{H_2}$ ($\times 10^{21} cm^{-2}$)	$N_{tot}^{C^{18}O}$ ($\times 10^{14} cm^{-2}$)	$N_{tot}^{H_2}$ ($\times 10^{21} cm^{-2}$)
CB29	5.31±0.25	4.81±0.22	5.74±068	2.68±0.34
BHR17	3.56±0.33	3.22±0.30	1.91±0.34	0.95±0.17
BHR31	3.25±0.20	2.94±0.19	3.14±0.54	1.56±0.22
BHR42	3.71±0.35	3.36±0.32	2.92±0.87	1.45±0.43
BHR34	3.88±0.29	3.52±0.27	4.61±0.62	2.30±0.31
BHR41	7.72±0.80	6.99±0.73	6.01±1.18	3.00±0.59
BHR40	2.66±0.29	2.41±0.26	1.84±0.50	0.92±0.25
BHR38	3.27±0.33	2.96±0.30	1.47±0.51	0.73±0.25
BHR39	4.48±0.45	4.06±0.41	1.89±0.59	0.94±0.29
BHR56	3.26±0.24	2.95±0.22	7.79±0.93	3.88±0.47
BHR48	0.79±0.14	0.71±0.13	0.95±0.24	0.47±0.12
BHR49	0.87±0.21	0.79±0.19	3.44±0.85	1.71±0.42
BHR50	3.20±0.66	2.90±0.60	4.09±1.64	2.04±0.82
DC2983-131a	4.04±0.47	3.66±0.42	7.71±1.32	3.84±0.66
DC2983-131b	2.43±0.57	2.20±0.52	14.3±3.53	7.21±1.76
BHR68	7.13±0.85	6.46±0.77	7.57±1.57	3.77±0.78
BHR74	2.81±0.27	2.55±0.24	3.45±0.76	1.72±0.38
BHR73	5.92±0.66	5.36±0.59	4.47±0.89	2.23±0.45
BHR76	3.34±0.34	3.02±0.31	9.14±7.34	4.55±0.67
DC3023-177	7.35±0.14	6.66±1.22	7.22±2.59	3.59±1.29
BHR79	2.42±0.45	2.20±0.40	0.39±0.19	0.192±0.10
BHR80	4.49±0.48	4.07±0.43	3.54±0.61	1.76±0.31
BHR81	3.98±0.80	3.61±0.72	3.78±1.01	1.88±0.50
DC3162+51	7.96±0.78	7.21±0.70	8.77±1.31	4.37±0.65
BHR95	2.39±0.37	2.16±0.33	6.28±1.35	3.13±0.65
BHR99	4.09±0.52	3.70±0.47	3.58±2.26	1.78±1.31
BHR100	3.90±0.42	3.53±0.38	3.34±0.96	1.67±0.49
BHR97	4.14±0.53	3.75±0.48	2.54±0.65	1.27±0.33
BHR119	4.94±0.43	4.47±0.39	0.79±0.43	0.39±0.21
BHR159	15.4±1.62	14.00±1.47	9.29±1.98	4.63±0.98
CB101	4.27±0.66	3.87±0.60	23.40±3.90	11.70±1.94
CB105	2.29±1.51	2.08±1.37	8.03±1.68	4.06±0.84
CB112	2.03±0.41	1.84±0.38	7.63±2.11	3.80±1.05
L422	0.92±0.24	0.83±0.22	23.70±7.28	11.80±3.63
CB175	5.18±0.24	4.69±0.89	8.12±2.60	4.04±1.30
CB176	1.02±0.38	0.92±0.34	5.43±2.57	2.70±1.28

Table 4.4: ^{13}CO and corresponding H_2 column density and C^{18}O and corresponding H_2 column density estimates.

4.2.4 CO Mass

The core mass derived from the observed the ^{13}CO and C^{18}O emission can be measured from the calculated column density of each core. From Garden et al. (1991):

$$M_{gas} = N(CO)[1/X]\mu m_{H_2}(\pi\theta^2/4)d^2 \tag{4.9}$$

where μ is the mean atomic weight of the gas, m_{H_2} is the mass of a hydrogen molecule, X is the abundance ratio of ^{12}CO/H$_2$ (Wilson & Rood, 1994), θ is the FWHM of the telescope beam and d^2 is the distance to the cloud. This relation can be rewritten in terms of an image pixel area $(\Delta\alpha, \Delta\beta)$ (Buckle et al., 2010):

$$M^{^{13}CO} = 1.13 \times 10^{-4}\mu m_{H_2} d^2 \Delta\alpha\Delta\beta \frac{1}{X^{13}} N(^{13}CO)\mathrm{M}_\odot \tag{4.10}$$

$$M^{C^{18}O} = 1.13 \times 10^{-4}\mu m_{H_2} d^2 \Delta\alpha\Delta\beta \frac{1}{X^{18}} N(C^{18}O)\mathrm{M}_\odot \tag{4.11}$$

The core masses derived from ^{13}CO observations are shown in column 2 of Table 4.5. The cores are seen to span a range of masses, from $\sim$1 - 50 M$_\odot$. The cores masses derived from C^{18}O observations are shown in column 4 of Table 4.5. The C^{18}O masses are observed to be lower than the ^{13}CO masses, and span a range of $\sim$0.05 - 25M$_\odot$.

As will be discussed in Section 5.3, the two tracers sample different regions of the cloud. The core size derived from ^{13}CO observations is larger than the core size derived from C^{18}O and so the core mass derived from ^{13}CO is larger than the core mass derived from C^{18}O. The ^{13}CO mass is likely to be underestimated as ^{13}CO is optically thick at moderate depths into the cloud and so does not see the mass contained in the centre of the core. As previously stated, the observations are not sensitive to C^{18}O in the outer part of the core, and so it is only detected

in the center of the core and so the core mass derived from $C^{18}O$ is smaller than the mass derived from ^{13}CO.

4.2.5 Virial Mass

A comparison of the core mass with the virial mass can be used to investigate the gravitational stability of the cores. However, to apply the virial theorem, we must impose the condition that the gas sampled by the $C^{18}O$ observations is characterised by an isotropic distribution (Rohlfs & Wilson, 2004),

$$M_{vir} = 250 \left(\frac{\sigma^2}{(\mathrm{kms}^{-1})^2} \frac{R_{eff}}{\mathrm{pc}} \right) \tag{4.12}$$

where σ is the FWHM 1D velocity dispersion in km s^{-1} and R_{eff}=$\sqrt{\theta_{maj} \times \theta_{min}}$ is the effective radius of the core, assuming spherical geometry. It is possible that there is mass in lower density material in which the ^{13}CO and $C^{18}O$ lines are not excited, leading to an underestimate of the derived masses.

The velocity dispersion for each core is measured from the FWHM linewidth reported in Tables 3.4 & 3.5 using the relation:

$$\sigma = \frac{FWHM}{\sqrt{8 \ln 2}} \tag{4.13}$$

Cores with an observed mass greater than the measured virial mass are believed to be gravitationally bound and are expected to eventually collapse and form stars unless they are supported by some other mechanism.

Cores with virial masses larger than their observed masses are not expected to be gravitationally bound and may disperse over time under the actions of its

own internal motions, unless confined by an external pressure.

The calculated virial masses and associated errors for ^{13}CO and C^{18}O are recorded alongside the observed masses in Table 4.5. A comparison of the observed and virial masses of each core is plotted in Figures 5.7 & 5.8 in the next Chapter. As further discussed in the next Chapter, the plots show that for C^{18}O $\sim$1/2 of the cores have an observed mass greater or equal to the virial mass, meaning they are gravitationally bound.

Core	^{13}CO M_{obs} ($M_\odot$)	^{13}CO M_{vir} ($M_\odot$)	$\alpha^{^{13}CO}$	C^{18}O M_{obs} ($M_\odot$)	C^{18}O M_{vir} ($M_\odot$)	$\alpha^{C^{18}O}$
CB29	5.94±0.64	21.31±2.84	0.27±0.07	4.18±1.78	6.22±1.20	0.67±0.41
BHR17	0.19±0.03	3.81±0.88	0.05±0.02	0.57±0.53	2.32±0.64	0.24±0.22
BHR31	0.94±0.1	1.83±0.49	0.51±0.19	0.41±0.28	0.31±0.19	1.32±1.21
BHR42	3.89±0.80	7.85±1.52	0.50±0.20	1.21±0.73	8.11±3.70	0.15±0.13
BHR34	1.64±0.15	2.76±0.83	0.59±0.02	1.23±1.16	3.53±2.23	0.35±0.29
BHR41	8.75±1.30	7.17±1.37	1.22±0.41	4.06±3.81	1.93±0.50	2.10±2.02
BHR40	2.82±0.20	6.71±1.53	0.42±0.13	0.63±0.38	3.36±1.02	0.19±0.17
BHR38	1.37±0.28	4.25±1.16	0.32±0.15	0.05±0.03	0.42±0.30	0.12±0.09
BHR39	0.43±0.04	6.57±2.73	0.07±0.04	0.25±0.16	0.79±0.58	0.32±0.28
BHR56	3.76±0.33	3.43±1.27	1.10±0.50	0.87±0.49	0.43±0.27	2.02±1.81
BHR48	0.76±0.50	2.40±0.65	0.32±0.30	0.30±0.13	0.10±0.08	3.00±2.70
BHR49	7.93±1.79	1.41±0.68	5.62±3.98	0.87±0.49	0.57±0.23	1.53±1.48
BHR50	0.59±0.26	2.89±0.57	0.20±0.13	0.58±0.33	1.42±0.53	0.41±0.38
DC2983-131a	4.11±2.01	6.18±1.19	0.67±0.46	6.98±3.21	1.76±0.50	3.97±3.06
DC2983-131b	11.84±6.57	8.68±1.10	1.80±1.23	5.80±3.49	0.88±0.21	6.59±5.53

Core	^{13}CO M_{obs} ($M_\odot$)	^{13}CO M_{vir} ($M_\odot$)	$\alpha^{^{13}CO}$	C^{18}O M_{obs} ($M_\odot$)	C^{18}O M_{vir} ($M_\odot$)	$\alpha^{C^{18}O}$
BHR68	2.47±1.36	19.98±4.74	0.12±0.09	0.65±0.32	10.68±2.61	0.06±0.04
BHR74	0.23±0.19	0.81±0.55	1.21±1.10	0.11±0.04	0.28±0.20	0.39±0.32
BHR73	0.39±0.24	2.03±1.33	0.19±0.17	0.35±0.17	1.76±1.37	0.20±0.15
BHR76	0.89±0.32	1.15±0.49	0.77±0.60	0.48±0.0.28	0.15±0.03	3.2±2.51
DC3023-177	1.78±1.14	3.03±1.13	0.59±0.57	0.26±0.15	0.34±0.24	0.76±0.67
BHR79	0.91±0.36	1.14±0.52	0.80±0.72	0.18±0.03	0.04±0.04	4.50±3.00
BHR80	0.55±0.29	0.69±0.35	0.80±0.74	0.13±0.07	0.09±0.07	1.44±1.36
BHR81	0.88±0.46	2.03±1.00	0.43±0.39	0.14±0.11	5.94±0.12	0.02±0.01
DC3162+51	3.59±1.78	2.73±0.72	1.32±1.00	2.75±1.77	0.75±0.68	3.67±3.45
BHR95	2.15±1.15	2.10±1.29	1.02±0.89	0.37±0.25	1.96±1.26	0.19±0.17
BHR99	0.53±0.15	3.52±1.26	0.14±0.10	0.28±0.21	0.60±0.52	0.47±0.40
BHR100	0.61±0.31	3.79±1.73	0.16±0.15	0.29±0.13	0.85±0.53	0.34±0.26
BHR97	3.25±1.51	16.03±3.28	0.20±0.13	0.94±0.55	2.92±1.08	0.32±0.22
BHR119	3.31±1.12	4.41±0.96	0.75±0.42	0.07±0.03	0.16±0.13	0.44±0.40
BHR159	0.69±0.16	2.32±1.96	0.30±0.26	0.20±0.14	1.04±1.03	0.19±0.17

Core	^{13}CO M_{obs} ($M_\odot$)	^{13}CO M_{vir} ($M_\odot$)	α^{13CO}	C^{18}O M_{obs} ($M_\odot$)	C^{18}O M_{vir} ($M_\odot$)	$\alpha^{C^{18}O}$
CB101	10.89±4.91	8.26±1.33	1.32±0.81	9.19±3.84	0.67±0.45	13.72±10.85
CB105	10.66±2.18	5.72±2.87	1.86±1.31	17.15±7.18	1.24±1.03	13.83±12.86
CB112	7.76±3.58	6.79±1.73	1.14±0.82	2.56±1.07	0.41±0.35	6.24±5.93
L422	4.59±1.79	8.95±2.56	0.51±0.34	2.01±1.56	0.84±0.41	2.39±2.19
CB175	6.93±2.16	6.99±2.88	0.99±0.72	2.77±1.16	0.69±0.27	4.01±2.30
CB176	5.68±2.11	2.90±0.64	1.96±1.16	1.02±0.43	0.39±0.21	2.62±1.23

Table 4.5: Column (2) shows the core mass derived derived from ^{13}CO observations; column (3) shows the virial mass calculated from ^{13}CO linewidths; column (4) shows the virial parameter (Observed mass/virial mass) calculated from ^{13}CO. Column (5) is the core mass derived from C^{18}O; column (6) is the virial mass calculated from C^{18}O linewidths; column (7) shows the virial parameter α for C^{18}O.

4.3 SIMBA Data

The SIMBA 1.2mm continuum data can be used as an independent column density and mass estimate to the CO gas mass estimates above. The dust is expected to remain optically thin even in the densest central parts of the core, compared to the ^{13}CO emission, which is observed in many cases to be optically thick. The C^{18}O gas and 1.2mm dust emission are expected to trace similar regions. An analysis of the column density and mass of each core observed by SIMBA is presented below.

4.3.1 Column Density

The H_2 column density derived from dust observations can be measured from the observed intensity of the source.

In the case of local thermal equilibrium (LTE), the intensity emitted by a medium of temperature T_d and optical depth τ_ν at the frequency ν is given by the equation of radiative transfer given by

$$I_\nu = B_\nu(T_d)(1 - e^{-\tau_\nu}) \tag{4.14}$$

where B_ν is the Planck function.

The optical depth is given by

$$\tau_\nu = \int \kappa_\nu Q ds \tag{4.15}$$

where κ_ν is the dust opacity. If most hydrogen is in molecules, the optical depth can be related to the column density of molecular hydrogen,

$$N_{H_2} = \int n_{H_2} ds = \int \frac{Q}{\mu_{H_2} m_H} ds = \frac{1}{\mu_{H_2} m_H \kappa_\nu} \int \kappa_{nu} Q ds \tag{4.16}$$

where n_{H_2} is the number density of H_2. Therefore:

$$N_{H_2} = \frac{\tau_\nu}{\mu_{H_2} m_H \kappa_\nu} \tag{4.17}$$

for optically thin conditions the equation of radiative transfer can be simplified to

$$I_\nu = B_\nu(T_d)\tau_\nu \tag{4.18}$$

The received flux per beam is related to the intensity by

$$S_\nu^{beam} = \int I_\nu P d\Omega \tag{4.19}$$

where P is the normalised power pattern of the telescope (i.e. max(P) = 1). Defining the beam solid angle as the integral

$$\Omega_A = \int P d\Omega \tag{4.20}$$

the beam averaged intensity can be expressed as

$$\langle I_\nu \rangle = S_\nu^{beam} \Omega_A. \tag{4.21}$$

Combining Equations 4.17, 4.18, 4.21, one obtains an expression linking the H_2 column density with the observed intensity:

$$N_{H_2} = \frac{\tau_\nu}{\mu_{H_2} m_H \kappa_\nu}$$

$$N_{H_2} = \frac{I_\nu}{B_\nu(T_d)} \frac{1}{\mu_{H_2} m_H \kappa_\nu}$$

and as

$$I_\nu = \frac{S_\nu}{\Omega_A}$$

$$N_{H_2} = \frac{S_\nu}{\Omega_A \mu_{H_2} m_H \kappa_\nu B_\nu(T_d)} \tag{4.22}$$

where S_ν is the peak intensity at 1.2mm, Ω_A is the beam solid angle, μ_H(=2.8) is the molecular mass per hydrogen atom, m_H the hydrogen atom mass, $\kappa_{1.2}$ is the total mass opacity at 1.2mm per gram of interstellar matter and $B_\nu(T_d)$is the Planck function at frequency ν, for dust temperature T_d.

Using the total intensity of the cores, presented in Table 3.6, the column density of the cores detected by SIMBA has been calculated. The results are shown in column 2 of Table 4.6.

4.3.2 Masses

If we assume the dust grains are identical and spherical with radius a_D and internal density ρ_D, then the mass of an individual spherical dust grain, m_D, is given by:

$$m_D = \frac{4\pi a_D^3 \rho_D}{3}.$$

The total mass of the cloud M_C is given by the mass of a dust grain, multiplied by the total number of dust grains in the cloud N_D,

$$M_C = m_D N_D,$$

so

$$N_D = \frac{M_C}{m_D}$$

assuming the core is spherical, the number of dust grains is:

$$N_D = \frac{3M_C}{4\pi a_D^3 \rho_D}.$$

$$\Rightarrow M_C = \frac{4\pi a_D^3 \rho_D N_D}{3}$$

Provided the dust is optically thin at frequency ν, the flux, S_ν, is given by,

$$S_\nu = \frac{N_D L_\nu}{4\pi D^2}.$$

$$\Rightarrow N_D = \frac{4\pi D^2 S_\nu}{L_\nu}$$

where L_ν, the luminosity of a dust grain, is given by,

$$L_\nu = 4\pi a_D^2 Q_\nu \pi B(\nu, T_D),$$

where Q_ν is the emissivity of the dust grain, T_D is the dust temperature and $B_\nu(T_d)$ is the blackbody function.

$$\Rightarrow N_D = \frac{4\pi D^2 S_\nu}{4\pi a^2 Q_\nu \pi B(\nu, T_D)}$$

This equation can be rearranged to give the mass of the dust in the cloud:

$$M_C = \frac{4a_D\rho_D D^2 S_\nu}{3Q_\nu B(\nu, T_D)}. \tag{4.23}$$

At a given frequency, ν, the dust mass opacity. κ_ν, can be defined by the equation (Hildebrand, 1983),

$$\frac{1}{\kappa_\nu} = \frac{4}{3}\frac{a\rho_D}{Q(\nu)}.$$

$$\Rightarrow Q_\nu = \frac{4}{3}a\rho_D\kappa_\nu$$

We can use this equation to simplify equation 4.23 to:

$$M_C = \frac{S(\nu)D^2}{B(\nu, T_D)\kappa_\nu}. \tag{4.24}$$

The dust opacity at 1.2mm, $\kappa_{1.2}$, has been taken from Ossenkopf & Henning (1994) and was divided by a gas-to-dust ratio of 100. An average dust temperature T_d=10K was adopted. A dust temperature of 10K is assumed as the cores are assumed to be isolated from heating sources and have column densities high enough to shield the interiors of the clouds from heating sources.

The mass for each of the 13 cores detected by SIMBA is calculated using the observed flux density reported in Table 3.6. The results are shown in Table 4.6. The cores are seen to have a 1.2mm dust mass in the range of $\sim$0.5 - 8M$\odot$.

Core	N(H_2) ($\times 10^{23} cm^{-2}$)	1.2mm Mass ($M_\odot$)
BHR17	0.99±1.91	0.40±0.22
BHR31	2.03±1.52	0.46±0.23
BHR42	2.03±1.05	1.29±0.59
BHR34	8.52±2.04	3.46±1.56
BHR41	9.60±1.35	3.90±1.24
BHR40	3.13±1.29	1.99±1.01
BHR68	24.3±3.98	7.56±3.40
BHR74	1.23±1.85	0.10±0.08
BHR99	3.40±0.65	1.06±0.41
BHR100	5.11±1.88	1.59±0.58
BHR97	0.64±0.93	0.40±0.12
BHR119	2.711±1.20	0.62±0.20
L422	22.9±3.03	5.24±2.41

Table 4.6: Column density and mass estimates from the analysis of 1.2mm SIMBA data.

4.4 Spitzer Data

The protostellar content of the cores can be investigated using multi-wavelength Spitzer data, which offer a means of establishing the evolutionary class of young stellar objects (YSOs) associated with the cores. The Spitzer observations of the core regions contain field sources and objects that may be associated with the core. In each of the four IRAC bands (3.6, 4.5, 5.8, 8.0 μm), a photometric analysis was carried out on all sources greater than the 3σ noise level.

The ratio of the fluxes measured at each waveband were recorded as infrared-colours (IR-colours), i.e [3.5] - [4.5], [4.5] - [5.6] etc. Analysis of the IR-colours can be used to distinguish between protostellar objects with infalling envelopes and more evolved pre-main-sequence stars with disks as devised by Gutermuth et al. (2008) and explained below.

The method uses the available IR-colours to identify and classify sources of contamination and reddening. Contamination arises from non-YSO sources with

excess infrared emission, including background star-forming galaxies and broad-line active galactic nuclei (AGNs). Once separated from unrelated field stars and contaminants, the YSOs are classified into the categories of Class I (protostars with infalling envelopes) and Class II (pre-main-sequence stars with optically thick discs).

To begin, infrared contaminants are separated from genuine YSO candidates. Contaminants are identified and removed from the sample by applying constraints in various colour spaces where the contaminant sources are considerably more prominent than YSOs.

Active star-forming galaxies are eliminated by identifying their strong PAH (polycyclic aromatic hydrocarbon) emission which yields very red 5.8μm and 8.0μm colours (Stern et al., 2005).

Any sources are considered PAH galaxies if they follow all of the following constraints:

$$[3.6] - [5.8] < 1.5,$$

and

$$[4.5] - [5.8] < 1.05,$$

and

$$[4.5] - [8.0] > 1,$$

and

$$[5.8] - [8.0] > 1,$$

and

$$[4.5] > 11.5.$$

Once a source has been flagged as a PAH galaxy, it is removed from further consideration in the classification scheme.

Broad-line AGNs have mid-IR colours that are largely consistent with YSOs (Stern et al., 2005). All sources that obey the following conditions are considered broad-line AGN contaminants:

$$[4.5] - [8.0] > 0.5,$$

and

$$[4.5] > 13.5 + ([4.5] - [8.0] - 2.3)/0.4,$$

and

$$[4.5] > 13.5.$$

Once a source has been flagged as a broad-line AGN, it is removed from further consideration in the classification scheme.

A number of sources were also observed with MIPS at 24μm. This detection allows for the identification of deeply embedded YSOs which would not be seen a shorter wavelengths. Many young sources are so deeply embedded that usable photometry cannot be extracted in one or more of the IRAC bands. As such, any source is likely to be a deeply embedded protostar if it lacks detection in some IRAC bands yet is bright at MIPS 24μm:

$$[24] < 7,$$

and

$$[X] - [24] > 4.5\text{mag},$$

where [X] is the photometry from the longest wavelength IRAC detection. The adopted magnitude limit at 24μm is needed to ensure there is no contamination due to extragalactic sources.

Of the sources that remain, Class I and Class II need to be identified against the surrounding unrelated field stars. Class I protostars have an extremely red discriminant colour i.e.:

$$[4.5] - [5.8] > 1.$$

In addition, any source with a moderately red discriminant colour that obeys the following two conditions are also defined as Class I protostars:

$$0.7 < [4.5] - [5.8] < 1.0,$$

and

$$[3.6] - [4.5] > 0.7.$$

Sources that obey the following constraints are Class II protostars:

$$[4.5] - [8.0] > 0.5,$$

and

$$[3.6] - [5.8] > 0.35.$$

Sources that fit into neither category are classified as field stars unrelated to the star formation associated with the isolated cores.

In this work, the above analysis was carried out to identify protostars and their positions relative to the isolated cores. The cores are split into three classes:

1. those that are starless, i.e. cores that as yet have no active sites of star

formation,

2. cores with embedded protostars,

3. those that have protostars nearby, i.e. protostars found within the 5‘ × 5‘ map, but not embedded in the core.

The results of the classification investigation are shown in Table 4.4. 26 cores are starless, 7 contain embedded protostars and 3 have protostars nearby.

4.5 Summary

I have presented the details of the analysis carried out on the data sets described in Chapter 3. I have performed an LTE analysis of the CO isotopologues to calculate the column density and mass of each core and presented the results. I have also conducted a similar analysis on the available SIMBA data. I have used a multi-wavelength infrared colour-excess method to identify protostars associated with each of the cores. In the next chapter I analyse the results in detail.

Starless	Embedded Protostars	Nearby Protostars
BHR31*	CB29	BHR42*
BHR34*	BHR17*	BHR73
BHR41*	DC2983-131a	BHR97
BHR40*	BHR68*	
BHR38	BHR99*	
BHR39	BHR100*	
BHR56	CB101	
BHR48		
BHR49		
BHR50		
DC2983-131b		
BHR74*		
BHR76		
DC3023-177		
BHR79		
BHR80		
BHR81		
DC3162+51		
BHR95		
BHR119*		
BHR159		
CB112		
L422*		
CB175		
CB176		

Table 4.7: Results from YSO identification procedure described in the text. 26 cores are starless, 7 have embedded protostars and 3 have nearby YSOs. Cores listed with a * superscript are cores with SIMBA 1.2mm data.

Chapter 5

Data Analysis and Discussion

5.1 Introduction

In this chapter, I present the analysis and discussion of the results presented in Chapter 4. In Section 5.2, I discuss the column density calculated for each core. In Section 5.3, I discuss the mass and assess the gravitational stability of each core. In Sections 5.4 & 5.5 I discuss the properties of cores with embedded protostars, and cores with nearby protostars. Section 5.6 contains a discussion of the properties of starless cores, and discusses the star forming potential of the cores. In Section 5.7 I describe the difference in linewidths for the observed cores, and finally in Section 5.8, I compare the observed core parameters to models of turbulent dissipation.

5.2 Column Density Estimates

In this Section, I discuss and compare the peak column density estimates for the ^{13}CO, C^{18}O and 1.2mm continuum observations of each core.

5.2.1 CO

Table 5.1 presents a summary of the column density estimates for the cores. The Table shows that the average column density derived from ^{13}CO is larger than the column density derived from C^{18}O. However, we would expect the C^{18}O emission to probe deeper into cores than ^{13}CO , as it remains optically thin into the centre of the core, whereas ^{13}CO is optically thick at moderate depths into the core. We would therefore expect the C^{18}O derived column density to be larger than the ^{13}CO derived column density. As the Table indicates the opposite, this suggests that the observations are not sensitive to C^{18}O in the outer regions of the core, and so the size of the core traced by ^{13}CO is larger than the core traced by C^{18}O. This is what is seen in Figures 5.1 - 5.6, where the core traced by ^{13}CO (represented by the black contour) is larger than the core size traced by C^{18}O (shown as the white contour in the Figures). As the size of the core derived from C^{18}O is smaller than the ^{13}CO core, the measured column density is smaller and the size of the column is smaller.

sample	$N(H_2)$ ^{13}CO	$N(H_2)$ $C^{18}O$	$N(H_2)$ 1.2mm	M_{obs} ^{13}CO	M_{vir} ^{13}CO	M_{obs} $C^{18}O$	M_{vir} $C^{18}O$	M_{obs} 1.2mm
	cm^{-2}	cm^{-2}	cm^{-2}	$M_\odot$	$M_\odot$	$M_\odot$	$M_\odot$	$M_\odot$
whole sample	6.8×10^{23}	5.6×10^{23}	6.6×10^{23}	3	5	2	2	2
starless	6.1×10^{23}	4.6×10^{23}	-	3.4	3.8	1.8	1.3	-
nearby protostars	5.2×10^{23}	3.8×10^{23}	-	2.5	9	0.7	4	-
embedded protostars	9.2×10^{23}	6.4×10^{23}	-	3.5	10	3	2	-

Table 5.1: Summary of column density and core mass estimates. The Table shows: Column (1) the column density derived from ^{13}CO; Column (2) the column density derived from $C^{18}O$; Column (3) the column density derived from 1.2mm dust; Column (4) the core mass derived from ^{13}CO observations; Column (5) the virial mass derived from ^{13}CO linewidths; Column (6) the core mass derived from $C^{18}O$ observations; Column (7) the virial mass derived from $C^{18}O$ linewidths; Column (8) core mass derived from 1.2mm dust observations.

5.2.2 1.2mm continuum

The average 1.2mm dust column density is shown in Column (3) of Table 5.1. The dust column density is larger than the average column density derived from ^{13}CO and C^{18}O observations. The 1.2mm continuum emission is expected to trace a similar region to the C^{18}O emission, but while the C^{18}O gas may eventually become optically thick in the densest regions of the core, the dust should remain optically thin. Therefore, the dust column density is more likely to give a true estimate of the column density of the cloud, while the CO estimates may be underestimated due to being optically thick. The CO column densities may also be underestimated as a fraction of the gas freezes out onto the dust grains in the centre of the core. This will be discussed further in a subsequent section.

5.2.3 Comparison of different data sets

Figures 5.1 - 5.6 show a comparison of all column density results. In each of the Figures, the background grey-scale image shows the 2MASS extinction. The black contour shows ^{13}CO column density, the white contour shows the C^{18}O column density, and where available, the red contour shows the 1.2mm dust column density. The contours are drawn at the 30% of the peak column density level in each case.

The location of the ^{13}CO, C^{18}O and 1.2mm contours are shown to be in good agreement with each other and with the peak extinction in the 2MASS maps in most cases. The ^{13}CO emission traces a large area that corresponds to the edge of the core, seen on the 2MASS maps as a rise in extinction. The C^{18}O emission traces the peak of the 2MASS extinction maps. The 1.2mm continuum emission

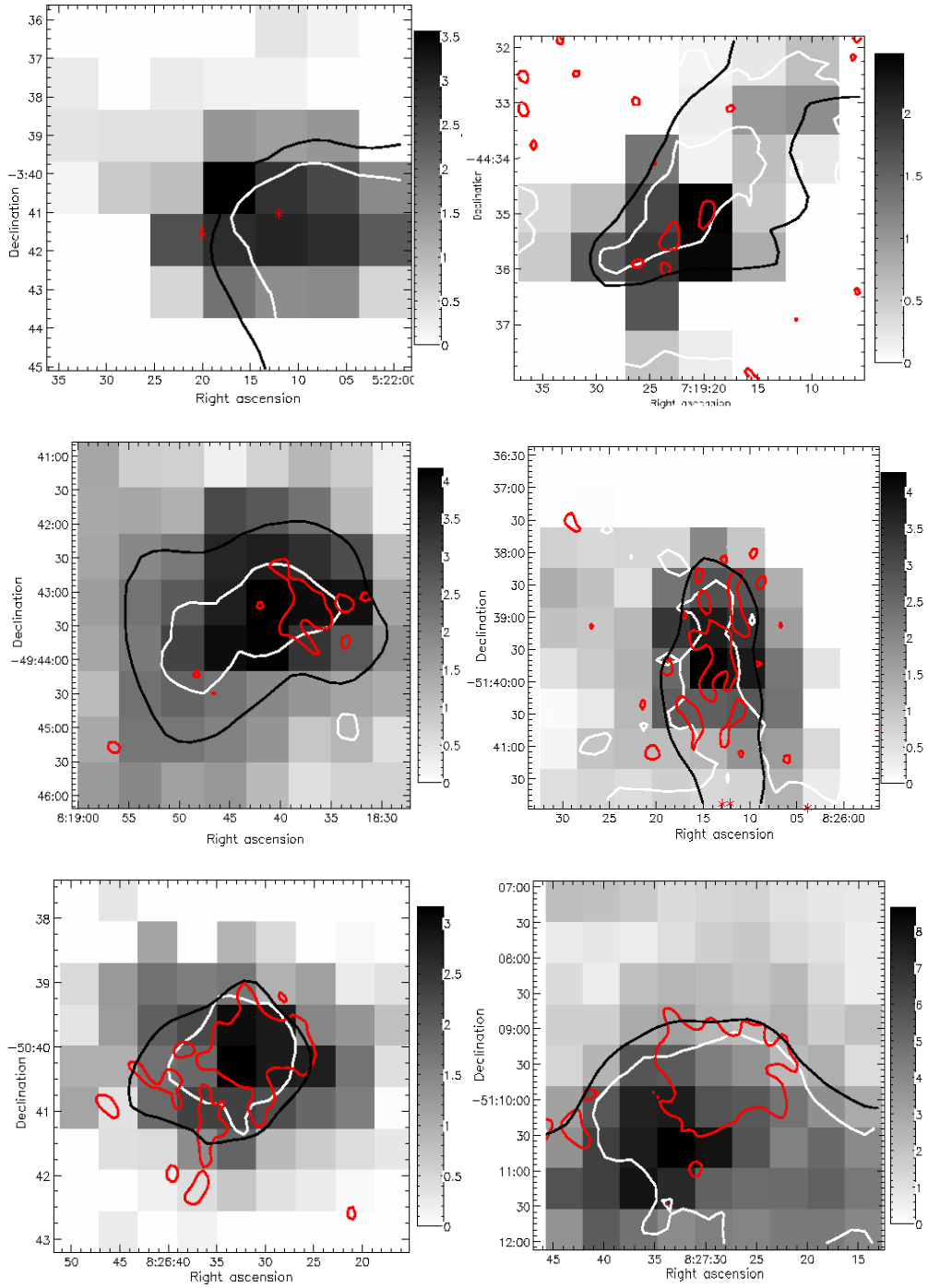

Figure 5.1: These images show the grey scale 2MASS extinction maps of cores (a)CB29, (b)BHR17, (c)BHR31, (d)BHR42, (e)BHR34, (f)BHR41. The overplotted black contour delineates emission at 30% of the peak ^{13}CO column density, the white contour delinates emission at 30% of the peak C^{18}O column density. Where available, the 3σ SIMBA column density is also overlaid with a red contour. Also shown overlaid on the extinction maps are the positions of protostars thought to be associated with the cores. The position of each protostar is shown with a red asterisk.

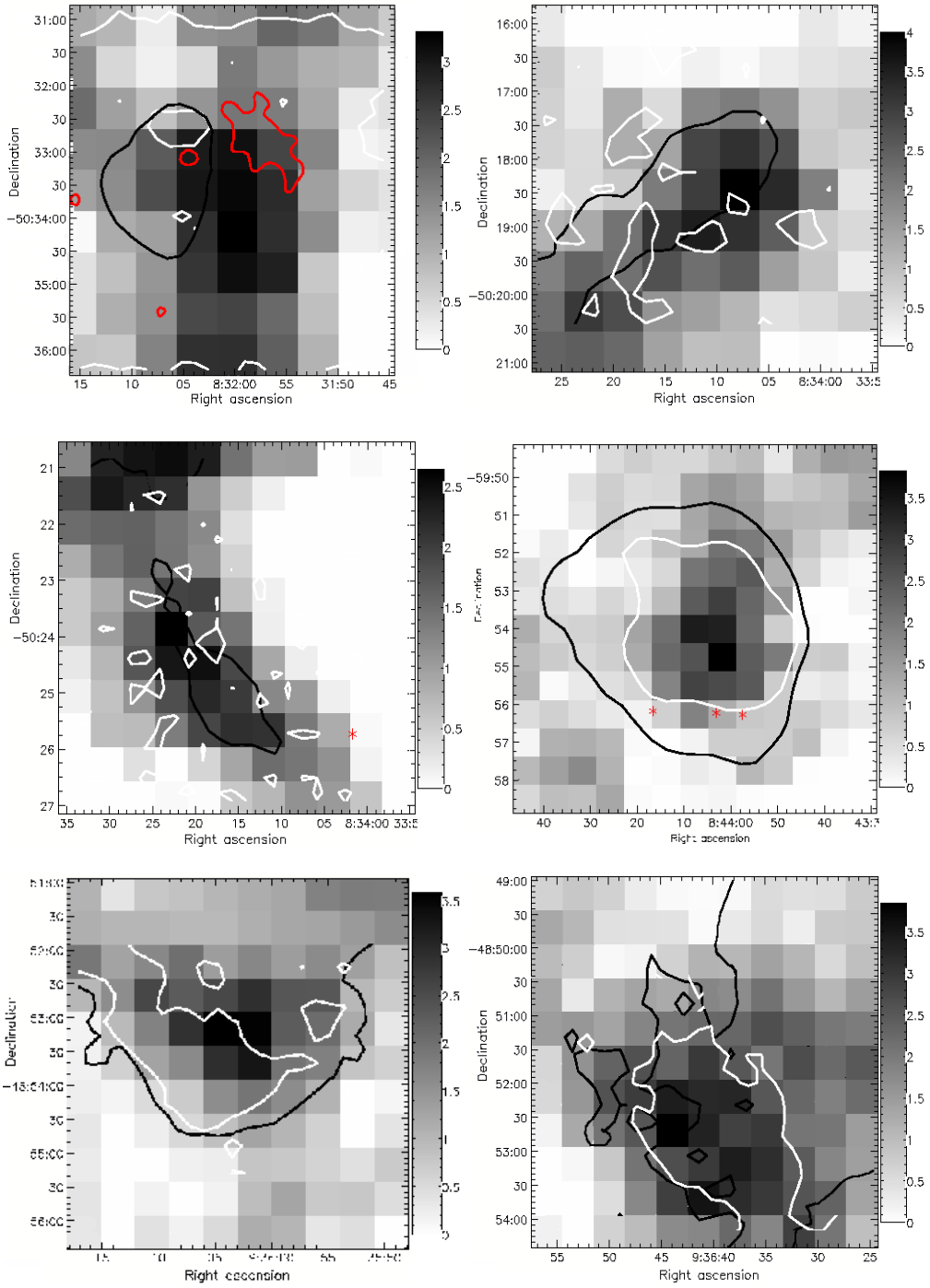

Figure 5.2: These images show the grey scale 2MASS extinction maps of cores (a)BHR40, (b)BHR38, (c)BHR39, (d)BHR56, (e)BHR48, (f)BHR49. The overplotted black contour delineates emission at 30% of the peak ^{13}CO column density, the white contour delinates emission at 30% of the peak C^{18}O column density. Where available, the 3σ SIMBA column density is also overlaid with a red contour. Also shown overlaid on the extinction maps are the positions of protostars thought to be associated with the cores. The position of each protostar is shown with a red asterisk.

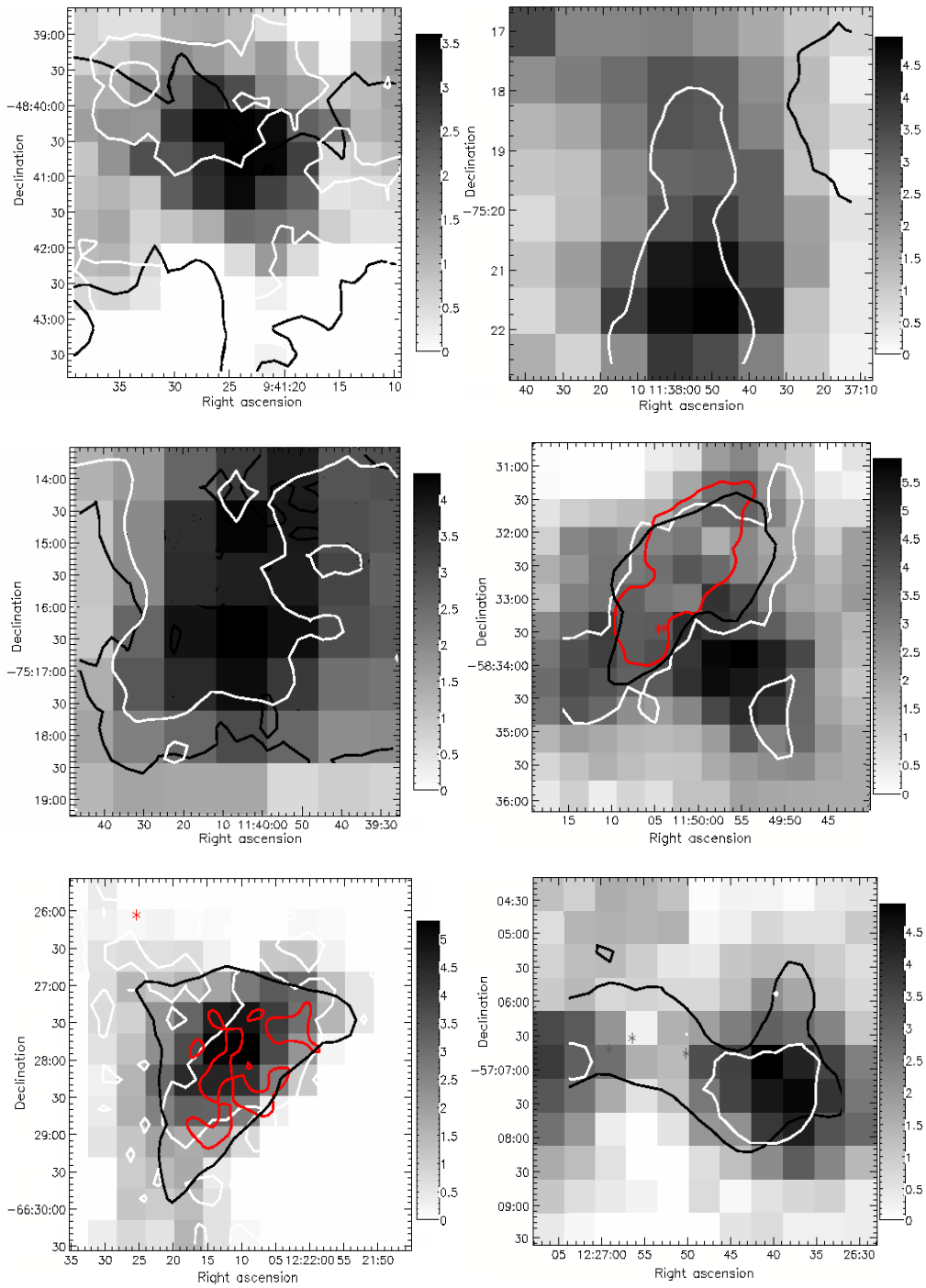

Figure 5.3: These images show the grey scale 2MASS extinction maps of cores (a)BHR50, (b)DC2983-131b, (c)DC2983-131a, (d)BHR68, (e)BHR74, (f)BHR73. The overplotted black contour delineates emission at 30% of the peak ^{13}CO column density, the white contour delinates emission at 30% of the peak C^{18}O column density. Where available, the 3σ SIMBA column density is also overlaid with a red contour. Also shown overlaid on the extinction maps are the positions of protostars thought to be associated with the cores. The position of each protostar is shown with a red asterisk.

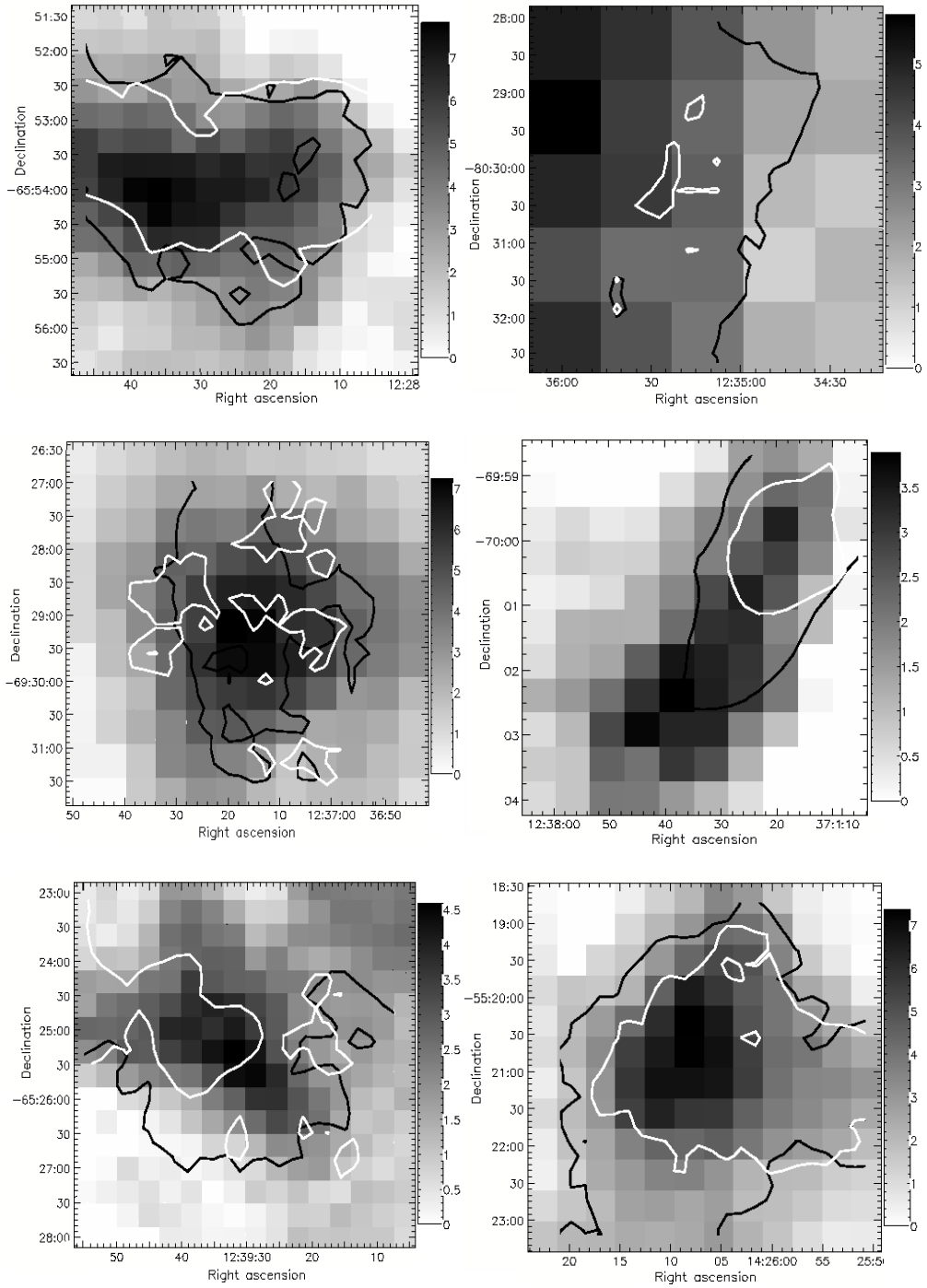

Figure 5.4: These images show the grey scale 2MASS extinction maps of cores (a)BHR76, (b)DC3023-177, (c)BHR79, (d)BHR80, (e)BHR81, (f)DC3162+51. The overplotted black contour delineates emission at 30% of the peak ^{13}CO column density, the white contour delinates emission at 30% of the peak C^{18}O column density. Where available, the 3σ SIMBA column density is also overlaid with a red contour. Also shown overlaid on the extinction maps are the positions of protostars thought to be associated with the cores. The position of each protostar is shown with a red asterisk.

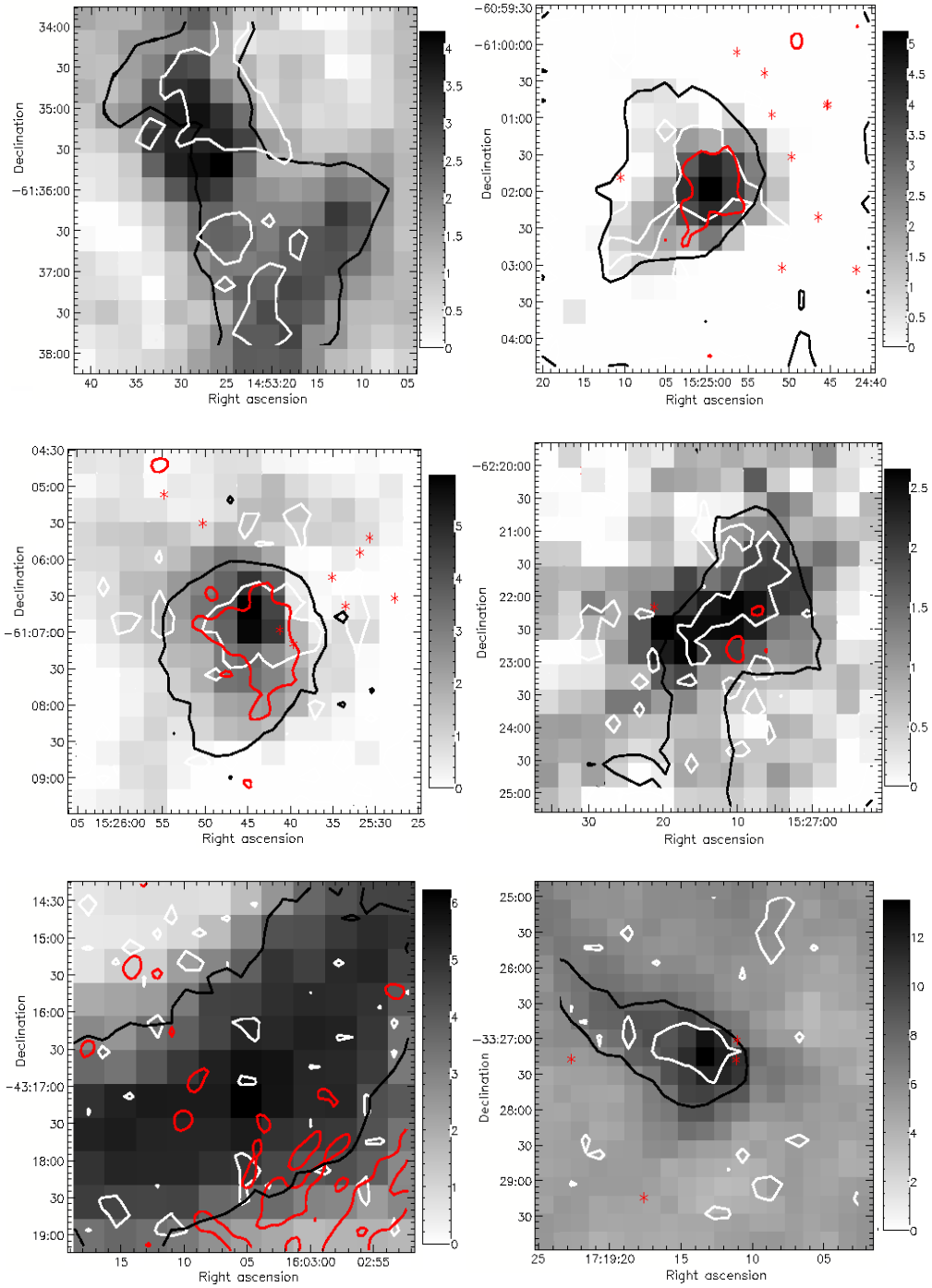

Figure 5.5: These images show the grey scale 2MASS extinction maps of cores (a)BHR95 (b)BHR99, (c)BHR100, (d)BHR97, (e)BHR119, (f)BHR159. The over-plotted black contour delineates emission at 30% of the peak ^{13}CO column density, the white contour delinates emission at 30% of the peak C^{18}O column density. Where available, the 3σ SIMBA column density is also overlaid with a red contour. Also shown overlaid on the extinction maps are the positions of protostars thought to be associated with the cores. The position of each protostar is shown with a red asterisk.

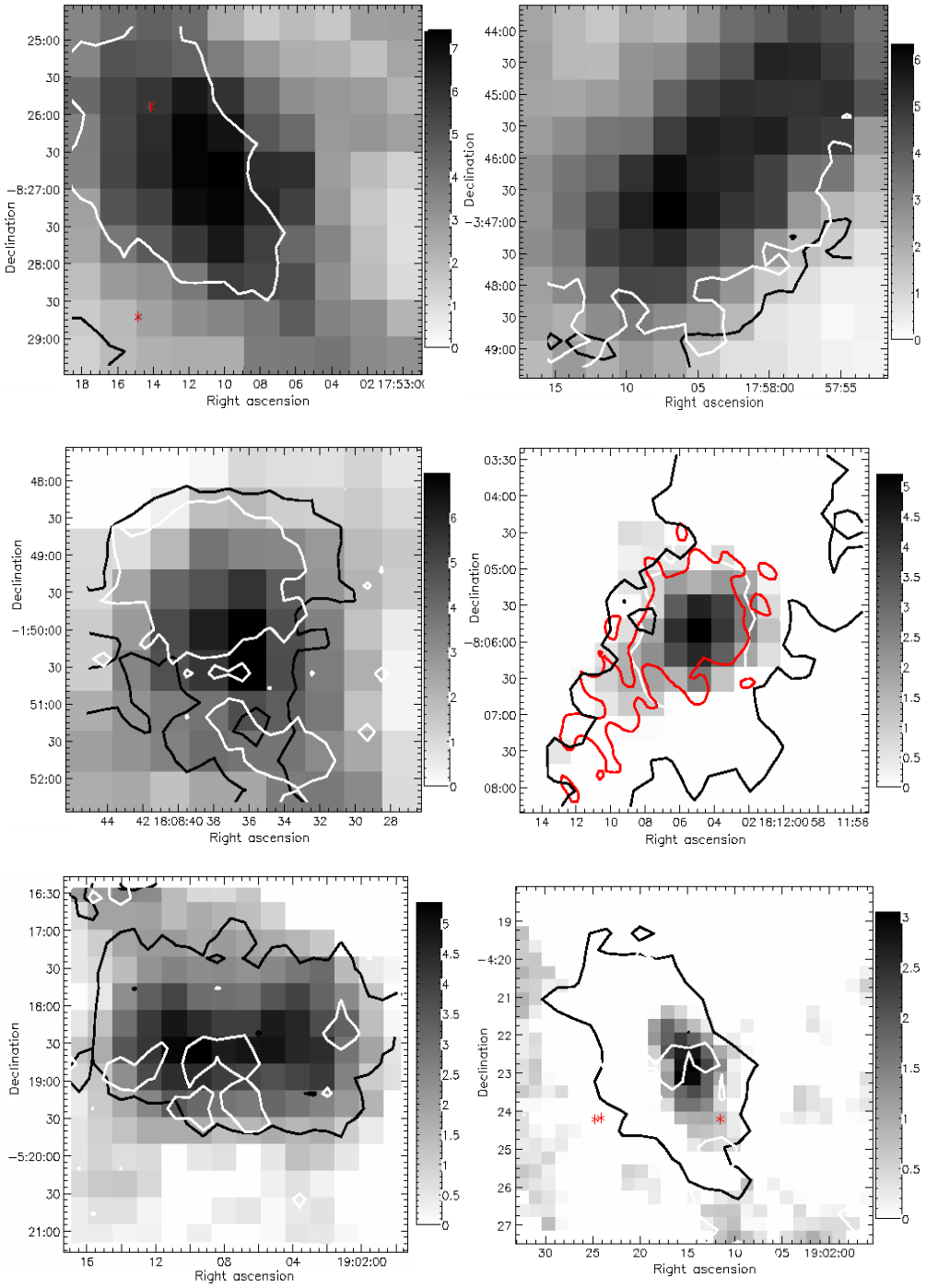

Figure 5.6: These images show the grey scale 2MASS extinction maps of cores (a)CB101, (b)CB105, (c)CB112, (d)L422, (e)CB175, (f)CB176. The overplotted black contour delineates emission at 30% of the peak ^{13}CO column density, the white contour delinates emission at 30% of the peak C^{18}O column density. Where available, the 3σ SIMBA column density is also overlaid with a red contour. Also shown overlaid on the extinction maps are the positions of protostars thought to be associated with the cores. The position of each protostar is shown with a red asterisk.

traces a smaller region than the $C^{18}O$, corresponding to the densest part of the core, where the highest 2MASS extinction is seen. This suggests that the ^{13}CO emission traces an outer layer of the cloud. The $C^{18}O$ traces a denser region of the core, while the 1.2mm dust traces the inner, densest part of the core.

Figures 5.1 - 5.6 also show the position of protostars associated with each core, listed in Table 4.4. The protostars are shown as red asterisks on the grey-scale images. Each core is classified according to its protostellar content. A core is defined as having an embedded protostar if the position of the protostar is found within the boundary of the core defined by 30% the peak ^{13}CO column density contour, as shown in Figures 5.1 - 5.6. A core is defined as having nearby protostars if a protostar is found within the 5 arcmin $\times$ 5 arcmin map. A core is classified as starless if it has neither an embedded protostar, nor any protostar within the 5 arcmin $\times$ 5 arcmin map area.

5.3 Mass Estimates

5.3.1 CO

Table 5.1 shows the average core mass derived from ^{13}CO and $C^{18}O$ observations, and the corresponding mean virial mass. The mean ^{13}CO derived core mass is slightly larger than the mean $C^{18}O$ derived core mass. This may be due to a lack of sensitivity to $C^{18}O$ in the outer regions of the core. The $C^{18}O$ core is typically smaller than the ^{13}CO core, and so has a smaller mass.

5.3.2 1.2mm Continuum

The mean core mass derived from 1.2mm dust observations for the subset of cores with 1.2mm observations are shown in Table 5.1. The average mass derived from 1.2mm continuum observations is equal to the average core mass derived from $C^{18}O$ observations, but is smaller than the core mass derived from ^{13}CO observations. The ^{13}CO traces a larger region of the cloud, and therefore, it will have a larger mass. The $C^{18}O$ is not detected in the outer parts of the cloud, so the typical $C^{18}O$ core is smaller than the ^{13}CO core, so the mass will be smaller. The 1.2mm continuum emission is sensitive to only the densest part of the cloud, similar to the $C^{18}O$ gas emission, so the mass derived from 1.2mm continuum and the mass derived from $C^{18}O$ emission is similar.

5.3.3 Gravitational Stability

The gravitational stability of the cores can be assessed by comparing the observed mass of the gas and dust to the virial mass of each core. Figure 5.7 shows the core mass derived from ^{13}CO observations plotted against the virial mass derived from ^{13}CO linewidths. Overplotted is the line of virial equilibrium, where the virial mass and observed mass are equal. Cores lying below and to the right of the line have greater observed masses than virial masses and have virial parameter $\alpha > 1$. These cores are believed to be gravitationally bound and may collapse to form stars. Cores lying above and to the left of the line of virial equilibrium, with virial parameter $\alpha < 1$ are not expected to be gravitationally bound. Figure 5.7 shows that 25/36 of the cores have $\alpha < 1$ suggesting that they are not gravitationally bound. However, when the error bars are considered, most of the cores are observed to be within 5σ of virial equilibrium.

Figure 5.8 shows the observed gas mass derived from $C^{18}O$, plotted against the virial mass. The line of virial equilibrium is overplotted. Figure 5.8 shows that 19/36 have $\alpha < 1$, suggesting that the cores are not gravitationally bound. However, when the error bars are considered, most of the cores are found to be within $\sim 5\sigma$ of virial equilibrium. This implies that most of the cores in the sample are consistent with being gravitationally bound.

The ^{13}CO emission only traces the outer shell of the core. $C^{18}O$ emission traces material in the centre of the core and provides a more accurate estimate of the core mass. A comparison of broad trends in Figures 5.7 & 5.8 shows that a larger number of cores lie below the line of virial equilibrium for the masses derived from the $C^{18}O$ observations than for the ^{13}CO. However, a core cannot have two virial masses. The discrepancy between the ^{13}CO and $C^{18}O$ derived values may be due to the fact that ^{13}Co only traces the outer shell of the core, and so only accurately describes the conditions in the outer layers of the core, whereas $C^{18}O$ traces material in the centre of the core, and therefore provides a more accurate estimate of the gravitational stability of the centre of the core where we expect star formation to occur.

This may be due to the fact that the ^{13}CO is optically thick at moderate depths in the core, and $C^{18}O$ remains optically thin to larger depths. In the case of ^{13}CO, this means that only the outer shell of the gas is observed, and the column density and mass are underestimated. The $C^{18}O$ derived gas mass will likely also be underestimated, but to a lesser extent, as it remains optically thin to larger depths into the cloud, which could account for the differences between the plots.

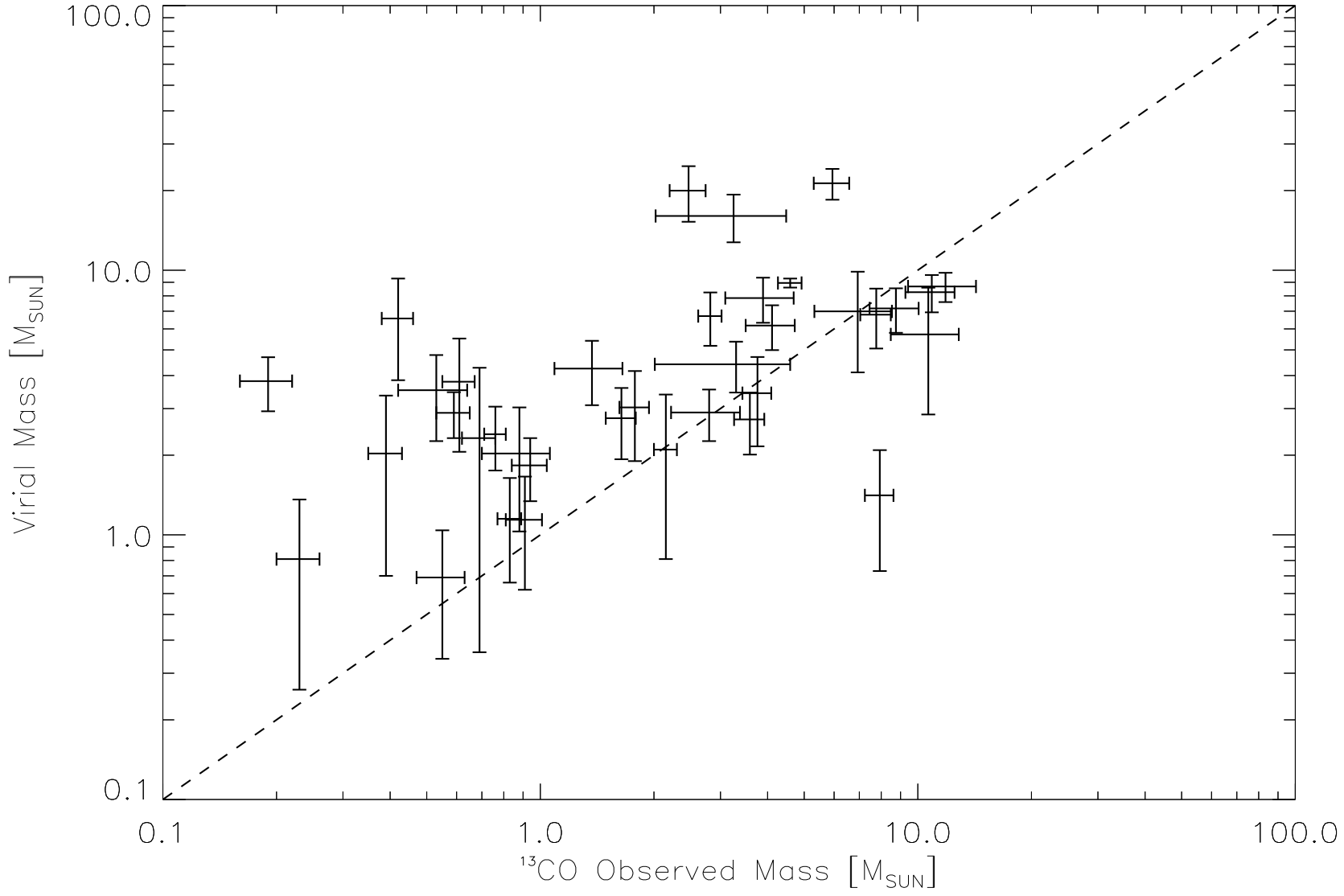

Figure 5.7: ^{13}CO derived mass versus virial mass derived from ^{13}CO linewidths. The dashed line overplotted on the data shows the 1:1 relation of virial equilibrium. Cores lying below and to the right of the line have an observed mass greater than their virial mass. These cores are gravitationally bound and may collapse to form stars. Cores lying above and to the left of the line have observed masses less than their virial masses. These cores are not expected to be gravitationally bound. However, the overplotted errors show that all cores are within $\sim 3\sigma$ of virial equilibrium.

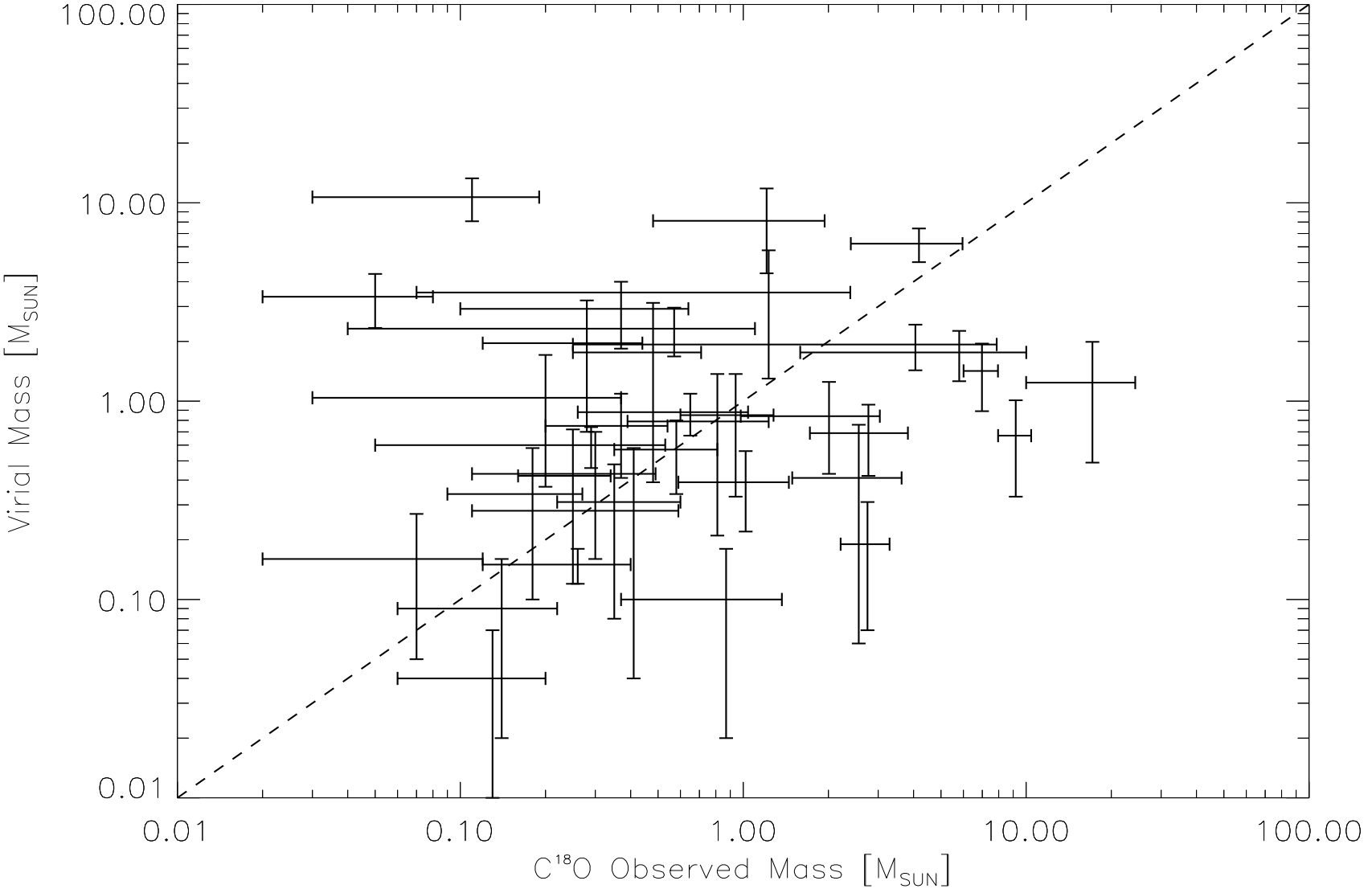

Figure 5.8: $C^{18}O$ derived mass plotted against virial mass. The dashed line overplotted on the data shows the 1:1 relation which shows virial equilibrium. Cores below and to the right of the line have observed masses greater than their virial masses. These cores are over virialised, and are expected to be gravitationally bound and may collapse to form stars. Cores above and to the left of the line have virial masses greater than their observed masses and are not expected to be gravitationally bound. However, when the errors are considered, all of the cores are seen to be within $\sim 3\sigma$ of virial equilibrium.

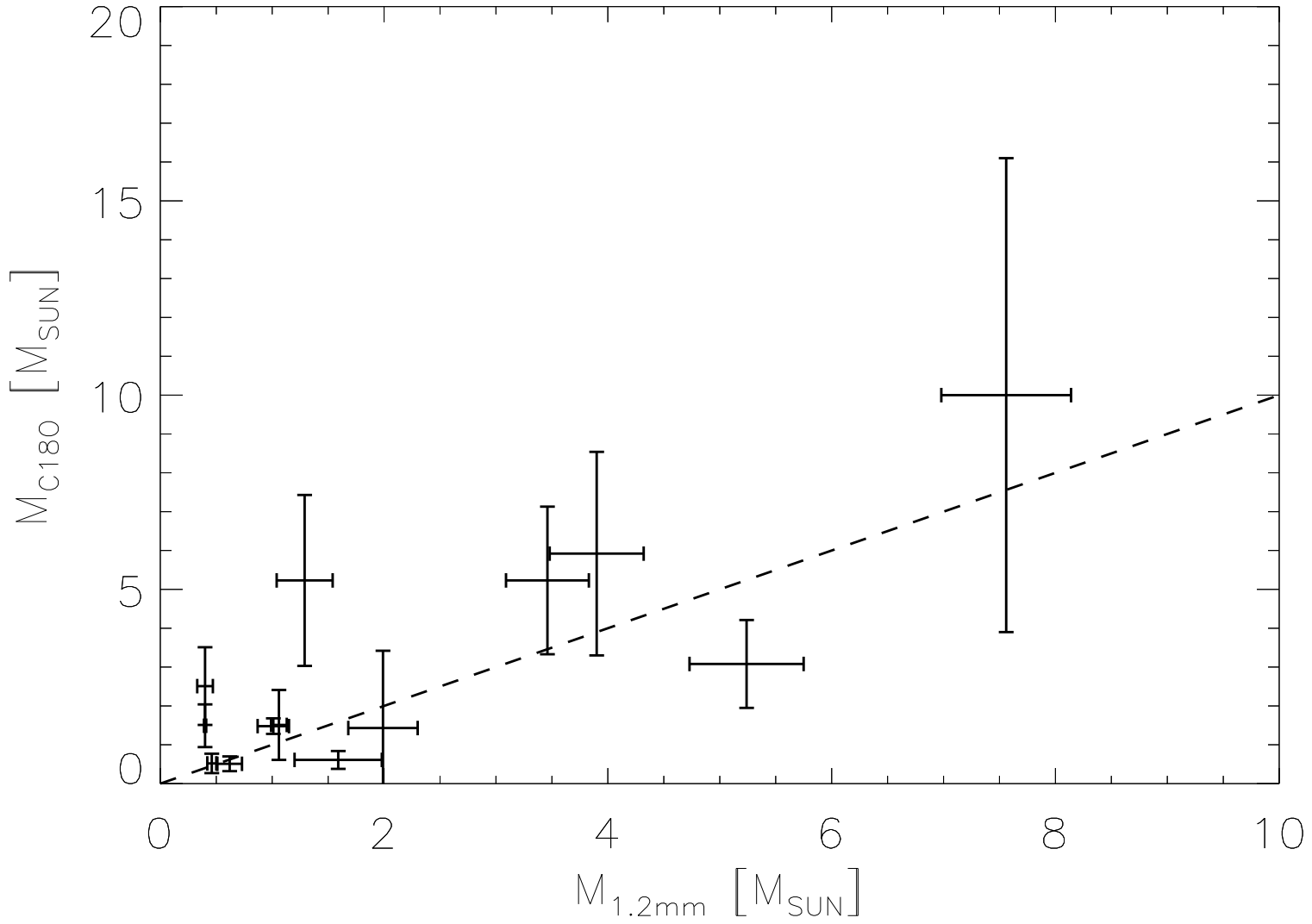

Figure 5.9: $C^{18}O$ derived mass plotted against the mass derived from 1.2mm continuum emission. The dashed line shows the 1:1 relation. Cores below and to the right of the line have $C^{18}O$ greater than the observed dust mass. Cores above and to the right of the line have a dust mass greater than the observed $C^{18}O$ gas mass. As the $C^{18}O$ gas and 1.2mm dust are expected to trace similar densities in the core, the cores should be expected to follow the 1:1 line.

Figure 5.9 shows the derived mass for the sub-sample of cores from 1.2mm continuum observations plotted against the corresponding $C^{18}O$ derived mass for the same core. The line of equal mass is overplotted. As the $C^{18}O$ gas and 1.2mm dust are likely to trace regions of similar density and so should produce similar masses, most cores should lie along this line. Figure 5.9 shows that the majority of cores lie along this line to within the 3σ errors.

Figure 5.10 shows the 1.2mm derived mass plotted against the virial mass calculated from the $C^{18}O$ linewidths, with the 1:1 relation overplotted. The $C^{18}O$ gas and 1.2mm dust are expected to trace similar volumes. Therefore, comparing the $C^{18}O$ virial mass with the 1.2mm derived mass, should be comparing like with like. Figure 5.10 shows that 10 of the 13 cores have $\alpha > 1$ and so are expected to be gravitationally bound. 2 of the remaining 3 cores are within 3σ of virialisation, which is consistent with the fact that most cores are gravitationally bound.

Using the core classifications assigned in Table 4.4, the properties of core found in different environments and star formation histories are now investigated.

5.4 Properties of Cores with Embedded Protostars

Table 5.1 shows the column density derived from ^{13}CO and $C^{18}O$ for cores with embedded protostars. The Table shows that the mean column density derived for this subsample of cores is greater than the mean column density estimates for the whole sample of cores. This suggests that protostars have so far only formed in the densest cores, and is consistent with the presence of a threshold column density, above which star formation can occur, discussed below.

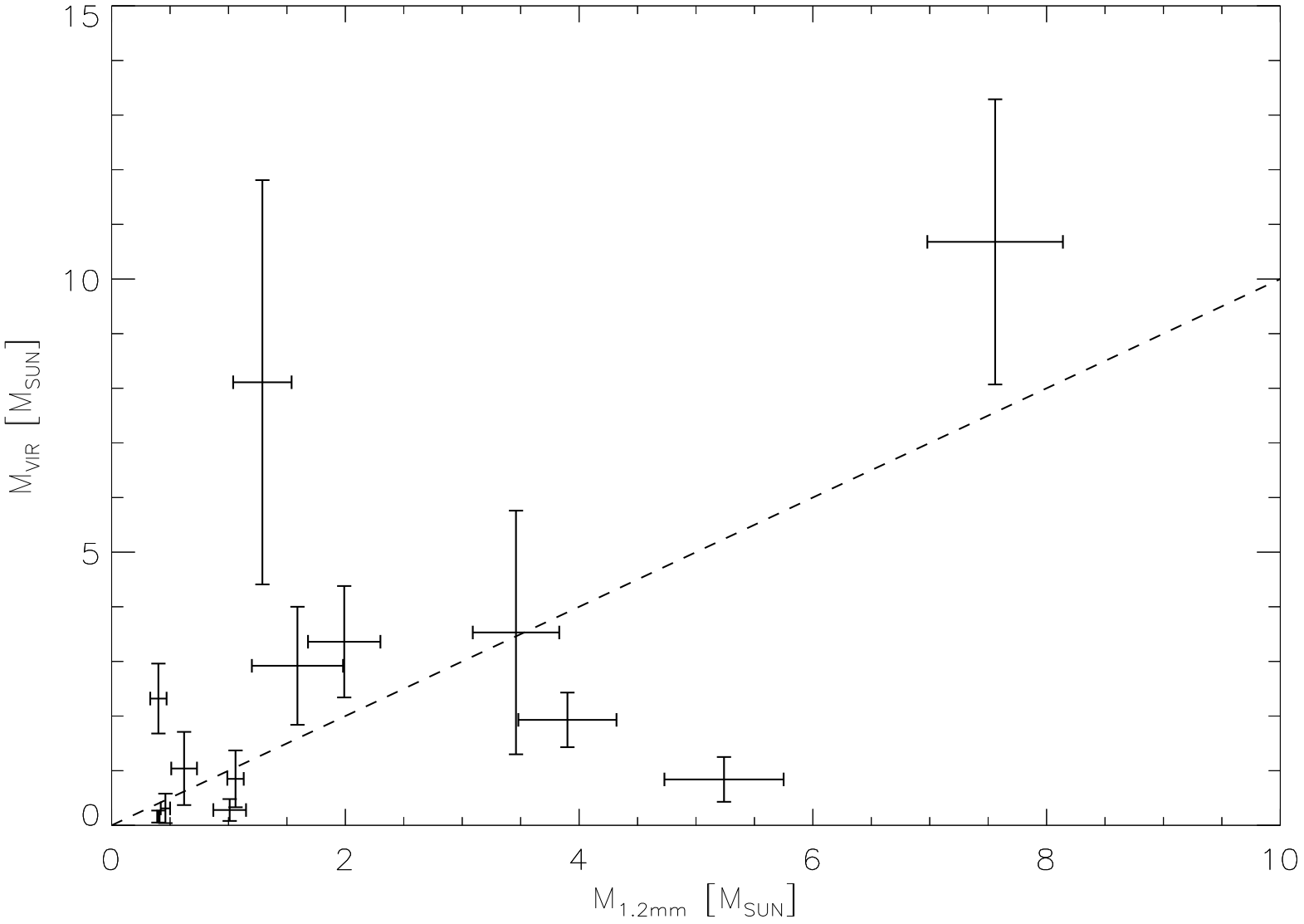

Figure 5.10: 1.2mm derived mass vs $C^{18}O$ derived virial mass

The mean core derived from ^{13}CO observations has $\alpha < 1$, meaning that, on average, the cores are not graviationally bound. The ^{13}CO derived gas mass is likely to be underestimated as the ^{13}CO gas is optically thick at moderate depths into the cloud, and as previously discussed, the ^{13}CO emission only describes the outer shell of the core, not the conditions at the centre. The mean core derived from C^{18}O has $\alpha > 1$, which suggests on average these cores are over virialised. This is consistent with gravitational collapse having occurred in the centre of the core and a protostar having formed there.

The ^{13}CO derived core mass for cores with embedded protostars is greater than the mean of the ^{13}CO derived core mass for all cores. The C^{18}O derived core mass for cores with embedded protostars is greater than the mean calculated for the whole sample of cores. The protostellar cores have a greater mean mass derived from C^{18}O observations than the starless cores, or cores with nearby protostars (see below). This suggests that the most massive cores are the cores most likely to have active star formation.

5.5 Properties of Cores with Nearby Protostars

Cores with nearby protostars give us the opportunity to investigate the effect of prior star formation on molecular cloud cores. Cores with nearby protostars are found to have a mean column density derived from ^{13}CO observations similar to the mean column density derived from ^{13}CO for the whole sample. For C^{18}O observations, the mean peak column density is lower than the mean C^{18}O derived column density calculated for the whole sample. The mean peak C^{18}O derived column density is lower for cores with nearby protostars than for starless cores (see

below). The lower column density estimates for cores with nearby protostars may be due to photodissociation of CO in low A_V regions in the outer part of the core, where there is insufficient column for the CO to be self-shielded against photons emitted from the nearby protostars.

As reported in Table 5.1, the mean ^{13}CO derived core greater than the mean mass derived for the subsample for cores with nearby protostars. The mean C^{18}O derived core has $\alpha < 1$. The mean ^{13}CO and C^{18}O derived virial masses are larger for cores with nearby protostars than the mean calculated from the whole sample of cores. This is likely due to the winds, outflows and radiation from the nearby protostars agitating the cores. This broadens the observed linewidths of the ^{13}CO and C^{18}O gas, resulting in a virial mass that is larger.

The mean observed ^{13}CO derived core mass for cores with nearby protostars is comparable to the mean calculated for the whole sample, but the C^{18}O derived core mass for cores with nearby protostars is considerably lower than the mean C^{18}O mass derived for the whole sample of cores. This is likely due to C^{18}O gas missing the outer parts of the core. The C^{18}O exists in these parts of the cores, but not in sufficient quantities to be detected.

5.6 Properties of Starless Cores

Starless cores provide the ideal location to study the gas and dust in a cloud, prior to the onset of star formation. As shown in Table 5.1, the mean column density calculated from ^{13}CO observations of the starless cores is equal to the average for the whole sample. The mean C^{18}O, derived column density is equal to the average for the whole sample.

The mean derived ^{13}CO starless core has $\alpha \sim 1$. The mean C^{18}O derived core has $\alpha > 1$. This suggests that on average, the starless cores are approximately virialised.

The mean virial masses derived from ^{13}CO and C^{18}O linewidths for starless cores are lower than the mean virial masses calculated for the whole sample. This is likely due to the quiescent nature of the cores. Starless cores do not experience agitation from nearby or embedded protostars and so the observed linewidths are narrower than cores with associated protostars, resulting in a smaller measured virial mass. This is also consistent with models of star formation invoking turbulent dissipation, as discussed below.

5.6.1 Star Formation Threshold

The idea of a column density threshold necessary for star formation was suggested by McKee (1989), who hypothesised that star formation in dense cores found in GMCs is regulated by photoionisation by the interstellar radiation field, which controls the structure of molecular clouds with active star formation. Molecular clouds undergo gravitational contraction, increasing the extinction and the star formation rate, until the cloud approaches equilibrium, when energy injected by newly formed stars supports the cloud against further contraction, and it is only in the regions of high extinction, and therefore high column density, that dense cores form, and hence stars form. In agreement with this, Johnstone, Di Francesco, & Kirk (2004) proposed that if the dominant mechanism for molecular cloud support is due to the magnetic fields of the cloud, then the timescale for ambipolar diffusion would be long in regions of high ionisation, limiting the number of dense cores forming in molecular clouds. Crutcher (1999) has shown that the typical magnetic

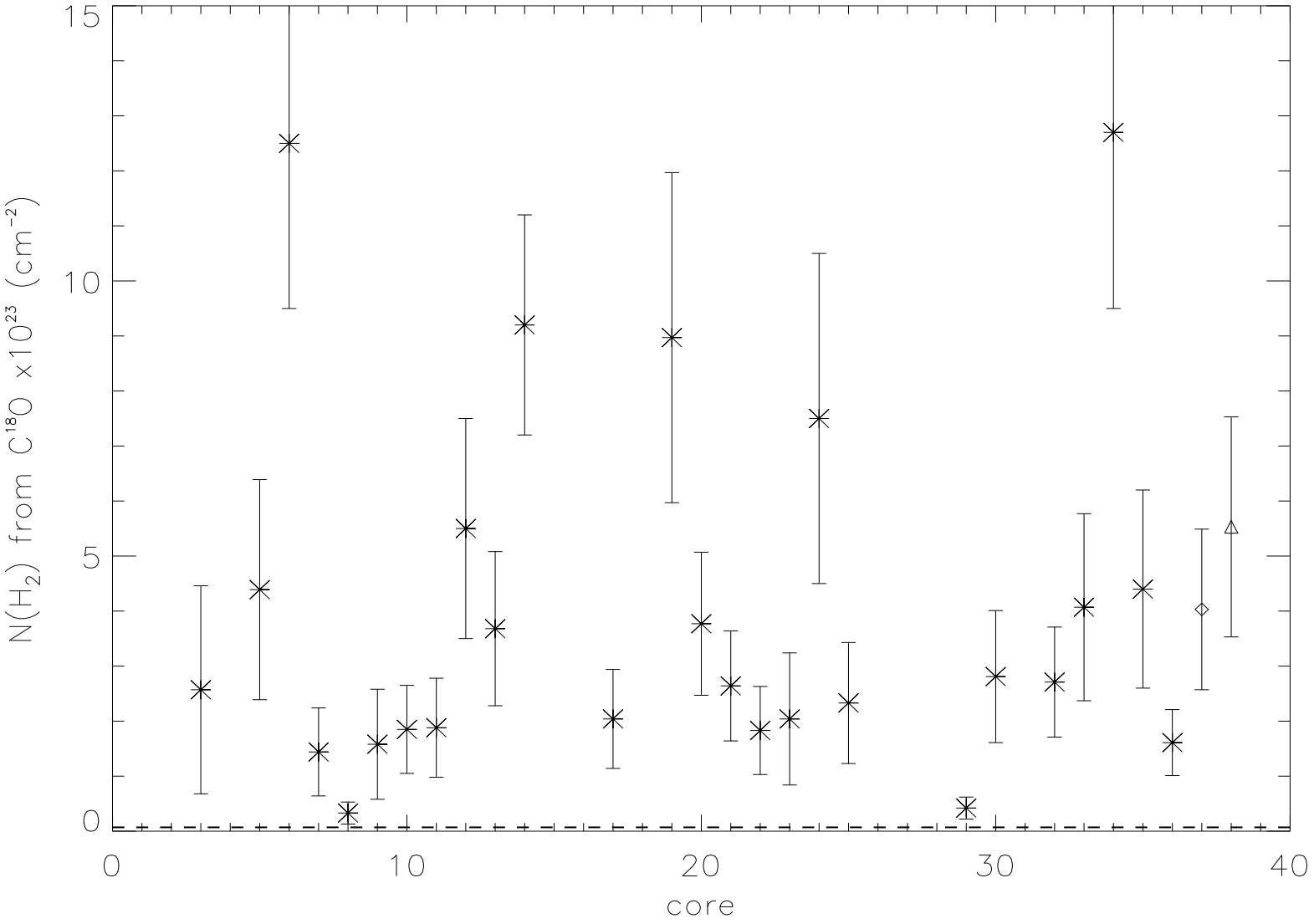

Figure 5.11: The column density derived from $C^{18}O$ for each starless core compared to the column density threshold for star formation of $N(H_2)= 7.0\times10^{21}cm^{-2}$ (André et al., 2011). The plot shows that most of the cores lie above the star formation threshold, and hence have sufficient column density to form stars. The diamond $\diamond$ represents the average column density of the starless cores, and shows that, on average, the cores have column density above the threshold value. The triangle $\triangle$ represents the average column density of the starless core sample after correction for gas freeze out is applied (Section 5.6.2).

field strength in a molecular cloud is strong enough to supply most of the required support against collapse. McKee (1989) demonstrated that in low column density regions of molecular clouds, where the extinction is $A_V < 4$, the interstellar radiation field is capable of maintaining the high ionisation fraction necessary to induce the required ambipolar diffusion to prevent collapse. Therefore, the total extinction in regions of the cloud where dense cores exist is expected to be $A_V > 8$. Johnstone et al. (2004) suggested that for Ophiuchus, star formation would only occur in regions with $A_V > 15$. This value has been updated by André et al. (2011) who calculated the column density necessary for future star formation to be $7\times10^{21}\mathrm{cm}^{-2}$, from Herschel dust observation of filaments in the Aquila Rift complex. For star formation to occur, a starless core must have column density greater than this threshold value. The column density of the starless cores can be compared to the star formation column density threshold. Figure 5.11 shows the peak H_2 column density for all starless cores, calculated from the $C^{18}O$ observations. Also plotted on Figure 5.11 is a horizontal line, corresponding to the star formation threshold. The Figure shows that all but two of the starless cores lie above the threshold. The diamond shape represents the average column density of the starless cores. This shows that on average, the cores have sufficient column density for star formation.

5.6.2 Depletion

Figure 5.12 shows the column density estimated from $C^{18}O$ observations of the cores, plotted against column density estimated from ^{13}CO emission. Overplotted is a line of gradient 5.5, which is the abundance ratio of $[^{13}CO]/[C^{18}O]= 5.5$

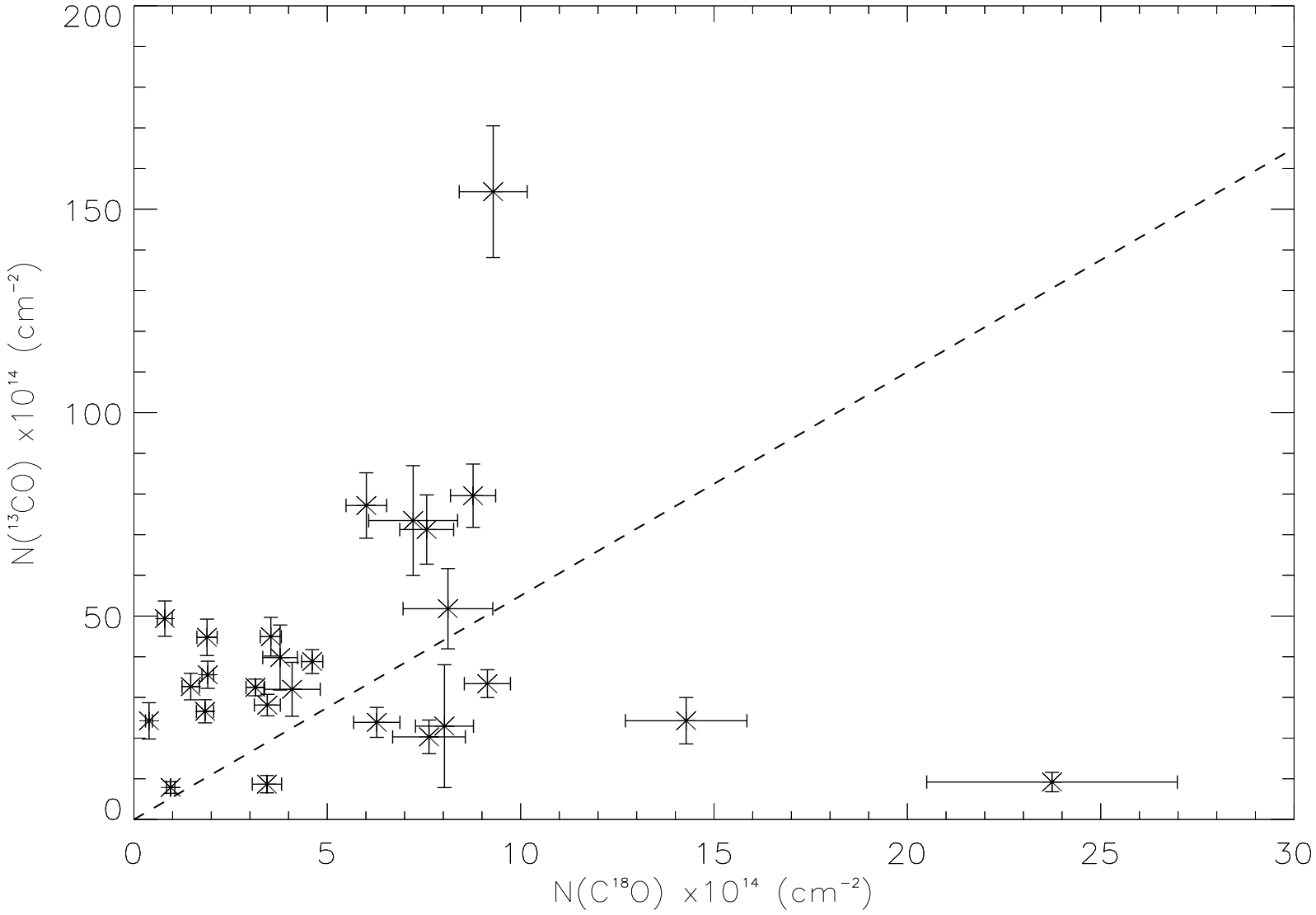

Figure 5.12: Peak $C^{18}O$ column density plotted against the peak ^{13}CO column density for starless core population.

(Frerking et al., 1982). Under the assumption that both the ^{13}CO and C^{18}O gas remains optically thin into the densest center of core, we would expect the peak column density values to lie along this line. However, as seen in Figure 5.12, a large number of cores do not follow this expectation, and lie a distance away from the line. This suggests that in the densest parts of the core, some of the gas is not being detected. This is consistent with the CO isotopes having different optical depths.

The cores detected in 1.2mm continuum offer an independent measurement of the freeze-out fraction, that is, the fraction of gas that has frozen onto dust grains, and so is removed from the gas phase and is therefore not observed by gas tracers. Figure 5.13 shows the H_2 column density derived from C^{18}O emission, plotted against H_2 column density derived from 1.2mm continuum observations. The values will lie along a line of 1:1 if the 1.2mm and C^{18}O gas trace similar regions of the cores, under the assumption that the gas remains optically thin in the densest regions of the core. However, Figure 5.13 shows that the data do not follow this expectation. This is consistent with molecules of gas freezing out onto the dust grains in the densest parts of the cores. The freeze-out fraction is estimated by calculating the gradient $\bar{R}$ of the best fit to the data from the expected fit.

$$\text{Freeze-out Fraction} = \quad (1 - \frac{1}{\bar{R}}) \times 100\%$$

$$\text{Freeze-out Fraction} = 27 \pm 16\%$$

This suggests that 58% of the gas has frozen-out onto dust grains.

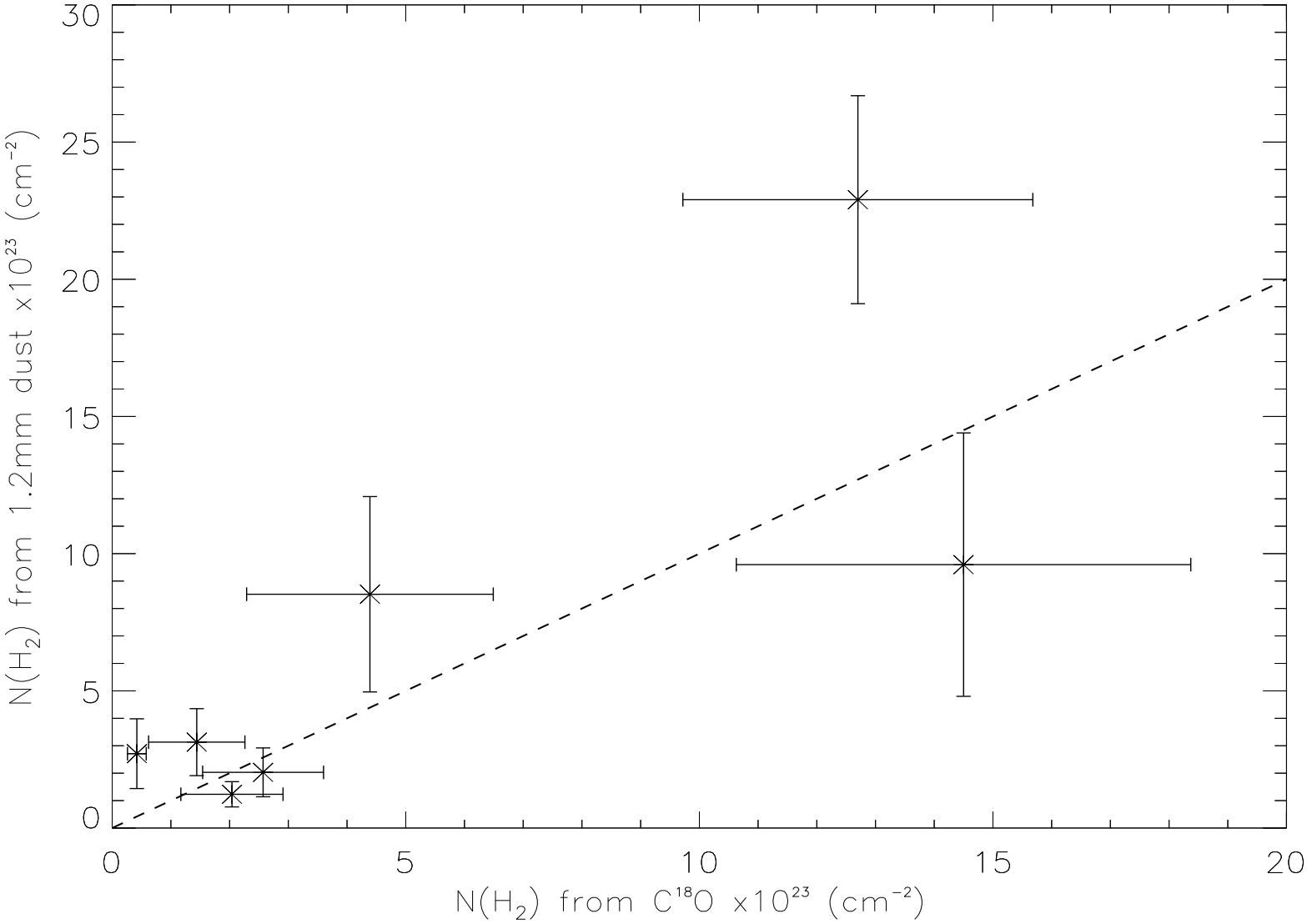

Figure 5.13: Peak H_2 column density estimates derived from $C^{18}O$ observations plotted against the peak H_2 column density from 1.2mm dust observations.

Reassessing Mean Column Density and Masses of Starless Cores

Using the freeze-out fraction calculated for the starless cores, of 27%, the average column density of the sample can be recalculated to include the "missing" gas fraction. The starless cores were determined to have an average column density of 4.06×10^{23} cm^{-2}, which was determined to be below the star formation threshold. However, by adding in the depleted fraction, the mean column density can be re-calculated to be 5.52×10^{23} cm^{-2}. This value is above the threshold of 7×10^{21} cm^{-2} proposed (e.g André et al., 2011) to be necessary for stars to form. Therefore, on average, the cores probably have a column density above the threshold for star formation.

A similar correction can be applied to the observed mass. The average mass of the starless cores is $\sim$1.8M$_\odot$. Thus the depletion corrected mass is $\sim$2.5 M$_\odot$. The average virial mass of the cores is $\sim$1.3M$_\odot$. This means that, on average, the starless cores have a gas mass greater than the virial mass. Therefore, on average, the starless cores are gravitationally bound and may collapse to form stars.

Together, these results suggest that, under the correct environmental conditions, the starless cores are expected to eventually form stars. This suggests that the observed starless cores are at an earlier evolutionary stage than the cores with embedded protostars.

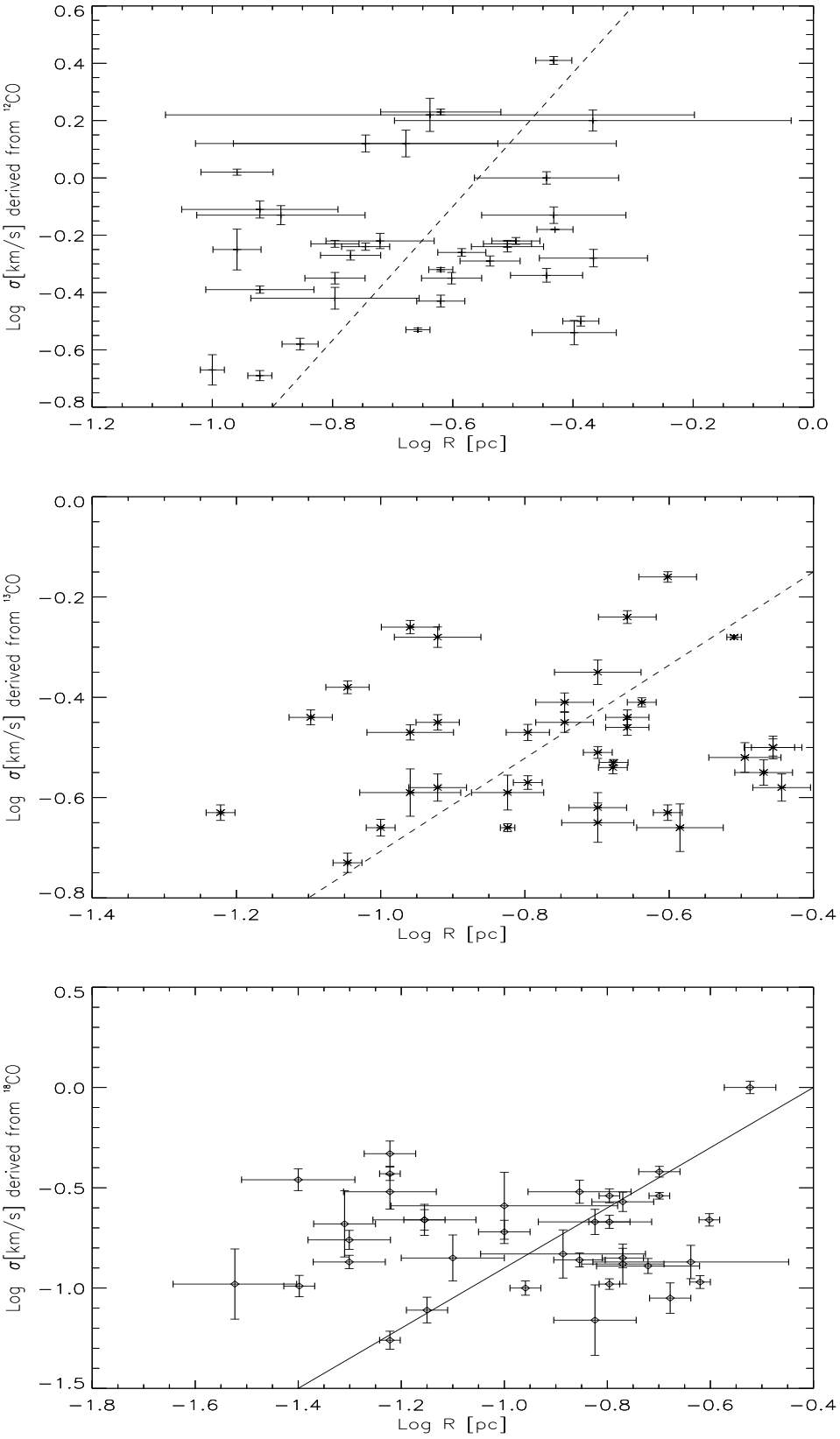

Figure 5.14: Measured velocity dispersion plotted against core radius for ^{12}CO (+), ^{13}CO ($*$) and C^{18}O ($\diamond$) core observations. The overplotted line of best fit shows the data fits the trend $\sigma \propto R^{0.45\pm0.25}$ which is in good agreement with the relation found by Solomon et al. (1987).

5.7 Scaling Relations

5.7.1 Size - Velocity Dispersion

Figure 5.14 shows the observed velocity dispersion plotted against the size of the core from ^{12}CO (+) (top panel), ^{13}CO ($*$) (middle panel) and C^{18}O ($\diamond$) emission (lower panel). An error weighted line of best fit is over plotted on the data in each case. The ^{12}CO line shows that the data is best fit with a power-law of the form:

$$\sigma \propto R^{0.33\pm0.20}.$$

The ^{13}CO fit is best represented by

$$\sigma \propto R^{0.39\pm0.19}$$

and the C^{18}O :

$$\sigma \propto R^{0.50\pm0.31}$$

This is in agreement with the Larson scaling relation which gives a power-law of the form $\sigma \propto R^{0.5}$ (Larson, 1981; Solomon et al., 1987). The plots show that smaller cores have smaller velocity dispersion than larger cores. Larson (1981) interpreted this as smaller regions having narrower non-thermal linewidths than larger regions, i.e large cores are more turbulent than smaller cores. This will be revisited in the next section.

5.7.2 Mass - Velocity Dispersion

Figure 5.15 shows the measured velocity dispersion plotted against the mass derived from ^{13}CO ($*$) and C^{18}O ($\diamond$) observations. The Figure shows that within the errors, the data follows a linear relationship. The cores with the largest masses are shown to have the largest velocity dispersion, while lower mass cores have smaller velocity dispersion. The plot shows a line of best fit overplotted on the data. The error-weighted line of best fit is represented by a power-law of the form:

$$\sigma \propto M^{0.3\pm0.16}.$$

This is in agreement with the dependence found by Larson (1981), who found a dependence of the form $\sigma \propto M^{0.2}$.

The difference in the fits may be due to the fraction of bound/unbound cores represented by this sample, compared to the Larson sample. The sample of cores presented in this work represent a range of evolutionary stages, some cores are young and unevolved and have virial parameter $\alpha < 1$. Others are observed to have embedded protostars, so must have already undergone gravitational collapse, suggesting that they have virial parameters $\alpha > 1$. Virial equilibrium is a necessary condition for Larson's relations to hold, and so cores with virial parameters $\alpha < 1$ would not be expected to follow the relation $\sigma \propto M^{0.2}$. The lower panel of Figure 5.15 shows the ^{13}CO and C^{18}O cores plotted with the clouds studies in Larson (1981). The plot shows that the CO cores and the Larson cores (represented by the square symbols $\square$) lie along the same trend line. This suggests that the relation derived is global, and may apply to cores that span a range of masses, and are found in a range of environments.

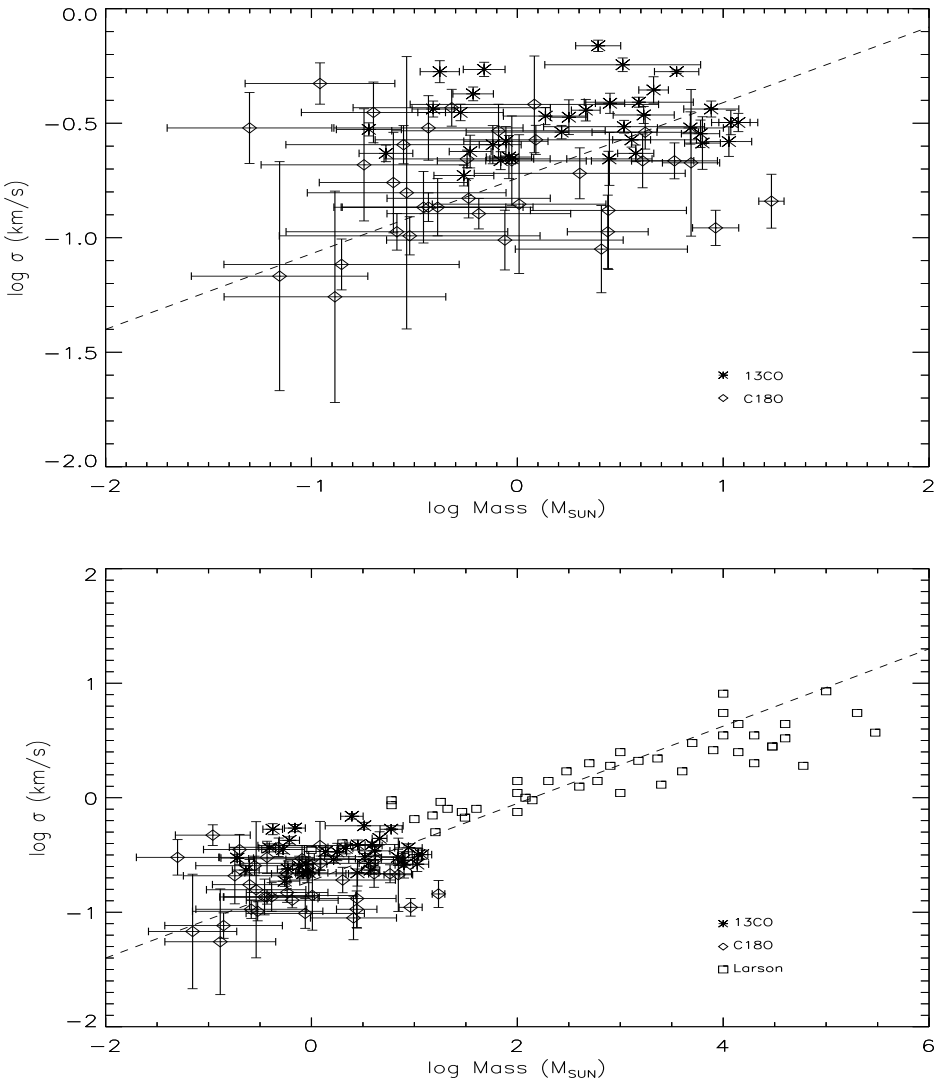

Figure 5.15: he upper plot shows the mass of core derived from ^{13}CO ($*$) and C^{18}O ($\diamond$) observations plotted against the measured velocity dispersion. The overplotted line of best fit shows the data are well represented by a power law of the form $\sigma \propto M^{0.3\pm0.16}$. This is in agreement with the relation found by Larson (1981). The lower plot shows the ^{13}CO and C^{18}O cores plotted with a sample from Larson (1981) (square symbol $\square$). The line of best fit derived from the Lonely Cores Sample is shown. The line is seen to be a reasonable fit to the Larson cores. This suggests that the relation derived here is global, and applied to large and small cores, in a range of enviroments, from complex crowded regions, to isolated cores.

5.7.3 Size - Mass

Figure 5.16 shows the radius of the core plotted against the core mass derived from ^{13}CO ($*$) and C^{18}O ($\diamond$) observations. The plot shows that cores with the largest radii have the largest masses, and cores with the smallest radii have the lowest masses. The line of best fit is shown on the Figure. The line of best fit is of the form

$$M \propto R^{1.6\pm0.5}.$$

This is in agreement with the relation proposed by Larson of $M \propto R^2$.

There is a large spread of masses associated with each radius. For example for a radius of R=0.16 pc there is a range of masses of $\sim$0.3 - 5 M$\odot$. This could be be due to the different core environments represented by the sample. It could also be due to the cores being in different evolutionary stages, some cores are in virial equilibrium, while others are undergoing gravitational contraction or collapse.

5.8 Comparison of Isotopologue Linewidths

The measured linewidths offer the opportunity to study the internal conditions of the gas in the cores. Figure 5.17 shows the measured linewidths for each core observed with each of the three isotopologues of CO. The plus (+) symbol represents the linewidth measured for the ^{12}CO emission in each core. The asterisk ($*$) symbol represents the ^{13}CO linewidth. The diamond ($\diamond$) symbol represents the C^{18}O linewidth. Each core is given an ID number in order of increasing Right Ascension. The ID number is plotted on the x-axis and the linewidths plotted on the y-axis. Also shown on the plot is a line representing the thermal linewidth for the C^{18}O emission (assuming a gas temperature of 10K). The thermal linewidth

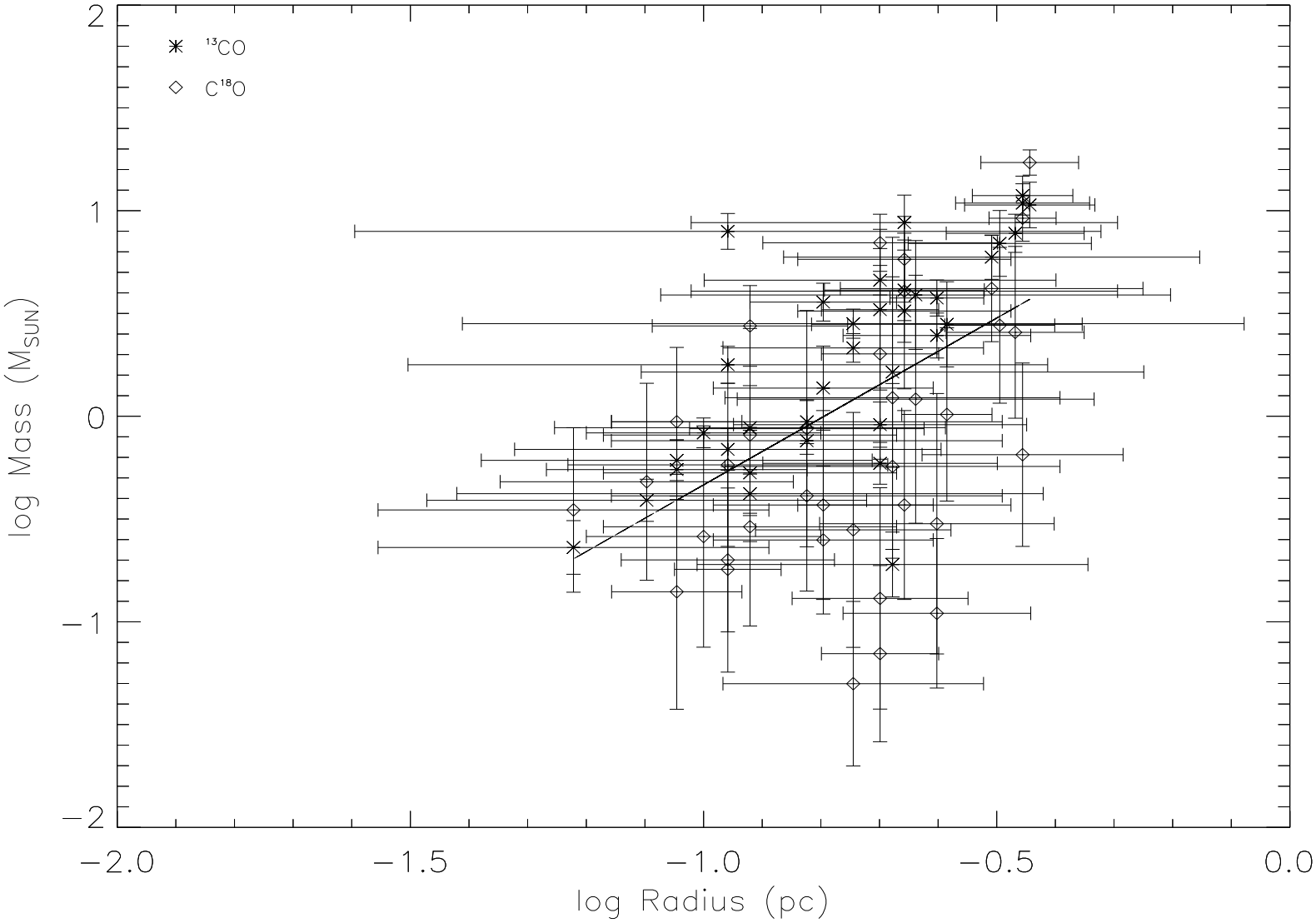

Figure 5.16: Radius plotted against mass derived from ^{13}CO ($*$) and C^{18}O ($\diamond$) observations. The overplotted line of best fit shows the trend $M \propto R^{1.6\pm0.5}$.

for $C^{18}O$ is 0.123 km/s.

The ^{12}CO is expected to trace the outer, least dense shell of the core. The ^{12}CO linewidths (+) are observed to be larger than the linewidths observed for ^{13}CO or $C^{18}O$. At a temperature of 10K, the thermal component of the ^{12}CO linewidth is 0.128 km/s in every case. The observed linewidth is much larger than 0.128 km/s. This suggests that the dominant component of the linewidth is due to non-thermal motions.

The ^{13}CO emission traces a more dense, inner shell of the core. At a temperature of 10K, the thermal component of the ^{13}CO linewidth is 0.126 km/s. The observed ^{13}CO linewidths ($*$) are all larger than 0.126 km/s, which implies that these lines are also broadened significantly by non-thermal motions in the cores. The observed ^{13}CO linewidths are narrower than the ^{12}CO linewidths. The difference in the linewidths due to thermal broadening between ^{12}CO and ^{13}CO is negligible. This suggests that the narrowing of the observed linewidths is due to a decrease in the non-thermal motions in the cores.

The $C^{18}O$ emission is expected to trace the inner, densest part of the core. At a temperature of 10K, the linewidth due to thermal broadening is 0.123 km/s. Figure 5.17 shows that a number of cores have observed $C^{18}O$ linewidths ($\diamond$) very close to this line of thermalisation, shown on the figure by the horizontal dashed line. The $C^{18}O$ linewidths are narrower than the ^{12}CO and ^{13}CO linewidths in all cases. As the difference between the thermal component of the linewidth between the three isotopologues is negligible, the narrower linewidths must be due to a decrease in non-thermal motions from ^{12}CO to ^{13}CO to $C^{18}O$. This suggests that, as the density of the tracer increases, the non-thermal motions in the core decrease, which cause narrower observed linewidths in the densest parts of the cores.

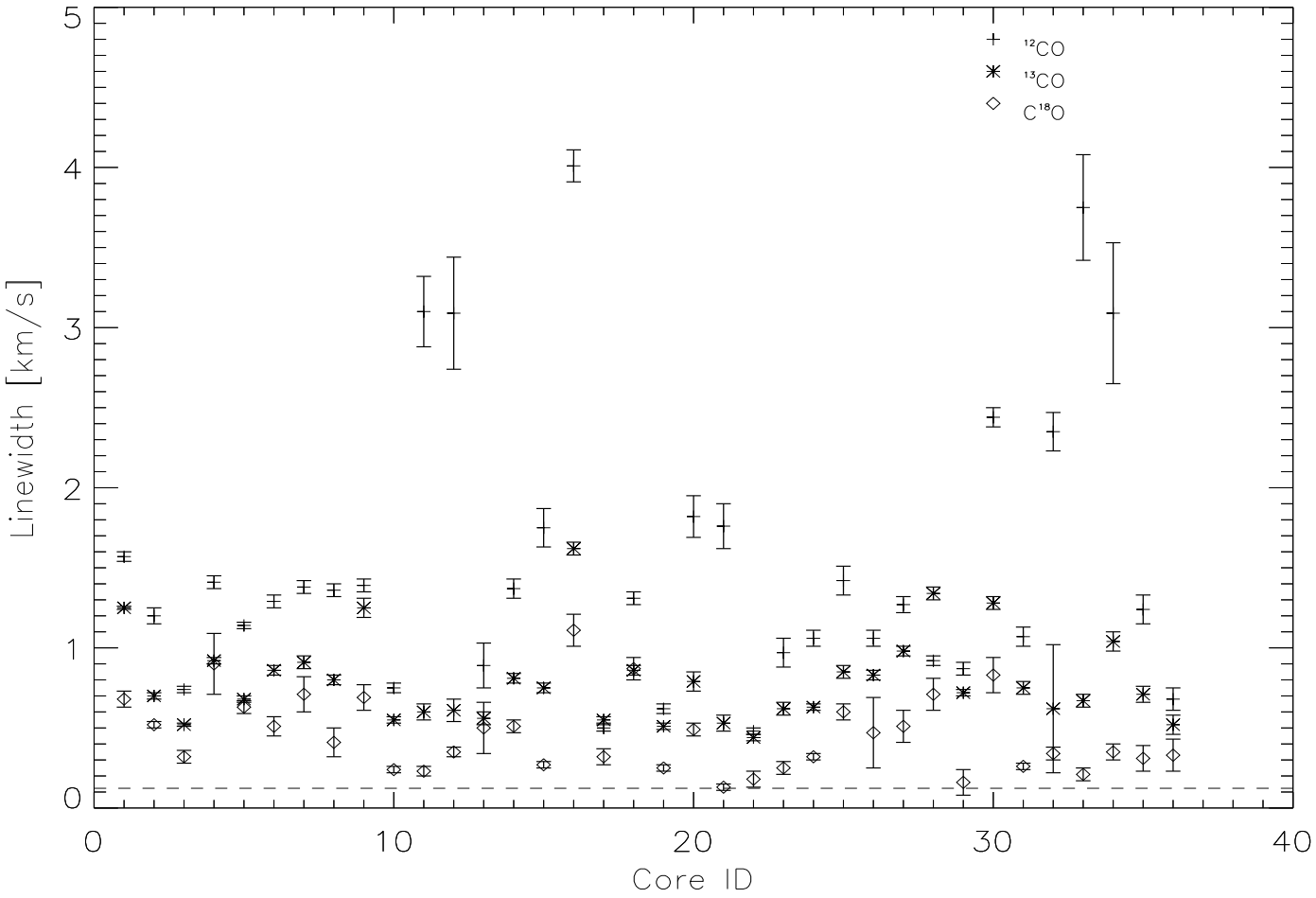

Figure 5.17: This figure shows the linewidths observed for each core with the three isotopologues of CO. The ^{12}CO linewidth is represented by the + symbol, the ^{13}CO linewidth by the $*$ symbol and the C^{18}O linewidth by the $\diamond$ symbol. The horizontal line shows the C^{18}O thermal linewidth component, assuming a gas temperature of 10K. The plot shows that the non-thermal or turbulent component dominates the total linewidth in all cases. The figure also shows that as the density of the tracer increases, the linewidth narrows.

Figure 5.18 plots the ratio of the non-thermal to total linewidth for each core. The upper panel shows the ratio of the non-thermal linewidth component to total linewidth for ^{12}CO. The Figure shows that the non-thermal component is responsible for >95% of the total linewidth. This implies that non-thermal motions in the core are the dominant component of the linewidth. The middle panel shows the ratio of non-thermal linewidth component to total linewidth for ^{13}CO. The figure shows that the non-thermal component is still the most dominant component of the total linewidths, with the non-thermal component responsible for >95% of the total linewidth. The lower panel shows the ratio of C^{18}O non-thermal linewidth component to total linewidth. The ratio is seen to be lower than in the ^{12}CO and ^{13}CO case. This suggests that in the densest part of the cores, the gas traced by the C^{18}O, the non-thermal motions in the cores are smallest.

5.9 Turbulent dissipation

As discussed in Chapter 1, a core is supported against gravitational collapse by internal motions in the core. In order for the core to collapse, the support must be eventually removed. Turbulent dissipation is one method of removing this support. Turbulence in molecular clouds is composed of "eddies" of different sizes (Kolmogorov, 1941). Large eddies are unstable and break up into smaller and smaller eddies, and the kinetic energy of the initial large eddy is divided between the smaller eddies. The smaller eddies undergo the same process, giving rise to even smaller eddies which inherit the energy from their predecessor. In this way, the energy is passed down from the large scales to smaller scales until it reaches a sufficiently small length scale such that the viscosity of the cloud can effectively radiate away the kinetic energy as thermal energy. When the kinetic energy is re-

moved, the turbulent motions of the cloud decrease, and the gravitational collapse of the cloud can proceed. It is expected that the regions that have progressed further toward the point of gravitational collapse by the dissipation of turbulence will have narrower linewidths than cores that have not dissipated turbulence.

The lower panel of Figure 5.18 is consistent with this theory. The $C^{18}O$ emission traces the densest part of the core. Every core is observed to be smaller in $C^{18}O$ than the core size traced by ^{12}CO and ^{13}CO gas. The $C^{18}O$ linewidth is observed to be narrower than ^{12}CO and ^{13}CO, and the non-thermal component of the linewidth is observed to be less dominant for $C^{18}O$. This theory can be further tested by exploring the effect the protostellar content of the core has on the observed linewidth.

In Figure 5.19 the blue points represent cores with embedded protostars, green points represent cores with nearby protostars and red points represent starless cores. As above, the ^{12}CO linewidths are shown as crosses (+), ^{13}CO linewidths are shown as asterisks ($*$) and the $C^{18}O$ linewidths are shown as diamonds ($\diamond$).

Cores with embedded protostars are observed to have the smallest difference between isotopologue linewidths. The ^{12}CO linewidth is broader than the ^{13}CO linewidth which is broader than the $C^{18}O$ linewidth. However the difference between the linewidths is small. This suggests that the turbulence has decayed in the ^{12}CO and ^{13}CO shells as well as in the dense $C^{18}O$ core at the center. This is consistent with models of star formation by turbulent dissipation, where the turbulence in the core has to decay to allow gravitational collapse to proceed and star formation to occur. The observed linewidths are larger than the thermal linewidths due to non-thermal broadening in each case as the embedded protostar agitates the remaining gas in the surrounding core.

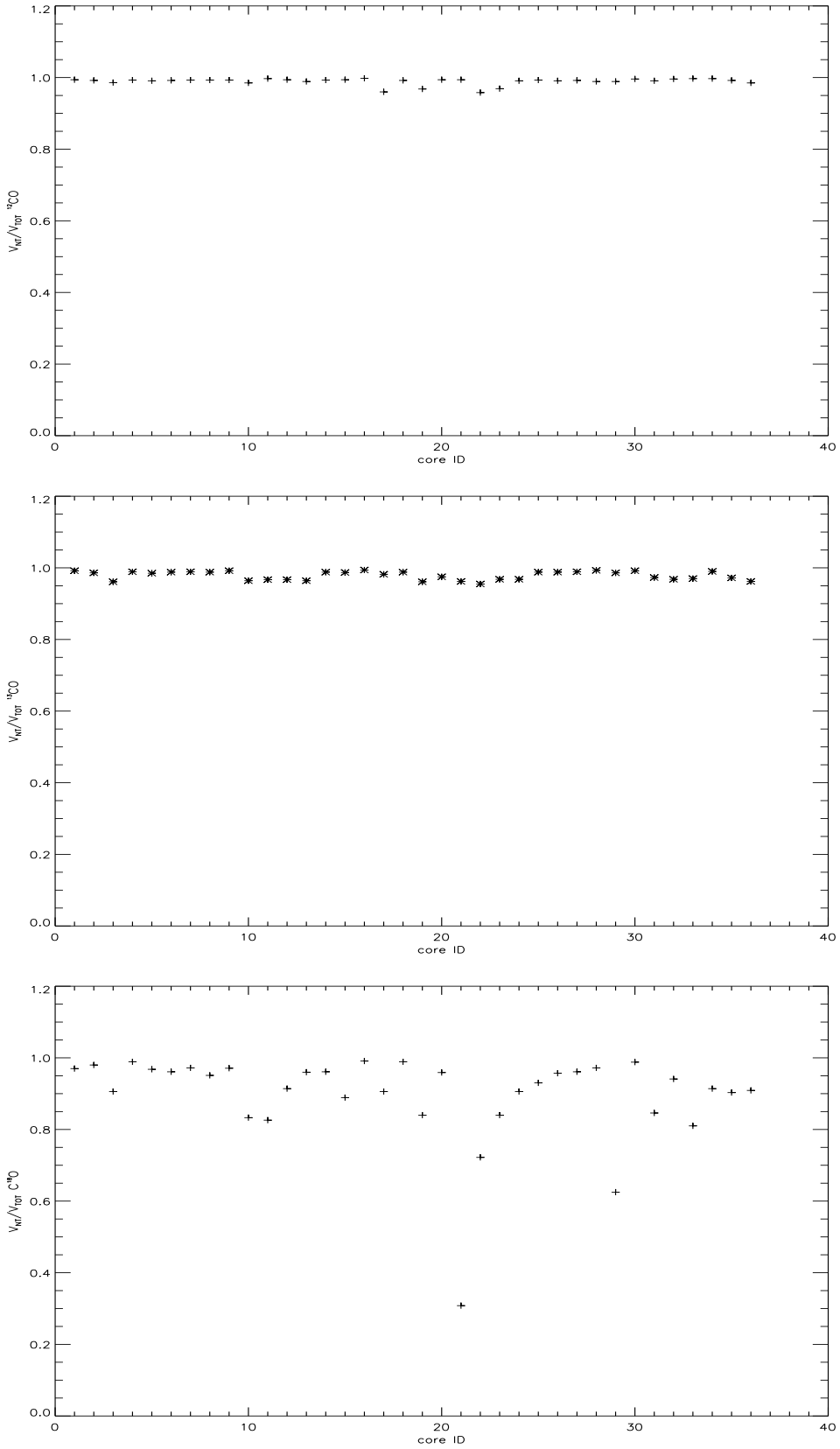

Figure 5.18: ratio of nonthermal to total line width for (a) ^{12}CO, (b) ^{13}CO and (c) C^{18}O.

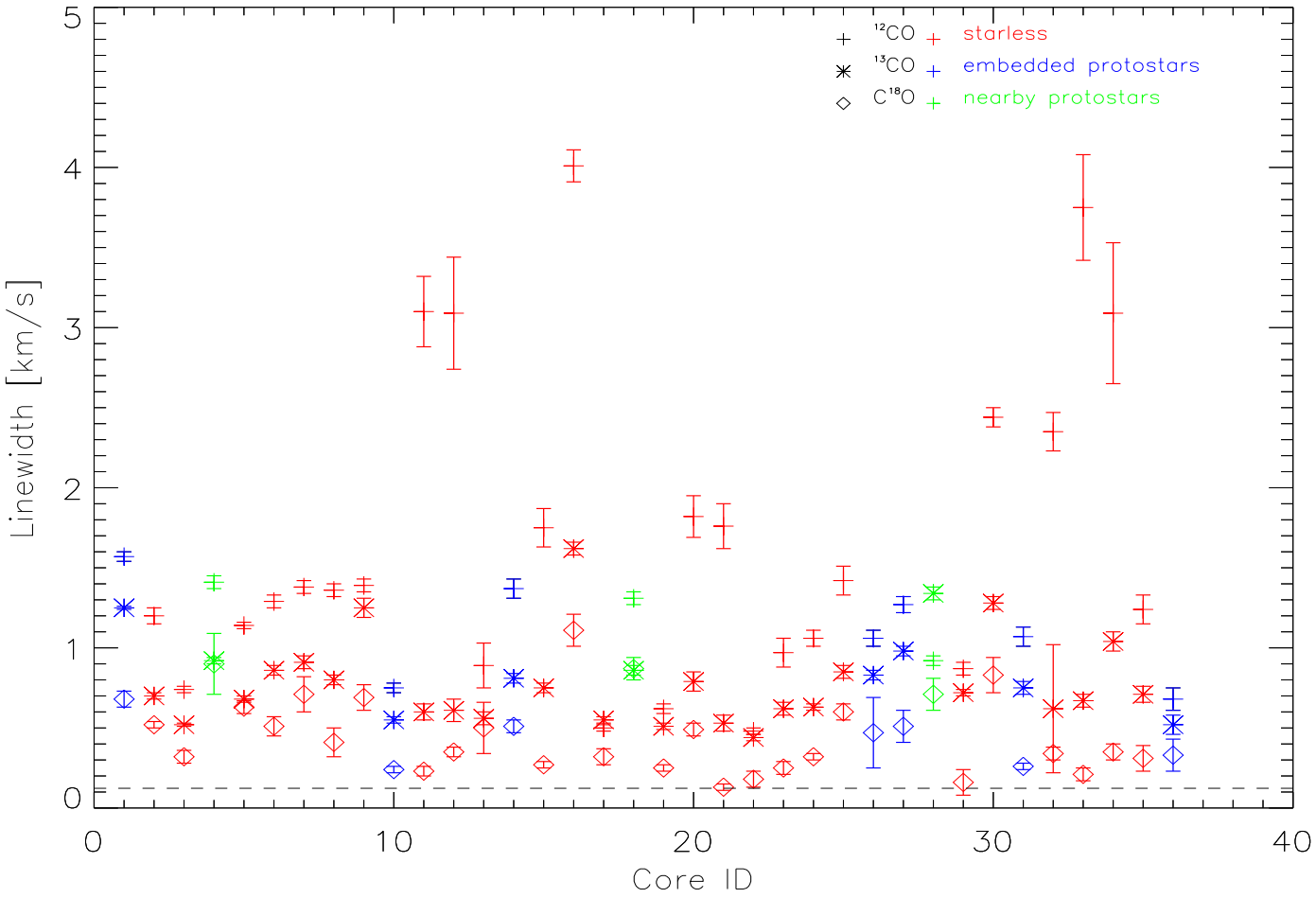

Figure 5.19: This figure shows the linewidths observed for each core with the three isotopologues of CO. The ^{12}CO linewidth is represented by the + symbol, the ^{13}CO linewidth by the $*$ symbol and the C^{18}O linewidth by the $\diamond$ symbol. The horizontal line shows the C^{18}O thermal linewidth component, assuming a gas temperature of 10K. The plot shows that the non-thermal or turbulent component dominates the total linewidth. The figure also shows that as the density of the tracer increases, the linewidth narrows.

Cores with nearby protostars have the largest $C^{18}O$ linewidths, which are observed to be very similar to the ^{13}CO linewidths of the cores. This suggests that the presence of a nearby protostar causes large non-thermal motions in the core which leads to large observed linewidths. The ^{12}CO linewidth is broader than that observed for ^{13}CO or $C^{18}O$. Due to the high optical depth, ^{12}CO effectively traces the surface of the core. Broader linewidths in the outer part of the core suggest that the presence of the nearby protostar affects the outer shell of the core more than the inner, denser parts, but all linewidths are broadened.

Starless cores are observed to have the largest ^{12}CO linewidths, this suggests that turbulence is decaying slowly in the outer layers of these cores. The ^{13}CO linewidth is observed to be lower than the ^{12}CO linewidth, and the $C^{18}O$ linewidths are seen to span a range of values. The $C^{18}O$ linewidths can be used to divide the starless cores into two groups, those with large $C^{18}O$ linewidths ($\Delta V > 0.4$km/s), and those with small $C^{18}O$ linewidths ($\Delta V < 0.4$km/s). For cores with large $C^{18}O$ linewidths, the non-thermal component of the linewidth is responsible for >80% of the total linewidth. For cores with small linewidths, the non-thermal component becomes less dominant. A number of cores have total $C^{18}O$ linewidths that are close to thermalisation, which implies that the non-thermal linewidths are very small in these cases. This is consistent with turbulent dissipation in the densest parts of the cores. We expect that these cores are more evolved than cores with larger $C^{18}O$ linewidths. Several of the cores which have small non-thermal $C^{18}O$ linewidths are observed to have broad ^{12}CO and ^{13}CO linewidths, which suggests that the dissipation of turbulence is currently limited to the inner, densest part of the core. Other cores are seen to exhibit large ^{12}CO linewidths, but small ^{13}CO and $C^{18}O$ linewidths. This implies that turbulence is decaying in the less dense, outer part as well as the central densest part of the core in each case.

5.10 Core Evolution

An evolutionary sequence is suggested by the linewidths of starless cores, under the turbulent dissipation scenario. Cores with large $C^{18}O$ linewidths can be considered to be young, as the turbulence has yet to dissipate. As this is expected to happen in less than a free-fall time (Mac Low, 1999), the cores with large $C^{18}O$ non-thermal linewidths are expected to be younger than cores with small $C^{18}O$ non-thermal linewidths, in which the turbulence has had time to decay. Cores with large ^{12}CO and ^{13}CO linewidths, but small $C^{18}O$ linewidths are slightly more evolved, as the turbulence in the densest part of the core has decayed. However, non-thermal motions in the outer part of the core remain large, which suggests the turbulence has yet to decay significantly in these parts. Cores with large ^{12}CO linewidths and smaller ^{13}CO and $C^{18}O$ linewidths represent a further evolved stage, where turbulence has decayed in the dense $C^{18}O$ core and the less dense ^{13}CO shell. Cores with small ^{12}CO, ^{13}CO and $C^{18}O$ linewidths represent a more advanced evolutionary stage, which is consistent with the turbulence decaying in all regions of the core. These cores are the most evolved of all starless cores. As the turbulence is decaying, it may reach a point where gravity can overcome the turbulent support in the core, and collapse can occur to form a protostar.

This agrees with the inside out model of star formation (Shu, Adams, & Lizano, 1987), in which the collapse of the cloud begins at the centre of the cloud, with the rest of the cloud subsequently collapsing onto the central over density.

Figure 5.20 shows the non-thermal component of the ^{12}CO linewidth plotted against the ratio of ^{12}CO to $C^{18}O$ non-thermal linewidth. Cores in the upper right-hand corner of the plot are seen to have large ^{12}CO non-thermal linewidths

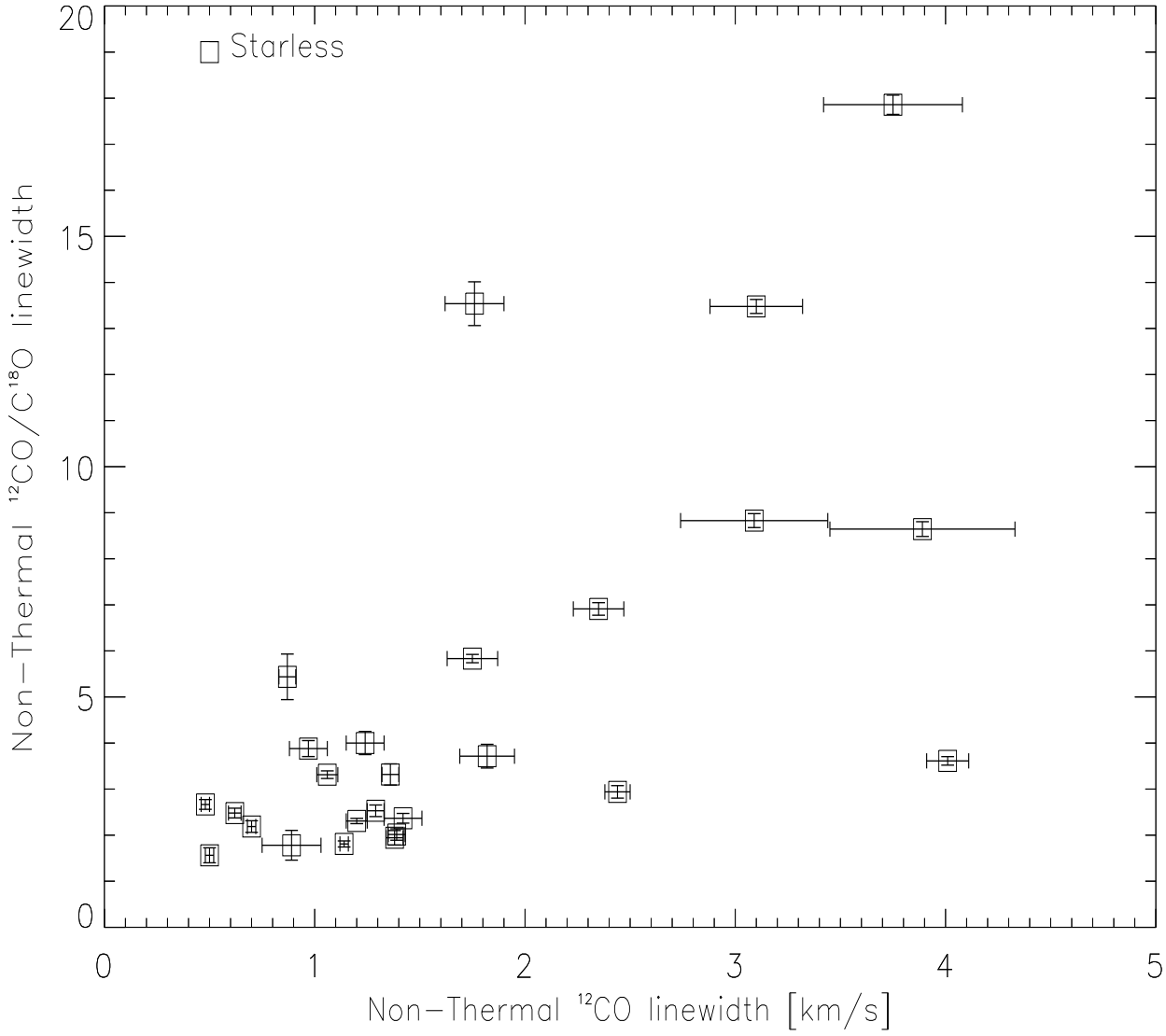

Figure 5.20: ^{12}CO linewidth plotted against ratio of ^{12}CO/C^{18}O linewidth for the starless core population. Cores in the upper right corner are expected to be younger and less evolved than cores in the lower left of the plot, as for these cores, the ^{12}CO linewidth is small, which is consistent with turbulent decay throughout the core. This suggests the plot shows an evolutionary path of starless cores, from, young, unevolved cores in the top right to older evolved cores on the lower left.

and large ^{12}CO/C^{18}O ratios. This implies that the C^{18}O nonthermal linewidths are much smaller than the ^{12}CO linewidths. This is consistent with turbulence dissipating in the central densest part of the core, but not in the outer shell of ^{12}CO. The cores that populate the lower left-hand side of the plot have low ^{12}CO non-thermal linewidths and small ^{12}CO/C^{18}O linewidth ratios. This is consistent with the turbulence decaying in the the outer shell of ^{12}CO as well as in the densest part of the core. As turbulence is expected to decay within a free fall time, we expect the cores which occupy the lower left corner of the plot to be more evolved than the cores in the upper right corner. This suggests that the inverse of the x-axis can be used as a proxy for time. The cores evolve from the right hand side, where they have small C^{18}O non-thermal linewidths and large ^{12}CO non-thermal linewidths, to the lower left-hand side, where both the ^{12}CO and C^{18}O non-thermal linewidths are small (< 1 kms^{-1}). We ignore the cores with nearby protostars since their evolutionary status is unknown.

Cores with embedded protostars are thought to be more evolved than starless cores. In these cores, the turbulence has previously decayed to the point where the gravitational force can overcome the opposing support due to non-thermal motions in the core, and the core can collapse and protostars can form. Therefore, these cores are expected to lie on the left-hand side of the plot, at the end of the proposed core evolutionary sequence. Figure 5.21 shows the starless cores plotted as above, but with linewidths from cores with embedded protostars overplotted. The Figure shows that, as expected, the cores with embedded protostars ($\diamond$) are located in the lower left corner of the plot. This supports our interpretation that the lower non-thermal linewidths are due to dissipation of turbulence in the core. We have suggested that in order for a core to collapse, the support provided by the turbulence must decay, not only in the dense core, traced by the C^{18}O gas, but also in the outer regions of the core, to allow collapse to occur. This is what

is observed for the cores with embedded protostars. The non-thermal motions are non-zero, but the turbulence does not need to decay to zero in order for collapse to occur. The support offered by the non-thermal motions decreases until eventually it is insufficient to support the core against gravitational collapse.

5.11 Summary

In this Chapter I have presented the analysis of the data described in the previous chapter, and discussed the results. I began by discussing the column density of the cores derived from ^{13}CO, C^{18}O and 1.2mm continuum measurements. From column density measures, the masses of the cores derived from ^{13}CO, C^{18}O and 1.2mm continuum were estimated. A comparison of the column density of cores with embedded protostars, cores with nearby protostars and starless cores was made. The starless cores were observed to be below the column density threshold necessary for star formation. However, when gas that has frozen out onto the dust grains was accounted for, on average, the starless cores had a column density greater than the threshold.

The linewidths of the CO isotopologues were considered. In all cases, the ^{12}CO linewidth was observed to be greater than the ^{13}CO linewidth, which is larger than the C^{18}O linewidth. The difference between thermal components of the linewidth for the isotopologues is not able to account for the difference in linewidths, and so we hypothesis, that the lower linewidths in denser regions is due to smaller non-thermal motions in the dense parts of the core. This is consistent with dissipation of turbulence inside the cores.

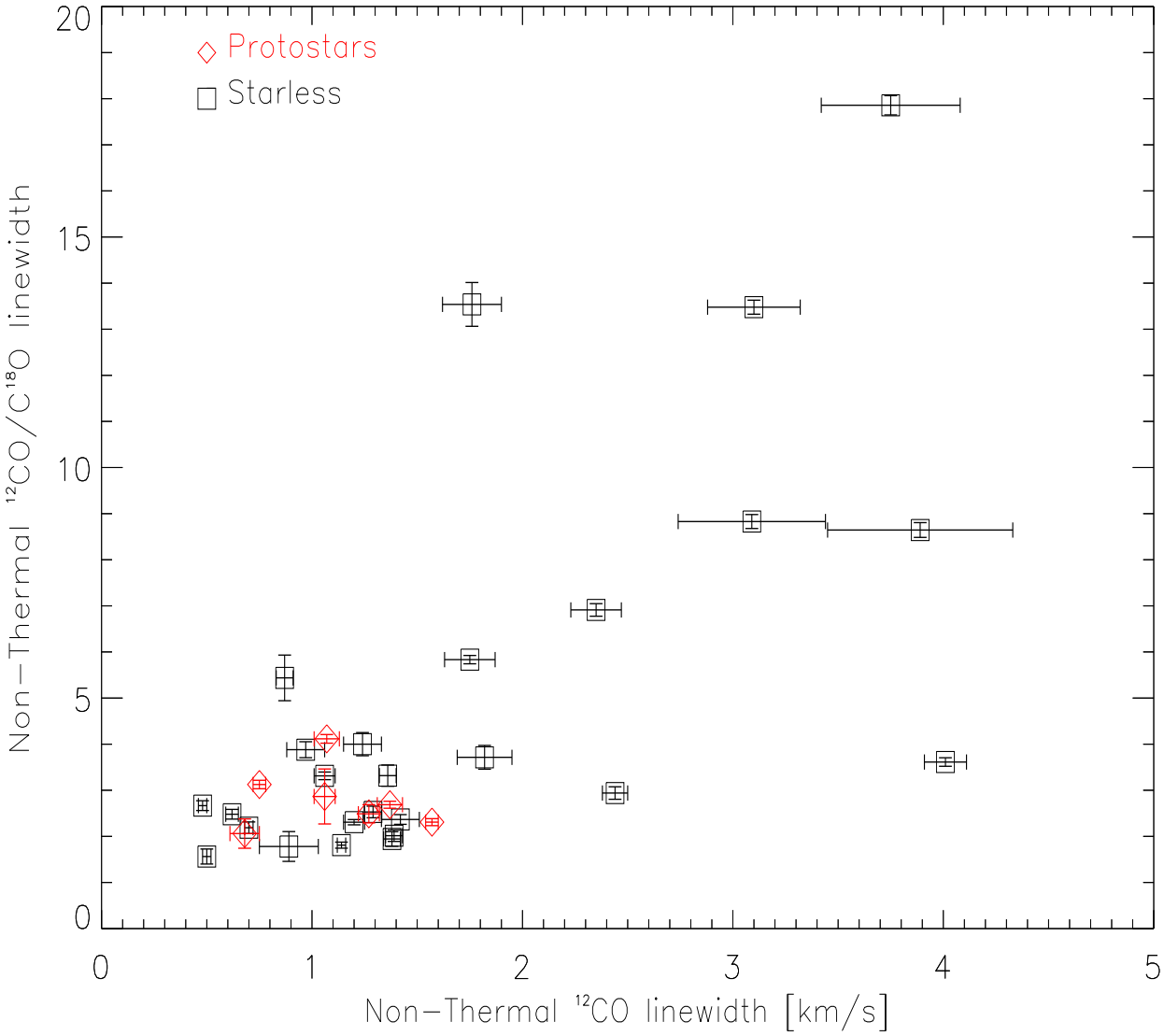

Figure 5.21: ^{12}CO linewidths plotted against ratio of ^{12}CO/C^{18}O linewidth for the entire sample of cores. The figure shows that the youngest, less evolved cores populate the upper right corner of the plot, and the more evolved cores, i.e those with embedded protostars are found in the lower left corner.

Chapter 6

Conclusions & Future Work

6.1 Conclusions

In this thesis, I have presented a multi-wavelength observational study of star formation in small, isolated molecular clouds. Star formation is a fundamental process at work in the Universe. It has implications for many other aspects of astronomy as well as being a complex field in its own right.

In Chapter 1, I discussed our current understanding of the star formation process. I outlined the necessity to study both the gas and dust content of molecular clouds. I outlined the basics of current models of cloud collapse and support. The measured physical properties of prestellar cores and protostars were also discussed. The sample of isolated cores was introduced, and the importance of observing star formation occurring in isolation as a comparison to studies of more complex, clustered regions was stated.

In Chapter 2, I reviewed the telescopes and detectors used to obtain the data in this thesis. The tools and techniques used to reduce the data were outlined in detail.

In Chapter 3, I presented the data used in the thesis, 2MASS extinction maps, J=1→0 transitions of ^{12}CO, ^{13}CO and C^{18}O integrated intensity maps and SIMBA 1.2mm intensity maps. The observed physical parameters, antenna temperature, linewidth, velocity dispersion and core semi-major and semi-minor axis were measured and presented in this chapter.

In Chapter 4, I measured the excitation temperature, optical depth, peak column density, observed mass and virial mass of each core, using the CO data. Peak column densities and masses were also calculated for the sub-sample of cores which were observed with SIMBA. The protostellar content of each core was assessed using Spitzer data, and the cores were classified as starless, cores containing an embedded protostar, or cores with nearby protostars accordingly.

In Chapter 5, I presented the analysis of the data. The results show that the location of the peak column density estimates for ^{13}CO, C^{18}O, and SIMBA observations are in good agreement with the 2MASS extinction plots. ^{13}CO is seen to trace an outer shell of the core, which corresponds to a rise in extinction on the 2MASS maps. The C^{18}O gas and 1.2mm dust estimates trace inner, denser regions of the cores.

The gravitational stability of the cores was assessed by comparing the observed ^{13}CO and C^{18}O masses with the calculated virial mass for each core. All cores were found to be approximately gravitationally bound. The C^{18}O mass was compared to the 1.2mm mass estimated from SIMBA observations. The dust mass estimates were observed to be higher than the gas estimates for a large fraction of the cores.

The properties of starless cores, cores with embedded protostars, and cores with nearby protostars were compared. The cores with embedded protostars were found to have a higher peak column density derived from C^{18}O observations than the starless cores. The masses of each population of core were compared. The cores with embedded protostars and cores with nearby protostars were seen to have a mean observed masses less than the mean virial mass. This is consistent with the protostars stirring up gas in the clouds. The starless cores had an average observed mass greater than the average virial mass, and so appeared to be gravitationally bound.

The peak column density derived from C^{18}O of the starless cores was compared to the star-formation column density threshold of 7×10^{21}cm^{-2} (André et al., 2011). The cores were found to have a peak column density lower than this, which suggests they have insufficient column density for star formation. In general, the peak ^{13}CO and C^{18}O derived column density was observed to be lower than the peak 1.2mm continuum derived column density for starless cores. This is consistent with gas molecules freezing out onto the dust grains in the densest regions of the cores, resulting in the gas mass being underestimated. The column density of the starless cores was assessed, and I estimated that $\sim$60% of the gas has frozen out onto the dust grains. When the freeze-out fraction is taken into account, the mean column density exceeded the star formation threshold.

The observed linewidths for ^{12}CO, ^{13}CO and C^{18}O were measured. The lines were observed to be broader than the line width expected due to thermal broaden-

ing. The broadening is interpreted as non-thermal motions in the gas. The ^{12}CO line is observed to be broader than the ^{13}CO linewidth, which is broader than the C^{18}O linewidth for each core. This suggests that as the density of the tracer increases, the nonthermal component of the linewidth decreases. This is consistent with models of star formation by turbulent dissipation, where the turbulent support of the cloud decays, decreasing the support against gravitational collapse, allowing star formation to begin.

A proposed evolutionary diagram is presented. Young cores are expected to have large ^{12}CO and C^{18}O nonthermal linewidth components, as the turbulence in the core has not had time to decay. As the core evolves, firstly the C^{18}O linewidth will decrease as the turbulence decays in the inner, densest part of the core. The most evolved cores, prior to the onset of collapse have small ^{12}CO and C^{18}O linewidths as the turbulence has decayed throughout the core. Therefore I hypothesise that the ^{12}CO and C^{18}O non-thermal linewidths can be used as a proxy for core evolution. This hypothesis is supported by plotting the linewidths for the starless core population and cores with embedded protostars.

6.2 Future Work

In future studies, it will be possible to combine data from the HARP and SCUBA-2 Gould Belt Survey, with data from the Herschel Gould Belt Survey. This multi-wavelength survey will enable one to explore the properties of cores more crowded regions for comparison with the study presented here. It will then be possible to fully explore the effect of environment on the star formation process. The combination of HARP, SCUBA-2 and Herschel Gould Belt data will form an equivalent data set to the data I already possess for the isolated cores and will allow a compar-

ison of the core properties between isolated and non-isolated regions. For example the multiplicity statistics of isolated cores compared to cores in more crowded regions could be studied.

Follow-up study of these cores will require very high resolution, which can only be achieved with a highly sensitive, high precision instrument like ALMA. An ALMA proposal to map the isolated cores to identify the number of protostars forming per core would be a logical follow up to this thesis.

Bibliography

Alves J. F., Lada C. J., Lada E. A., Internal structure of a cold dark molecular cloud inferred from the extinction of background starlight, 2001, Nature, 409, 159

Anderson L. D., Bania T. M., Jackson J. M., Clemens D. P., Heyer M., Simon R., Shah R. Y., Rathborne J. M., The Molecular Properties of Galactic H II Regions, 2009, ApJS, 181, 255

André P., Men'shchikov A., Könyves V., Arzoumanian D., 2011, in EAS Publications Series, Vol. 52, Röllig M., Simon R., Ossenkopf V., Stutzki J., ed, EAS Publications Series, p. 167

Andre P., Montmerle T., From T Tauri stars to protostars: Circumstellar material and young stellar objects in the rho Ophiuchi cloud, 1994, ApJ, 420, 837

Andre P., Ward-Thompson D., Barsony M., Submillimeter continuum observations of Rho Ophiuchi A - The candidate protostar VLA 1623 and prestellar clumps, 1993, ApJ, 406, 122

Andre P., Ward-Thompson D., Barsony M., From Prestellar Cores to Protostars: the Initial Conditions of Star Formation, 2000, Protostars and Planets IV, 59

Andre P., Ward-Thompson D., Motte F., Probing the initial conditions of star formation: the structure of the prestellar core L 1689B., 1996, A&A, 314, 625

Appenzeller I., Mundt R., T Tauri stars, 1989, A&A Rev., 1, 291

Arendt R. G., Odegard N., Weiland J. L., Sodroski T. J., Hauser M. G., Dwek E., Kelsall T., Moseley S. H., Silverberg R. F., Leisawitz D., Mitchell K., Reach W. T., Wright E. L., The COBE Diffuse Infrared Background Experiment Search for the Cosmic Infrared Background. III. Separation of Galactic Emission from the Infrared Sky Brightness, 1998, ApJ, 508, 74

Bacmann A., André P., Puget J.-L., Abergel A., Bontemps S., Ward-Thompson D., An ISOCAM absorption survey of the structure of pre-stellar cloud cores, 2000, A&A, 361, 555

Bally J., Langer W. D., Isotope-selective photodestruction of carbon monoxide, 1982, ApJ, 255, 143

Barnes D. G. et al., The Hi Parkes All Sky Survey: southern observations, calibration and robust imaging, 2001, MNRAS, 322, 486

Beichman C. A., Myers P. C., Emerson J. P., Harris S., Mathieu R., Benson P. J., Jennings R. E., Candidate solar-type protostars in nearby molecular cloud cores, 1986, ApJ, 307, 337

Bernstein R. A., Freedman W. L., Madore B. F., The First Detections of the Extragalactic Background Light at 3000, 5500, and 8000 Å. III. Cosmological Implications, 2002, ApJ, 571, 107

Bok B. J., Reilly E. F., Small Dark Nebulae., 1947, ApJ, 105, 255

Booth R. S., Delgado G., Hagstrom M., Johansson L. E. B., Murphy D. C., Olberg M., Whyborn N. D., Greve A., Hansson B., Lindstrom C. O., Rydberg A., The Swedish-ESO Submillimetre Telescope (SEST), 1989, A&A, 216, 315

Bourke T., di Francesco J., Dunham M., Gutermuth R., Hatchell J., Huard T., Jorgensen J., Kauffmann J., Kirk J., Lee J.-E., Myers P., Peterson D., Stutz A., Ward-Thompson D., Lonely Cores: Star Formation in Isolation, 2008, Spitzer Proposal, 50477

Bourke T. L., Hyland A. R., Robinson G., James S. D., Wright C. M., Studies of star formation in isolated small dark clouds - II. A southern ammonia survey, 1995, MNRAS, 276, 1067

Buckle J. V. et al., The JCMT Legacy Survey of the Gould Belt: a first look at Orion B with HARP, 2010, MNRAS, 401, 204

Burrus C. A., Stark Effect from 1.1 to 2.6 Millimeters Wavelegnth: PH3, PD3, DI and CO., 1958, Journal of Physical and Chemical Reference Data, 28, 427

Cardelli J. A., Clayton G. C., Mathis J. S., The relationship between infrared, optical, and ultraviolet extinction, 1989, ApJ, 345, 245

Cieza L., Padgett D. L., Stapelfeldt K. R., Augereau J.-C., Harvey P., Evans N. J., II, Merín B., Koerner D., Sargent A., van Dishoeck E. F., Allen L., Blake G., Brooke T., Chapman N., Huard T., Lai S.-P., Mundy L., Myers P. C., Spiesman W., Wahhaj Z., The Spitzer c2d Survey of Weak-Line T Tauri Stars. II. New Constraints on the Timescale for Planet Building, 2007, ApJ, 667, 308

Clemens D. P., Barvainis R., A catalog of small, optically selected molecular clouds - Optical, infrared, and millimeter properties, 1988, ApJS, 68, 257

Cohen J. G., Persson S. E., Elias J. H., Frogel J. A., Bolometric luminosities and infrared properties of carbon stars in the Magellanic Clouds and the Galaxy, 1981, ApJ, 249, 481

Cohen S. A., Molecular hydrogen formation on interstellar dust grains, 1976, Nature, 261, 215

Combes F., Distribution of CO in the Milky Way, 1991, ARA&A, 29, 195

Crutcher R. M., Magnetic Fields in Molecular Clouds: Observations Confront Theory, 1999, ApJ, 520, 706

Dame T. M., Ungerechts H., Cohen R. S., de Geus E. J., Grenier I. A., May J., Murphy D. C., Nyman L.-A., Thaddeus P., A composite CO survey of the entire Milky Way, 1987, ApJ, 322, 706

Deiss B. M., Just A., Kegel W. H., Fluctuations of the interstellar medium induced by the stellar system - Mechanical heating and dynamical friction, 1990, A&A, 240, 123

di Francesco J., Evans N. J., II, Caselli P., Myers P. C., Shirley Y., Aikawa Y., Tafalla M., An Observational Perspective of Low-Mass Dense Cores I: Internal Physical and Chemical Properties, 2007, Protostars and Planets V, 17

Djorgovski S., A preliminary optical study of the intergalactic H I cloud in Virgo, 1990, AJ, 99, 31

Draine B. T., Interstellar Dust Grains, 2003, ARA&A, 41, 241

Emerson D., 1996, Interpreting Astronomical Spectra

Evans N. J., Dunham M. M., Jorgensen J. K., Enoch M. L., Merin B., van Dishoeck E. F., Alcala J. M., Myers P. C., Stapelfeldt K. R., Huard T. L., Allen L. E., Harvey P. M., van Kempen T., Blake G. A., Koerner D. W., Mundy L. G., Padgett D. L., Sargent A. I., Properties of Spitzer c2d dark clouds (Evans+, 2009), 2009, VizieR Online Data Catalog, 218, 10321

Evans N. J., II, Allen L. E., Blake G. A., Boogert A. C. A., Bourke T., Harvey P. M., Kessler J. E., Koerner D. W., Lee C. W., Mundy L. G., Myers P. C., Padgett D. L., Pontoppidan K., Sargent A. I., Stapelfeldt K. R., van Dishoeck E. F., Young C. H., Young K. E., From Molecular Cores to Planet-forming Disks: An SIRTF Legacy Program, 2003, PASP, 115, 965

Evans N. J., II, Rawlings J. M. C., Shirley Y. L., Mundy L. G., Tracing the Mass during Low-Mass Star Formation. II. Modeling the Submillimeter Emission from Preprotostellar Cores, 2001, ApJ, 557, 193

Ewen H. I., Purcell E. M., Observation of a Line in the Galactic Radio Spectrum: Radiation from Galactic Hydrogen at 1,420 Mc./sec., 1951, Nature, 168, 356

Fazio G. G. et al., The Infrared Array Camera (IRAC) for the Spitzer Space Telescope, 2004, ApJS, 154, 10

Fiedler R. A., Mouschovias T. C., Ambipolar diffusion and star formation: Formation and contraction of axisymmetric cloud cores. I - Formulation of the problem and method of solution, 1992, ApJ, 391, 199

Field G. B., Goldsmith D. W., Habing H. J., Cosmic-Ray Heating of the Interstellar Gas, 1969, ApJ, 155, L149

Fleck R. C., Jr., Clark F. O., A turbulent origin for the rotation of molecular clouds, 1981, ApJ, 245, 898

Foster P. N., Chevalier R. A., Gravitational Collapse of an Isothermal Sphere, 1993, ApJ, 416, 303

Frerking M. A., Langer W. D., Wilson R. W., The relationship between carbon monoxide abundance and visual extinction in interstellar clouds, 1982, ApJ, 262, 590

Garden R. P., Hayashi M., Hasegawa T., Gatley I., Kaifu N., A spectroscopic study of the DR 21 outflow source. III - The CO line emission, 1991, ApJ, 374, 540

Gazol A., Vázquez-Semadeni E., Kim J., 2005, in Revista Mexicana de Astronomia y Astrofisica, vol. 27, Vol. 23, Torres-Peimbert S., MacAlpine G., ed, Revista Mexicana de Astronomia y Astrofisica Conference Series, p. 23

Greene T. P., Wilking B. A., Andre P., Young E. T., Lada C. J., Further mid-infrared study of the rho Ophiuchi cloud young stellar population: Luminosities and masses of pre-main-sequence stars, 1994, ApJ, 434, 614

Griffin M. J., Ade P. A. R., Orton G. S., Robson E. I., Gear W. K., Nolt I. G., Radostitz J. V., Submillimeter and millimeter observations of Jupiter, 1986, Icarus, 65, 244

Griffin M. J., Orton G. S., The near-millimeter brightness temperature spectra of Uranus and Neptune, 1993, Icarus, 105, 537

Gutermuth R. A., Megeath S. T., Pipher J. L., Williams J. P., Allen L. E., Myers P. C., Raines S. N., The Initial Configuration of Young Stellar Clusters: A K-Band Number Counts Analysis of the Surface Density of Stars, 2005, ApJ, 632, 397

Gutermuth R. A., Myers P. C., Megeath S. T., Allen L. E., Pipher J. L., Muzerolle J., Porras A., Winston E., Fazio G., Spitzer Observations of NGC 1333: A Study of Structure and Evolution in a Nearby Embedded Cluster, 2008, ApJ, 674, 336

Hartley M., Tritton S. B., Manchester R. N., Smith R. M., Goss W. M., A catalogue of southern dark clouds, 1986, A&AS, 63, 27

Hildebrand R. H., The Determination of Cloud Masses and Dust Characteristics from Submillimetre Thermal Emission, 1983, QJRAS, 24, 267

Hoare M. G., Kurtz S. E., Lizano S., Keto E., Hofner P., Ultracompact Hii Regions and the Early Lives of Massive Stars, 2007, Protostars and Planets V, 181

Hora J. L. et al., 2004, in Society of Photo-Optical Instrumentation Engineers (SPIE) Conference Series, Vol. 5487, Mather J. C., ed, Society of Photo-Optical Instrumentation Engineers (SPIE) Conference Series, p. 77

Houck J. R. et al., 2004, in Society of Photo-Optical Instrumentation Engineers (SPIE) Conference Series, Vol. 5487, Mather J. C., ed, Optical, Infrared, and Millimeter Space Telescopes, p. 62

Ikeuchi S., Spitzer L., Jr., Scattering of shock waves by a spherical cloud, 1984, ApJ, 283, 825

Jeans J. H., The Stability of a Spherical Nebula, 1902, Royal Society of London Philosophical Transactions Series A, 199, 1

Jenkins E. B., Savage B. D., Ultraviolet photometry from the Orbiting Astronomical Observatory. XIV. An extension of the survey of Lyman-alpha absorption from interstellar hydrogen., 1974, ApJ, 187, 243

Johnson H. L., Infrared Stellar Photometry., 1962, ApJ, 135, 69

Johnstone D., Di Francesco J., Kirk H., An Extinction Threshold for Protostellar Cores in Ophiuchus, 2004, ApJ, 611, L45

Johnstone D., Fich M., Mitchell G. F., Moriarty-Schieven G., Large Area Mapping at 850 Microns. III. Analysis of the Clump Distribution in the Orion B Molecular Cloud, 2001, ApJ, 559, 307

Kauffmann J., Bertoldi F., Bourke T. L., Evans N. J., II, Lee C. W., MAMBO mapping of Spitzer c2d small clouds and cores, 2008, A&A, 487, 993

Kenyon S. J., Hartmann L., Pre-Main-Sequence Evolution in the Taurus-Auriga Molecular Cloud, 1995, ApJS, 101, 117

Kirk J. M., Ward-Thompson D., André P., The initial conditions of isolated star formation - VI. SCUBA mappingof pre-stellar cores, 2005, MNRAS, 360, 1506

Kleinmann S. G., 1992, in Astronomical Society of the Pacific Conference Series, Vol. 34, Filippenko A. V., ed, Robotic Telescopes in the 1990s, p. 203

Kolmogorov A., The Local Structure of Turbulence in Incompressible Viscous Fluid for Very Large Reynolds' Numbers, 1941, Akademiia Nauk SSSR Doklady, 30, 301

Lada C. J., 1987, in IAU Symposium, Vol. 115, Peimbert M., Jugaku J., ed, Star Forming Regions, p. 1

Lada C. J., Wilking B. A., The nature of the embedded population in the Rho Ophiuchi dark cloud - Mid-infrared observations, 1984, ApJ, 287, 610

Ladd N., Purcell C., Wong T., Robertson S., Beam Size, Shape and Efficiencies for the ATNF Mopra Radio Telescope at 86-115 GHz, 2005, , 22, 62

Landsman W. B., 1993, in Astronomical Society of the Pacific Conference Series, Vol. 52, Hanisch R. J., Brissenden R. J. V., Barnes J., ed, Astronomical Data Analysis Software and Systems II, p. 246

Lang K. R., 1980, Astrophysical Formulae. A Compendium for the Physicist and Astrophysicist.

Langer W. D., Goldsmith P. F., Carlson E. R., Wilson R. W., Evidence for isotopic fractionation of carbon monoxide in dark clouds, 1980, ApJ, 235, L39

Larson R. B., Turbulence and star formation in molecular clouds, 1981, MNRAS, 194, 809

Lee C. W., Myers P. C., A Catalog of Optically Selected Cores, 1999, ApJS, 123, 233

Lilley A. E., The Association of Gas and Dust from 21-CM Hydrogen Radio Observations., 1955, ApJ, 121, 559

Lo K. Y., Sargent W. L. W., A search for intergalactic neutral hydrogen in three nearby groups of galaxies, 1979, ApJ, 227, 756

Lombardi M., Alves J., Mapping the interstellar dust with near-infrared observations: An optimized multi-band technique, 2001, A&A, 377, 1023

Lovas F. J., Krupenie P. H., Microwave spectra of molecules of astrophysical interest. 7. Carbon monoxide, carbon monosulfide, and silicon monoxide., 1974, Journal of Physical and Chemical Reference Data, 3, 245

Mac Low M.-M., The Energy Dissipation Rate of Supersonic, Magnetohydrodynamic Turbulence in Molecular Clouds, 1999, ApJ, 524, 169

Makovoz D., Roby T., Khan I., Booth H., 2006, in Society of Photo-Optical Instrumentation Engineers (SPIE) Conference Series, Vol. 6274, Society of Photo-Optical Instrumentation Engineers (SPIE) Conference Series

Mathis J. S., Interstellar dust and extinction, 1990, ARA&A, 28, 37

McKee C. F., Photoionization-regulated star formation and the structure of molecular clouds, 1989, ApJ, 345, 782

Melnick J., 1977, Ph.D. thesis, CALIFORNIA INSTITUTE OF TECHNOLOGY.

Mestel L., Spitzer L., Jr., Star formation in magnetic dust clouds, 1956, MNRAS, 116, 503

Motte F., André P., The circumstellar environment of low-mass protostars: A millimeter continuum mapping survey, 2001, A&A, 365, 440

Motte F., Andre P., Neri R., The initial conditions of star formation in the rho Ophiuchi main cloud: wide-field millimeter continuum mapping, 1998, A&A, 336, 150

Myers P. C., Dense cores in dark clouds. III - Subsonic turbulence, 1983, ApJ, 270, 105

Myers P. C., Benson P. J., Dense cores in dark clouds. II - NH3 observations and star formation, 1983, ApJ, 266, 309

Myers P. C., Fuller G. A., Mathieu R. D., Beichman C. A., Benson P. J., Schild R. E., Emerson J. P., Near-infrared and optical observations of IRAS sources in and near dense cores, 1987, ApJ, 319, 340

Myers P. C., Ladd E. F., Bolometric temperatures of young stellar objects, 1993, ApJ, 413, L47

Myers P. C., Linke R. A., Benson P. J., Dense cores in dark clouds. I - CO observations and column densities of high-extinction regions, 1983, ApJ, 264, 517

Nyman L.-Å., Lerner M., Nielbock M., Anciaux M., Brooks K., Chini R., Albrecht M., Lemke R., Kreysa E., Zylka R., Johansson L. E. B., Bronfman L., Kontinen S., Linz H., Stecklum B., SIMBA explores the southern sky, 2001, The Messenger, 106, 40

Obukhov A. M., Some Specific Features of Atmospheric Turbulence, 1962, J. Geophys. Res., 67, 3011

Ossenkopf V., Henning T., Dust opacities for protostellar cores, 1994, A&A, 291, 943

Persson S. E., Murphy D. C., Krzeminski W., Roth M., Rieke M. J., A New System of Faint Near-Infrared Standard Stars, 1998, AJ, 116, 2475

Pipher J. L. et al., 2004, in Society of Photo-Optical Instrumentation Engineers (SPIE) Conference Series, Vol. 5487, Mather J. C., ed, Society of Photo-Optical Instrumentation Engineers (SPIE) Conference Series, p. 234

Pringle J. E., Allen R. J., Lubow S. H., The formation of molecular clouds, 2001, MNRAS, 327, 663

Rieke G. H. et al., 2004, in Society of Photo-Optical Instrumentation Engineers (SPIE) Conference Series, Vol. 5487, Mather J. C., ed, Society of Photo-Optical Instrumentation Engineers (SPIE) Conference Series, p. 50

Rohlfs K., Wilson T. L., 2004, Tools of radio astronomy

Savage B. D., Bohlin R. C., Drake J. F., Budich W., A survey of interstellar molecular hydrogen. I, 1977, ApJ, 216, 291

Schuller F., Omont A., Felli M., Testi L., Bertoldi F., Menten K. M., 2005, in ESA Special Publication, Vol. 577, Wilson A., ed, ESA Special Publication, p. 235

Shaw A. M., 2006, Astrochemistry: From Astronomy to Astrobiology

Shu F. H., Adams F. C., Lizano S., Star formation in molecular clouds - Observation and theory, 1987, ARA&A, 25, 23

Skrutskie M. F. et al., The Two Micron All Sky Survey (2MASS), 2006, AJ, 131, 1163

Solomon P. M., Rivolo A. R., Barrett J., Yahil A., Mass, luminosity, and line width relations of Galactic molecular clouds, 1987, ApJ, 319, 730

Spezzi L., Alcalá J. M., Covino E., Frasca A., Gandolfi D., Oliveira I., Chapman N., Evans N. J., II, Huard T. L., Jørgensen J. K., Merín B., Stapelfeldt K. R., The Young Population of the Chamaeleon II Dark Cloud, 2008, ApJ, 680, 1295

Stahler S. W., Shu F. H., Taam R. E., The evolution of protostars. I - Global formulation and results, 1980, ApJ, 241, 637

Stamatellos D., Whitworth A. P., Ward-Thompson D., The dust temperatures of the pre-stellar cores in the ρ Oph main cloud and in other star-forming regions: consequences for the core mass function, 2007, MNRAS, 379, 1390

Stern D., Eisenhardt P., Gorjian V., Kochanek C. S., Caldwell N., Eisenstein D., Brodwin M., Brown M. J. I., Cool R., Dey A., Green P., Jannuzi B. T., Murray S. S., Pahre M. A., Willner S. P., Mid-Infrared Selection of Active Galaxies, 2005, ApJ, 631, 163

Sternberg A., Neufeld D. A., The Ratio of Ortho- to Para-H_2 in Photodissociation Regions, 1999, ApJ, 516, 371

Stone J. M., Ostriker E. C., Gammie C. F., Dissipation in Compressible Magnetohydrodynamic Turbulence, 1998, ApJ, 508, L99

Tafalla M., Mardones D., Myers P. C., Caselli P., Bachiller R., Benson P. J., L1544: A Starless Dense Core with Extended Inward Motions, 1998, ApJ, 504, 900

Tafalla M., Myers P. C., Caselli P., Walmsley C. M., Comito C., Systematic Molecular Differentiation in Starless Cores, 2002, ApJ, 569, 815

Thomson W., Is the Sun becoming Colder or Hotter?, 1892, PASP, 4, 105

Trumpler R. J., Observational Evidence of a Relativity Red Shift in Class O Stars, 1935, PASP, 47, 249

Ulich B. L., Haas R. W., Absolute calibration of millimeter-wavelength spectral lines., 1976, ApJS, 30, 247

van Buren D., The initial mass function and global rates of mass, momentum, and energy input to the interstellar medium via stellar winds, 1985, ApJ, 294, 567

Ward-Thompson D., André P., Crutcher R., Johnstone D., Onishi T., Wilson C., An Observational Perspective of Low-Mass Dense Cores II: Evolution Toward the Initial Mass Function, 2007, Protostars and Planets V, 33

Ward-Thompson D., André P., Kirk J. M., The initial conditions of isolated star formation - V. ISOPHOT imaging and the temperature and energy balance of pre-stellar cores, 2002, MNRAS, 329, 257

Ward-Thompson D., Motte F., Andre P., The initial conditions of isolated star formation - III. Millimetre continuum mapping of pre-stellar cores, 1999, MNRAS, 305, 143

Ward-Thompson D., Scott P. F., Hills R. E., Andre P., A Submillimetre Continuum Survey of Pre Protostellar Cores, 1994, MNRAS, 268, 276

Weir N., 1994, Automated analysis of the Digitized Second Palomar Sky Survey: System design, implementation, and initial results

Wentzel D. G., Pulsar Scintillations due to Distant Streaming Cosmic Rays, 1969, ApJ, 156, L91

Whitney B. A., Wood K., Bjorkman J. E., Cohen M., Two-dimensional Radiative Transfer in Protostellar Envelopes. II. An Evolutionary Sequence, 2003, ApJ, 598, 1079

Wilking B. A., Lada C. J., Young E. T., IRAS observations of the Rho Ophiuchi infrared cluster - Spectral energy distributions and luminosity function, 1989, ApJ, 340, 823

Williams J. P., Blitz L., McKee C. F., The Structure and Evolution of Molecular Clouds: from Clumps to Cores to the IMF, 2000, Protostars and Planets IV, 97

Wilson E., W. Muller, Ferris D., MOPS - Mopra Spectrometer, 2006, url-http://www.atnf.csiro.au/news/newsletter/jun06

Wilson T. L., Rood R., Abundances in the Interstellar Medium, 1994, ARA&A, 32, 191

Wolfire M. G., Hollenbach D., McKee C. F., Tielens A. G. G. M., Bakes E. L. O., The neutral atomic phases of the interstellar medium, 1995, ApJ, 443, 152

Wright E. L., Recalibration of the far-infrared brightness temperatures of the planets, 1976, ApJ, 210, 250

Zylka R., Pocket Cookbook for MOPSI software, 1996, url-http://www.iram.es/IRAMES/otherDocuments/manuals/Datared/pockcoo.ps